

# **CAD-integrated constitutive modelling, analysis, and design of masonry structures**

**Tobias Christoph Teschemacher**

Vollständiger Abdruck der von der School of Engineering and Design der Technischen Universität München zur Erlangung eines

**Doktors der Ingenieurwissenschaften**

genehmigten Dissertation.

Vorsitz:

Priv.-Doz. Dr.-Ing. habil. Stefan Kollmannsberger

Prüfer:innen der Dissertation:

1. Prof. Dr.-Ing. Kai-Uwe Bletzinger
2. Prof. Dr.-Ing. Alexander Scheuermann
3. Assoc. Prof. Dr. Pooyan Dadvand

Die Dissertation wurde am 21.06.2022 bei der Technischen Universität München eingereicht und durch die TUM School of Engineering and Design am 10.04.2023 angenommen.



Schriftenreihe des Lehrstuhls für Statik  
TU München

Band 57

**Tobias Teschemacher**

**CAD-INTEGRATED CONSTITUTIVE MODELLING, ANALYSIS,  
AND DESIGN OF MASONRY STRUCTURES**

München 2023

Veröffentlicht durch

Kai-Uwe Bletzinger  
Lehrstuhl für Statik  
Technische Universität München  
Arcisstr. 21  
80333 München

Telefon: +49(0)89 289 22422  
Telefax: +49(0)89 289 22421  
E-Mail: [kub@tum.de](mailto:kub@tum.de)  
Internet: [www.cee.ed.tum.de/st](http://www.cee.ed.tum.de/st)

ISBN: 978-3-943683-70-7

© Lehrstuhl für Statik, TU München

---

## Abstract

This thesis presents innovative methodological developments for a seamless computer-aided design-integrated simulation and structural assessment of masonry in a numerical multiphysics environment.

A numerically classified experimental program is processed to obtain a quantitative classification of masonry, for which a novel computational constitutive law is developed and presented. Furthermore, finite element-based physics are enhanced to cope with the properties of computer-aided design descriptions towards the demands of masonry structures. With the presented avenues increased possibilities arise in the structural assessment of buildings, including post-damage load-carrying behaviors and limit stress states for various impact scenarios. This is demonstrated in a selection of relevant benchmark problems. With the presented choice of small-scale tests, an eventual solution scheme towards the predictability by simulation of historic and new buildings shall be introduced.

The development of the computer-aided design-integrated methods is presented in a manner that reaches beyond the needs of masonry and shall enlighten the general applicability of the proposed approaches. The established technologies are introduced along with realized code developments, specifically addressing a unified implementation for a generic integration within various finite element software environments.

---

## Kurzfassung

In dieser Arbeit werden neuartige methodische Entwicklungen für eine nahtlose CAD-integrierte Simulation und statische Bewertung von Mauerwerk in einer numerischen Multiphysik-Umgebung vorgestellt.

Ein numerisch klassifiziertes Versuchsprogramm wird vorgestellt, um eine quantitative Klassifizierung von Mauerwerk zu erhalten, für die ein neuartiges konstitutives Gesetz entwickelt und vorgestellt wird. Darüber hinaus wird die Finite-Elemente-Physik erweitert, um die Eigenschaften von CAD-Beschreibungen auf die Anforderungen von Mauerwerksbauten abzustimmen. Mit den vorgestellten Ansätzen ergeben sich erweiterte Möglichkeiten in der bautechnischen Bewertung von Bauwerken, einschließlich des Tragverhaltens nach Schäden und der Grenzspannungszustände für verschiedene Einwirkungsszenarien. Dies wird an einer Auswahl von relevanten Benchmark-Problemen demonstriert. Mit der vorgestellten Selektion von kleinmaßstäblichen Versuchen soll ein möglicher Weg zur Vorhersagbarkeit durch Simulation von historischen und neuen Gebäuden aufgezeigt werden.

Die Entwicklung der CAD-integrierten Methoden wird in einer Weise dargestellt, die über die Anforderungen des Mauerwerks hinausgehen und die allgemeine Anwendbarkeit der Methoden beleuchten soll. Die etablierten Technologien werden zusammen mit realisierten Software-Entwicklungen vorgestellt, wobei insbesondere auf eine einheitliche Implementierung für eine generische Integration in verschiedene Finite-Elemente-Softwareumgebungen eingegangen wird.

---

## Acknowledgements

This work would not have been possible without the incredible help from my colleagues, supervisors, friends, family, and my partner.

I want to express my gratitude to all of my colleagues at the Chair of Structural Analysis for their unwavering support during my time there. Specifically, Philipp Bucher for his continuous support in finding weird bugs and for the endless amount of coffees. Furthermore, Klaus Sautter who has consistently helped me in staying motivated. Thanks for a lot of fun with my long term room colleagues Iñigo López Canalejo, Andreas Apostolatos, and Altuğ Emiroğlu. And the others, among all: Ihar Antanou, Daniel Baumgärtner, Anna Bauer, Michael Breitenberger, Martin Fußeder, Aditya Ghantasala, Ann-Kathrin Goldbach, Manuel Meßmer, Reza Najian Asl, Thomas Oberbichler, Máté Pentek, Benedikt Philipp, Sharokh Shayegan, Veronika Singer, and Suneth Warnakulasuriya. I also want to thank my colleagues at CIMNE, who have supported me since my master's thesis: Vicente Mataix Ferrándiz, Carlos Roig, and Ruben Zorrilla Martínez. A big thank you as well to all of my UQ colleagues who have helped me through Seddon: Kristie Higginson, Ezgi Kaya, Christian Kudisonga, Julian Mendez, Chuang Miao, Silvia Palmieri, Nicolas Soro, Peter Wilson, and Davide Wüthrich.

I wish to thank my supervisors for their constant encouragement and advice: Kai-Uwe Bletzinger for getting me to the chair and giving me great freedom, and achieving to guide me to a good outcome. Roland Wüchner for the endless discussions, motivation, and overall guidance. Riccardo Rossi for great advises in a broader field of computational mechanics. Antonia Larese for many discussions about various simulations. Pooyan Dadvand for endless detailed meetings and teaching me programming. Dilum Fernando for getting me to Brisbane and helping me to run the experimental tests. Alexander Scheuermann for overtaking the supervision in Brisbane and for great professional advises.

My family deserves a big thank you for their support during but also until the time of my dissertation. Having their support was a great help in achieving this goal. The biggest thanks goes to my girlfriend and partner in crime who has supported me through ups and downs and helped me finish everything up.

Tobias Teschemacher  
München  
2023



# Contents

1	Introduction	1
2	Building Information Modeling and Computer-Aided Design-Integrated Analysis	7
2.1	CAD boundary representation models . . . . .	9
2.2	Parametric modeling . . . . .	11
2.3	Analysis enhanced CAD models . . . . .	11
2.4	BIM-induced digital twin with CAD . . . . .	13
3	Finite Element Methods	15
3.1	Fundamentals of geometrical expressions . . . . .	17
3.1.1	Numerical integration of surfaces . . . . .	17
3.1.2	Numerical integration of curves . . . . .	19
3.1.3	Numerical integration of curves on surfaces . . . . .	19
3.2	Non-Uniform Rational B-Spline (NURBS) entities . . . . .	20
3.2.1	Continuity of NURBS . . . . .	21
3.2.2	NURBS refinement . . . . .	21
3.3	Continuum mechanics and kinematic formulations for structural analyses	22
3.3.1	Solid-based formulations . . . . .	22
3.3.2	Surface-based formulations . . . . .	22
3.3.3	Curve-based formulations . . . . .	28
3.4	Isogeometric Analysis (IGA) and Isogeometric B-Rep Analysis (IBRA) . .	28
3.4.1	Numerical integration of trimmed surfaces . . . . .	29
3.4.2	Numerical integration of curves on surfaces/edges . . . . .	31
3.4.3	Numerical integration of coupling edges . . . . .	31
3.5	Properties of CAD-based analysis . . . . .	33
3.5.1	Solid model . . . . .	35
3.5.2	Surface model vs. mid surface model . . . . .	36
3.5.3	Inter-patch connections for geometrical continuities . . . . .	36
3.5.4	Geometrical discontinuities . . . . .	38
3.5.5	Model tolerance . . . . .	39
3.5.6	Patch conditioning . . . . .	39
3.5.7	Trimming . . . . .	40
3.5.8	Preparation of the model . . . . .	42
3.6	Immersed methods . . . . .	42

3.7	Material Point Method (MPM) . . . . .	46
3.8	Multiphysics and multidomain coupling . . . . .	48
3.8.1	Monolithic coupling approaches . . . . .	49
3.8.2	Partitioned approaches . . . . .	54
4	Simulation of Masonry Structures . . . . .	57
4.1	Macro parameter definition and numerical driven design of the test specimens . . . . .	59
4.1.1	Masonry reference volume element . . . . .	60
4.1.2	Determination of experiment specimen size . . . . .	61
4.2	Experimental macro characterization of masonry structures . . . . .	66
4.2.1	Instrumentation - Digital Image Correlation (DIC) . . . . .	67
4.2.2	Fabrication of test specimen . . . . .	68
4.2.3	Compression tests . . . . .	69
4.2.4	Tension tests . . . . .	74
4.2.5	Shear tests . . . . .	76
4.2.6	Bending tests . . . . .	85
4.2.7	Summary of masonry macro material properties . . . . .	89
4.2.8	Conclusion of material tests . . . . .	89
4.3	Orthotropic damage model for masonry . . . . .	90
4.3.1	Continuum tension/compression damage model . . . . .	91
4.3.2	Orthotropic damage model . . . . .	94
4.4	Numerical discretization methods for masonry . . . . .	98
4.4.1	FEM approaches for masonry simulation . . . . .	98
4.4.2	Stabilization to different shape descriptions . . . . .	101
5	Examples and Investigations . . . . .	103
5.1	Uniaxial numerical tests of <i>Brisbane</i> masonry . . . . .	103
5.2	Shear wall . . . . .	106
5.2.1	Wall with varying pre-pressure . . . . .	108
5.2.2	Wall with window opening . . . . .	109
5.2.3	Discussion of results and methodology . . . . .	115
5.3	Out-of-plane strength of unreinforced masonry wall . . . . .	117
5.3.1	Variation of pre-compression . . . . .	119
5.3.2	Discussion of results and methodology . . . . .	121
5.4	Masonry arch . . . . .	124
5.4.1	Asymmetric loaded masonry arch . . . . .	124
5.4.2	Symmetric loading . . . . .	128
5.4.3	Thick arch . . . . .	129
5.4.4	Parametric arch model . . . . .	132
5.4.5	Discussion of results and methodology . . . . .	134

5.5	Masonry cross vault . . . . .	135
5.5.1	Simulation of masonry cross vault . . . . .	137
5.5.2	Turned masonry bond layout . . . . .	140
5.5.3	Discussion of results and methodology . . . . .	142
5.6	Church roof . . . . .	143
5.7	Masonry house . . . . .	150
6	Computer Aided Engineering (CAE) Workflow . . . . .	155
6.1	FEM-based CAE workflow . . . . .	155
6.2	CAD-based CAE workflow . . . . .	158
6.2.1	Interface between CAD and IBRA solver . . . . .	160
6.2.2	Solver-integrated CAD geometry kernel . . . . .	162
6.3	Geometrical interfaces . . . . .	164
6.4	Analysis embedded Modelers and Processes . . . . .	167
6.5	Quadrature point geometry based unified FEM simulations . . . . .	169
6.5.1	IBRA simulation with CAD-based geometries . . . . .	171
6.5.2	The MPM as extension of FEM . . . . .	172
6.5.3	Unifying inter physic coupling . . . . .	174
6.6	Cocodrilo: Pre- and post-processing . . . . .	177
6.6.1	Interaction with the CAD-data . . . . .	177
6.6.2	Software architecture . . . . .	180
6.6.3	Data preparation algorithms . . . . .	182
6.6.4	Post-processing . . . . .	184
7	Summary and Outlook . . . . .	185
7.1	Summary of simulation of masonry . . . . .	185
7.2	Summary of CAD-integrated analysis methodologies . . . . .	187
A	Uniaxial compression Bézier-curve based relaxation . . . . .	189
B	Regularization . . . . .	193



# 1 Introduction

Civil engineering is among the oldest guilds in the world with structural analysis being one of its major duties, which itself has evolved heavily throughout many centuries. Ancient Egyptians, Greeks, and Romans are famous for having created monuments and buildings which endured many centuries even though it is not known that they have followed deep theoretical fundamentals in the construction design, rather than empirically driven methods [4]. However, with ancient mathematicians like Pythagoras (about 582 -500 B.C.) and Archimedes (287-212 B.C.) initial principles about angle theorems, static and gravity terms were introduced and helped the analyses to gain more fundamental bases. Throughout the middle ages, the subject had a deduction of professionalism and it was up to Sir Isaac Newton (1642-1727) to put the foundations of modern structural analysis, with the science of gravitation, forces, and motion, spanning the field of mechanics. Since then, the area has found an immense growth with broad scientific fundamentals. Finally, the digitalization in the twentieth century aided to develop almost infinite possibilities for structural analyses, with the introduction of the finite element method being probably one of the most significant milestones.

Even though the scientific development was immense, the challenges of exhaustively estimating and describing the structural behavior of some ancient monuments remain. Furthermore, environmental phenomena and aging has a significant impact on the structural safety of those historical structures, whereby, natural disasters as fire, earth quakes, flood loads, or heavy wind loads can lead to fatal consequences. With the apparent climate change, those events are likely to increase to yet unknown magnitudes. Thus, a large amount of our cultural heritage is in urgent danger of collapsing, which makes it inevitable to continuously analyze existing structures to prevent failure. Meanwhile, appropriate predictions might help to avoid unnecessary structural reinforcements for economic reasons.

In the process of structural analysis on existing buildings, initially, the structure needs to be captured geometrically, which is habitually a difficult duty as many times few construction plans or models exist. The digital remodeling is mostly done in Computer-Aided Design (CAD) software, as this provides simplified opportunities in drawing and editing shapes. Furthermore, it provides endless opportunities to visualize and render the drafts. The resulting CAD models are a pure digital visualization, without any physical information. To gain deeper insights in the structural behavior they need to

be enhanced by information about material, kinematic behavior, supports, connections, and loading. This merge of geometrical and physical properties provides a data base for the analyses, which lately may be seen as a specification of Building Information Modeling (BIM).

To step into the field of Computer-Aided Engineering (CAE), the CAD-described models require a transformation into an analysis suitable model, which is commonly named the *Digital Twin* of the structure. Apart from analytical schemes, using the finite element method (FEM) is nowadays one of the most prominent approaches for structural assessments. FEM procedures [258, 22, 86] are relying on a finite amount of geometrical shapes, called elements. Within classical approaches those geometries are required to be in the form of primitives such as e.g. triangles or quadrilaterals, whereby the group of primitives is called mesh. It is specifically suitable to compute on primitives as those are handled and evaluated easily and most geometrical operations are computationally efficient. However, for an accurate expression of a complex shape also a vast amount of primitives is required, which increases the computational costs and memory consumption.

CAD on the other end is mostly relying on Non-Uniform B-Splines (NURBS) for the expression of complex shapes. One of the reasons for its application is that NURBS require only few control points for the expression of highly curved shapes. This decreases memory consumption, which may be critical for large models. Additionally, simple transformations, such as translations or rotations would require a significant overhead once many nodes of the mesh are needed to be considered. However, to achieve an automated FEM analysis on CAD-models those would need to be remodeled within the so-called meshing process. Meshing intrinsically applies a geometrical model error, may be costly, may require user interaction and needs to fulfill certain criteria, above the chordal error to achieve reliable results from the FEM simulations ([124, 19, 233, 137]). Specifically for free form shapes, which are habitually given for membrane or shell structures, it may be required to create a very fine mesh to reduce the chordal error of each primitive and to better approximate the expected solution. To avoid the remedy of meshing and being capable of keeping the exact geometry, Hughes et al. [107] introduced the so called Isogeometric Analysis (IGA), which is directly employing NURBS shapes as the geometrical counterpart of the finite elements. The original form of this FEM specification is relying on untrimmed NURBS patches with their mathematical boundaries. However, most CAD systems do provide a collection of connected NURBS forms which are frequently trimmed to express complex objects with more simplified efforts. This way of expressing bodies is commonly called Boundary Representation (B-Rep). Accordingly, IGA has been enhanced by Breitenberger et al. [40] with the possibility to simulate on multiple trimmed and coupled NURBS-based patches. This extension has been named the Isogeometric B-Rep Analysis (IBRA).

---

CAD systems provide various possibilities to technically draw objects. The B-Rep technique is hereby one of the most common approaches. It expresses physical objects by its geometrical delineations, the boundaries. For the CAD-integrated simulation this provides an intrinsic problematic as no native description of solids is provided from CAD. Accordingly, CAD-integrated analysis with IGA/IBRA is mostly limited to the analysis on one- and two-dimensional shapes.

For the structural assessment, finite element simulations employ numerous kinematic element formulations including solids, shells, beams, and auxiliary elements as e.g. springs, which each represent a compromise between dimensional fidelity and computational expense. Apart from analytical and continuum based approaches, mesh free or numerical particle methods find increasing application as well. The research of this dissertation aims to facilitate simulations capable to express complex geometries and structures with justifiable computational costs to analyze full-scale buildings. On this end, auxiliary elements and beams typically have increasing challenges when modeling complexly shaped structures. Solid and particle based modeling allows almost infinite possibilities in the geometrical specification of constructions, however, frequently the computational efforts prevent the application in large structural analyses processes. Thus, within this thesis the focus shall be placed on the description of surface-based shell structures, which allow the accurate expression of many geometrical shapes, under consideration of reasonable computation costs.

IGA forms are suitable to express shell-based numerical analyses and intrinsically enables CAD-integrated analysis on B-Rep models. Thus, it is chosen as the core numerical technology within this research.

After all, IGA is one of numerous FEM discretizations. Distinct avenues are required to be able to cope with different problems, where frequently one approach may have advantages on some issues and disadvantages on others. Whereas IGA is specifically suitable to precisely express highly curved thin-walled structures, it may be less informative on largely deflecting objects or solid-described structures. A famous group among FEMs are the particle-based methods, as e.g. the Discrete Element Method (DEM) or the Material Point Method (MPM). Those approaches are typically strong in expressing large deflections, however, have increasing complexities in the quantitatively correct simulation of stresses within continua. Accordingly, some models require a combination of approaches to cope with the apparent physical properties, which results in the field of multiphysics. Famous examples in this area are e.g. the Fluid-Structure Interaction (FSI) [250, 109], the DEM-FEM interaction for impacts [150, 201, 205, 203], DEM-IGA [226, 89] or the MPM-FEM coupling [51, 136].

Multiphysics simulations require two important steps, among others: a mathematical formulation which tries to enforce equilibrium between the domains and geometrical identities which are capable of translating the information of one domain to the other. To address the latter requirement, the properties of the FEM geometry have to be

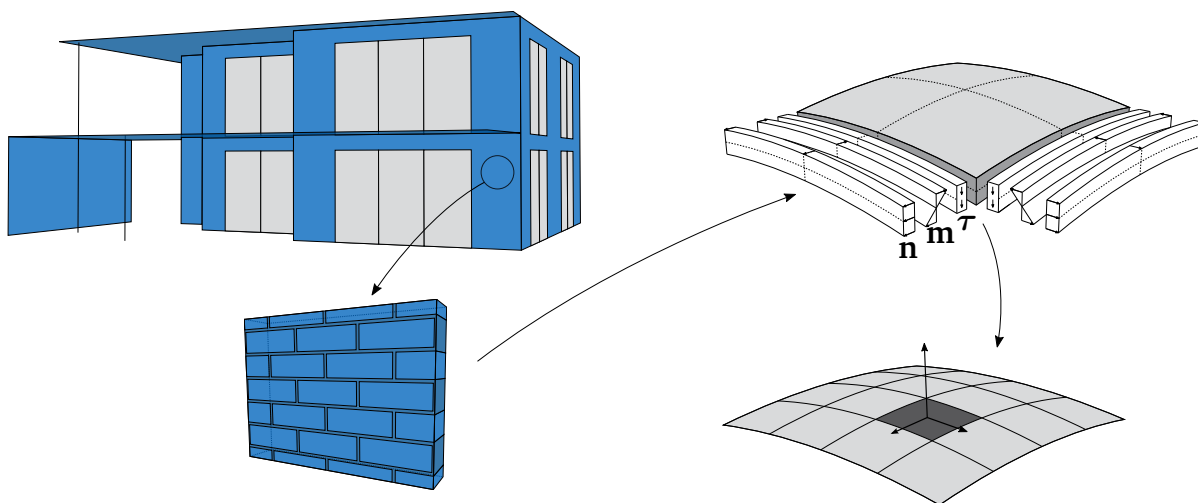


**Figure 1.1:** Masonry building towards a numerical simulation.

streamlined towards the similarities to extract the exchange information. Accordingly, a variety of finite element approaches to a multiphysics simulation are presented in this dissertation. These approaches are either monolithic or staggered in their resolution. The presented research does not concentrate on the informative mathematical operations that were obtained from the literature. The geometrical streamlining of various approaches is the main focus.

The previously discussed numerical avenues are primarily presented in a problem independent arrangement. In the subsequent discussion those are merged with the apparent physical properties of masonry. Figure 1.1 is presenting the challenges of this dissertation. The mechanical material information of the brick-mortar composite must be gathered first. The next step is to identify a constitutive relation. This knowledge can be scaled up, incorporated within a kinematic expression, and placed in numerical simulation environment (such as IGA). Those steps are required to understand masonry and digitally represent it. This is a milestone towards being able to predict the behaviour of existing historical structures, or future buildings.

Masonry can be studied within different scales: micro, meso, and macro. The focus of this dissertation concentrates on full scale structures, which typically demand the usage of macro models for efficiency. Local impacts are of lesser significance in this work than the macroscopic structural behaviour. This requires the study of constitutive models to make them more suitable for the assessment of the employed orthotropic construction material. Whilst developing a model, also the estimation of the material parameters play a crucial role in an accurate assessment. This can either rely on detailed micro models from all constituents up to experimental tests from larger specimen. In this scope, a homogenization of the material parameters is achieved through a comprehensive experimental study. The presented research will examine the material characteristics for

---

a full orthotropic expression of the material. To numerically express the results of the experimental tests, a novel constitutive model is presented. This model is based on the merge of the isotropic model from Petracca et al. [181] and an orthotropic mapping as per Pelà et al. [179]. This model is suitable to accurately cover most of the macroscopic masonry phenomena.

The discussed numerical methods are combined with the constitutive model to enable a fully CAD-integrated large scale structural analyses of masonry buildings. Possibilities for evaluating limit states, force distributions, and load bearing behaviors emerge with the novelties that have been suggested. This is demonstrated within a selection of examples. These cover the main structural members that are apparent in the majority of masonry buildings.

To process the CAD-integrated analyses of the previously mentioned numerical methods in an efficient way, a novel software architecture needs to be designed. Most apparent concepts are capable of expressing sole problems, however, a unified code structure may eliminate errors and facilitate subsequent developments. This covers a novel CAD geometry kernel within the solver, which is capable to handle trimmed NURBS-based shapes and to e.g. obtain feasible integration fields, create meshes, or provide spacial delineations. A geometrical entity based upon a single quadrature point is introduced. This geometrical entity can be used as the basis for most numerical problems and is accordingly peculiarly advantageous for the interexchange within multiphysics. Additionally, the unification of the geometry allows fast and eased code developments with complex formulations and methods. Furthermore, conceptual procedures for a software design within CAD are required for the collection and storage of physical information with the connection to the geometries. Therefore, a novel plugin is developed covering user-driven data gathering and formulating the information needed by solvers at specified interfaces.

In summary, the aim of this thesis is the development of a seamless CAD-integrated analysis workflow for masonry structures. Experimental material tests are employed to quantitatively obtain information about the orthotropic behavior of masonry. A novel constitutive law is formulated with the use of the experimental information. Finally, the successful merge of the numerical methods with the material model is presented. This can be seen as a further step in providing correct estimates for historic masonry structures that may need to be reviewed or on new buildings for a more efficient material consumption. A second goal of this research is the generic embodiment of various numerical methods in the scope of CAD-integrated analyses, such as IGA, MPM, and multiphysics problems.

This dissertation is structured as following:

**Chapter 2 – Building Information Modeling and Computer-Aided Design-Integrated Analysis** introduces the concepts and possibilities for the CAD-integrated analysis with respect to BIM.

**Chapter 3 – Finite Element Methods** provides the employed numerical physics and kinematic formulations, with CAD-NURBS-based B-Rep models.

**Chapter 4 – Simulation of Masonry Structures** presents an numerical study for the definition of a masonry test specimen, followed by a experimental material program, aiming to appropriately represent the material behaviour. Furthermore, a novel orthotropic constitutive model for plane stress problems is presented, which can express the observed material phenomena.

**Chapter 5 – Examples and Investigations** displays possible applications of the numerical methods and presents various benchmarks of structural members which are apparent in most masonry buildings. This involves in-plane and out-of-plane problems of flat and curved structures.

**Chapter 6 – Computer Aided Engineering (CAE) Workflow** gives a description of the developed and required software facilities to succeed the CAD-integrated numerical simulations.

**Chapter 7 – Summary and Outlook** summarizes this work and gives an outlook to future developments.

Throughout this dissertation, following footnotes are used to reference the original publications and to mark literal transposition. <sup>a b c d e f</sup>

---

<sup>a</sup>[222] The main scientific research as well as the textual elaboration of the publication were performed by the author of this work.

<sup>b</sup>[246] The main scientific research as well as the textual elaboration of the publication were co-authored by the author of this work.

<sup>c</sup>[228] The main scientific research as well as the textual elaboration of the publication were performed by the author of this work.

<sup>d</sup>[223] The main scientific research as well as the textual elaboration of the publication were performed by the author of this work.

<sup>e</sup>[227] The main scientific research as well as the textual elaboration of the publication were performed by the author of this work.

<sup>f</sup>[229] The main scientific research as well as the textual elaboration of the publication were performed by the author of this work.

## 2 Building Information Modeling and Computer-Aided Design-Integrated Analysis

Within the engineering design process, iterations between different working groups lead to significant overhead in re-drafting and re-modeling of problems, which obstructs the progress, generates preventable errors in necessary conversion including a probable loss of information, and may prevent innovations as reconsideration would come along with larger costs than retaining a more inadequate design. No possible, no provided or no defined interface between individual stages of simulations are some of the apparent problems. A common platform or eased interfaces, that combine and merge geometrical draft, physical properties, different use cases, and external impacts at all stages and times are required to facilitate the design process.

In civil engineering, Building Information Modeling (BIM) is understood as the merge of design with engineering information to provide architecture, civil engineering, construction, and operations an extensive knowledge of the project [215]. However, definitions about the extension of BIM, yet vary largely. Sometimes, it is understood as 3D models instead of various 2D plans, up to scenarios with full integration of processes from construction, life time, until destruction [65, 129, 39]. The necessity of such techniques and tools is nowadays understood widely and plans and stages to establish this in public and private projects are largely in place [239].

An imaginable life time cycle of civil engineering projects is displayed in figure 2.1, including exemplary applications with a focus on structural analyses purposes. The stream exhibits significant advantages where numerous feasibility proofs between the different working groups are required. On the other hand, it turns out as specifically beneficial if numerically evaluated solutions would be directly applied for the design, as e.g. certain optimizations, or load, and internal stress-based form-finding of structures. But not only planning is an essential stage, the environment of BIM is also widely used as the data collector which shall maintain the history of a building, e.g. to cross-validate or assess with measured values the current state. This allows an accurate analysis of the apparent situation and gives an outlook towards future structural safety. To achieve the

## 2 Building Information Modeling and Computer-Aided Design-Integrated Analysis

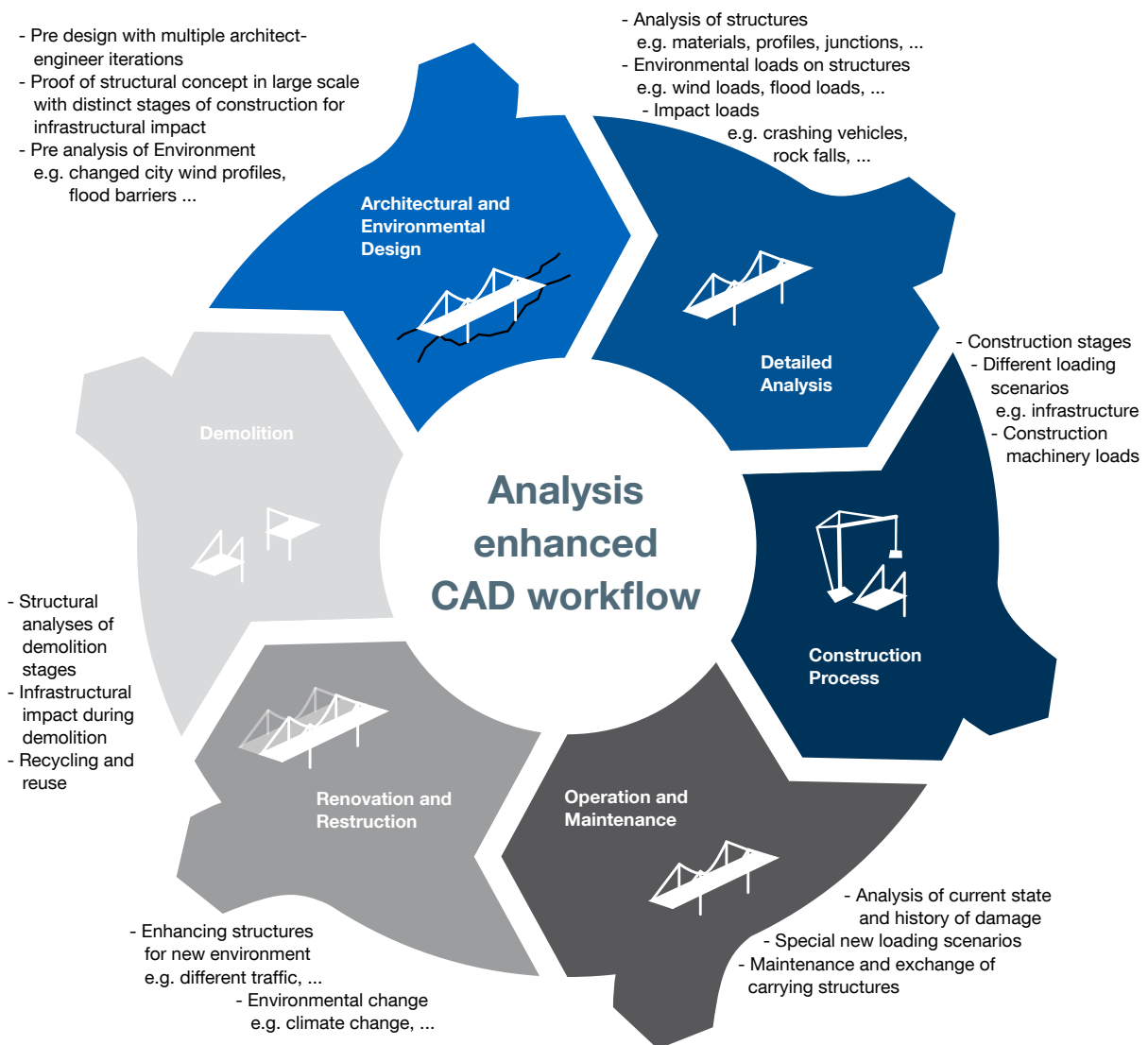


**Figure 2.1:** BIM life cycle for structural analyses problems driven by numerical simulations.

life cycle, it is suggested to employ a consistent usage of digital twins, which shall be detailed further within section 2.4.

Practice shows that succeeding the unified model within a single draft is rather theoretical and is currently complicating the work more than simplifying exchanges. However, many possibilities will arise in near future amid seamless innovations in the field. Accordingly, understanding the apparent state of investigation will help to introduce facilitated exchanges where possible and especially shall enlighten the reasons of the involved complexities.

It shall be noted that the data structure of classical CAD-models typically address the geometrical entities, without enhancing or connecting physical information, but focusing on fast and error-free visualization. BIM on the other hand is organized more constituent entity-wise, as e.g. a truss or beam of the carrying structure, instead of merely identifying the shapes. Structuring the data in such a form allows to efficiently estimate information as material consumption, required resources up to initial project costs, whereby the advantage in that approach is given by the possibilities to retain the option to automatically generate geometrical shapes and drafts according to varying needs of design or analysis. BIM-models shall not be addressed further within this work, however, the proposed numerical approaches are designed in such a form that those may be embedded seamlessly.

This chapter starts with introducing the standards of CAD-described geometries and entities in section 2.1 and parametric modeling in section 2.2. With this knowledge, the discussion about enhancing the models with physical information for pre- and post-processing is presented within section 2.3. Section 2.4 is describing digital twins of structures and detailing some of its needs, which justifies the consequently proposed approaches.

The originality in this chapter is about the way to comprehend BIM, CAD, and digital twins to connect numerical simulations to facilitate the everyday structural engineering. This guides the path towards section 6, where a potential software architecture is presented along a realized implementation.

## 2.1 CAD Boundary Representation (B-Rep) models

Amid the increasing improvement of computation capabilities, the use of computers for design has evolved and has introduced the field of CAD [202, 58]. CAD makes use of computers for the creation and the design of various types of paperless models. Nevertheless, it is not only the digitization of the manual drawing board as since its introduction it opened never ending possibilities reaching from creation, parametrization, modification, simulation, to optimization and form-finding of geometrical shapes. With the increasing demands for the building of complex bodies from architecture and engineering the explicit shape description by B-Rep models became the major design representation technique as those are well suited for a precise modeling of complex shapes, with a reasonable consumption of data and computation power. Implicit geometry description, as Constructive Solid Geometry (CSG) form a famous alternative to B-Rep models. However, it shows off as rather complex to represent free-form shapes. Additionally, those models do not provide nodes, or control points, which would be the prerequisite to directly use the geometry description as basis for a finite element

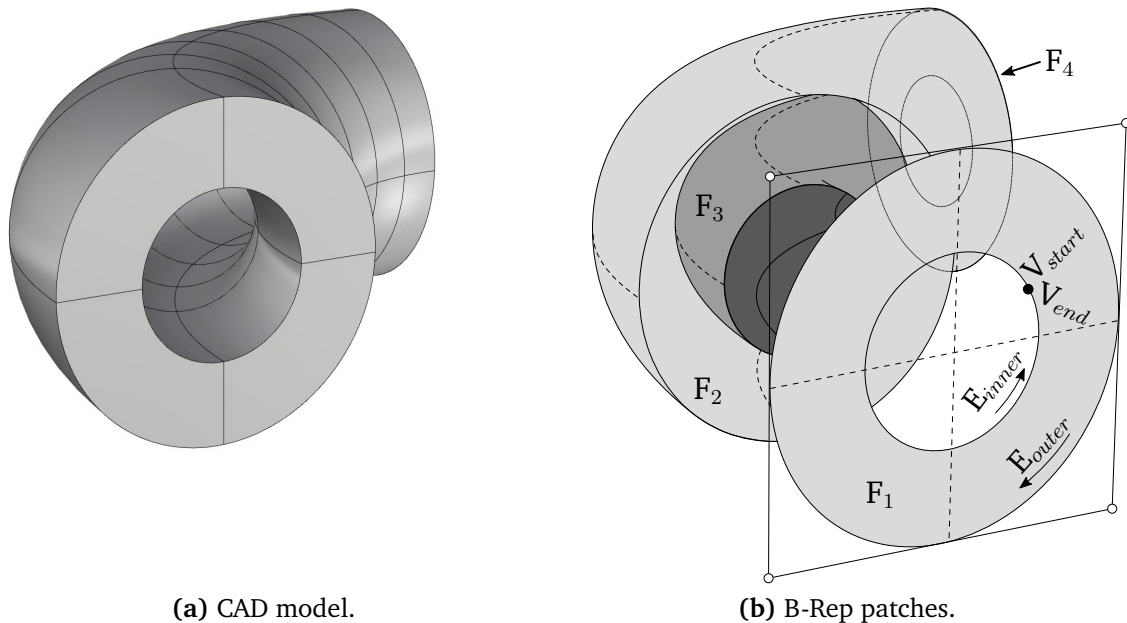


**Figure 2.2:** CAD model of a pipe.

simulation. Accordingly, the concept of B-Rep shall be considered as the chosen path for the CAD-integrated simulation.

In geometric modeling, B-Rep is a methodology for adequately representing shapes using its spatial boundaries, whereby the representation of an object consists of two parts:

**geometry** defines the spatial position, shapes, curvatures, etc.

**topology** relates between geometrical entities

The main topologies, with its corresponding geometry entities are:

- solids (volumes)
- faces (surfaces)
- edges (curves)
- vertices (points)

Accordingly, a solid is delineated by a set of enclosing faces (F), which itself are bounded by edges (E), described by curves within the parameter space of the underlying surface description. Conclusively, the curves are bounded and trimmed by points named vertices (V).

**Remark 2.1.1: Independence of mathematical geometry description for B-Reps**

It shall be noted that frequently it is understood that the B-Rep description relies on NURBS-based geometry entities. However, this is not the general case as those could be using any mathematical representation, such as e.g. primitives like triangles and quadrilaterals or linearized line segments and polygons. In CAD this is increasingly employed to increase efficiency. For CAD-integrated isogeometric simulations this demands additional efforts in introducing suitable NURBS-entities.

## 2.2 Parametric modeling

Parametric modeling is an approach to capture designs by parameters, which are defining objects by certain algorithms and mathematic procedures. This is in controversy to a direct draw and design. In this way multiple components can be introduced in a model and repetitive objects can be created easily, while still adopting to apparent environments. It can be mentioned that a parametric model comes with many advantages, however, it may be more involved to build up such a model, which may make it less economic for singular objects. The procedures of parametric modeling can either be script based, such as python scripts or may contain GUIs, which are mostly known under the category of graphical programming.

In architecture, parametric modeling became already a major part in the design. However, in engineering, yet it is not employed frequently. Though, in the combination of architecture and engineering and specifically in the design-through-analysis, it brings major advantages, as changes from iterative processes may be updated easily. Mostly, the outcome of a parametric model is similar to the structure of a CAD model, which makes it a great complementation to IGA. Additional to geometrical parameters, analysis parameters, such as e.g. materials or load cases may be considered as well in the parametric model.

Along with the CAD-integrated analysis, parametric modeling is playing a significant role within this dissertation. More about the parametric procedures is explained within section 6.6.1.

## 2.3 Analysis enhanced CAD models <sup>d</sup>

Commonly, two directions are imaginable for merging geometrical shapes and physical objects. One is to structure physical objects as entities of a given type and define specific

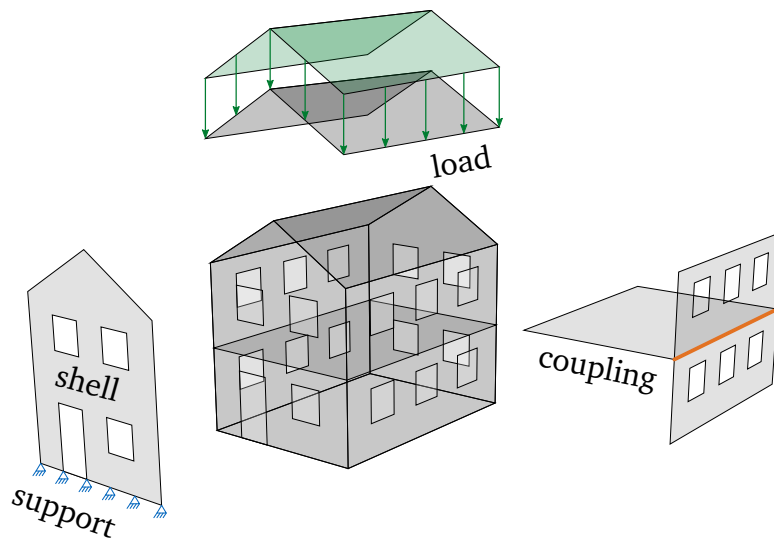


**Figure 2.3:** Analysis enhanced CAD model.

geometrical expansions and scaling, with which the shape is extrapolated into a single or more geometrical bodies. Second, a set of geometries can be collected and defined as part of a specific object.

The first avenue shows off as advantageous, once the focus is set on highly repetitive objects within a model where its specific forms do not vary highly, which is given for many civil engineering purposes, mainly in building construction. This way of defining the model would allow to give multiple ways of the shape determination of the body and accordingly design and engineering purposes could be fulfilled at the same time. Accordingly, many known BIM models usually rely on this type of data acquisition. However, typically the restrictions of those types of data collectors are that it may become complex once sophisticated shapes are involved or objects cannot be specifically identified.

As this work focuses on the comprehensive evaluation of numerical approaches, strong communication and shape control are more important than data handling. As a result, the latter-mentioned strategy of endowing geometrical entities with physical attributes is favoured. It should be emphasized, however, that some of the findings of this study may be closely connected to suggestions for how to generate the geometrical model from a collection of objects.

Considering a model which follows the suggestions from section 3.5 various possibilities exist for enhancing the geometrical model with the essential physical information for consistent numerical simulations. Initially, user defined properties may be assigned to various topology items of the draft, which can be virtually connected. Those data types

involve kinematic formulations for all geometry types and additionally include a set of load and support conditions. As contrast, some entities are generally not directly accessible for the user interface, which are the inter geometrical coupling conditions. This is a very important group of entities which need to be controlled mostly via the connected user provided information, which in practice shows off as a complicated operation.

Within figure 2.3 is shown an example of a theoretical building which is enhanced by various entities. This shall display the possibilities and also the facilities which are to be enabled by the proposed avenue.

Enhancing the model with additional information results also in the need of novel interfaces to correctly control the respective numerical solver. A possible avenue, including required data and a feasible formatting is presented within [222]. Apart from the pure geometrical description, a major focus is set hereby on the unique identification of entities for the correct connection between geometry and physics. This makes it impossible to directly use standardized CAD-formats.

For some types of simulations it might not be required to access information from specific geometry entities, as the geometry group might be sufficient. This may involve embedded simulations with the use of CAD models, where all provided geometries of a specific type are considered. In this scenario, the solver could be addressed with common standards as step [214] or iges [111]. Accordingly, the pre-processing would be reduced to generic solver settings which do not require an involved CAD-based data acquisition.

## 2.4 BIM-induced digital twin with CAD

According to Forbes [245] and Gartner [90] digital twins have been named as top strategic technology trends throughout many years and will play a fundamental role in the near future. The digital twin can be seen as a fictitious representation of an existing building or infrastructure, which contains a strict link in-between the two worlds, as per figure 2.4, whereby the scope and use cases are manifold and endless.

Generally spoken, the digital twin realizes a, often in-time, simulation of the reality to gain insights which are not measurable, however, can be computed according to model approximations, which itself are triggered from visible inputs. For example, due to measured deflections of the apparent state, stresses and limit states may be estimated, which itself are evaluated from the numerical counterpart. Accordingly, the digital twin does not only contain the exact geometrical extensions, also physical information need to be implied to enable possibilities for an accurate prediction of the current state. The digital twin, however, shall not only be applied within apparent scenarios as it holds

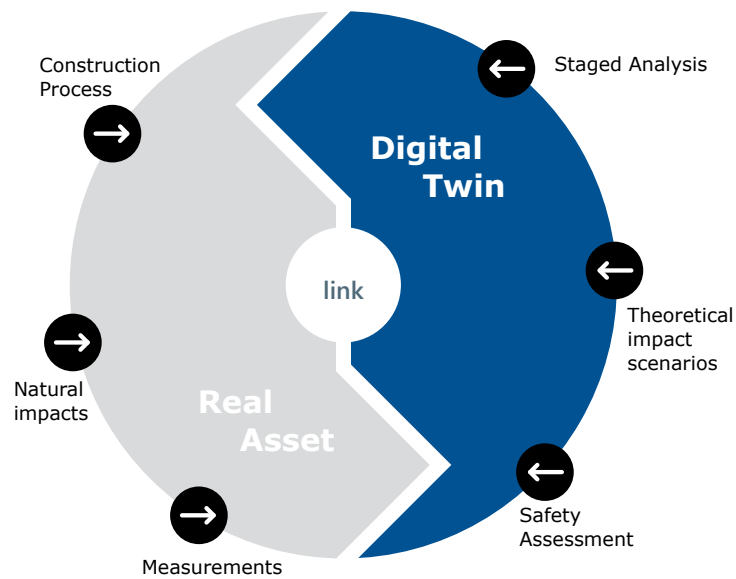


**Figure 2.4:** Link between real asset and digital twin.

capabilities to be used as well for the prediction of possible impact scenarios, as e.g. the simulation of eventual natural disasters.

For many scenarios, it is essential to bring the loading history of an objects to provide better assessments from the digital counterpart. This brings back the BIM-model which itself holds capabilities for a watertight storage of structurally necessary information. This can be, e.g. the staging of the construction process, impacts as soil movements, heavy floods, hitting objects and more.

This thesis shall not present avenues to design digital twins and BIM models, however, its presented methods are selected with the restricting needs. In the following shall be given a summary of this thesis with respect to the BIM-induced digital twin. General modeling possibilities are discussed within section 3, with a focus on CAD-integrity. As external impacts are frequently modeled through multiphysics problems, the whole set of basis functionalities is put and discussed within the scope of multi-domain coupling to theoretically enable interacting physics. Within the consecutive section 4 the digitization of masonry is discussed, beginning with tests, whereby a novel technology as DIC have been applied (see section 4.2), which shows off as specifically suitable for the in-time integration within digital twins. Concluding with the experimentally tested material parameters, possible modeling avenues, including a proposed constitutive law are discussed. Finally, suggestions are provided for an implementation of the methods, as per section 6, in such a way that they may be smoothly incorporated in existing FEM-solvers, which itself may already be part of a digital twin environment.

### 3 Finite Element Methods

The idea of FEM is driven by the split of a problem into a finite amount of sub-problems, called elements. In a mathematical way this is achieved by transforming the *strong form* of the equilibrium into an integral-like *weak form*. This process and its different capabilities shall be outlined within this chapter, with the focus to a range of static geometrically non-linear problems and transient simulations.

The *strong form* of the equilibrium (see figure 3.1) shall be denoted in the reference state and in the deformed state as:

$$\operatorname{div} \mathbf{P} + \rho_0 \mathbf{B} = \mathbf{0} \quad \text{and} \quad \operatorname{div} \boldsymbol{\sigma} + \rho \mathbf{b} = \mathbf{0} . \quad (3.1)$$

where  $\mathbf{P}$  expresses the reference internal PK1 stresses,  $\boldsymbol{\sigma}$  the internal Cauchy stresses,  $\rho_0$  the initial density,  $\rho$  the current density of the body,  $\mathbf{B}$  the reference, and  $\mathbf{b}$  the external vector of body forces [21, 251, 257]. Since finding a closed-form solution is sophisticated and many times impossible, it is reformulated within an integral-like form,

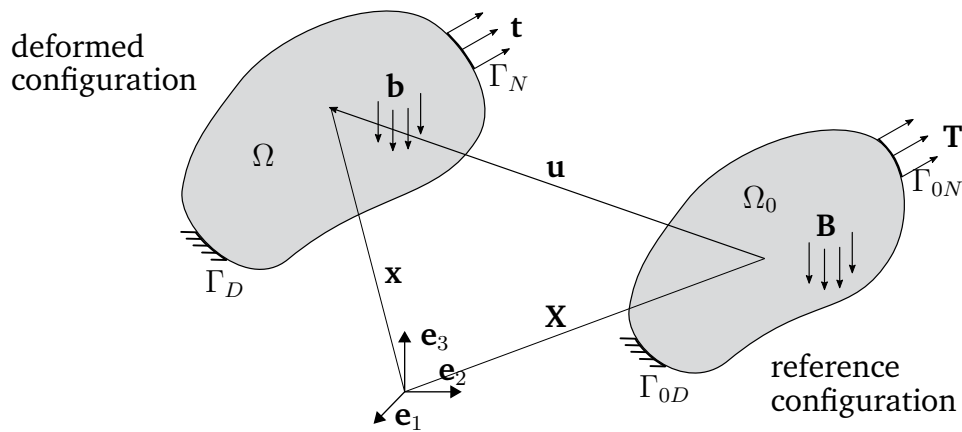


**Figure 3.1:** The *strong form* of the equilibrium in undeformed reference and deformed configuration.

which leads to the *weak form* of the equilibrium and can be expressed with the principle of virtual work:

$$\delta W = \delta W_{int} + \delta W_{ext} , \quad (3.2)$$

$$\delta W_{int} = - \int_{\Omega_0} \mathbf{S} : \delta \mathbf{E} \, d\Omega_0 = - \int_{\Omega} \boldsymbol{\sigma} : \delta \mathbf{e} \, d\Omega , \quad (3.3)$$

$$\delta W_{ext} = \int_{\Gamma_0} \mathbf{T} : \delta \mathbf{u} \, d\Gamma_0 + \int_{\Omega_0} \rho_0 \mathbf{B} : \delta \mathbf{u} \, d\Omega_0 = \int_{\Gamma} \mathbf{t} : \delta \mathbf{u} \, d\Gamma + \int_{\Omega} \rho \mathbf{b} : \delta \mathbf{u} \, d\Omega , \quad (3.4)$$

where  $\mathbf{S}$  is the 2<sup>nd</sup> Piola-Kirchhoff (PK2) stress tensor in the domain  $\Omega$  and  $\mathbf{T}$  are the force vectors on the boundary domain  $\Gamma$ . Capital symbols and  $(\cdot)_0$  are referring to the initial configuration.  $\mathbf{e}$  is used as the global coordinate system.

From the principle of virtual work, FEM provides different avenues to cope with highly problem dependent necessities. Within this section the constituents of the *weak form* shall be discussed with various possible variations.

Initially, the required geometrical and spatial mapping terms for the integrative domain  $\Omega$ , and  $\Gamma$  are being introduced, which are repeatedly apparent throughout this work and the fundamental of all presented numerical finite element discretization (see section 3.1). This similarity will be reflected within section 6, where a generic implementation avenue is presented. The geometrical mapping is followed by the presentation of NURBS (see section 3.2), one of many mathematical possibilities to express geometrical forms. NURBS are mainly dominant within this work as those are the employed in many CAD systems and therefore the basis for CAD-integrated simulation. Within the consequent section, different ways to express the internal kinematics are outlined by the presentation of various structural element formulations, with a special focus to dimensionally reduced surface-based shells, as those are relevant for the addressed masonry structures (see section 3.3).

Miscellaneous ways of spatial description and geometrical integration are enlightened consecutively, beginning with IGA/IBRA (see section 3.4). As IGA/IBRA is the chosen path for CAD-integrated analysis, the suitability and properties of CAD-provided geometry descriptions are discussed (see section 3.5). IBRA is a specification of an immersed method. This concept shall be studied for the application of composites by embedding distinct domains of different material properties within the same geometrical description (see section 3.6). The apparent framework is highly limited to the chosen patches or mesh, which can be a dis-qualifier for localized large deformations. Thus, the MPM (see section 3.7) is presented which itself updates the previous integration with a consequent mesh reset or exchange. As different parts of the problems may have distinct optimal methods this chapter concludes with a study of approaches to combine various FEM procedures to enlarge the simulation scope with coupled multiphysics simulations (see section 3.8).

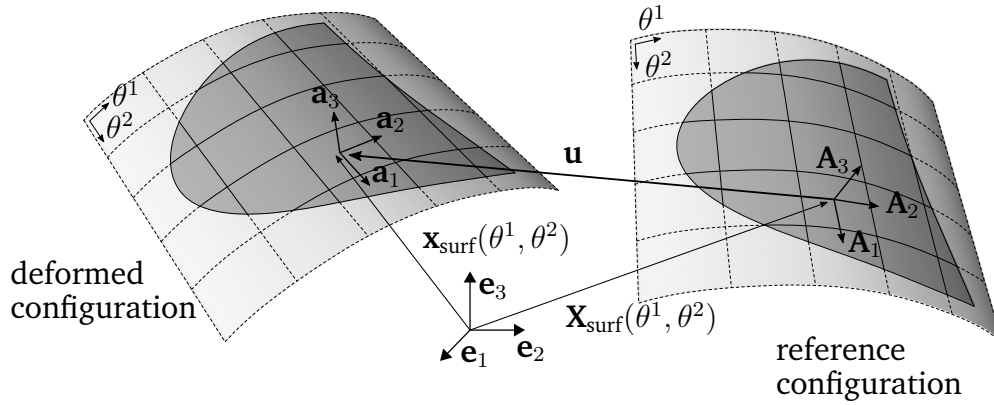


**Figure 3.2:** Metric of a surface in undeformed and deformed configuration.

## 3.1 Fundamentals of geometrical expressions

In continuum mechanics notation, within a solid, the covariant base vectors  $\mathbf{a}_i$  shall be defined within the curvilinear coordinate system  $\theta$  as:

$$\mathbf{a}_i = \frac{\partial \mathbf{x}}{\partial \theta^\alpha} . \quad (3.5)$$

Consequently, capital letters are used to describe the initial state ( $\mathbf{A}_i$  and  $\mathbf{X}$ ), whereas lower case letters are the denotation within the current state. The base vectors are linearly independent and may be used to describe any geometrical point in space. The shape of a surface, being a dimension reduced geometrical entity from the solid, is made upon the two base vectors  $\mathbf{a}_1$  and  $\mathbf{a}_2$ , as per equation 3.5. If the third base vector  $\mathbf{a}_3$  is perpendicular to the surface (some formulations may incorporate non-perpendicular base vectors  $\mathbf{a}_3$ , see section 3.3) it may be expressed by the latter:

$$\mathbf{a}_3 = \frac{\mathbf{a}_1 \times \mathbf{a}_2}{\|\mathbf{a}_1 \times \mathbf{a}_2\|_2} . \quad (3.6)$$

With the use of either systems an arbitrary point in space can be similarly described by:

$$\mathbf{x}_P = \mathbf{x}(\theta^1, \theta^2, \theta^3) = \mathbf{x}_{surface}(\theta^1, \theta^2) + \theta^3 \mathbf{a}_3 \quad (3.7)$$

from where the displacements  $\mathbf{u}$  are defined as:

$$\mathbf{u} = \mathbf{X} - \mathbf{x} . \quad (3.8)$$

### 3.1.1 Numerical integration of surfaces

For a finite element analysis of thin wall shell structures, typically 3 spaces need to be considered: the global space, the parameter space of the surface and the Gaussian

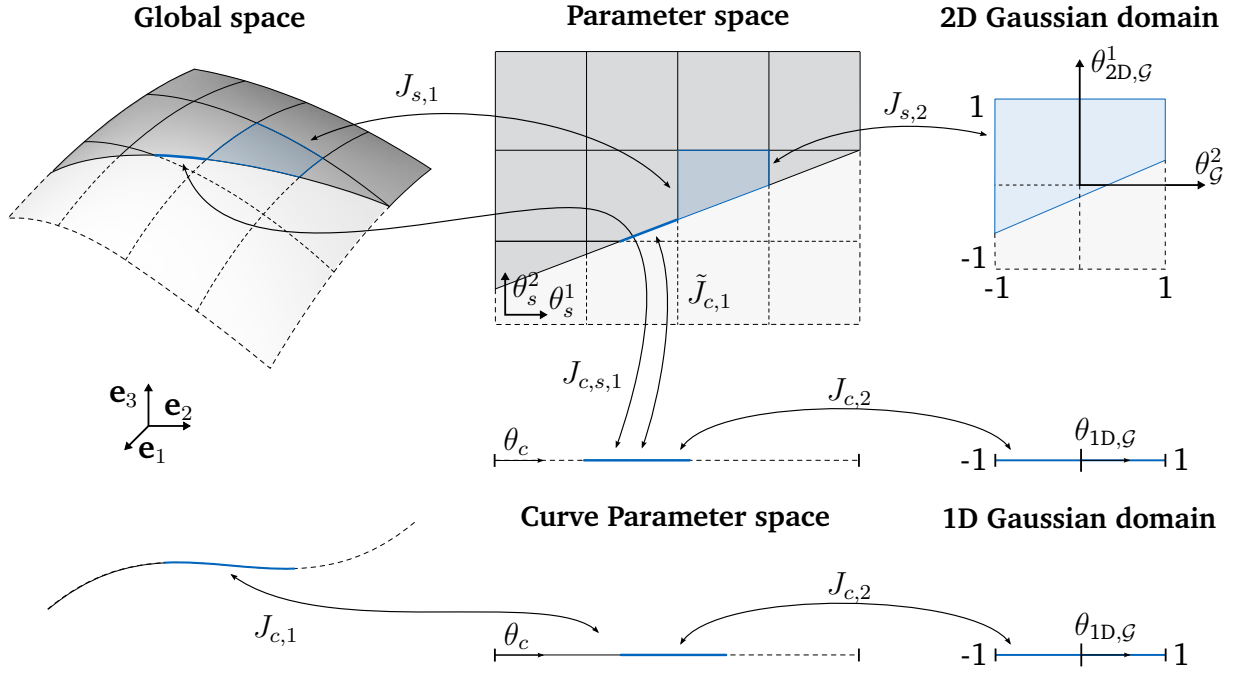


**Figure 3.3:** Mapping between physical space, parameter spaces and Gaussian domain (modified from [222]).

domain. Generally spoken, the global space defines the shape of the geometries, whereby the parameter space is used to delineate the shape or describe embedded additional entities. Finally, the Gaussian space is applied as latitude where locations of integration points are known from quadrature rules.

Between each space a Jacobian is defined for the transformation of shape configurations. Following,  $J_{s,1}$  represents the mapping between global and parameter space (with  $\theta^1 \in [\theta_s^1, \theta_e^1] \times \theta^2 \in [\theta_s^2, \theta_e^2]$ , see also figure 3.3) with  $J_{s,2}$  being the mapping between the parameter space and Gaussian domain  $\mathcal{G}$  (with  $\theta_{2D,G}^1 \in [-1, 1] \times \theta_{2D,G}^2 \in [-1, 1]$ ).

$$J_{s,1} = \frac{\partial \mathbf{x}}{\partial \theta_s^1} \frac{\partial \mathbf{x}}{\partial \theta_s^2} \quad \text{and} \quad J_{s,2} = \frac{\partial \theta_s}{\partial \theta_{2D,G}^1} \frac{\partial \theta_s}{\partial \theta_{2D,G}^2}. \quad (3.9)$$

Consequently, the area, or generally domain size of a trimmed surface element is given by the dual integration between domains:

$$\Omega = A = \int_A dA = \int_{\theta} \det(J_{s,1}(\theta_s)) \underbrace{\int_{2D,G} \det(J_2(\theta_{2D,G})) d\theta_{2D,G}}_{\text{integration weight: } w_s} d\theta. \quad (3.10)$$

Within classic FEM simulations<sup>a</sup>, the mapping  $J_{s,2}$  is deformation independent and thusly precomputed and may be included within the integration weight  $w_i$ , which is being the respective quadrature weighting factor for integration point  $i$  (see also [41, 222]) with  $w_{i,\mathcal{G}}$  being the integration weight within the Gaussian domain. Considering this, the approximation with the areal integral can be written as:

$$\Omega = A = \sum_{i=1}^{n_{qp}} \det(J_{s,1}(\boldsymbol{\theta})) \cdot w_{i,s} \quad \text{with} \quad w_{i,s} = \det(J_{s,2}(\boldsymbol{\theta}_{2D,\mathcal{G}})) \cdot w_{i,s,2D,\mathcal{G}}. \quad (3.11)$$

### 3.1.2 Numerical integration of curves

Similarly as surfaces, 3 spaces are required for a consistent analysis with curve-based formulations, whereby the notation is using  $(\cdot)_c$  to differentiate the mappings to the surface mapping. The corresponding spaces are defined within  $\theta_c \in [\theta_{c,s}, \theta_{c,e}^2]$  and  $\theta_{c,\mathcal{G}} \in [-1, 1]$ .

$$J_{c,1} = \frac{\partial \mathbf{x}}{\partial \theta_c}, \quad \text{and} \quad J_{c,2} = \frac{\partial \boldsymbol{\theta}_c}{\partial \theta_{c,\mathcal{G}}}. \quad (3.12)$$

By using the two mappings, the length of the curve can be obtained as:

$$\Omega = L = \int_L dL = \int_{\theta_c} \det(J_{c,1}(\boldsymbol{\theta}_c)) \underbrace{\int_{1D,\mathcal{G}} \det(J_{c,2}(\boldsymbol{\theta}_{1D,\mathcal{G}})) d\boldsymbol{\theta}_{1D,\mathcal{G}}}_{\text{integration weight: } w} d\theta_c, \quad (3.13)$$

and the corresponding approximating integral form:

$$L = \sum_{i=1}^{n_{qp}} \det(J_{c,1}(\boldsymbol{\theta}_c)) \cdot w_{c,i} \quad \text{with} \quad w_{i,c} = \det(J_{c,2}(\boldsymbol{\theta}_{1D,\mathcal{G}})) \cdot w_{i,c,1D,\mathcal{G}}. \quad (3.14)$$

### 3.1.3 Numerical integration of curves on surfaces

A curve on surface is a curve, which is described in the parameter space of the surface. That is in contrast to the previously described curves where the description of shape is independent. As shown within figure 3.3, 4 spaces are being considered for curves on surfaces, the global space, the parameter space of the surface which is correspondingly the global space of the curve, the parameter space of the curve and finally the 1

<sup>a</sup>Being in contrast to the later described MPM (see section 3.7) where the locations within parameter space are updated, which results in an eventual update of  $J_2$ .

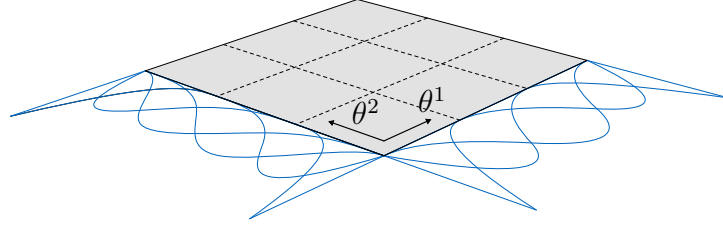


**Figure 3.4:** 2D B-Spline-based patch, with  $3 \times 3$  knot spans and a polynomial degree of  $2 \times 3$ .

dimensional Gaussian domain. Consequently,  $(\tilde{\cdot})$  is used to express operations and mappings which are defined within the parameter space of the surface.

$$J_{c,s,1} = J_{s,1} \cdot \tilde{J}_{c,1} = (\mathbf{a}_1 \cdot t_1 + \mathbf{a}_2 \cdot t_2) \quad \text{with:} \quad \tilde{J}_{c,1} = \frac{\partial \boldsymbol{\theta}}{\partial \theta_c}. \quad (3.15)$$

The global length is accordingly defined by  $J_{c,s,1}$  as:

$$\Omega = L = \int_L dL = \int_{\theta_c} \det(J_{c,1}(\boldsymbol{\theta}_c)) \underbrace{\int_{c,\mathcal{G}} \det(J_{c,s,1}(\boldsymbol{\theta}_{c,1D,\mathcal{G}})) d\mathcal{G}}_{\text{integration weight: } w_c} d\boldsymbol{\theta}, \quad (3.16)$$

and the corresponding approximating integral form:

$$\Omega = L = \sum_{i=1}^{n_{qp}} \det(J_{c,s,1}(\boldsymbol{\theta}_c)) \cdot w_{c,i} \quad \text{with} \quad w_{c,i} = \det(J_{c,s,1}(\boldsymbol{\theta}_{c,1D,\mathcal{G}})) \cdot w_{i,c,\mathcal{G}}. \quad (3.17)$$

## 3.2 Non-Uniform Rational B-Spline (NURBS) entities

The previously described mappings are generic for any shape function, including NURBS. Consequently, the mathematical fundamentals of B-Splines and NURBS shall be enlightened, whereby the latter are seen as a specification of B-Splines. For a detailed classification it shall be referred to [185].

B-Spline basis functions  $N_i$ , defined by the recursive *Cox-deBoor* formula [63, 38] are described by the knot vector  $\Xi$ , containing a sorted set of parameters defined within the parametric coordinates  $\theta \in [\theta_s, \theta_e]$ , and a polynomial degree  $p$ . Accordingly, the shape of a curve described by B-Splines is given as  $\mathbf{C}(\theta^1)$ , with a surface  $\mathbf{S}(\theta^1, \theta^2)$  being defined by the tensor product of the shape functions in the respective parametric coordinates  $\theta^1$  and  $\theta^2$ .  $\mathbf{P}_i/\mathbf{P}_{ij}$  are the corresponding control points:

$$\mathbf{C}(\theta) = \sum_{i=1}^k N_i(\theta^1) \cdot \mathbf{P}_i, \quad \text{and} \quad \mathbf{S}(\theta^1, \theta^2) = \sum_{i=1}^n \sum_{j=1}^m N_i(\theta^1) \cdot N_j(\theta^2) \cdot \mathbf{P}_{ij}. \quad (3.18)$$

Considering an independent weight per control point  $w_{cp,i}$  extends the B-Splines towards NURBS, with the rational basis functions  $R_i$ :

$$\mathbf{C}(\theta) = \sum_{i=1}^k \frac{N_i(\theta) \cdot w_{cp,i}}{\sum_{j=1}^k N_j(\theta) \cdot w_{cp,i}} \cdot \mathbf{P}_i = \sum_{i=1}^k R_i(\theta) \cdot \mathbf{P}_i, \quad (3.19)$$

$$\mathbf{S}(\theta^1, \theta^2) = \sum_{i=1}^n \sum_{j=1}^m \frac{N_i(\theta^1) \cdot N_j(\theta^2) \cdot w_{cp,ij}}{\sum_{k=1}^n \sum_{l=1}^m N_k(\theta^1) \cdot N_l(\theta^2) \cdot w_{cp,kl}} \cdot \mathbf{P}_{ij} = \sum_{i=1}^n \sum_{j=1}^m R_{ij}(\theta^1, \theta^2) \cdot \mathbf{P}_{ij}. \quad (3.20)$$

### 3.2.1 Continuity of NURBS

The apparent continuity is one of the features and many times reasons for the application of B-Splines and more generally NURBS. Hereby, it shall be differentiated between the geometric continuity  $G^k$  and the parametric continuity  $C^k$ , whereby  $G^k$  only enforces parallelism of the  $k$ -th trajectory,  $C^k$  demands that the corresponding lengths are similar. As  $C^0$  is presenting the location, without any length, it yields that  $C^0 = G^0$ . For numerical simulations, the parametric space may vary between domains or patches, accordingly, wrongly enforcing parametric continuity would lead to the introduction of model errors. Following, while enforcing  $C^0$ , only  $G^1$  continuities are addressed, which is similarly valid for all  $k > 1$ .

Within NURBS, the continuity can be obtained from the multiplicity  $i$  of a certain knot  $\theta$  within the knot span  $\Xi$  as:  $k = p - i$ .

### 3.2.2 NURBS refinement

Typically, drafts require less degrees of freedoms derived from control points than eventual simulation driven deformed geometries [107], which contradicts the direct use for analyses purposes. Accordingly, geometrical refinement is essential. NURBS are specially suitable for refinement, as those operations are applicable without modifying the shape. Two ways of refinement shall be mentioned, the degree elevation (p-refinement) and the knot insertion (h-refinement). The according mathematical descriptions and numerical algorithms can be taken from [185].

Both refinement operations add additional control points to a NURBS-entity. Increasing the polynomial degree allows an increase of continuity which might improve simulation accuracy and convergence rates. However, it will decrease the possibility to appropriately express localized effects. As contrast, h-refinement introduces additional knots which helps in expressing effects with large gradient changes. It can additionally be used to multiply certain knots, which decreases the continuity at the specific knot span location (see [185]).

An issue about refinement operations with NURBS is that those cannot be operated locally. Accordingly, the entire length of a patch would be affected. Coupled refined patches, subdivision surfaces [56, 192, 254] or distinct spline generalization technologies as T-Splines [30, 208], hierarchical splines and refinement [67, 59] and more [163, 253] have been introduced to cope with this problematic. However, those avenues require a remodeling of the initial problem which is in contrast to the seamless CAD integration, which is given for the application with NURBS.

### 3.3 Continuum mechanics and kinematic formulations for structural analyses

In this section shall be discussed some fundamentals, required to express physical bodies. Those formulations may be defined within various geometrical spaces, from 3d solids, 2d surfaces and 1d curves. The expressions are independent on the chosen discretization, integration and update schemes.

#### 3.3.1 Solid-based formulations

Solid formulations, in comparison to surface or curve-based formulations are typically known as the simplest expressions as no geometrical extraction/static condensation need to be applied. They allow the expression of almost any geometrical shape. However, for some problems those would require many elements and thusly not be computationally efficient.

#### 3.3.2 Surface-based formulations

Surface based formulations are specifically advantageous for structures where the extension in one direction is significantly shorter than the extension in the other 2 directions. Via the condensation of the 3rd dimension towards a surface formulation, mostly represented at a middle surface, the amount of finite elements and accordingly the number of degrees of freedoms can be reduced significantly, which resolves into an improvement of computational complexity.

The most popular surface-based formulations are:

**Membranes** have only a structural membrane stiffness without any bending strength.

In practice, membrane formulations often come along with an internal pre-stress.

**Plates** are used for initially plane problems. Mostly, those contain curvature stiffness and no dedicated membrane stiffness.

**Shells** contain both membrane and curvature stiffness.

The focus of this dissertation are the latter structural components, the shells. Those can be structured within various groups. Thereby, the most significant factors are the geometrical extensions and the physical properties of the material.

**Thin shells** are considering the membrane and bending stiffness. The most common structural pendant is the Kirchhoff-Love (KL/ Euler-Bernoulli for 1D structures) theory.

**Thick shells** are generally considering additional shear or rotational deflections. The Reissner-Mindlin (RM/ Timoshenko for 1D structures) formulation is the characteristic representative.

**Solid/ 3D shells** are typically the most demanding formulations, as those are additionally excogitating the extension of the shell towards the thickness. The aforementioned structural members require static condensations of continuum based 3D constitutive materials, whereas solid shells intrinsically deal with those.

Consequently, the concept of the hierarchic shells (see [76, 168]) is discussed as shown in figure 3.5 as this set of formulations is covering a large spectrum of shells and is specifically suitable for IGA. Furthermore, it is employed within the given scope. The basis of this shell formulation is the KL-assumption (see Kiendl et al. [118]). This assumption is enhanced by the shear parameters towards a hierarchic 5p/RM shell. Furthermore, the 6th and 7th parameter are used to express locking free thickness deviations. Equation 3.21 is displaying the disassembly of the respective terms:

$$\mathbf{x}^{7p-hier.} = \underbrace{\mathbf{x} + \Theta^3 \underbrace{(\mathbf{A}_3 + \Phi \times \mathbf{A}_3)}_{\mathbf{x}^{3p/KL}}}_{\mathbf{x}^{5p-hier./RM}} + \Theta^3 \mathbf{w}^{5p} + \Theta^3 \mathbf{w}^{6p} + \underbrace{(\Theta^3)^2 \mathbf{w}^{7p}}_{\mathbf{x}^{7p-hier.}} \quad (3.21)$$

$\mathbf{x}^{7p-hier.}$  is defined at the surface of the shell and not the mid surface.  $\Phi$  is notated as the rotation vector. By locking the additional parameters, the formulation would immediately fall back to the respective lower shell theory. The formulation shows off as being less sensitive to some shear locking phenomena (see remark 3.3.1). Other known Reissner-Mindlin shell formulation in the context of IGA are e.g. Benson et al. [31] Dornisch et al. [72, 73] and Müller et al. [158]. Typically, by adding additional

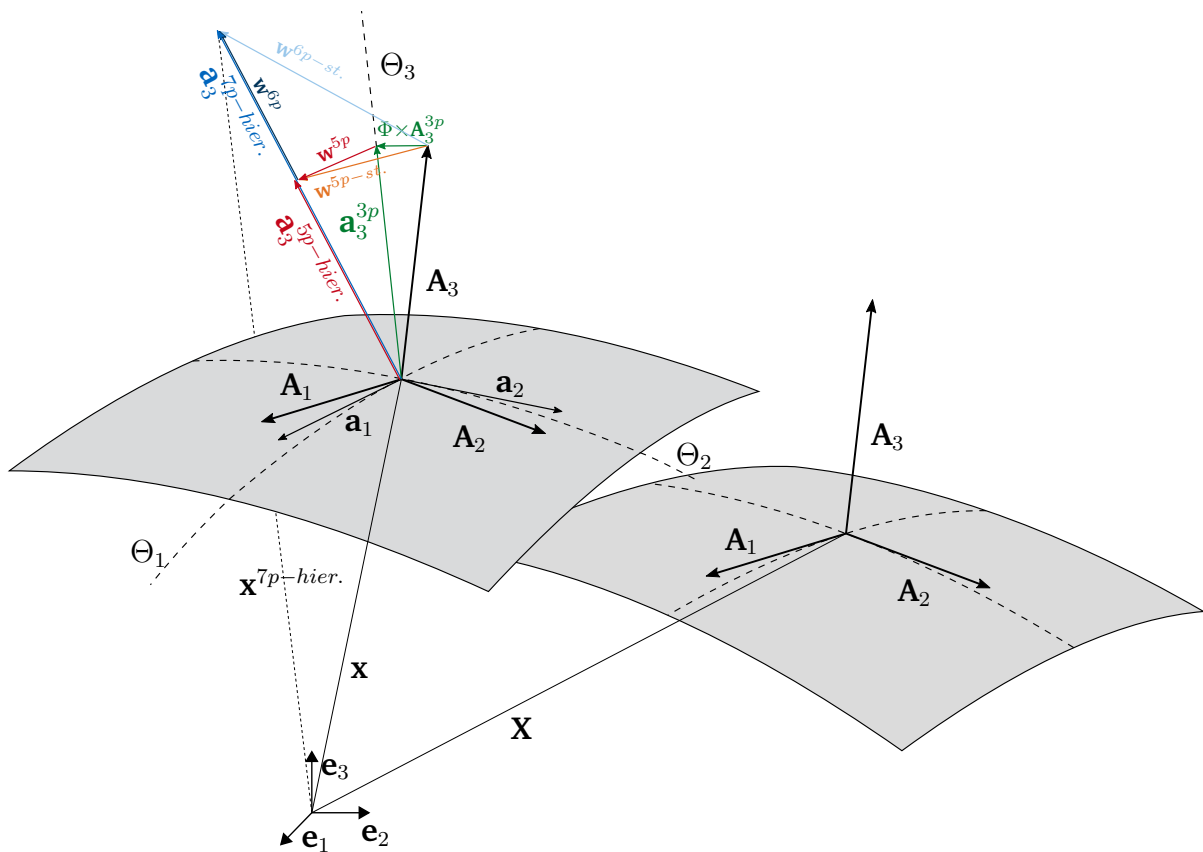


**Figure 3.5:** Concept of the hierarchic shell formulations (adapted from [76, 168]).

parameters, further deflections are enabled and the structures behave less stiff and thusly deflect more.

For the apparent numerical problems, mostly the KL-shell has been employed. The 5p shell has been used once for quantitative comparison (see section 5.4.3). However, no shell with thickness change has been applied within the present studies.

**Remark 3.3.1: Locking of shells**

Locking is a common problem within the analysis of thin-walled structures, whereby the effects can be described by:

- underestimation of deflections (stiffness of structures are overestimated)
- oscillation of stress solutions

All kinematic theorems come along with distinct locking phenomena, characteristic for shape or material and it shall be noted that also with solid based formulations certain similar properties may appear. Table 3.1 summarize the apparent locking scenarios within the hierarchical shell family [77, 168]:

	3p	5p-st.	5p-hier.	6p-st.	7p-st.	7p-hier.
transverse shear		x		x	x	
in-plane shear	x	x	x	x	x	x
membrane	x	x	x	x	x	x
curvature thickness				x	x	
poisson thickness				x		

**Table 3.1:** Dominant locking phenoma for each shell formulation

**Influence of respective shape function:**

In analytical structural analysis, the physical relation between load, shear force, moment, rotation, and deflections comprise a system of partial differential equations. To exactly represent all modes, the system would require a polynomial degree of 4 in addition to the polynomial degree required to adequately express the load itself. The fundamental concept of FEM is to approximate the partial differential equation as closely with respective primitives. Thereby, the exact shape and accordingly expected results can only be estimated. For engineering purposes it is generally sufficient to rely on those estimations, however, it should be genuinely understood how the quantitative values distribute throughout the physical system.

Accordingly, a numerical study is being presented which displays the evaluated internal values according to the integration point position. For the example, a simply supported beam is evaluated with a dead load, as shown in figure 3.6, with the corresponding characteristic values. The beam is modeled by two different shell formulations (KL and 5p-hierarchical). The Poisson’s ratio is being 0 for the given study. The example is containing 10 equally distributed knot spans. It is being refined by the polynomial degree.

This example requires a  $p=2$  or higher to express the bending stiffness, which is required for both the 3p KL shell and the 5p hierarchical shell. With this polynomial degree the displacements can be estimated properly according to the accuracy of the refinement, as per figure 3.7. When the polynomial degree of the background is  $p=2$ , the values for the moments remain constant throughout a knot span. With  $p=3$ , the moment graph is almost approximated correctly, however, it still shows that there are  $C_1$  discontinuities. With higher degrees the moment can be expressed exactly. The shear forces require a minimal polynomial degree of  $p=3$  to approximate any value within the KL-shell. Shear forces are the third derivative of the deflections, which would be permanently 0 for the case of a shape described by  $p=2$ . On the other hand, as the hierarchic shell carries separate degrees of freedom, specifically for shear, it is capable to express those with a

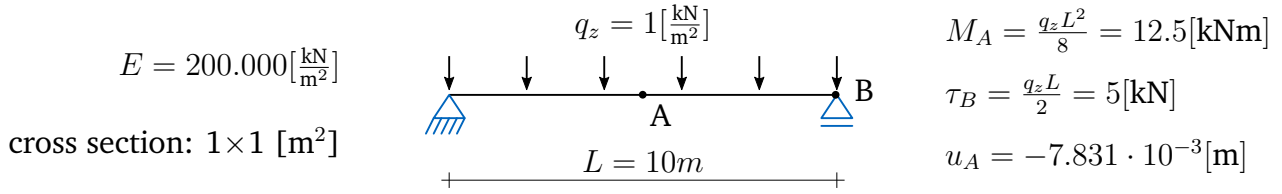


Figure 3.6: Example for evaluation of internals of the selected shell formulations.

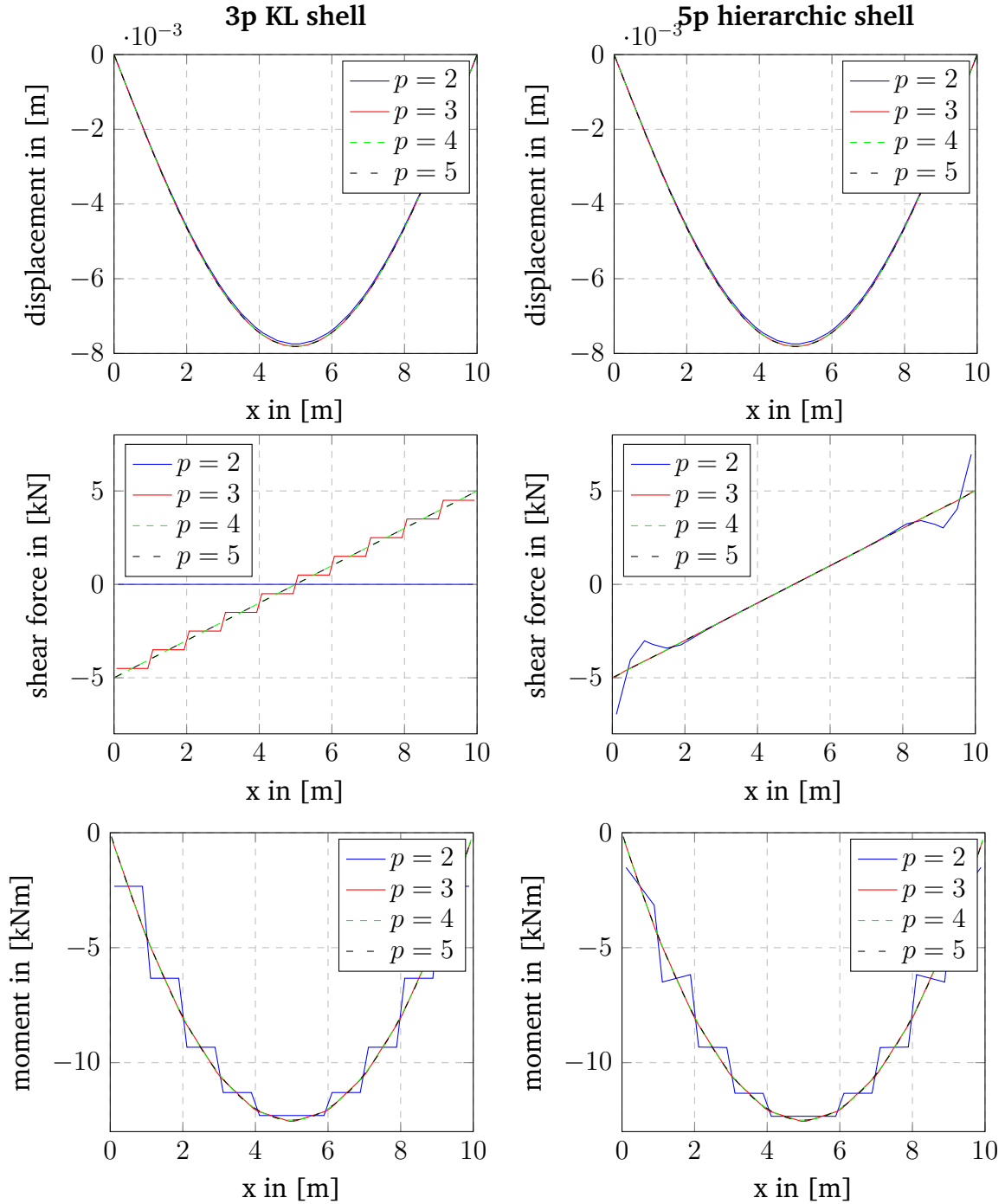
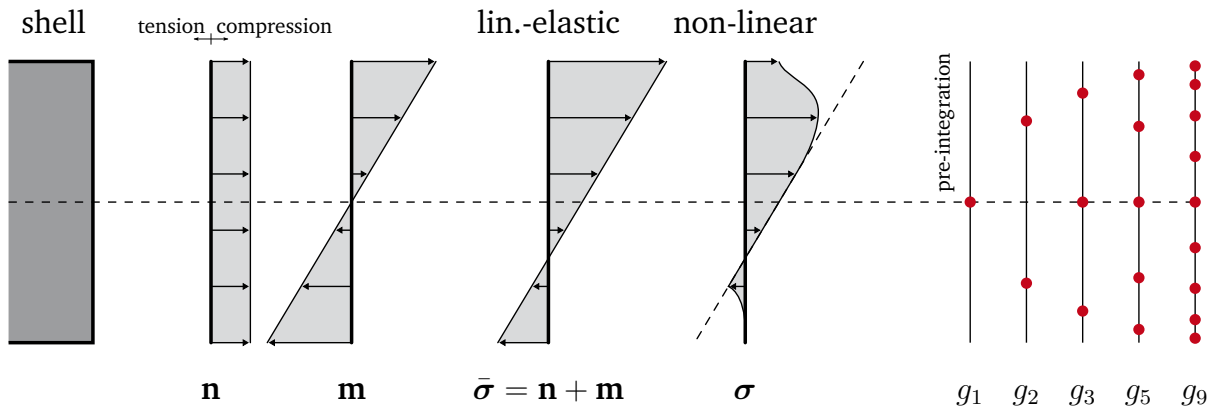


Figure 3.7: Internals from the different shells.



**Figure 3.8:** Thickness integration for shell-based structures.

lower polynomial degree. According to the moments, the KL shell first represents the shear forces in a stair-like form, constantly within a knot span with  $p=3$ , after better approximating the solutions for any value higher than this.

The 5p hierarchic shell displays some numerical issues close to the boundaries for all internal variables of  $p=2$ . A possible avenue for the stabilization is addressed by [168]. This problem shall not be considered further within this scope.

### Stress resultant vs. stress-based integration:

As shells are dimension reduced formulations they typically carry their degrees of freedom on the mid surface (generally, offsetting is possible as well). In the stress resultant-based avenue the cross section is pre-integrated throughout the thickness of the shell (see Kiendl et al. [118]). This is an efficient way, which reduces the assembly costs. However, this implies that materials are only evaluated on the middle surface, which basically means that the non-linearity within the bending part is generally neglected. This becomes crucial once non-linear materials are employed, as e.g. concrete or masonry (see section 4). Figure 3.8 is showcasing the controversy between the response of linear materials and non-linear materials. In this scenario, another avenue may be preferred, the stress-based integration. This considers integration points in the thickness of the shell (as per figure 3.8). At each of those thickness integration points, the material may be evaluated distinctly, which allows to adapt to local material characteristic. Specifically in the bending case this allows to model more accurately (the out-of-plane examples from section 5 are presenting cases where the thickness properties are crucial). It shall be noted that both types of integration would be imaginable for most shell formulations.

Different integration rules are imaginable for the thickness integration. A comprehensive comparison is presented within [44]. Among the most common rules shall be mentioned

the Gauss quadrature rule and the Simpson's rule. Within this work, all thickness integrations have been processed by the Gauss quadrature.

### 3.3.3 Curve-based formulations

The highest dimensional reduction from 3D solid formulations are curve-based formulations, where the structure is significantly slimmer within two directions than in the remaining 3rd direction. Two different shape expressions shall be considered: the geometry curves, which are containing their independent geometrical description, and the curves expressed upon the parameter space of higher dimensional geometries. Within this scope, the latter are predominantly curves on surfaces, however, also curves in solids or even curves on surfaces in solids are imaginable.

Due to their geometrical properties curves can be used to model following formulations:

- Neumann
- Dirichlet (see remark 3.8.2)
- Coupling interfaces (see [40, 11] within the scope of IGA)
- Mechanical motivated e.g. trusses, cables or beams (see [184, 24] within the scope of IGA)

## 3.4 Isogeometric Analysis (IGA) and Isogeometric B-Rep Analysis (IBRA) <sup>a</sup>

Ever since the introduction of finite element methods the choice of shape functions has been a great challenge and has been investigated within various studies [220, 219]. Whereby linear shape function have large advantages with comparative simplicity, higher order shape functions are typically more capable to express complex shapes and come along with typically better accuracy and convergence rates. Among the high order shape functions shall be mentioned different groups, with local and non local shape functions. Whereas local shape functions are defined within certain element boundaries, non-local shape functions exceed those and have a higher impact zone, which might be of advantage if high continuity with low gradients are aimed, as controversy, it seems less suitable to express localized phenomena.

NURBS (see section 3.2), as a specification of B-Splines, which itself are based on Bézier descriptions are part of the group of non-local high order shape functions. However, it shall be noted that with the choice of mathematical control parameters those can also be local and linear. They come along with a respectively simple mathematical expression,

require a small amount of control points for the definition of complex shapes and are typically capable for simplified parameterizations [3], which makes them specifically suitable for CAD. Following, aiming a CAD-integrated analysis, the application of NURBS within finite element methods eases interfaces significantly. Applied within different research [207, 103] it showed that the application of NURBS has multiple advantages apart from the continuous CAD integration. With Hughes et al. [107, 62], the research field got named isogeometric analysis (IGA). Within its original definition, full untrimmed patches are required in the simulation, however, as section 2.1 notes, typical CAD models contain more sophisticated shape descriptions. Accordingly, to allow analyses on a broader bandwidth of CAD models, Breitenberger et al. [40, 41] enhanced the numerical method with the B-Rep description (see section 2.1). This involves trimming of patches, weak application of boundary elements and weak enforcement of various continuities between patches. Simultaneously, it allows a seamless integration of the numerical simulation in CAD. This enables the possibility of a watertight data base for physical, kinematic, and material properties.

IBRA and IGA in general differ from classical FEM simulations by its geometrical integration as this focuses on NURBS. However, the kinematical formulations discussed in section 3.3 shall be applied consistently within the framework. CAD provides a geometry description based upon surfaces and curves, which consistently limits IBRA to the according dimension reduced kinematic formulations. Thus, this section mainly discusses the integration of trimmed surfaces and curves, which are either having their own geometrical description or are defined upon a parameter space of a surface. The section concludes with the integration of coupled edges, allowing to impress geometrical or kinematic driven continuities between various geometries. Refer to [149] for the description of solids.

#### 3.4.1 Numerical integration of trimmed surfaces

A quantitatively good integration of untrimmed NURBS geometries is given by the Gauss-point locations within the respective knot spans, with the number of integration points being defined by the polynomial degree of the NURBS-patches. For structural analysis purposes this provides good results, however, it shall be noted that not always as many integration points would be required [108], which results in a significant overhead in computational costs, which is specifically crucial for explicit problems (see Leidingner et al. [133]).

In contrast, the simulation with trimmed surfaces is significantly more involved [40, 222]. IBRA evaluates element functions over trimmed NURBS surfaces by integration points inside the trimmed domain. A possible avenue for the evaluation of those is presented within figure 3.9.

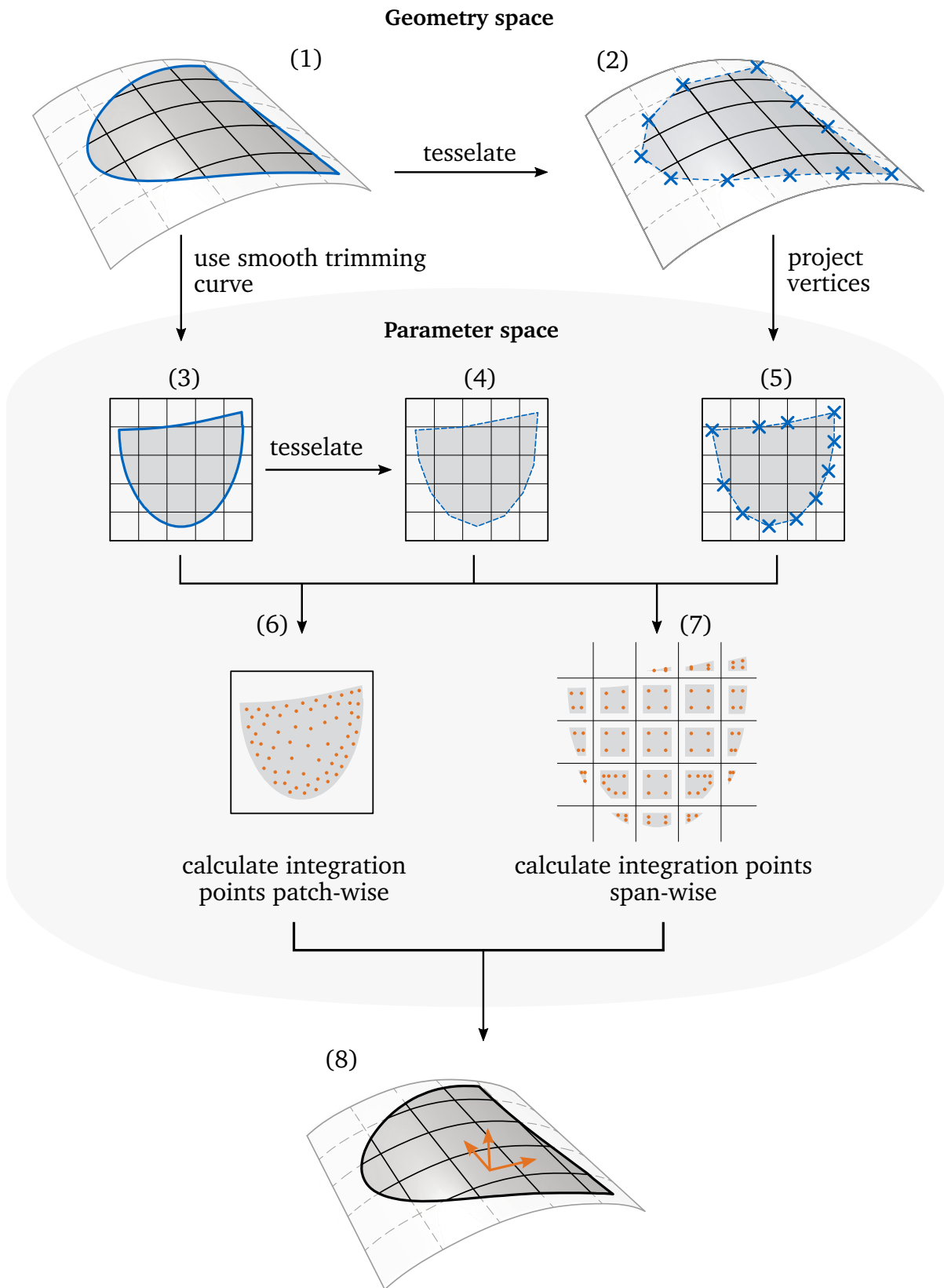


**Figure 3.9:** Procedure of trimmed surface integration (modified from [222]).

- Either the NURBS-described (1 and 3) curves or a polygonized tessellation (3 and 5) is considered as the physical limits within the parameter spaces of the surfaces. Using the smooth boundary curves (1 and 3) leads to an exact representation of the trimming domain but involved geometrical operations.
- Considering the tessellation within the geometry space (2) or the parameter space (4) may result into coarse polygons. Mostly, the tessellation in the parameter space would provide less points as the curvature of surface is not considered. For the integration of the surface, this is mostly sufficient.
- Consequently, either patch-wise (6) and span-wise integration (7) may be operated. Patch-wise integration typically results less integration points, whereas span-wise segmentation deals with less trimming scenarios. By latter, it is typically differentiated between trimmed and untrimmed domains. The correct integration of the trimmed domains is an open research topic, whereby multiple avenues have been proposed: e.g. AGIP from Breitenberger et al. [40], and other references [206, 145, 149].
- Integration point defined entities can be formulated within the geometry space (8).

Further literature on trimming and the achievable quality of the solutions can be found within [108, 197, 159, 145, 146, 256]. A computationally efficient yet accurate integration of the bilinear forms of cut elements is an important topic for any immersed boundary method. A recent comparison of such techniques is given e.g. in [105].

#### 3.4.2 Numerical integration of curves on surfaces/edges

Curves on surfaces are integrated in the parameter space of the underlying patch. Therefore, the intersections between curve  $\tilde{C}$  and knot-lines are found (see figure 3.10). The outcoming curve sections are integrated by a chosen quadrature rule. Within the scope of this work, mostly  $p + q + 1$  points have been employed per section (covering the case of a curve going diagonally through the knot span). This amount of integration points is on the safe side and it is suggested to reduce this for more efficient computations.

#### 3.4.3 Numerical integration of coupling edges

Coupling edges are a specific scenario of the previously discussed curve on surface integration. Here, one side needs to be selected as the master curve, which consequently will be named with the index (1), the other edge is the corresponding slave edge,

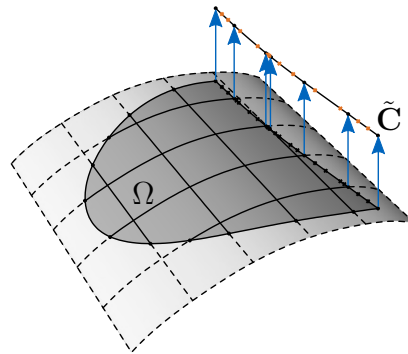


**Figure 3.10:** Integration of curves on surfaces/ edges.

being (2). The integration will be applied on the master curve, following the mappings described in section 3.4.2. Theoretically, the selection is random, however, it has to be noted that eventual numerical differences might appear (see also [246]), which should vanish with an increased and matching refinement on both sides.

The numerical integration domain is dependent on the trimming curves of both patches. In the following two different projection avenues shall be outlined (see figure 3.11). One is considering the parameter curve of one patch as reference, whereas one is describing the discretization on a interpolated 3d-curve.

1. The discretization is operated on the parameter curve  $\tilde{\mathbf{C}}^{(1)}$ :
  - find surface knot span intersections of  $\tilde{\mathbf{C}}^{(2)}$  (see section 3.4.2)
  - project found intersections to global space and map onto  $\tilde{\mathbf{C}}^{(1)}$
  - find surface knot span intersections of  $\tilde{\mathbf{C}}^{(1)}$  (see section 3.4.2)
  - merge both intersections
  - define integration within the spans
  - project integration to global space and map onto  $\tilde{\mathbf{C}}^{(2)}$
2. The discretization is operated on the interpolated 3d-curve  $\tilde{\mathbf{C}}^{(1)}$ :
  - Interpolate curve fitting to both parameter curves.
  - find surface knot span intersections of  $\tilde{\mathbf{C}}^{(1)}$  and  $\tilde{\mathbf{C}}^{(2)}$
  - project found intersections to  $C(\xi)$ .
  - merge both intersections
  - define integration within the spans

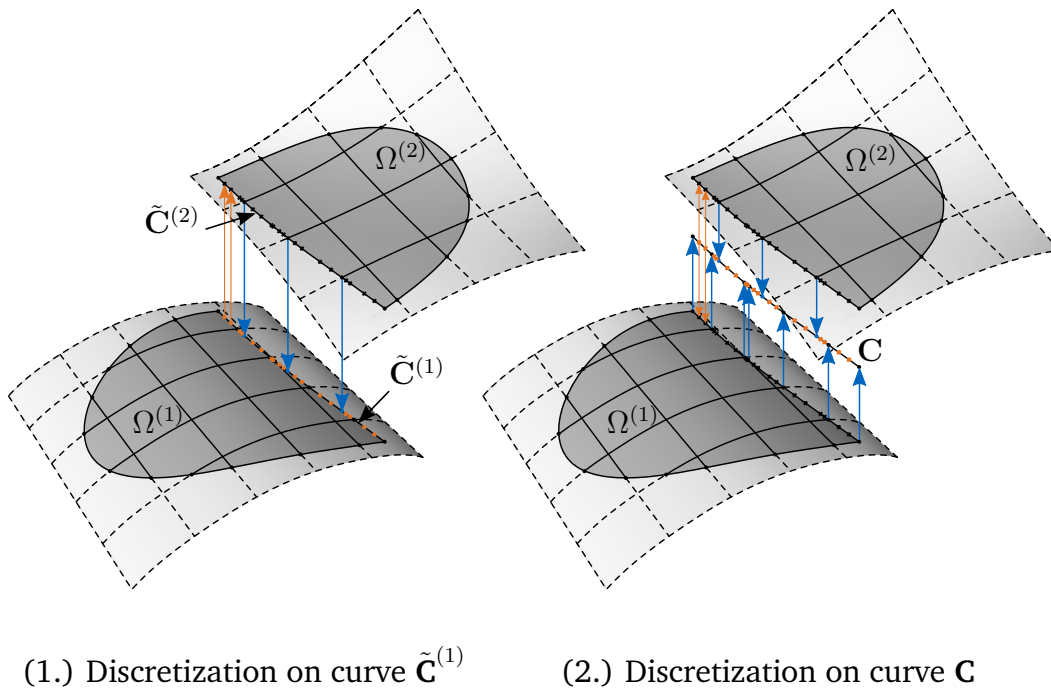


**Figure 3.11:** Integration of coupling edges.

- map integration onto  $\tilde{\mathbf{C}}^{(1)}$  and  $\tilde{\mathbf{C}}^{(2)}$

The mapping from geometry space towards parameter spaces can be a comparatively involved operation as it requires appropriate initial guesses and is accordingly error prone. Whereas, procedure 1. relies on the projection of the integration towards only on patch, procedure 2. requires projections of the integration points onto both patches. Accordingly, within this scope procedure 1. is preferred. However, both solutions shall converge.

Once a curve on surface is coupled with a 3d curve, the procedure to detect the integration can be referred to a simplified procedure 1., whereby the curve  $\mathbf{C}(\eta)$  can be seen as the 3d curve.

### 3.5 Properties of CAD-based analysis <sup>d</sup>

Within figure 3.12 is presented the CAD model and the displacement results of an IGA simulation of a plane structure (Further results are presented within figure 3.13; an uplifting pressure force is applied at the wing of the plane). The model is taken from [237] and has initially been designed for CFD purposes and as such, it is used frequently for benchmarking. The model appears to be suitable for IGA, however,

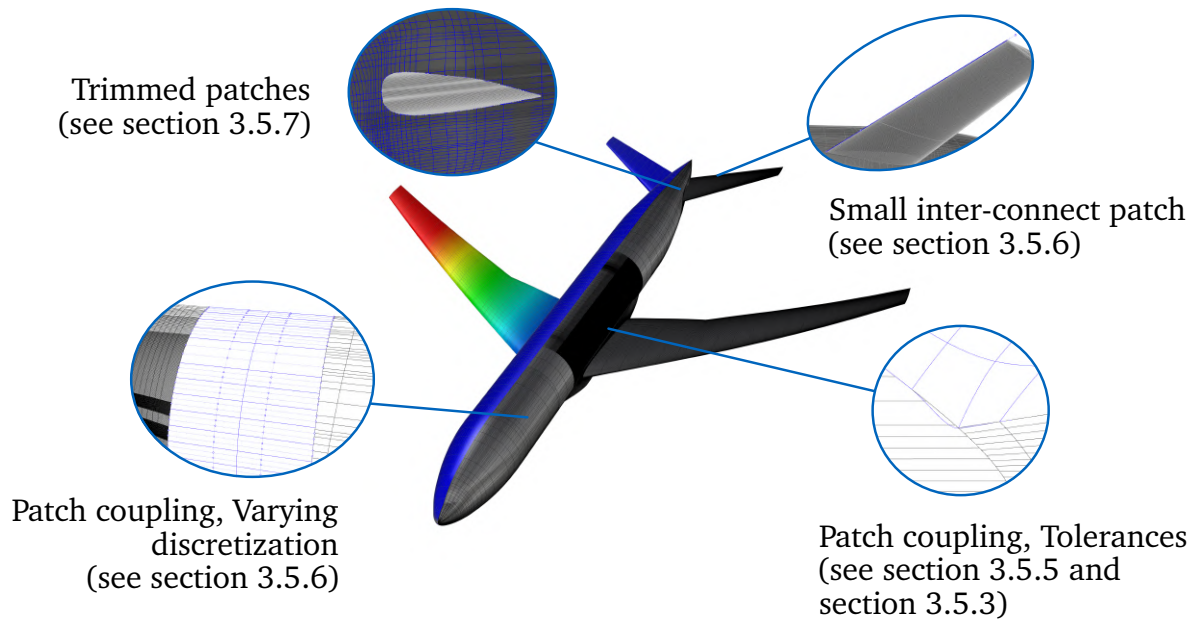


**Figure 3.12:** Plane common research model geometry [237] including IGA results with apparent geometry description issues.

requires special attention on some details for reliable analyses results. Among others, those cover: trimming, patch coupling of 28 patches with varying discretization, small inter-connection patches, and high tolerances in gaps. If treated weakly, those issues may result in unfeasible solutions.

Although the CAD-integrated analysis with IGA is based on the exact geometrical shapes provided from the CAD software, the description might not be well-suited for simulations. One of the key challenges in using CAD-provided geometries is that the design and visualization typically need a different, usually lower, level of refinement in the shape description since the model has to represent only the undeformed geometry. Whereas the FE model and its mathematical description have to represent various sets of information, such as the deformed shape and stresses. Accordingly, some issues in the CAD-based context with respect to direct use for structural analysis shall be discussed within this section.

It shall be noted, some of the critical challenges resulting from poor geometry descriptions are intrinsically present in the model and would manifest themselves equivalently in an automated meshing process prior to classical FEM-based simulation [222].

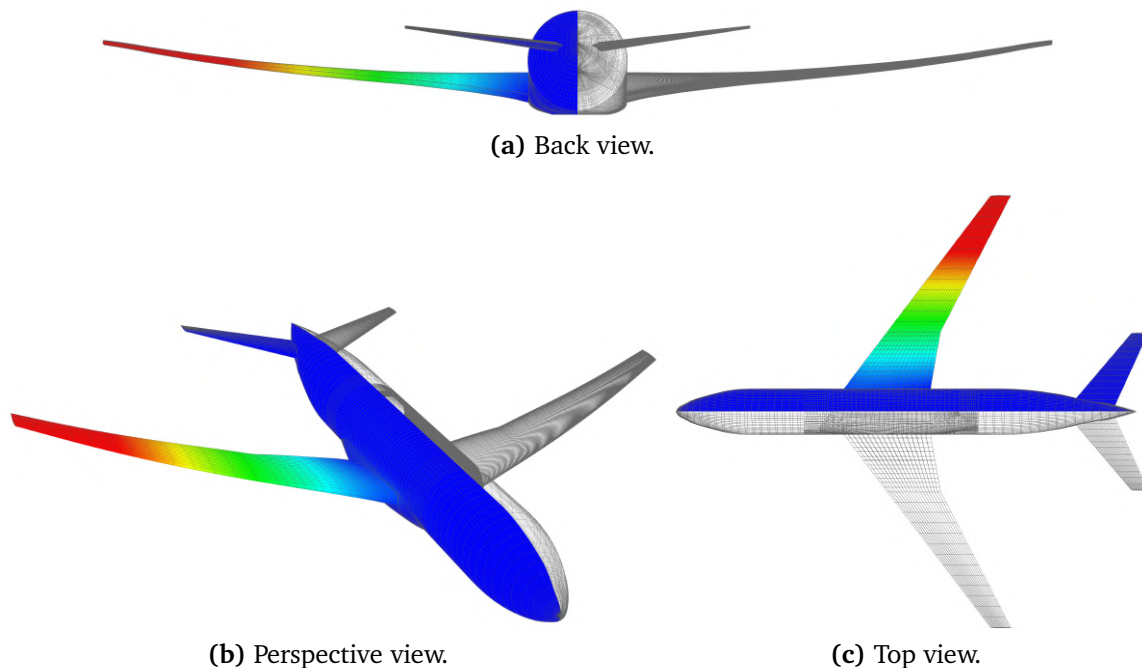


**Figure 3.13:** Plane common research model [237] displacement results from pinched wing and geometry.

### 3.5.1 Solid model

B-Rep based CAD models are constructed with 1D curves or 2D surfaces, which is especially suitable for fast and stable graphical design purposes. Accordingly, the simulations may rely on 1D or 2D shapes which can be the description for dimension-reduced formulations such as beams [24] and shells [118, 76, 169, 170]. Those come along with simplified computational efforts, however, are limited in the expression of very complex shapes.

If 3D solid-based computation is inevitable, increased efforts are required as CAD does not intrinsically provide a mathematical volumetric solid description. One possible avenue is the embedding of the enclosing surfaces into a grid, or a 3-dimensional B-Spline/NURBS-cube background. This technique is frequently applied within the Finite Cell Method (FCM) [177, 75] and allows for handling various types of geometries such as trimmed solid models [190], CSG (see section 2.1) models [243], B-Rep models which may be flawed [244], or point cloud based models [128].

Another possible avenue for the computation of solids within boundary representation has been introduced and described by [122, 123, 52]. They propose to construct a NURBS-based solid from the radial scaling center of the physical domain towards the NURBS description of the faces, which seems to be another effective approach for CAD-integrated simulation.

#### 3.5.2 Surface model vs. mid surface model

Thin-walled structures, which are suitable for the computation with dimensionally reduced FE elements are often expressed as solids in industrial applications since the enclosing surface is decisive in the design. This obstructs a direct evaluation with surface-based formulations since many of them rely on the mid surface of a thin-walled structure. Figure 3.14a shows two steel plates which are welded. The model is displayed as the boundary surface model and its reduction towards the mid surface. It shows clearly that the solid surfaces appears watertight, whereas the mid surface model has severe gaps and an automated detection of a coupling is highly dependent on the user-defined threshold. This tolerance can be chosen for certain types of structures. However, it is not possible to automate this process if there are gaps within the same chosen tolerance that should remain open or if other objects are close but should remain uncoupled. Another example, which appears frequently in civil engineering, is the corner case of two intersecting walls as figure 3.14b shows.<sup>b</sup> If the volumes do not overlap, which would be the correct volumetric modelling, the mid surfaces do not intersect and coupling cannot be detected in an automated way beside a certain tolerance. If they do overlap, the mid surfaces intersect and the coupling is detected but the correct modelling of meeting curves in the corner point is still not gained.

To summarize, the extraction towards middle surfaces needs additional understanding of the specific geometrical issue and accordingly manual work load or very sophisticated, problem dependent algorithms, especially at intersections.

#### 3.5.3 Inter-patch connections for geometrical continuities

Some CAD programs intrinsically provide operations to join geometry items to fewer objects if there is a geometrical connection. Intersections are detected within a given accuracy, and model tolerance and additional interface shapes are appended. Those operations are typically carried out in a way helping to seamlessly and efficiently visualize the drafts, however, for engineering purposes, it is often not suitable or not sufficient.

Considering a broad model tolerance, the join operation would find many coupling edges or points, which indeed are decently distanced and it would visualize them as a gap-free object. An example of the coupling edge between two visually non-matching patches is shown in figure 3.15. Figure 3.15a is displaying the original shape of the two

---

<sup>b</sup>[104] presents a Mortar-based approach to model such corners and [175] is presenting the numerical simulation of a timber connection, where the interface itself is enhanced by a material law to represent an elastic material layer.

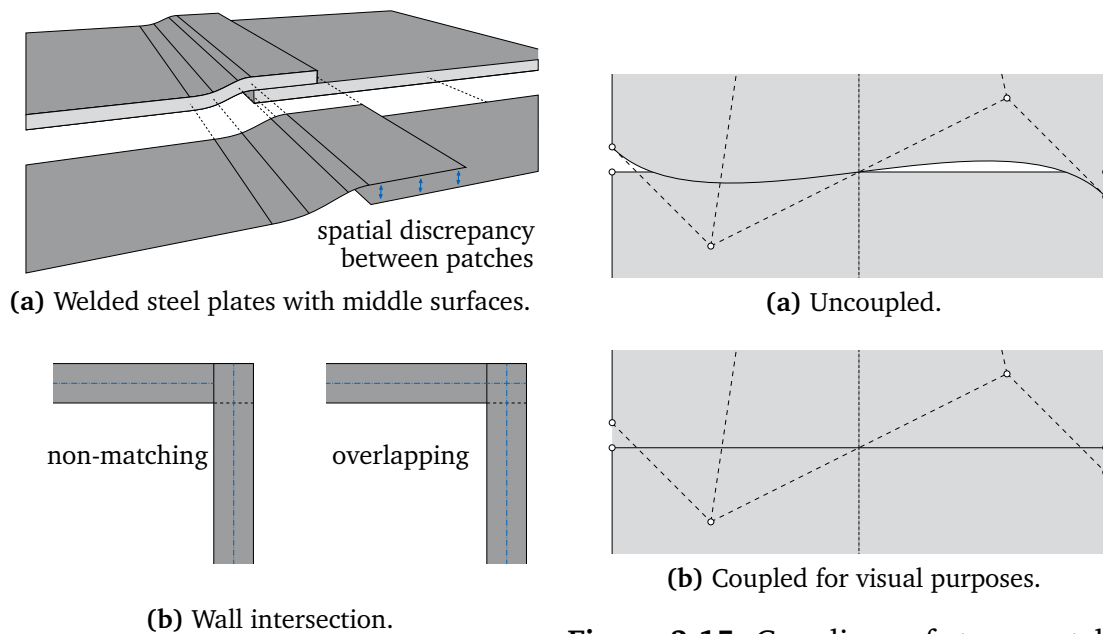
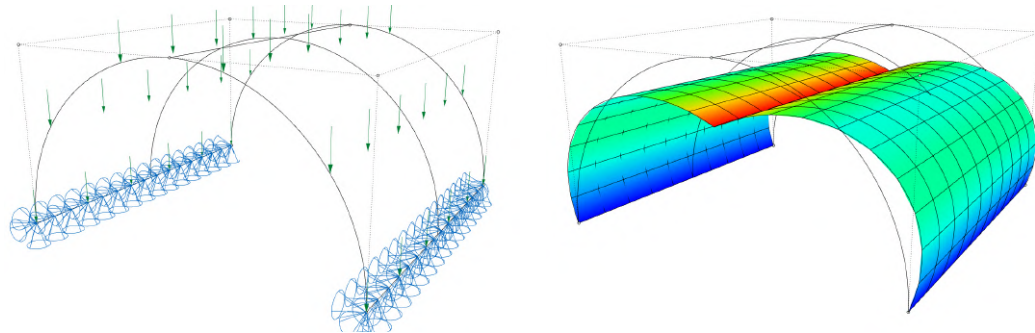


**Figure 3.14:** Projection towards middle surface.

**Figure 3.15:** Coupling of two patches with high allowed model tolerance.

patches. Within figure 3.15b is shown the same configuration after a join command. It shows that the visible discrepancy between the two patches is disappearing, even though that the discretization does not match. The analysis, however, would not be suitable to perform a stable simulation or maybe does not even detect the ordinary integration. The gap might also be eccentric for improper modelling, which introduces not existing stresses into the structure. Furthermore, the gap is assigned with a certain behavior when a coupling condition is added. This typically involves different behavior in the area of the gap than inside the material domain, which might affect the results depending on the gap size. Choosing a suitable model tolerance (see section 3.5.5) avoids this or decreases the error to a tolerable level. Considering this while modeling or repairing the geometries in a way that the wanted connections do not consider overly large gaps would lead to better solutions.

Furthermore, CAD-integrated join operations do typically just consider couplings amongst the boundaries of the shapes and each edge usually has only one other counterpart since the software structure is adjusted to handle boundary models. It may happen that e.g. T-joints (as shown in figure 2.3) remain undetected and get discarded. This concerns joints at the boundary involving 3 surfaces or one surface intersecting with another one inside its domain. Undetected couplings, especially those manifold joints, are usually not a big problem in CAD software if the geometry is constructed with sufficient accuracy since the geometries are still close and visually connected. However, the necessary information for the engineering part is not retrieved. Consequently, it



(a) Problem description with discontinuity at top mid line.

(b) Deformed problem.

**Figure 3.16:**  $C^0$  and  $G^1$  continuous geometry with possibly undetected  $G^1$  discontinuity in middle of the patch, due to duplicated knots. The knot vector of this example for  $p = 2$  may read:  $\Xi = [0, 0, 0, \frac{\pi}{2}, \frac{\pi}{2}, \pi, \pi, \pi]$ , whereby the inner knot (orange) is duplicated (for further notes about NURBS see [185]).

is advised to perform further intersection checks even though doing so is frequently computationally expensive.

Bauer et al. [25] present a range of possible applications for 1D structures, whereby intersection checks between the presented beams are processed to obtain all required couplings. Some shell based problems with T-junctions are presented by Hirschler et al. [102] or Herrema et al. [99].

#### 3.5.4 Geometrical discontinuities

Even though shapes may exhibit visual continuities, it is possible that the corresponding continuities in the mathematical description are not present <sup>c</sup> This may result into unexpected results, once the geometrical continuity is used to express the bending stiffness, as e.g. the KL-shell [118] or the Bernoulli-beam [24].

Among many scenarios, this happens frequently in the description of circular hulls, as per 3.16a. Here, the middle knot is duplicated, which results in a  $C^0$  (location) continuity.  $G^1$  (bending/rotation) and further would not be ensured. Even if the geometry were refined, this discontinuity would still exist. The outcome of a simulation with this specific problem is given within 3.16b. It should be noticed that a considerable rotational discontinuity can be seen in the center line.

<sup>c</sup>Discontinuities are frequently introduced in NURBS-based domains by duplicating knots.

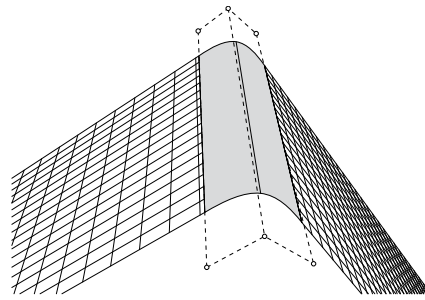


**Figure 3.17:** Badly conditioned connection patch.

It is possible to find numerous different geometry descriptions that, without discontinuity, describe the same shape. However, the initial forms would be distorted. Accordingly, to not exchange any geometries, the required continuities may be enforced by the bending strip method approach [119] or by weakly applying the rotational stiffness, similarly as for patch-couplings [40].

### 3.5.5 Model tolerance

Dirty CAD descriptions with high model tolerances can lead to gaps between the provided patches, which might be filled visually by the software and accordingly, sophisticated to detect. The model quality may be such poor that the CAD utility cannot set up the coupling conditions within appropriate tolerances. Additionally, with unbridgeable gaps between patches some coupling methods fail or converge towards wrong solutions and a proper physical description is not ensured (see also [41, 26]).

### 3.5.6 Patch conditioning

Many CAD programs provide operations to visually eliminate gaps between existent patches. Those operations are optimized for visual purposes. However, the additional patches are repeatedly showing difficult mathematical properties for structural analysis purposes. Those patches have often substantial differences in the geometry extensions of the knot spans causing badly conditioned numerical elements. Efficient automated refinement operations and robust integration techniques are recommended to prevent this issue. The refinement derives from the respective span length. However, in some of those patches, boundary effects, introduced by weak coupling approaches might predominate the kinematic properties of the surface formulations, which may lead to an

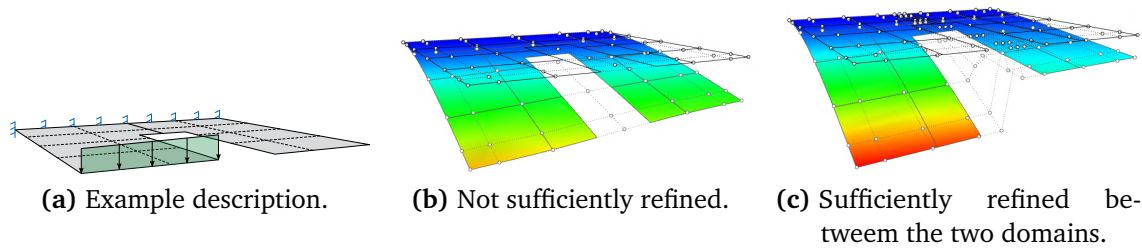


**Figure 3.18:** Trimmed example with possible unwanted interaction within the domain

artificial stiffness.<sup>d</sup> A further critical issue is that even if solving appears to converge, the solution might still be unreliable. The assessment of the result quality may become challenging, which could lead to a loss of trust in the numerical method.

This happens for example if a rounded connection patch between two patches is being created by an automated process. Figure 3.17 is presenting such a problematic patch. The patch has been constructed during a smoothening corner operation. It contains only 6 control points. Thus, by connecting it to the neighboring patches it would create a numerical stiffness. Sometimes it is hard to detect those patches in larger models, as they are very slim and tiny. However, their effect may have severe impacts on the solution. Figure 3.12 is showing a similar problem. At the corner of the wings have been created connecting patches between the top and bottom to create a tight model. Even though the remaining patches would be greatly refined, those connecting patches would completely stiffen the wings.

#### 3.5.7 Trimming

Trimming is independent of the knot span description and may therefore arbitrarily cut through the domain. Knot spans with a small physical domain may result from this operation and cause additional challenges for the FE solver regarding the stability of the system. Typically, contributions associated to some degrees of freedom will be badly conditioned, which might spoil the solutions. Additionally, boundary effects might outweigh the numerical properties. There are control points that have minor influence on the shape/solution resulting in very small entries in the respective stiffness matrix, which is consequently badly conditioned. The resulting solution may contain close to infinite values. Furthermore, the results for the degrees of freedom on those control points may differ a lot in all iterations and obstruct the convergence in the solver.

<sup>d</sup>E.g. the penalty approach is achieving continuity by indicating a spring between the domains. The selected spring stiffness, namely penalty factor is therefore apparent in the solution. With patches of small sizes this effect might dominate the results.

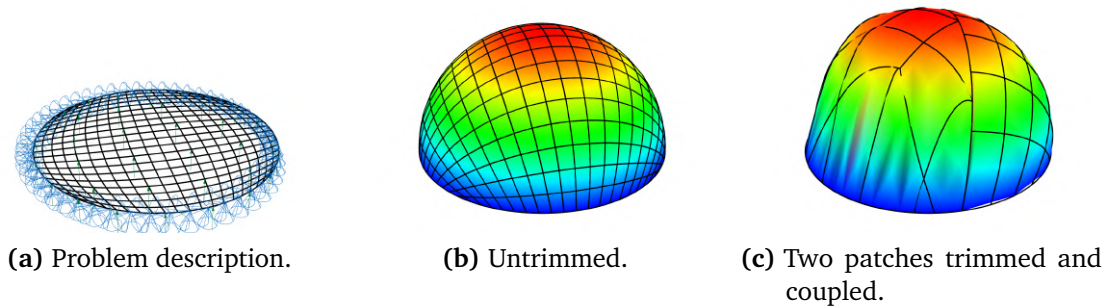


**Figure 3.19:** Formfinding under pressure load.

Different technologies have been proposed to limit the deflections of those control points, e.g. modifying basis functions [103, 110, 253], stabilization terms [132] or conditioning of solvers [114].

Figure 3.18 presents a different problem with trimming. A rectangular cantilever plate with a split in the middle is modeled by one trimmed patch generating two almost independent cantilevers. One of them is loaded at the tip and should consequently deform whereas the other should not deform. Figure 3.18b shows the simulation results with an unwanted interaction between the two ends, whereas figure 3.18c is sufficiently refined to properly simulate this problem. This example shall point out the apparent problematic, which becomes even more severe if the trimming is not aligned with the knot span description. The necessary refinement in order to generate independent knot spans that do not share control points and consequently to decouple the boundaries may spread out over the whole domain due to the tensor product structure of NURBS surfaces.

One problem with trimmed domains is that even though analysis may be suitable for some models, the apparent geometry description might be weak or even distorted, which directly affects the solution accuracy [40, 41, 223, 149].

Another example containing a similar issue due to trimming and eventual quantitatively weaker results than the untrimmed model is the form-finding problem [36] of a membrane plate with out-of-plane loads [184, 12]. Given that the radius of the support and the pressure load relate via the *Boiler* formula, the outcome of this problem should be a perfect hemisphere. This solution is approximated almost perfectly in the untrimmed configuration 3.19a. In contrast, the trimmed-multipatch scenario shows severe problems in the description of the aimed shape 3.19c. With an increased refinement this problem may appear differently. However, it will always be slightly visible. Here, the multipatch coupling is implemented by the penalty approach (see [40, 184, 133, 60] for IBRA), which results in a corrupted stiffness at the interface. Accordingly, to optimize

the results it is suggested to use different coupling approaches (see e.g. [11, 98, 222]) or a more advanced penalty computation [178].

As a summary, it shall be noted that enabling an analysis with trimmed domains allows the simulation of complex models without any re-discretization. On the other side it may introduce flexural limitation, which should be studied carefully to avoid corrupted results.

#### 3.5.8 Preparation of the model

Some of the previously mentioned issues may suggest a revision of the B-Rep-based CAD model before eventual simulation. One proposed possibility is the patch degeneration of multiple patches towards fewer patches [130]. Typically, this introduces slight chordal errors, however, the positive effects may outweigh the instabilities from the original model. The outcome of this operation is a more continuous distribution of control points throughout the patches and a reasonable polynomial order. Therefore, the model preparation can improve the stability of the simulation for many scenarios. However, it non-reversibly modifies the CAD model, which itself adds complexity in the CAD-integrated (automated) workflow and opposes the original concepts.

The long-term goal is to incorporate the requirements for an eligible simulation within the design phase and not as part of the pre-processing in the analysis step. Then one model would be sufficient and iterations between the two disciplines become simplified. Accordingly, knowing about the mathematical properties of a chosen design path, as explained within this chapter, helps to select the appropriate avenues for a quantitatively good and seamless design-through analysis workflow within CAD.

### 3.6 Immersed methods

Embedding physical entities into a non-matching mathematical formulation is a well-known procedure within numerical approaches [173]. Peculiarly, in CFD simulations with large-scale models, it gained popularity within the last years as it significantly facilitates the modeling process [69, 259]. IBRA can likewise be seen as an embedding problem, as with trimming, the domain finally is not matching with the mathematical shape description. A similar procedure of trimming has been enhanced to apply boundary conditions, as Dirichlet or Neumann on any parametric shape within the primary domain [40, 41]. [23] introduces embedded 1D-based kinematically driven formulations as beams and trusses within the NURBS-surface shapes, which shows the tremendous opportunities provided with this effective approach. However, it concludes the non-matching mathematical description of the additional entities may require a

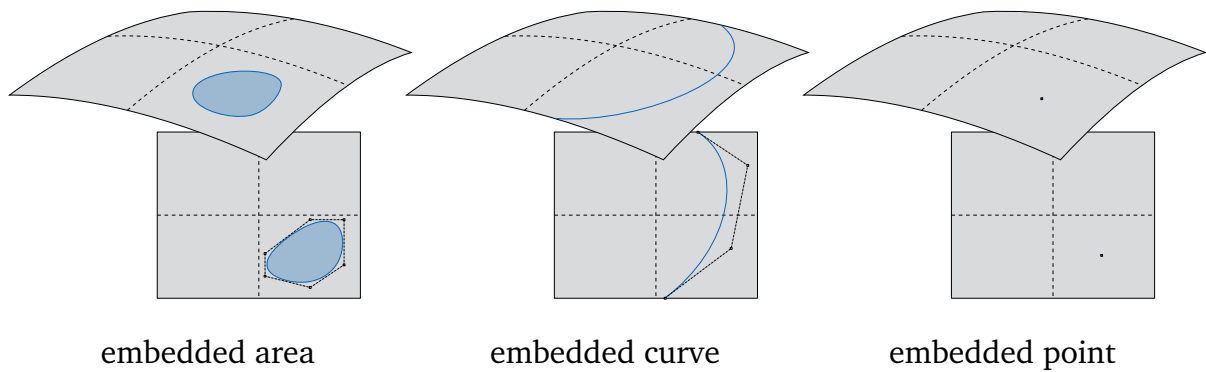


**Figure 3.20:** Embedded entities in surface based geometries.

considerably higher amount of degrees of freedom for the accurate prediction of the expected physical behaviors, which also results in a comparatively slow convergence compared e.g. with coupled approaches (see section 3.8.1 and [26]). [102] employs a similar concept, however, embeds more involved shapes and respectively kinematics, delineated by KL-shells into a different discretization.

For surface-based geometrical entities, three distinctive parametric shapes are imaginable for embedded objects, which comprise areas, curves, and points as shown in figure 3.20. 3D domains would allow additionally to embed volumes themselves.

Consequently, the usage of embedded areal domains shall be studied to examine the applicability of this approach for masonry structures (see section 4). A beam, as per

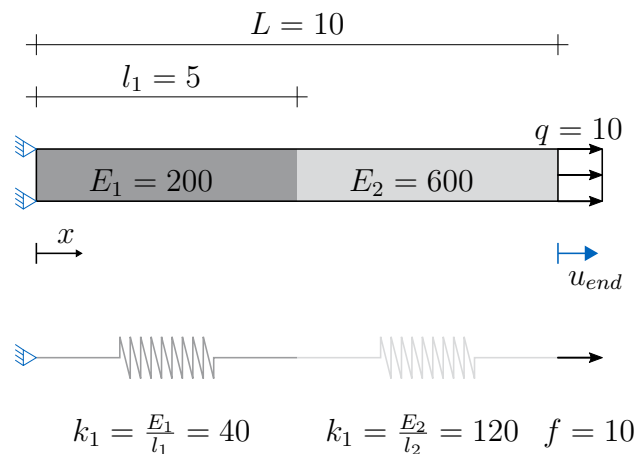


**Figure 3.21:** Embedded entities in pulled beam and respective corresponding 1D-spring system.

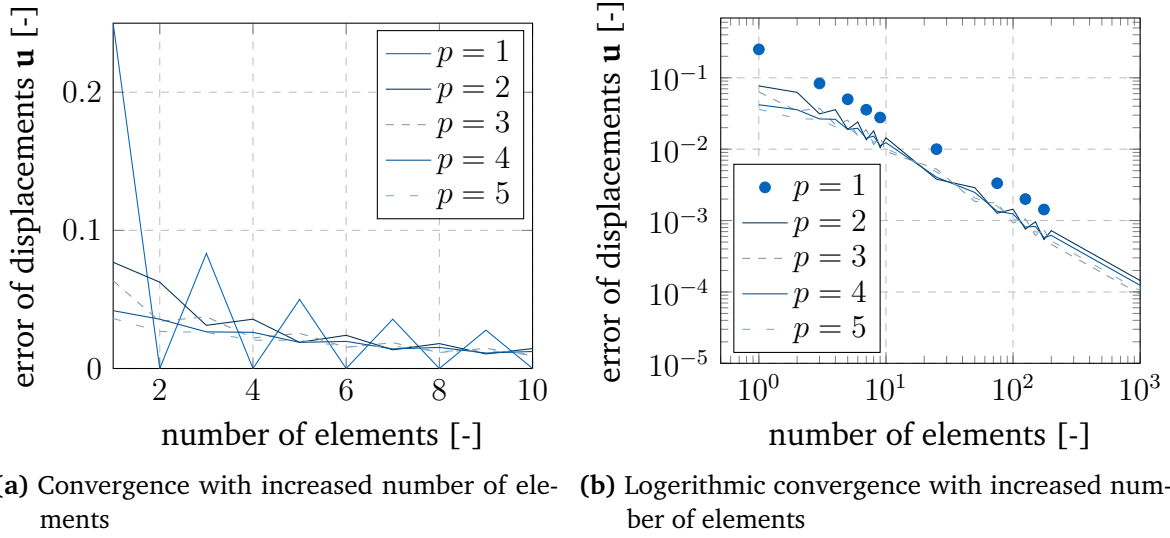


**Figure 3.22:** Convergence of pulled beam (see figure 3.21) with the error being defined

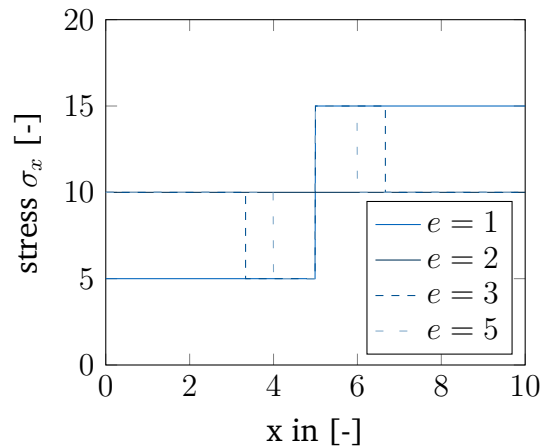
$$\text{by } \frac{u_{exp.} - u}{u_{exp.}} = \frac{\frac{1}{3} - u}{\frac{1}{3}}.$$

figure 3.21 is made upon two dissimilar materials with the stiffnesses  $E_1$  and  $E_2$ , whereby the overall stiffness of the system can be noted as follows:

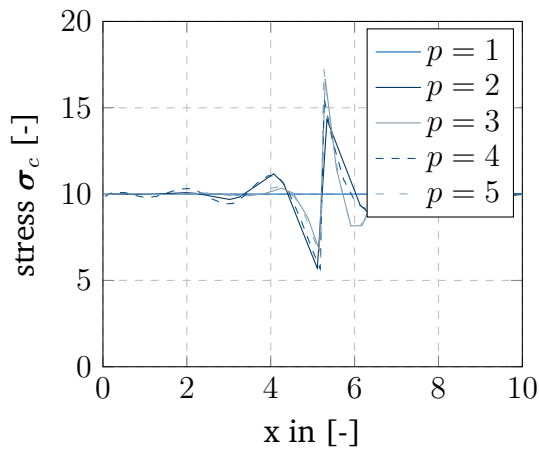
$$\frac{1}{k_{tot}} = \frac{1}{k_1} + \frac{1}{k_2} = \frac{1}{40} + \frac{1}{120} \quad \Rightarrow \quad k_{tot} = 30, \quad u = \frac{f}{k} = \frac{10}{30} \quad (3.22)$$

Following, the performance of embedding the respective entities within the domain are evaluated, with a varying number of elements and polynomial degrees of the shape functions (considering geometrically linear). The convergence of the problem can be seen within figure 3.22a for a low number of elements and the respective convergence with a longer convergence in logarithmic scale within figure 3.22b. The graphs show a convergence of the solution towards a large refinement, with the higher degrees having less variations. It displays that the linear discretization is flawless once the element boundaries overlap with the embedding lines, which suggests a deeper investigation of this phenomena.

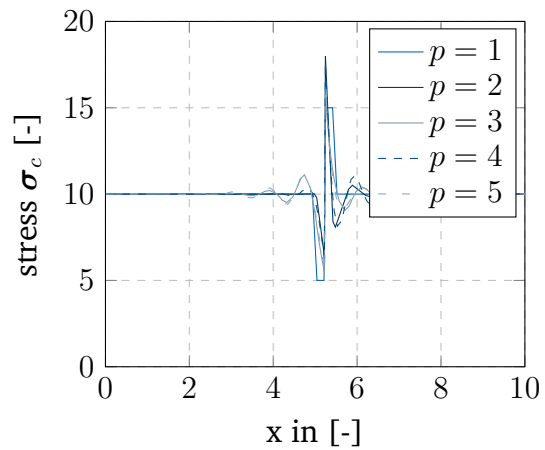
Given that the displacement being  $u_{end}=0.25$  for a single element, it follows that the respective spring stiffness would be  $k=40$ , or the Young's modulus  $E=400$ , which precisely coincides with the mixed stiffnesses between the 2 domains, which contradicts with mechanical problem of two springs in row. Considering this effect, refining the system would result into the problematic element vanishing by becoming small compared to the entire problem, which resolves into a convergence, as per figure 3.22b.



(a) 1, 2, 3, and 4 elements for linear shape functions ( $p=1$ ).



(b) 10 elements.



(c) 25 elements.

**Figure 3.23:** Stresses (Cauchy) of pulled beam (see figure 3.21) with varying polynomial degrees.

To gain a deeper understanding of the problematic of various stiffnesses within a single FEM element, the obtained stresses shall be discussed. Therefore, following problems are resolved in geometrically non-linear manner. Accordingly, the stresses are plotted in figure 3.23a for the linear shaped case for 1, 2, 3, and 5 elements. As per the previous analysis the stresses are analytically correct for 2 elements, which coincides with the embedding boundary. However, the stresses are crucially overestimated for the embedded elements, whereby the softer system shows lower stresses as the stiffer part, which is in contradiction to the reality.

Proceeding this investigation different polynomial degrees shall be analyzed for a refinement of either 10 elements (figure 3.23b) or 25 elements (figure 3.23c). It similarly shows an overestimation around the cut element. Furthermore, the higher the

order of the shape function, the more oscillations occur around the cut. For the linear case ( $p=1$ ), 10 elements cut the element properly, however, 25 have a cut element which shows the same jumps as in the previous test (see figure 3.23a).

It shall be summarized, that even though there exists a convergence with an increased number of elements, the usage of embedding stiffnesses becomes heavily involved for non-linear materials, thus, stress-dependent behaviors would be crucially overestimated at the cut element. Accordingly, without additional stabilization, the approach would not be generically suitable. This approach will not be considered further, as specifically for masonry structures it would critically influence the solution. However, as the embedding phenomena is employed frequently, this discussion was stated within this dissertation.

## 3.7 Material Point Method (MPM)

The material point method [216] is a particle-mesh based approach, containing a hybrid Lagrangian-Eulerian interpretation, which gained significant attention in engineering simulations, as e.g. soil, and geomechanics and in computer graphics, and movie industry, as it is capable to adequately express large deformations involving continuum based history-dependent materials. The numerical approach can be classified within 4 main stages as shown in figure 3.24.

- (a) The updated Lagrangian calculation phase is conducted, whereby material points act as integration points, similarly as known for other FEM methods. It results in a deformed grid and deformed material points, whereby its new location is defined by the deflections of the background mesh.
- (b) Simulated results from this timestep are interpolated and mapped to the material points.
- (c) Update or reset of the mesh. It shall be noted that this step would allow an exchange of the background grid, as now the entire historical information is stored upon the material points and all dependencies are resolved.
- (d) The new locally described positions of the particles are detected and subsequently the internals of the material points are extrapolated to the background grid.

In comparison to the previously described approaches, MPM enhances the standard simulation by the continuous inter-and extrapolation of information between background grid and material points **(b)-(d)**, whereby within this stage the method transforms towards a particle method. Within phase **(a)** it behaves similarly as trimming known from IBRA, as per section 3.4 or as an embedded approach, likewise section 3.6.

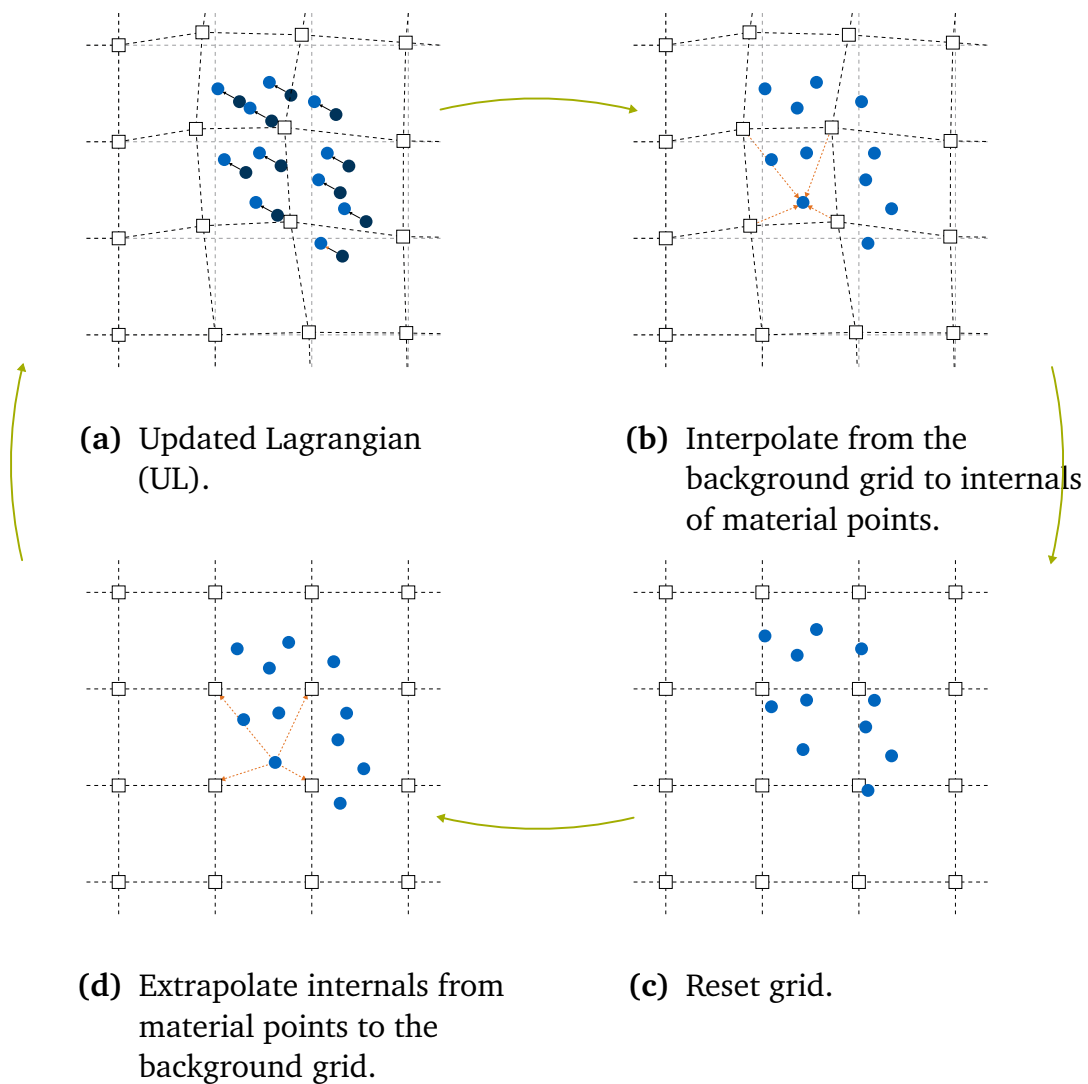


**Figure 3.24:** Procedure of MPM.

**Remark 3.7.1: Similarities and differences to transient FEM**

MPM has strong similarities with FEM, which enabled a fast development of the method within the last decades. Considering quasi-static and implicit integration schemes, standard FEM procedures can be reached by reducing the 4 stages (figure 3.24) to one and only realizing stage **(a)**. Vice-versa MPM contains numerous procedural resemblance with FEM [96].

As contrast, the explicit integration scheme does not allow this continuous reduction, as here, the stress updates are applied within different positions of the simulation steps and accordingly require a more involved implementation.

#### Remark 3.7.2: Smearing effect through continuous inter-and extrapolation

Considering an MPM variation that does not reset the location of the background grid, however, still executes the inter-and extrapolation before and after each time step, as figure 3.24(a) and 3.24(c). With this functional modification, one basic MPM-characteristic can be extracted and it results that an irreversible error is introduced within each timestep as shown by Wilson [248]. It is expected that this inaccuracy is even more severe once the mesh is reset to its initial position.

The MPM has shown strong capabilities in the simulation of highly deforming objects, specifically mentioning soil mechanics and fast contact simulations [112, 97], where the correct deflection can only be approximated, however the focus is set on the visualization of a close-to-reality.

Apart from inaccuracies evolving from material points, or respectively integration points which are not placed at ideal locations, there are two major problems appearing in the MPM. One is the cell-crossing problematic, occurring once particles pass from one to another cell of the mesh and the other is the numerical fracture which appears when within two particles appear another element and accordingly the connection gets falsely lost. Both issues appear to be significantly dependent on the mesh and chosen integration, however, can never be completely diminished without additional stabilization.

Since the introduction of MPM, various approaches have been introduced to minimize the effects of cell crossing and numerical fracture. Amongst the famous cell crossing-adjusting approaches shall be mentioned the Generalized Interpolation Material Point Method (GIMP) [198], the convected particle domain interpolation (CPDI) [199], Total Lagrangian Material Point Method (TLMPM) [238] and the partitioned quadrature material point method (PQMMPM) [247]. The majority of those methodologies work on extrapolating the integrational domain towards non-local geometrically neighbouring elements, which typically results in a modification of the apparent shape functions, towards smoothening the mesh interface jumps. Considering those modification, the question arises if generally non-local shape functions within the background domain may rectify the problems in a similar way. Accordingly, various studies intent a variation of the background mesh (some of which are summarized within [217, 238]), as with B-Splines/NURBS [213, 232, 252].

## 3.8 Multiphysics and multidomain coupling <sup>a</sup> and <sup>b</sup>

With the development of FEM methods various novel technologies have been established to solve varying types of problems. Each FEM physic has different properties and is

accordingly specially suitable for distinct fields of application. Frequently, problems appear where a combination of methods is the most suitable approach, which often involves contact, or a split of the domain. To achieve the coupling between different physics, those methods have to be broken down to an instance where an inter-facial exchange of physical properties is possible. Once the system, including the interfaces is established, it needs to be solved. Hereby, two possibilities exist:

**Monolithic** the governing equations of all involved approaches are solved simultaneously within a single solver.

**Partitioned** the governing equations of all involved approaches are solved independently within multiple solvers (also known as staggered).

As partitioned problems do not rely on the same solver, those problems can be split into different software environments, whereby monolithic problems are typically limited to the availabilities within a single product.

Fluid-structure interaction is one of the most famous engineering multiphysics problems [250, 210] which has lead research and industry within the past years and is nowadays available with many varying numerical discretizations. Other famous approaches are for example contact and impact problems. However, multiphysics is not the only problem demanding a split of the domain, as sometimes using a single domain is not beneficial due to mathematical limitation or might be computationally too costly.

IBRA is a prominent example where sub-domains, namely patches require computational efforts to be connected. Here, the division within sub-domains arises from the geometrical description in CAD, which itself is driven by optimal geometrical operations with a minimal amount of control points, which is arguably beneficial for numerical simulations (see section 2.1). Typically, IBRA relies on monolithic approaches for the so-called patch coupling, as generally many patches would be involved. However, a partitioned coupling, which generally covers only few domains would be feasible as well.

The challenge to apply appropriate continuities between patches and Dirichlet boundary conditions has as well been addressed in other variants of immersed methods such as for FCM see e.g. [125, 78, 176].

### 3.8.1 Monolithic coupling approaches <sup>a</sup>

A monolithic coupling typically works with enhancing the virtual work with an additional term for the interconnections between the involved sub-domains, whereby the outcome is a single linear system. This is specifically advantageous once both domains contain similar stiffness, which is mostly the case in IBRA. Within the following, approaches

shall be discussed, which mainly appear in the scope of IBRA. However, those shall be seen as generic descriptions, as those may be used within other numerical methods equally.

Consequently, the main focus is put on:

- penalty approach
- Lagrange multiplier method

for enforcing continuity between two sub-domains (namely patches within the framework of IBRA). It shall be mentioned that additionally the Nitsche-based [11] coupling and Mortar methods [43] are other famous approaches in the constitution of boundary and continuity conditions. However, as those are generally non-local and computationally more involved they shall not be considered within this scope. Another famous approach of the monolithic coupling is the multipoint constraints (MPC) [113], however, it is only valid for limited scenarios in the scope of IGA and thusly not considered, here.

#### **Penalty approach:**

The weak form (see equation 3.2) of the independent sub-domains can be extended by adding the virtual work for the penalty continuity coupling as following:

$$\delta W^{C_0} = -\alpha \int_{\Gamma^{(1)}} (u^{(1)} - u^{(2)}) (\delta u^{(1)} - \delta u^{(2)}) \, d\Gamma^{(1)} \quad (3.23)$$

$u^{(1)}$  represents the respective degrees of freedom around the coupling boundary of the master patch, whereby the index (2) dedicates the corresponding quantities on the slave side and  $\alpha$  is being the selected penalty factor. The virtual work  $\delta W^{C_0}$  between two patches vanishes once continuity is given.

Consequently, the contribution of the penalty coupling within the system state of equilibrium can be summarized as:

$$(\mathbf{K} + \mathbf{C}_\alpha) \cdot \mathbf{u} = -(\mathbf{R} + \mathbf{R}_\alpha) \quad (3.24)$$

in accordance, it may be split into the respective sub-domains:

$$\begin{bmatrix} \mathbf{K}^{(1)} + \mathbf{C}_\alpha^{(1,1)} & \mathbf{C}_\alpha^{(1,2)} \\ \mathbf{C}_\alpha^{(2,1)} & \mathbf{K}^{(2)} + \mathbf{C}_\alpha^{(2,2)} \end{bmatrix} \cdot \begin{bmatrix} \mathbf{u}^{(1)} \\ \mathbf{u}^{(2)} \end{bmatrix} = - \begin{bmatrix} \mathbf{R}^{(1)} + \mathbf{R}_\alpha^{(1)} \\ \mathbf{R}^{(2)} + \mathbf{R}_\alpha^{(2)} \end{bmatrix} \quad (3.25)$$

with  $\mathbf{K}^{(i)}$  and  $\mathbf{R}^{(i)}$  being the stiffnesses and residua of the respective domains. Accordingly,  $\mathbf{C}_\alpha^{(i,j)}$  and  $\mathbf{R}_\alpha^{(i)}$  are expressing the additional penalty contributions, being defined as following (considering  $^e$ ):

$$\mathbf{C}_\alpha^{(i,j)} = \alpha \int_{\Gamma^{(1)}} \mathbf{H}^{(i)T} \mathbf{H}^{(j)} d\Gamma^{(1)} \quad \text{and} \quad \mathbf{R}_\alpha^{(i)} = \mathbf{C}_\alpha^{(i,i)} \mathbf{u}^{(i)} + \mathbf{C}_\alpha^{(i,j)} \mathbf{u}^{(j)}, \text{ for } i \neq j \quad (3.26)$$

The approach is not introducing additional degrees of freedom and is simple to implement with a good computational efficiency. Even though that the stability is dependent upon the penalty factor, generally it is fairly simple to achieve good convergence, however, with the drawback that the quantitative solutions are corrupted by the penalty factor. The penalty method is variationally inconsistent as the penalty introduces a modeling factor which results that the weak form cannot be reverted from the strong form.

The stability and the quantitative quality of a solution is dependent on the selection of the penalty factor, which typically is a-priori selected by the user and can vary per connected degree of freedom (see also [40, 184]). [178] suggests a scheme to evaluate a suitable penalty factor with a minimal effect on the introduced model error, however, the estimation is still an approximation of the exact solution.

### Lagrange multiplier method:

To avoid the a-priori estimation of the penalty factor the Lagrange multiplier method uses a function  $\lambda$  (see also [11]) with its own degrees of freedom. Those may be duplicated from the degrees of freedom on the interface, as e.g. the control points of the master curve, however, also independent fields may be introduced.

The corresponding virtual work of the Lagrange multiplier method is given as:

$$\delta W^{C_0} = \int_{\Gamma^{(1)}} \partial \lambda^{(1)} (u^{(1)} - u^{(2)}) d\Gamma^{(1)} + \int_{\Gamma^{(1)}} \lambda^{(1)} (\delta u^{(1)} - \delta u^{(2)}) d\Gamma^{(1)} \quad (3.27)$$

with  $u^{(1)}$  being the coupled degrees of freedom with the additional field  $\lambda$  for the Lagrange multiplier. The discrete form of the Lagrange method in matrix vector notation is given by:

$$\begin{bmatrix} \mathbf{K}^{(1)} & \mathbf{0} & \mathbf{\Lambda}^T \\ \mathbf{0} & \mathbf{K}^{(2)} & \mathbf{0} \\ \mathbf{\Lambda} & \mathbf{0} & \mathbf{0} \end{bmatrix} \cdot \begin{bmatrix} \mathbf{u}^{(1)} \\ \mathbf{u}^{(2)} \\ \lambda \end{bmatrix} = - \begin{bmatrix} \mathbf{R}^{(1)} + \mathbf{\Lambda}^T \lambda \\ \mathbf{R}^{(2)} + \mathbf{\Lambda}^T \lambda \\ \mathbf{\Lambda} \mathbf{u} \end{bmatrix} \quad (3.28)$$

---


$${}^e \mathbf{H}^{(i)} = \begin{bmatrix} R_{cp}^{(i)} & 0 & 0 & \dots \\ 0 & R_{cp}^{(i)} & 0 & \dots \\ 0 & 0 & R_{cp}^{(i)} & \dots \end{bmatrix} \text{ with } i \text{ being the respective domain or field and } cp \text{ the index of the corresponding control point.}$$

with  $\mathbf{K}^{(i)}$  and  $\mathbf{R}^{(i)}$  being the stiffness and residua of the respective domains. The additional field  $\Lambda$  for the Lagrange multiplier is defined consequently as (considering e):

$$\Lambda = \int_{\Gamma^{(1)}} \mathbf{H}^{(1,\lambda)T} \mathbf{H}^{(1,2)} d\Gamma^{(1)} \quad (3.29)$$

For the suggested procedure only the corresponding nodes or control points of the master domain do have shape function values  $N_{\lambda,j}$  unequal to zero within  $\mathbf{H}^{(1,\lambda)T}$ .  $\mathbf{H}^{(1,2)}$  is first master, consequently slave control points.

The Lagrange multiplier approach is variationally consistent and fairly easy to implement within existing environments. However, the scheme is a saddle point formulation having zeros on the diagonal of the stiffness contribution, which may result in a unique solution only if the LBB (Ladyzhenskaya–Babuška–Brezzi) are satisfied, whereby otherwise the system may be singular. Accordingly, the selection of linear solver is crucial for the resolvability of the system evolving from the introduction of the Lagrange multipliers, which in any way can be described as computationally extensive.

**Remark 3.8.1: Coupling  $G_1$  continuity for IBRA**

Coupling the  $G_1$ -continuities is a special case, mainly important for surface or curve described formulations within IBRA if the curvature stiffness is relying on a high order background, as for the KL-shell and the hierarchic-shell family. In other scenarios, it often is sufficient to couple all involved degrees of freedom with a  $C_0$  continuity between the sub-domains. The virtual work for the enhanced coupling can be, independently on the chosen approach, described as following:

$$\delta W = \delta W^{C_0/disp} + \delta W^{G_1/rot} \quad (3.30)$$

Once it is provided that the vector  $\mathbf{a}_3$  is perpendicular to the surface, as it is the case for the KL-shell, the  $G_1$ -continuity enforcement can be applied through imposing the differentiation between the torsional vectors  $\omega_{T_2}^{(1)}$  and  $\omega_{T_2}^{(2)}$ :

**Penalty method:**

$$\delta W^{G_1/rot} = -\alpha_{rot} \int_{\Gamma^{(1)}} \left( \omega_{T_2}^{(1)} - \omega_{T_2}^{(2)} \right) \cdot \left( \delta \omega_{T_2}^{(1)} - \delta \omega_{T_2}^{(2)} \right) d\Gamma^{(1)} \quad (3.31)$$

**Lagrange multiplier:**

$$\delta W^{G_1/rot} = \int_{\Gamma^{(1)}} \partial \lambda^{(1)} \left( \omega_{T_2}^{(1)} - \omega_{T_2}^{(2)} \right) d\Gamma^{(1)} + \int_{\Gamma^{(1)}} \lambda^{(1)} \left( \delta \omega_{T_2}^{(1)} - \delta \omega_{T_2}^{(2)} \right) d\Gamma^{(1)} \quad (3.32)$$

A more generic coupling could be formulated by enforcing the difference between the respective  $\mathbf{a}_3$  vectors on either sides [25, 26, 167]. This could be specifically beneficial for other shell formulations like the hierarchic shell. In this manner, the involved shear and thickness contributions would be covered, too.

**Remark 3.8.2: Boundary conditions**

Dirichlet boundary conditions are special cases of the aforementioned coupling formulations, coupling the boundary with defined values. In the following equations Dirichlet conditions considering prescribed displacements  $d_0$  and rotations  $\beta_0$ , around  $T_2$  are shown:

**Penalty method:**

$$\delta W^{C_0} = -\alpha_{C_0} \int_{\Gamma^{(1)}} \partial \lambda^{(1)} (u^{(1)} - d_0) d\Gamma^{(1)} + \int_{\Gamma^{(1)}} \lambda^{(1)} (\delta u^{(1)} - d_0) d\Gamma^{(1)} \quad (3.33)$$

$$\delta W^{G_1/rot} = -\alpha_{rot} \int_{\Gamma^{(1)}} (\omega_{T_2}^{(1)} - \beta_0) (\delta \omega_{T_2}^{(1)} - \beta_0) d\Gamma^{(1)} \quad (3.34)$$

**Lagrange multiplier:**

$$\delta W^{C_0} = \int_{\Gamma^{(1)}} \delta \lambda^{(1)} (u^{(1)} - d_0) d\Gamma^{(1)} + \int_{\Gamma^{(1)}} \lambda^{(1)} (\delta u^{(1)} - d_0) d\Gamma^{(1)} \quad (3.35)$$

$$\delta W^{G_1/rot} = \int_{\Gamma^{(1)}} \partial \lambda^{(1)} (\omega_{T_2}^{(1)} - \beta_0) d\Gamma^{(1)} + \int_{\Gamma^{(1)}} \lambda^{(1)} (\delta \omega_{T_2}^{(1)} - \beta_0) d\Gamma^{(1)} \quad (3.36)$$

**Numerical comparison:**

Consequently, the example from figure 3.21 is considered, however, instead of embedding the different stiffness two sub-domains are taken which are weakly coupled with the penalty approach with varying stiffness and compared to the Lagrange multiplier formulations. The results are presented in figure 3.25a.

It shall be noted that for this example the ideal penalty factor is being around  $10^{11}$ , whereby, smaller values are steadily converging towards this solution with larger values making the solving unstable. The Lagrange multiplier method present itself with a solution accuracy around  $10^{-13}$ , which is close the apparent machine precision and independent on any penalty factor.

Consequently, the same example is repeated with a varying stiffness between the domains as  $\frac{E_1}{E_2}$  being either  $\frac{10^2}{10^2}$ ,  $\frac{10^2}{10^5}$  or  $\frac{10^2}{10^7}$ . The results of this study are shown within 3.25b, suggesting that the penalty approach becomes more stable and accurate once the stiffness difference between the patches is increasing, which is additionally aligned with a generally increased accuracy with a higher stiffness. Simultaneously, the Lagrange multiplier performs constantly well throughout all tests.

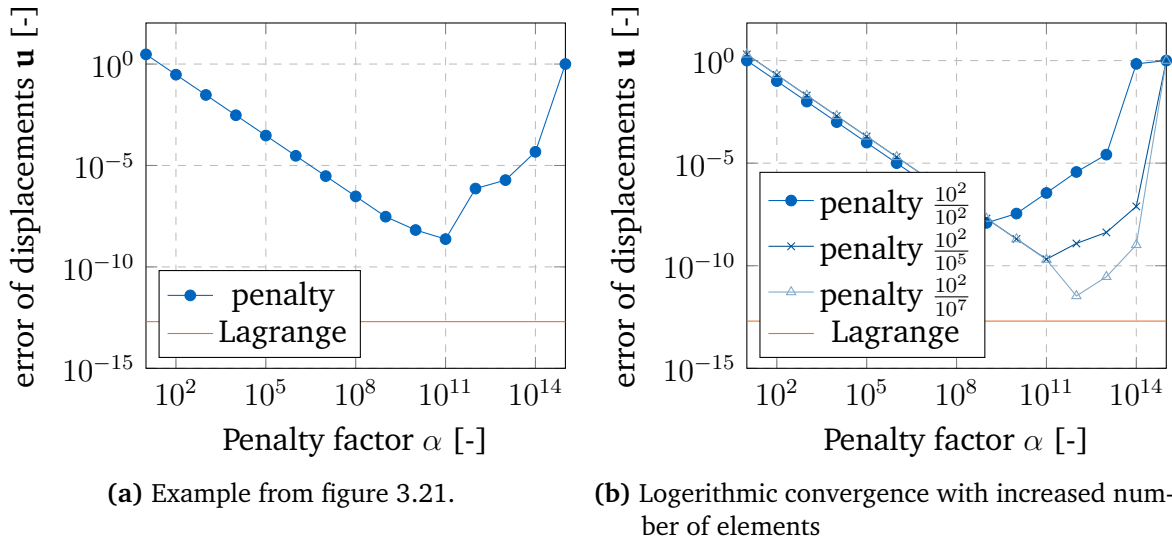


**Figure 3.25:** Comparison of convergence of penalty towards correct solution vs. Lagrange multiplier, with the error being defined by  $\frac{u_{exp.} - u}{u_{exp.}}$ .

### 3.8.2 Partitioned approaches <sup>b</sup>

In contrast to monolithic methodologies, partitioned approaches split the simulation problem into an amount of sub-problems which are solved independently. To achieve an equilibrium between the two domains, information is exchanged at a defined common interfaces, which involves either Dirichlet, or Neumann formulations. Another form can be a resolved interface which applies corrections on either side. Consequently, both avenues shall be presented and compared for different problems.

#### Gauss-Seidel (GS):

For many cases the exchange of information between domains means that deflections are mapped from one side to the other and applied as support boundary conditions. On the other domain, the corresponding reactions are evaluated at the external supports and applied as Neumann conditions on the first domain. Following loop describes the general procedure of the simplest partitioned coupling, frequently named weak coupling, as it does not resolve the equilibrium:

1. Solve origin domain
2. Map origin domain interface forces to destination
3. Solve destination domain

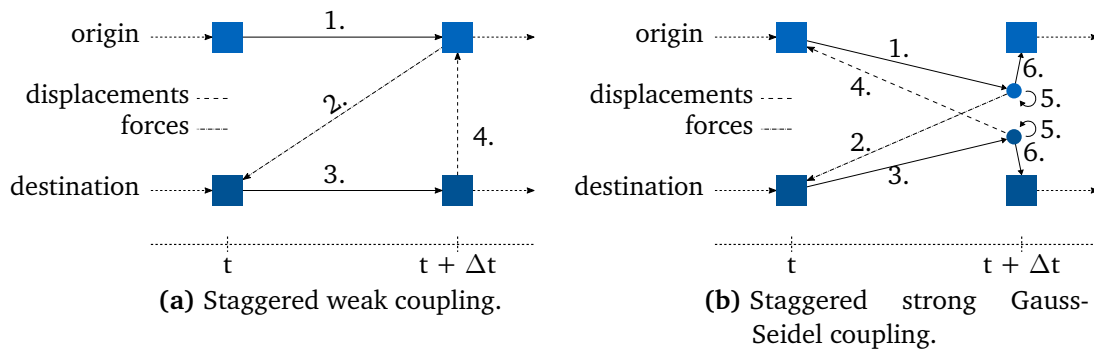


**Figure 3.26:** Staggered weak and strong Gauss-Seidel (GS) coupling ([246], adapted from [205]).

4. Map destination domain interface displacements (and derivatives) to origin

→ Advance in time

The weak coupling is a very efficient and comparatively easy to develop algorithm which provides accurate results in many scenarios. However, once the in-equilibrium, namely the forces between both domains becomes excessively large, a proper solve is unguaranteed and the problem-solution might diverge from the correct result. To circumvent this and to improve the accuracy an additional Gauss-Seidel loop, ensuring a resolved equilibrium between the two domains shall be introduced, typically allowing to resolve more complex problems.

The updated system loop is enhanced accordingly:

*Gauss-Seidel* loop:

1. Solve origin domain
2. Map origin domain interface forces to destination
3. Solve destination domain
4. Map destination domain interface displacements (and derivatives) to origin
5. Compute residual and repeat 1.-4. until convergence is reached

End *Gauss-Seidel* loop

→ Advance in time

The presented procedure is habitually called strong coupling and found popularity in various couplings as e.g. in fluid structure interaction [250], but also impact problems, as resolved by FEM-DEM coupling [205].

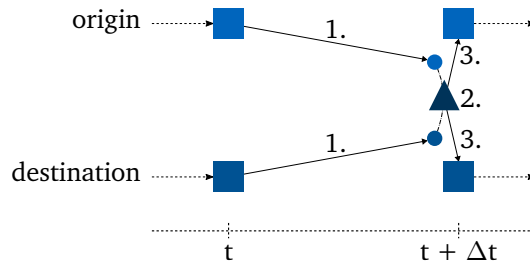


**Figure 3.27:** FETI-based coupling [246].

A study [246] showed that this coupling is powerful for domains with highly different stiffnesses, including small computation costs and good convergences. However, once the stiffnesses between the sub-domains approach themselves, the procedure has challenges in finding feasible solutions and accordingly diverges [246].

### Finite Element Tearing and Interconnecting (FETI) <sup>b</sup>:

The FETI as proposed by [83], connects non-overlapping domains with a dual Schur formulation [161] and enforces the interfacial equilibrium with Lagrange multipliers. Later, the formulation was enhanced to transient problems [82] and gained additional attention through allowing different timesteps within the sub-domains [57].

A comprehensive numerical study has been processed [246] to question the applicability ranges of either of the approaches, with the outcome that once the stiffness of both domains approaches themselves GS solutions become unstable, while FETI still operates robustly. However, FETI has disadvantages compared to GS, starting from computational costs as of the necessity to compute the interface formulation. For geometrically linear simulations this may be optimized towards a single solve, with a repetitive application of the inverted matrix. However, this heavily limits the applicability. Furthermore, compared to GS the implementation is largely involved, which makes it the less user-friendly approach.

## 4 Simulation of Masonry Structures c and e

Masonry and brick bonds have ever been a popular choice in the construction of various civil structures including buildings, bridges, monuments, and heritage sites of cultural significance. Some types of masonry are employed for their architectural and design properties [144], while other types are chosen due to their mechanical properties, including strengths and resistances and their relatively low cost and the possibility of constructing complex shapes without heavy machinery [121]. Compared to the empirical methods used in the design of many historical structures [92], modern engineering techniques and tools offer unprecedented insights into structural performance and safety assessment. Despite the advanced progress of engineering analysis, understanding and predicting the behaviour of masonry structures remains particularly challenging due to distinct involved constituents and their complex interactions resulting in multiple failure modes.

Existing approaches in the assessment of masonry can be categorised into three main scales, fully detailed micro models (figure 4.1a), simplified micro models/meta models (figure 4.1b), and macro models (figure 4.1c) [92, 139, 212].

Fully detailed micro-models explicitly consider each component, i.e. bricks, mortar and the interfaces between mortar and bricks. Such modelling can appropriately analyse complex geometries and heterogeneous materials and is capable of capturing localized phenomena such as crack propagation through different constituents and/or interfaces [138, 139, 142, 74]. However, due to its numerical complexity micro-scale models are typically used in modeling of detailed small-scale structures, and can be too computationally costly for analysing full-scaled structures [181].

Meta or mesoscale models simplify some properties of the micro-scale to allow a computationally more efficient simulation. Typically, the brick-mortar interface and the mortar layer is condensed into a single interface condition, resulting in a simplified masonry structure composed of two constituents (illustrative examples are presented in references [115, 212, 188, 55]). It is not aimed to capture explicit propagation of cracks at the bi-material interface or within the mortar layer, however capturing cracks within bricks and the interfaces is possible (e.g. [255] presents a mesoscale simulation of masonry arches).

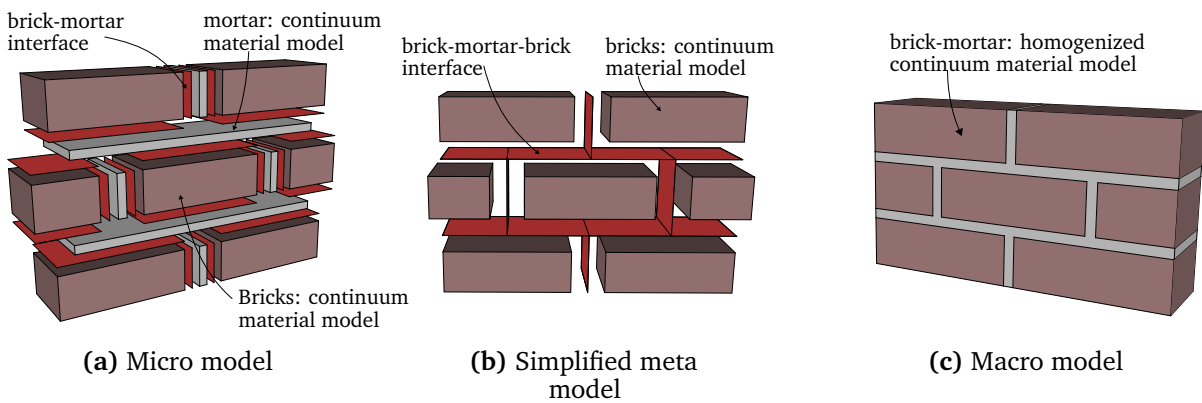


**Figure 4.1:** Scales of masonry simulations.

Macro models, often used for simulating the behaviour of large-scale structures, frequently rely on Reference Volume Elements (RVE) within the modelling and analyses. The kinematical behaviour of these are captured by approximating the combined behaviour of bricks, mortar and their interface [260, 261, 181]. Typically, the micro scale of certain RVEs are expressed by solid, shell, beam and spring elements within masonry modelling. While macro models do not capture details such as localized cracking or strain jumps the overall structural response can be captured accurately [179]. Even though solid and shell elements can represent the true geometry of masonry structures, dimensionally reduced 1D and spring elements are extensively used for seismic and blast simulations due to reduced computational costs [211]. Regardless of the element selection, critical to accurate simulation of the structure is the ability of micro scale to capture the kinematics of all constituents and their interactions ([181] describes it as major difficulty to adequately capture boundary conditions).

The material behaviour of the RVEs, which results into the constitutive law of the finite element can be derived either experimentally or can be obtained from separate micro-scale models. Micro-scale models are used frequently in multi-scale modelling approaches to simulate the behaviour of specific masonry patterns, which are used to express the behaviour of the full scale structure [181, 182]. Although this approach effectively links the macro and micro scale behaviours, it is computationally costly and prone to errors due to certain simplification assumptions made in the micro-scale model (e.g. idealized geometry, homogeneity, perfect interface, definition of boundary and interface conditions, etc.). Alternatively, experimental methods to determine the constitutive behaviour might be capable to relax some of the assumptions within micro-scale models and thusly can be more accurate. However, in order to achieve high accuracy, the design of the experiments must consider appropriate boundary conditions to ensure a scaleable and reasonably well represented behaviour of the masonry pattern.

## 4.1 Macro parameter definition and numerical driven design of the test specimens

---

Experimental studies on masonry structures vary significantly in the scope of setups and the applied specimen dimensions. Material properties are obtained from specimen sizes ranging from quartered bricks and mortar, via macro seized specimen to full scale wall sections and complete structures and buildings [174, 139, 61, 140, 148]. Nevertheless, many studies provide few justification in terms of specimen size choices and the influence of the apparent boundary conditions. A systematic approach of the specimen size selection from a chosen RVE and the design of test methods including the test setup boundary conditions to accurately capture the behaviour of the masonry pattern is inevitable.

Consequently, an experimentally driven study aiming a macro characterization of the mechanical properties of a structured masonry bond suitable for macro-scale numerical analyses is presented. The experiments themselves were initially simulated across different configurations, sizes and loading scenarios to determine the minimal specimen size invariant to boundary and experimental size effects that scales consistently (see section 4.1). From the gained experience of the simulations, a numerically-informed experimental program was executed across compression, tension, shear, triplet shear, and out-of-plane bending conditions to quantify orthotropic material parameters of the given masonry pattern suitable for macro scale simulation (see section 4.2). The gained knowledge of the experimental data is considered to formulate a constitutive damage model, which shall be capable of expressing the major kinematic effects of the anisotropic material (see section 4.3). Finally are compared some numerical discretization techniques for masonry and it is shown how the constitutive model can be embedded into various finite element discretizations.

The novelty of this chapter can be defined through the constitutive relation-driven test program, resulting in a specifically comprehensive amount of parameters. Furthermore, existing constitutive laws are enhanced for a qualitatively adequate and computationally efficient macro scale simulation. This presented scheme addresses a prediction of masonry structures from experimentally evaluated small scale tests instead of parameter calibrations from large scale tests to fit the test results.

## 4.1 Macro parameter definition and numerical driven design of the test specimens <sup>c</sup>

Considering a structured masonry bond, an isotropic constitutive behavior would not be valid, as the material possess direction dependent properties. With a limited increase of complexity within the allowance of small inaccuracies, the approximation with an orthotropic constitutive material provides more appropriate results [179]. The aim of this research is finding appropriate orthotropic material parameters suitable for macro

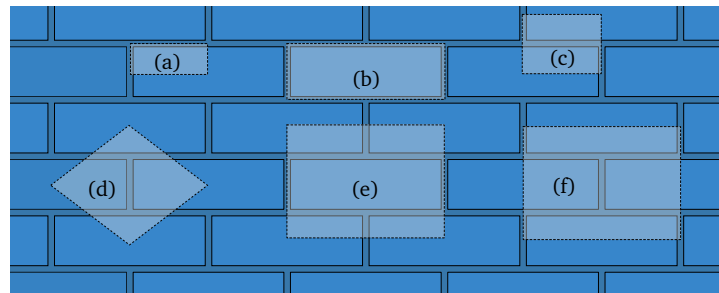


**Figure 4.2:** Selection of eligible masonry RVEs for the studied masonry pattern.

scale shell based numerical analyses. Accordingly, a reference volume element (RVE) suiting constitutive prerequisites needs to be justified.

#### 4.1.1 Masonry reference volume element (RVE)

A masonry RVE represents an irreducible volume element, which, when repeated, properly fulfills the kinematics of any shape of the structure. Therefore, the selection of RVE is essential to ensure the behaviours of all constituents and their interactions in a scaleable manner. This study concerns itself with structured masonry composed of bricks and mortar as depicted in figure 4.1c, with brick details presented in figure 4.3b and a uniform mortar width of 10mm throughout. The applied masonry pattern allows a selection of different RVEs, some of which are displayed in figure 4.2. Where all RVEs comply with the previous conditions, (a; eg. [260]), (b; eg. [10, 74, 164]), (c; eg. [260]), and (d; eg. [221]) cannot be repeated in a homogeneous structured manner. Either mirroring or offsetting is required to properly scale to structural level. (e; eg. [5, 182, 74, 9]) and (f; eg. [48], specifically for quasi-periodic bonds), both fulfill the scaleability, however, as (e) contains a full brick, rather than only cut pieces, it is favoured within this research. This RVE including all dimensions is illustrated in figure 4.3d.

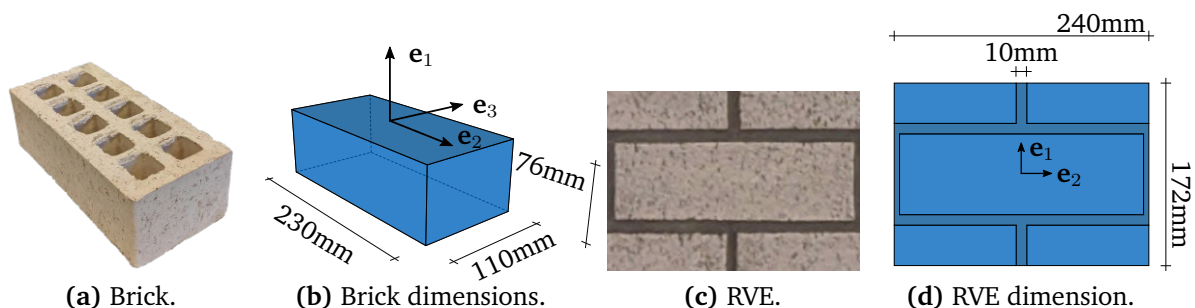


**Figure 4.3:** Brick and RVE dimensions.

## 4.1 Macro parameter definition and numerical driven design of the test specimens

Throughout the following numerical analyses, the brick and mortar components of the RVE were modelled as distinct continua with linear elastic isotropic material properties. Experimentally derived material parameters of bricks and mortar are discussed within [228] and summarized as following:

Young's modulus $E$ in [MPa]	
Brick direction $\mathbf{e}_1$ :	18000
Brick direction $\mathbf{e}_2$ :	1500
Mortar:	2000

### 4.1.2 Determination of experiment specimen size

The appropriate minimum experiment specimen size (invariant to boundary and size effects) is expressed as a multiple of RVEs, and occurs when numerically-derived bulk elastic moduli no longer vary with additional RVEs.

#### 2D orthotropic material moduli:

The aforementioned numerical RVE is considered to follow 2D plane stress orthotropic material behaviour, which is determined by:

$$\boldsymbol{\sigma} = \mathbf{C} \cdot \boldsymbol{\epsilon} \begin{pmatrix} \sigma_1 \\ \sigma_2 \\ \tau_{12} \end{pmatrix} = \begin{pmatrix} \frac{E_1}{1 - \nu_{12}\nu_{21}} & \frac{\nu_{12}E_2}{1 - \nu_{12}\nu_{21}} & 0 \\ \frac{\nu_{21}E_1}{1 - \nu_{12}\nu_{21}} & \frac{E_2}{1 - \nu_{12}\nu_{21}} & 0 \\ 0 & 0 & G \end{pmatrix} \cdot \begin{pmatrix} \epsilon_1 \\ \epsilon_2 \\ \gamma_{12} \end{pmatrix} \quad (4.1)$$

where:

$E_1, E_2$  Young's moduli in direction  $\mathbf{e}_1$  and  $\mathbf{e}_2$

$\nu_{12}, \nu_{21}$  Poisson's ratios

$G$  Symmetric in-plane shear modulus

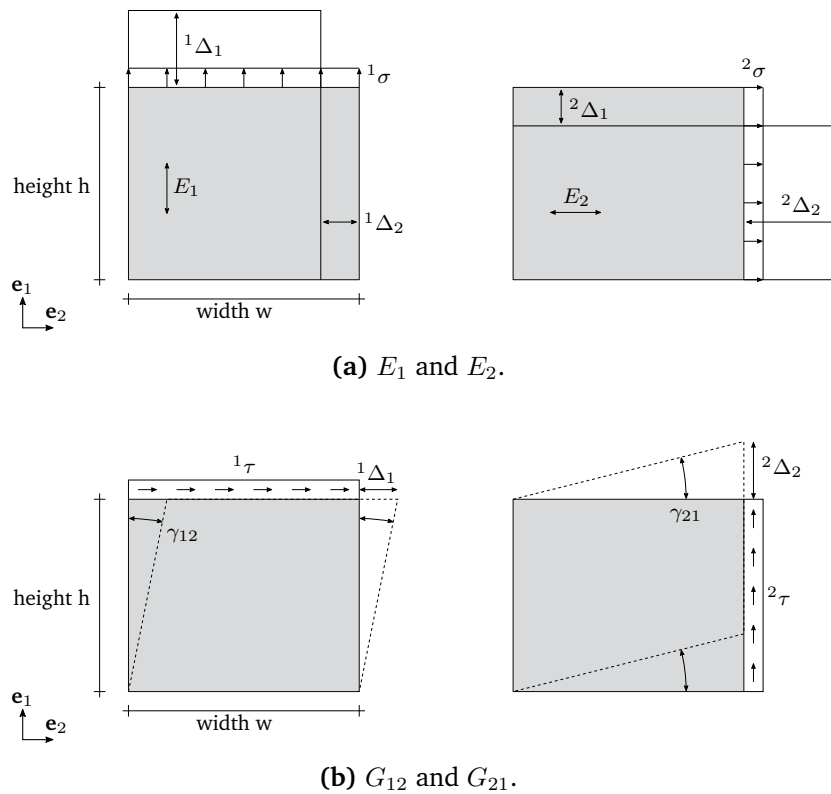


**Figure 4.4:** Parameter definition per direction. Graphics are containing the opposite sign as the description.

**Simulation setup:**

According to figure 4.4a and figure 4.4b the orthotropic normal and shear moduli may be numerically computed by analysing the specimen edge deformations under specific load conditions.

With the objective of determining the minimum acceptable experiment specimen size, 2D numerical simulations were conducted on systems composed of  $1 \times 1$ ,  $3 \times 3$  and  $4 \times 4$  RVEs. Displacement control of applied edge displacements (nominally  ${}^i\Delta_i = 0.01\text{m}$  for normal moduli and  ${}^i\Delta_j = 0.01\text{m}$  for shear moduli) was adopted to ensure numerical stability and avoid varying edge displacements. Restraints were considered under two configurations as illustrated in figure 4.5: free and fixed. For the example of vertical compression, free restraints allow lateral movement induced by the Poisson effect, while fixed restraints prevented such movement (which is expected to dominate during physical experiments).

#### 4.1 Macro parameter definition and numerical driven design of the test specimens

Accordingly, the corresponding edge reaction force  $F_{Reaction}$  was evaluated which allows subsequent estimation of averaged stress components. Under this approach, the Young's modulus in test direction  $\mathbf{e}_1$  is determined by:

$${}^1\epsilon_1 = \frac{{}^1\Delta_1}{h}, \quad {}^1\sigma = \frac{F_{Reaction}}{w \cdot t}, \quad E_1 = \frac{{}^1\sigma}{{}^1\epsilon_1}, \quad (4.2)$$

while the Young's modulus in direction  $\mathbf{e}_2$  is calculated via:

$${}^2\epsilon_2 = \frac{{}^2\Delta_2}{w}, \quad {}^2\sigma = \frac{F_{Reaction}}{h \cdot t}, \quad E_2 = \frac{{}^2\sigma}{{}^2\epsilon_2}, \quad (4.3)$$

where  $t = 110\text{mm}$  is the plane stress brick thickness.

The orthotropic symmetric in-plane shear modulus  $G$  (as per equation 4.1), for the theory of plane stress implies that  $G_{12}$  is identical to  $G_{21}$ , which is generally not the case for masonry structures. Nonetheless, for the purposes of this numerical specimen convergence study where the variance (instead of absolute values) of moduli over RVE multiples is important, the symmetric shear modulus is considered as the mean of the anisotropic in-plane shear moduli:

$$G = \frac{1}{2}(G_{12} + G_{21}) \quad (4.4)$$

The shear modulus  $G_{12}$  is computed with only  ${}^1\Delta_1 \neq 0$ :

$${}^1\gamma_{12} = \frac{{}^1\Delta_1}{h}, \quad {}^1\tau_{12} = \frac{F_{Reaction}}{w \cdot t}, \quad G_{12} = \frac{{}^1\tau_{12}}{{}^1\gamma_{12}}, \quad (4.5)$$

and  $G_{21}$  being calculated with only  ${}^2\Delta_2 \neq 0$ :

$${}^2\gamma_{21} = \frac{{}^2\Delta_2}{w}, \quad {}^2\tau_{21} = \frac{F_{Reaction}}{h \cdot t}, \quad G_{21} = \frac{{}^2\tau_{21}}{{}^2\gamma_{21}}. \quad (4.6)$$

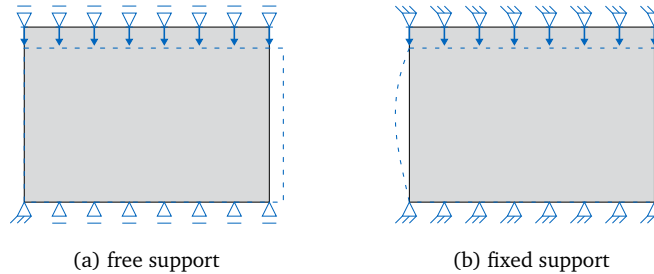


**Figure 4.5:** Free of fixed support in transversal direction.

**Simulation results:**

The numerically predicted moduli vs number of RVEs ( $1 \times 1$ ,  $3 \times 3$  and  $4 \times 4$ ) are illustrated in figure 4.6 and confirm that the normal Young's moduli  $E_1$  and  $E_2$  do not depend significantly on the number of RVEs. However, it showed that the effect of the chosen boundary condition, being free or fixed (Figure 4.5), significantly involves in the results. Furthermore, it shall be noted that the fixed or free boundary condition largely influences  $E_1$  but has a negligible impact on  $E_2$ , which is corresponding to the factors obtained by the relations  $E_1/E_2$  or  $E_2/E_1$ . Following, it becomes necessary to introduce a transversely relatively softer layer between the loading plates and the specimens to reduce the severe effects of the boundary conditions.

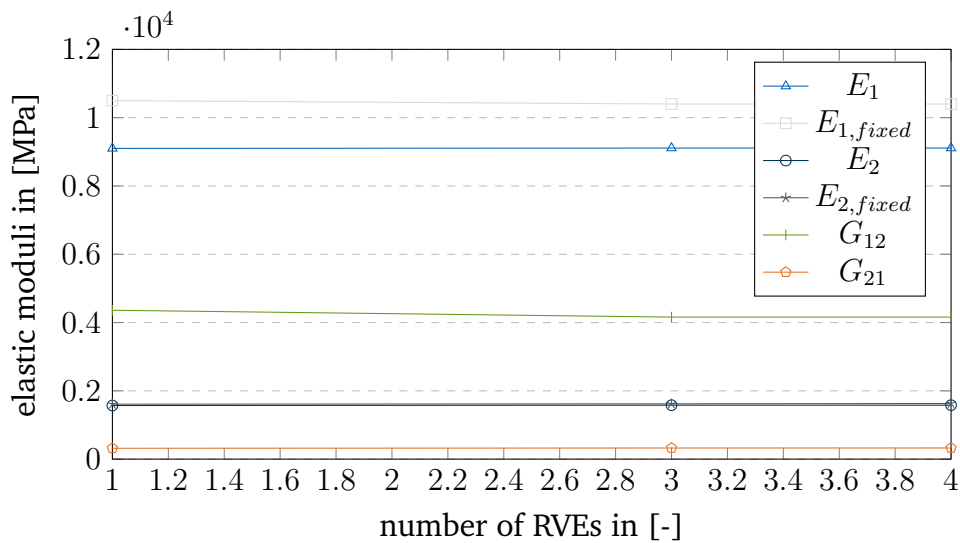


**Figure 4.6:** Results of numerical computation of  $E_1$ ,  $E_2$ ,  $G_{12}$  and  $G_{21}$ .

**Validity of numerical determined specimen size:**

The numerical studies confirm that the choice of specimen size does have little impact on derived bulk material properties. Normal and shear moduli were largely insensitive to varying specimen extents. The specimen size is chosen to be  $3 \times 3$  RVEs to comply with most requirements from international codes, as discussed subsequently. Note that subscript indices follow the direction index of the coordinate system (see figure 4.3b and figure 4.7).

The EN 1052-1 [79] and RILEM TC24-BW [195] standards suggest that the masonry specimen size for bricks with a length of  $l_{brick,2} \leq 300\text{mm}$  and a height of  $l_{brick,1} \leq 150\text{mm}$  shall have an overall length of  $l_{specimen,2} \geq 2 \cdot l_{brick,2} = 460\text{mm}$  and a height of  $l_{specimen,1} \geq 5 \cdot l_1 = 380\text{mm}$ . Furthermore it restricts the height by  $l_{specimen,1} \geq$

#### 4.1 Macro parameter definition and numerical driven design of the test specimens

---

$3 \cdot l_3 = 300\text{mm}$  and  $l_{specimen,1} \leq 15 \cdot l_{brick,3} = 1650\text{mm}$ . It is noted that these guidelines are fulfilled with the 3x3 RVE model with the exception of the  $l_{specimen,1} \geq l_{specimen,2}$  recommendation which would require a quadratic test setup due to the 2 test directions considered.

ASTM C1717-19 [17] suggests the specimen size as follows: "*Length or Height* — The specimen shall be long enough (for horizontal testing) or tall enough (for vertical testing) so that its behavior under load will simulate that of the element that the specimen is intended to represent." (Chapter 5.2). The previous studies intend to question if other phenomena are apparent within the experimental test setup. Thus, those shall be taken into account to prove if the specimens dimensions are long or tall enough.

The ASTM C1314-21 [16], AS 3700-18 [13] and CSA S304-14 (R2019) [66] define the compressive strength of masonry on masonry prisms instead of wallettes. The ASTM C1314-21 recommends a height-to-thickness ratio of  $1.3 \leq h_p/t_p \leq 5.0$  ( $h_p$  being the height of the specimen and  $t_p$  the thickness of the employed brick which is equal to the thickness of the specimen). This is fulfilled for  $\mathbf{e}_1$  direction tests with  $h_p/t_p = 4.72 \leq 5.0$ , however,  $\mathbf{e}_2$  direction tests lay outside this range  $h_p/t_p = 6.54 > 5.0$ . It is noted this is in contrast to EN 1052-1[79] where the  $\mathbf{e}_2$  direction complies with height recommendations. Literature suggests that masonry wallettes may exhibit lower compressive strength than masonry prisms with similar heights [230]. A study by [1] confirms with numerical simulations that the  $l_{specimen,1}/l_3$  ratio has an impact on the compressive strength of the specimen. This matches the message that wallettes made of the same materials have different strengths than prisms. The impact of this link shall be suggested to be studied within future research.

Within FEM-simulations noticeable differences between 2D plane stress and 3D analysis may be apparent (refer to reference [10] for the study of various masonry RVEs and [20] for the study of the compressive strength of masonry prisms) due to Poisson's effects and triaxial stiffness effects, amongst others. However, the study presented here focuses mainly on scalability, rather than exact estimations, which renders the plane stress assumption pragmatically appropriate.

It shall be noted that the numerically justified specimen size is mainly valid and accurate for linear elastic properties. Furthermore, it questions certain boundary conditions, even though, those would require a more detailed assessment. In the proceeding, properties are measured at internal points, whereby it showed that throughout the measurement points, localized effects have more severe impacts rather than boundary conditions. Additionally, the damage relaxation is not justified thoroughly, whereby, the given specimen size would directly affect possible failure modes, which respectively have different limit stresses.

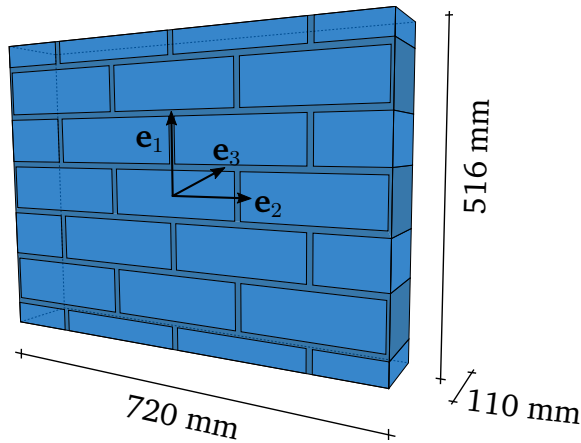


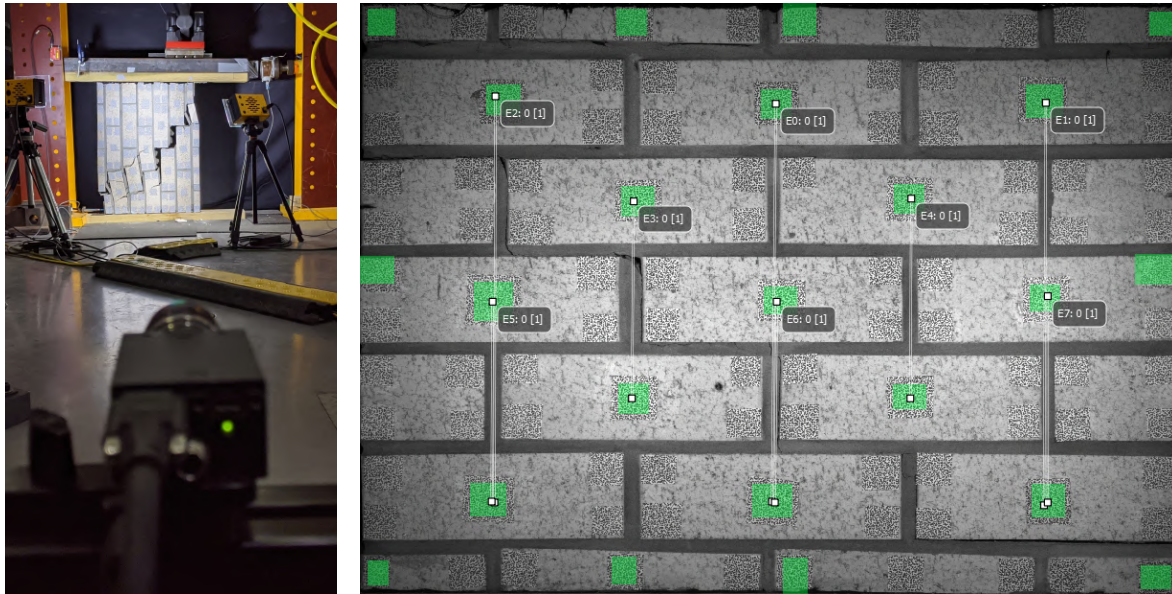
**Figure 4.7:** Numerically-justified experimental specimen.

## 4.2 Experimental macro characterization of masonry structures <sup>c</sup>

A comprehensive experimental program was conducted with the objective of establishing a consistent macro-characterisation of masonry material behaviour suitable for future macro-scale simulations. Employing the boundary and size invariant specimen proportions of 3x3 RVEs illustrated in figure 4.7 (and numerically justified in section 4.1), the following tests, each characterising certain material parameters, were performed:

- Compression:  $E_1$ ,  $E_2$ ,  $f_{c1}$  and  $f_{c2}$  (section 4.2.3)
- Tension:  $f_{t1}$  and  $f_{t2}$  (section 4.2.4)
- Shear (section 4.2.5)
  - Triplet shear:  $f_{vo}$  (section 4.2.5)
  - Macro shear:  $G_{12}$ ,  $G_{21}$ ,  $f_{s12}$  and  $f_{s21}$  (section 4.2.5)
- Bending:  $M_{max1}$ ,  $M_{max2}$  (section 4.2.6)

It shall be noted that the large bandwidth of tested parameters across a consistent and numerically-justified specimen size is particularly unique. The experimental brick and mortar dimensions are identical to those simulated (illustrated in Figures 4.3b and 4.3d) except that the experimental bricks contain 2x5 holes filled partly with mortar during construction. As considerable disparities between the simulated and experimental results are expected, the primary role of the numerical study was to establish the minimum viable experimental specimen size, not to predict the experimental results themselves. Furthermore, since the models shown are still too preliminary, future developments will need to provide more detailed information about the necessary



(a) DIC setup for the macro shear tests from section 4.2.5.

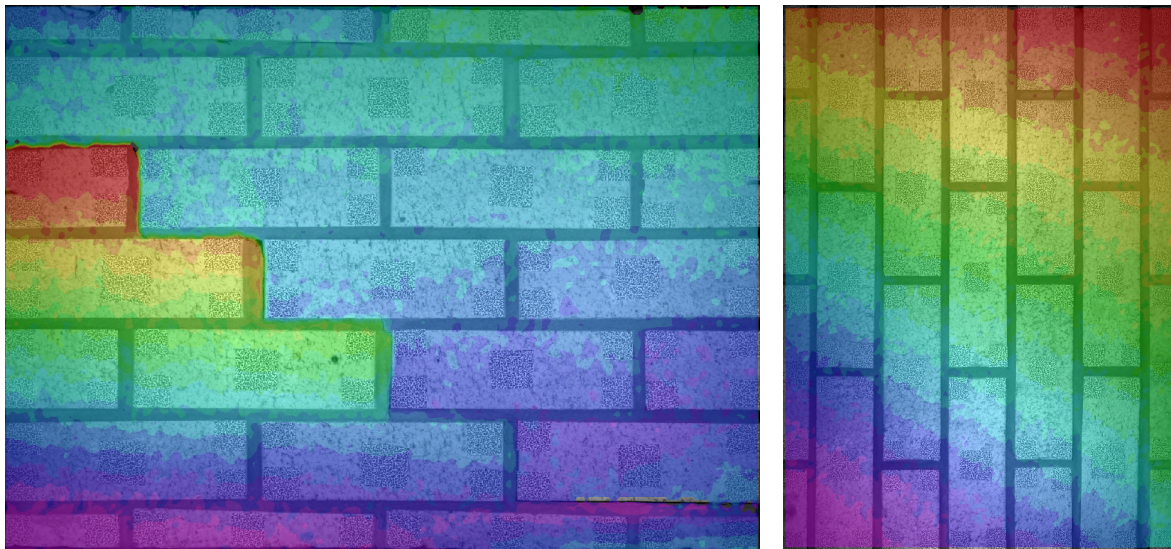
(b) DIC measurement points and extensometers.

**Figure 4.8:** DIC setup and measurement points.

specimen size. In total 32 specimens were tested: 6 compression tests per direction (4 undamaged and 2 pre-damaged from tension tests), 2 tensile tests per direction, 4 shear tests per direction and 4 bending tests per direction.

### 4.2.1 Instrumentation - Digital Image Correlation (DIC)

Concentrated or distributed forces were applied by hydraulic actuators. The specific load was controlled by additional load cells for the macro shear tests while compression and tension tests were displacement-controlled. A DIC measurement system (see [218], for masonry tests [189, 200]) illustrated in figure 4.8a was employed to noninvasively measure displacements and strains from speckle patterns glued on the specimens. Since the objective of the experiments was the macro-characterisation of masonry properties, localized strains (see figure 4.9a for localized phenomena within the masonry specimen) within single speckle patterns were neglected, with the focus instead on relative measurements spanning across multiple bricks. An example set of relative measure points are illustrated in figure 4.8b. This spanning relative measurement also confers the additional advantage of removing rigid body motion (as e.g. figure 4.9b) of the systems to ensure true displacement (and therefore correct strains) results.



(a) Local movement of selected bricks.

(b) Rotated movement of specimen.

**Figure 4.9:** Selected DIC-clusters with qualitative results to show masonry specific phenomena.

### 4.2.2 Fabrication of test specimen

To ensure quantitatively correct properties, bricks were halved or quartered if needed to fulfill the required test specimen setup. The applied bricks are  $5 \times 2$  holed Commons clay [18], whereby its mechanical properties are studied within [228]. Premixed Mortex [157] was used to ensure continuity within all constructed brick walls, whereby its properties has been tested and is similarly reported in [228]. All samples were produced on timber studs, however not bonded to the studs. Accordingly, both direction walls were produced in horizontal brick laying and rotated, if needed, after curing. The timber studs were used to safely transport the samples to the respective test setup location without damaging. However, it showed that the specimen had enough stiffness to be transported without any casting. Figure 4.10b shows some of the samples, in both directions after finished curing.

Specimen which required adhesive bonding to the timber studs (tension and shear samples) were glued after complete curing of the mortar. [6] was used as it showed good bonding to both the brick surface and the timber and had enough stiffness to not influence the test results. As the chosen epoxy had a low viscosity it needed to be applied multiple times to avoid imperfections and thusly a non-continuous force transmission of forces. Additionally, at least 7 days were waited after application of the epoxy and testing to ensure maximal stiffness.



(a) Construction of specimen.

(b) Finished specimen in correct position.

**Figure 4.10:** Masonry test specimen.

### 4.2.3 Compression tests

Compression tests were conducted using an actuator setup with a bottom and top steel plate shown in Figure 4.11b. The masonry samples were placed between timber studs to apply an evenly-distributed force into the system regardless of specimen edge imperfections. Additionally, this reduces the transverse clamping, which effect is discussed in section 4.1. The relative DIC measurements spanning across bricks render all measurements truly, and the effects of timber are not taken into account.

#### Compression test results in $e_1$ :

Compression in direction  $e_1$  stress-strain curves are illustrated in Figure 4.12a with undamaged specimen results below ( $F_{c1}$  and  $f_{c1}$  denote ultimate compressive force and stress respectively):

	$F_{c1}$ in [kN]	$f_{c1}$ in [MPa]
specimen 1	588.1	7.61
specimen 2	604.0	7.83
specimen 3	542.3	7.01
specimen 4	546.3	7.05
mean	570.0	7.38

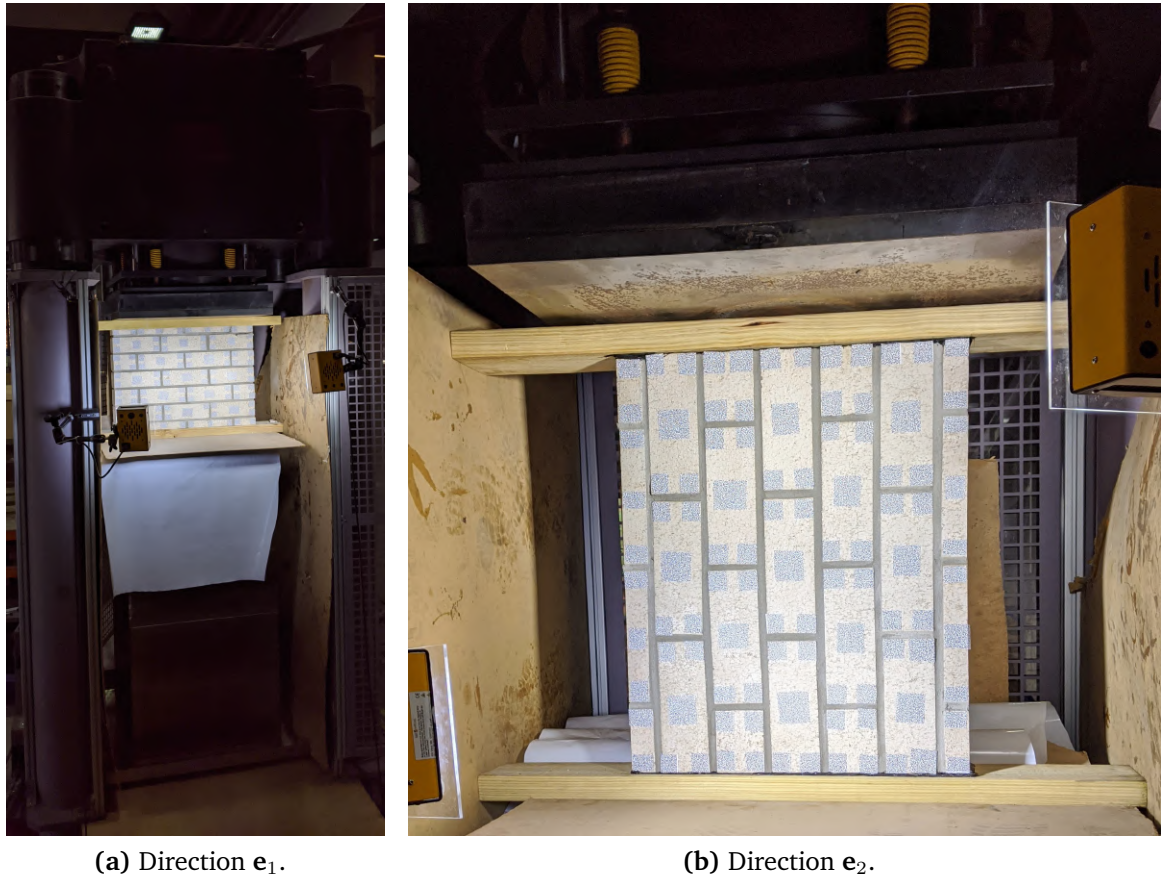
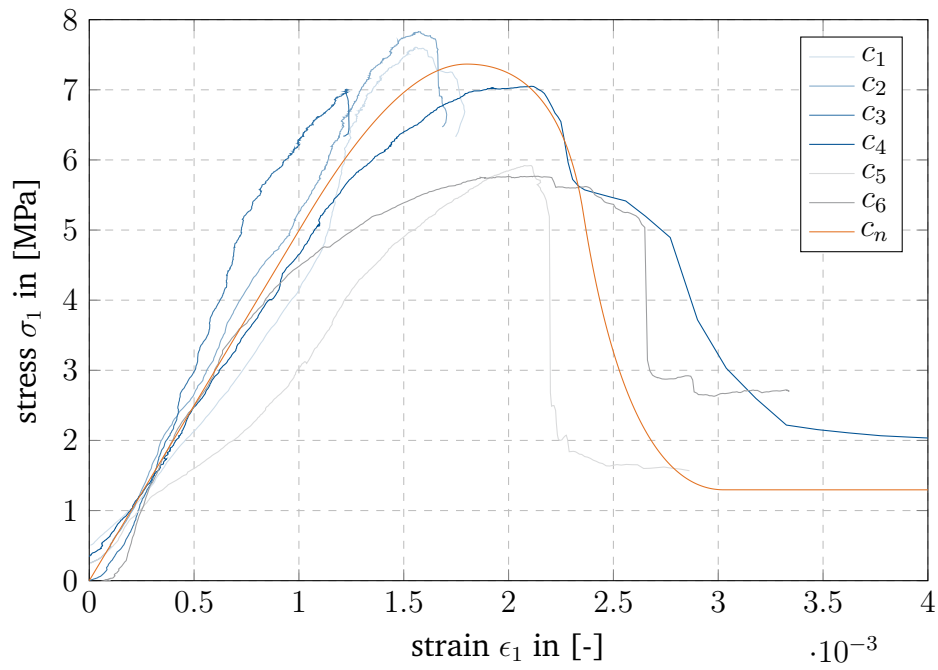


**Figure 4.11:** Compression test setup.

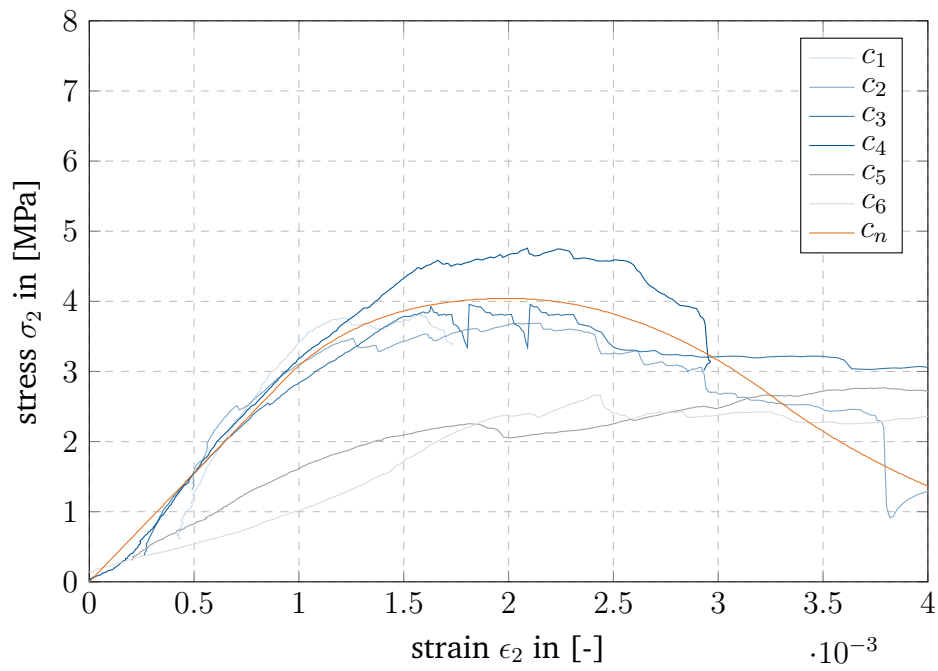
The elastic Young's modulus  $E_1$  of the tests is in a range between  $4.4 \times 10^3$  and  $7.5e3 \times 10^3$ MPa, with an approximate averaged value of  $5e3 \times 10^3$ MPa (being a graphically averaged secant modulus). Furthermore, the initial elastic limit strength was estimated with 5.2MPa and the residual strength showed being around 1.3MPa. The fracture energy was estimated with  $G_c = 1.2 \times 10^4 \frac{N}{mm}$ . With those material parameters, the orange softening relation (see figure 4.12a) was estimated with the constitutive law from section 4.3.

In the following, the specimen with a pre-damage from the tensile tests (see section 4.2.4) were tested to measure the impact of the pre-damage in the samples:

	$F_{c1}$ in [kN]	$f_{c1}$ in [MPa]
pre-damaged 1	455.9	5.92
pre-damaged 2	447.5	5.76
mean	451.7	5.84



(a) Direction  $e_1$



(b) Direction  $e_2$

**Figure 4.12:** Stress strain relation of compression tests. Undamaged tests are displayed in blue, pre-damaged tests are displayed in grey. The orange graphs show the corresponding numerical model (see section 4.3).

The specimen had no visible damages, however, it was noticeable that one or two layers were not detached anymore. It can be observed that the Young's modulus keeps being roughly the same. However, the failure load  $f_t$  is reduced by around 20%.

### Compression test results in $e_2$ :

Compression in  $e_2$  stress-strain curves are illustrated in figure 4.12b with the key failure results tabulated below:

	$F_{c1}$ in [kN]	$f_{c1}$ in [MPa]
specimen 1	203.8	3.67
specimen 2	219.5	3.95
specimen 3	212.2	3.82
specimen 4	259.1	4.76
mean	223.7	4.05

The elastic Young's modulus  $E_2$  of the tests ranged between  $2.3 \times 10^3$  and  $3.6 \times 10^3$ MPa, with a graphically-weighted average taken to be  $3.1 \times 10^3$ MPa. The initial elastic limit strength was estimated with 2.9MPa and the residual strength showed being negligible, with a respective fracture energy of  $G_c = 1.1 \times 10^4 \frac{N}{mm}$ . With those material parameters, the orange softening relation (see figure 4.12b) was estimated with the constitutive law from section 4.3 (remaining parameters have been obtained by calibration).

Compression tests introduced additional complexity due to out-of-plane deformations of the damaging parts (see figure 4.14). Post-failure out-of-plane deflections were often substantial, as illustrated in figure 4.13b, occasionally leading to DIC results being cut off. Those effects do not influence the center line of the material and are therefore not required to be included in the numerical model at the chosen level of detail.

In the following, the specimen with a pre-damage from the tensile tests (see section 4.2.4) were tested to measure the impact of the pre-damage in the samples:

	$F_{c2}$ in [kN]	$f_{c2}$ in [MPa]
pre-damaged 1	149.9	2.67
pre-damaged 2	157.7	2.77
mean	153.8	2.72

In comparison to direction  $e_1$ , the reduction of strengthness in direction  $e_2$  is bigger with around 32%. Additionally, the Young's modulus of the samples was significantly impacted and reduced by the damages (see figure 4.13b). Furthermore, it can be noticed



(a) Direction  $e_1$ .

(b) Direction  $e_2$ .

**Figure 4.13:** Compression failure of masonry samples in direction  $e_1$  and  $e_2$ .

that the fracture zones of the pre-damaged samples is similar or even higher than the undamaged specimen.

It shall be noted that  $E_1 > E_2$  is a typical phenomena for hollow bricks, with the brick under consideration exhibiting a ratio of  $\frac{E_1}{E_2} = 1.6$ . Other researchers studying different bricks have noted ratios of  $\frac{E_1}{E_2} = \frac{12000}{8000} = 1.5$  [160] and  $\frac{E_1}{E_2} = \frac{7520}{3960} = 1.9$  [241, 139].

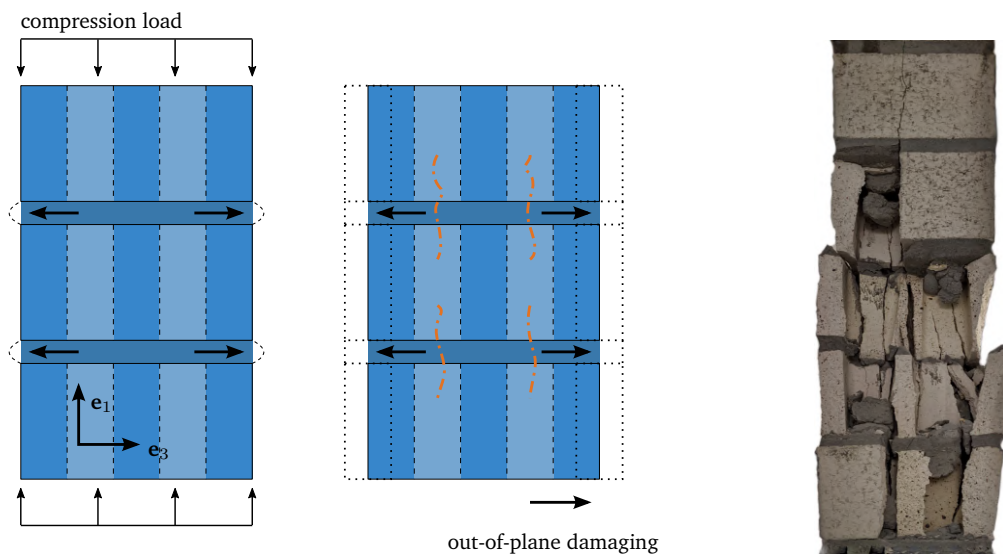


**Figure 4.14:** Failure mode in out-of-plane of the masonry samples in compression.

### Compression damage:

The masonry damage sustained during compressive testing illustrated in Figures 4.13a and 4.13b may be described as dispersed crushing and/or fracturing instead of localized discrete cracking. During the damage evolution, the mortar initially appeared to damage and plastically deform followed by occasional fracturing of the front/rear brick layers, which drastically reduced the ultimate specimen strength.

The mortar, which more compliant than the bricks, tends to displace outwards and, due to the strong mortar-brick bond, breaks the bricks in the region around the holes (see figure 4.14). This is a known damage phenomena, classified within ASTM C1314-21 in Fig.4(7)B as Face Shell Separation and considered in reference [155].

### 4.2.4 Tension tests

Tension tests were conducted according to the setup illustrated in Figure 4.15. Timber sleepers were bonded to the specimen edges to mitigate edge imperfections and apply the tensile loads in the system, while the sleepers themselves were fixed to rigid parallel flange channels (PFCs) to ensure even constant load application and restraint. The top PFC was attached to a hydraulic actuator, with a vertically welded steel plate from



**Figure 4.15:** Tensile test setup with horizontal brick specimen.



(a) Direction  $e_1$ .



(b) Direction  $e_2$ .

**Figure 4.16:** Tensile failure of masonry samples in direction  $e_1$  and  $e_2$ .

which the tensile load was applied and the bottom PFC securely restrained to the bottom of the actuator setup.

**Tension test results:**

Stress-strain tension results across both  $\mathbf{e}_1$  and  $\mathbf{e}_2$  directions are illustrated in Figure 4.17.

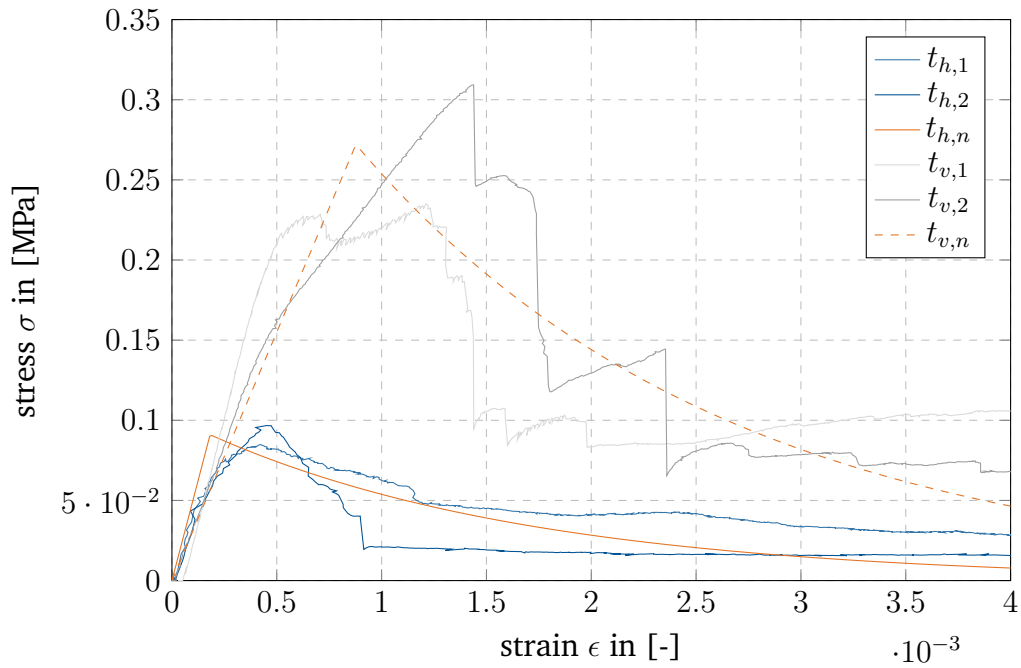


**Figure 4.17:** Stress strain relation of tensile tests. The horizontal tests are displayed in blue, the vertical tests in gray. The corresponding numerical graphs (see section 4.3) are expressed in orange.

The ultimate loads of the tension results are significantly lower than the compression tests and it is expected that boundary effects and the self weight of the specimen would influence the parameters significantly. Accordingly, the elastic Young’s moduli in each direction  $E_1$  and  $E_2$  are taken from the compression tests since the elastic zone itself is larger and facilitates a wider strain range to linearize across. The tensile fracture loads  $f_t$  for each direction are tabulated below:

	$f_{t1}$ in $\mathbf{e}_1$ in [MPa]	$f_{t2}$ in $\mathbf{e}_2$ in [MPa]
specimen 1	0.0848	0.235
specimen 2	0.0967	0.309
mean	0.091	0.272

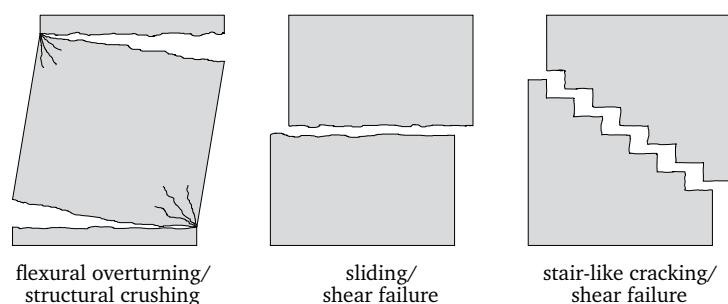


**Figure 4.18:** Typical shear failure modes of masonry structures.

### Tension damage:

Figures 4.16a and 4.16b illustrate the typical crack patterns of the horizontal  $e_1$  and vertical  $e_2$  tensile tests respectively.

The damage progression of both orientations was primarily dominated by discrete crack propagation along the brick and mortar interface, although the vertical specimens demonstrated occasionally crack branching through bricks as well. This additional damage mechanism of the vertical orientation is responsible for its greater fracture load and fracture energy compared to the horizontal orientation, clearly visible in figure 4.17. Both orientations display variations in their non-smooth damage evolution, suggesting that the overall failure mode is locally directed by manufacturing and material defects.

### 4.2.5 Shear tests

As illustrated in figure 4.18, masonry structures have multiple failure modes such as flexural overturning (structural cracking), sliding shear failure and diagonal cracking shear failure. These modes all feature shear failure as a predominant mechanism and necessitate the understanding of masonry shear behaviour. Corresponding to the variety of local/global shear phenomena, a range of masonry shear tests may be applied [8] with References [242, 61] reviewing and summarising popular test methods. Some tests, such as the triplet test (EN 1052-3 [80] or the diagonal compression test (defined in ASTM E519-2010 and RILEM LUMB6) are defined in national codes, whereas other studies focus on specific shear arrangements and are not standardized. Small scale triplet shear tests may effectively describe sliding shear failure behaviour but have limited insight into macro-scale shear phenomena such as flexural overturning where more complex custom testing schemes are required. However, the sliding shear strength does provide important information for micro and meta scale modelling approaches as it contains less geometrical effects.

In this study shear tests were conducted across two arrangements: the small three brick triplet shear test and a custom macro-scale shear test employing the numerically-

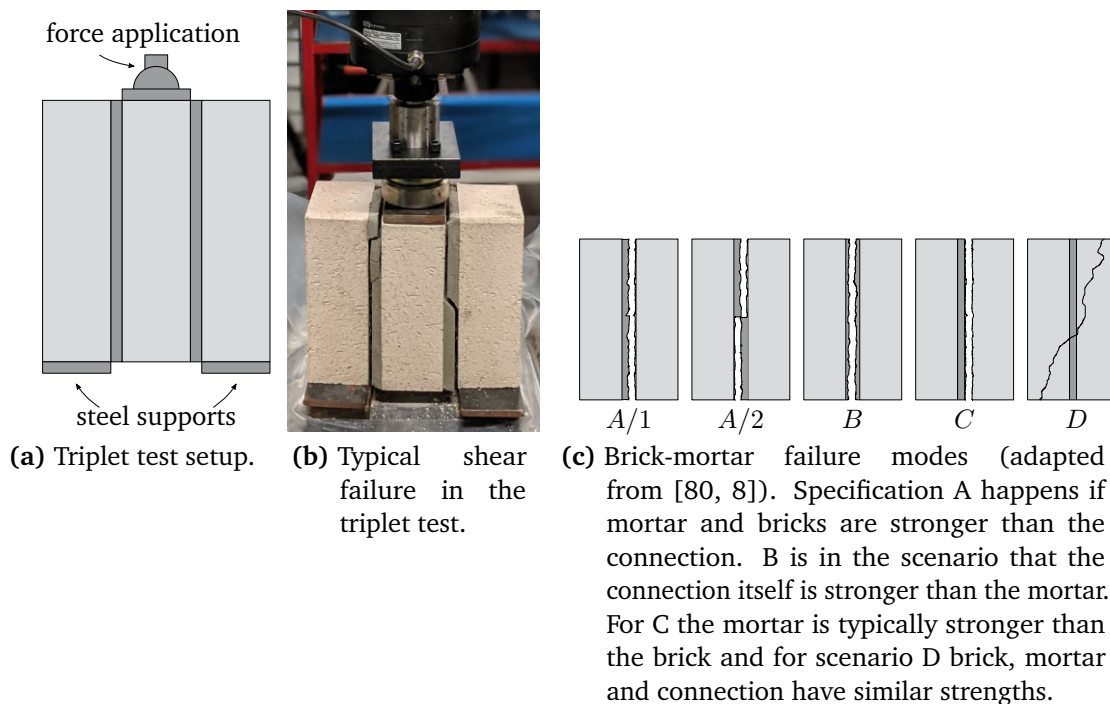


**Figure 4.19:** Triplet test setup, typical failure and brick failure modes.

justified specimen size. Not only does this dual-approach offer a more holistic view of masonry shear behaviour across different scales, it may also indicate the relative strengths and limits of each shear test for future researchers interested in exploring particular shear mechanisms.

#### Small scale triplet shear tests:

The triplet tests were conducted in accordance to Eurocode EN 1052-3 specifications procedure B [80] (procedure B was preferred over A to avoid bi-axial stress states) as illustrated in figure 4.19a. Eight specimens, exceeding the prescribed EN 1052-3 minimum of six, were tested, with the outer bricks of each specimen simply supported while the central brick was subjected to a vertically compressive load from a hydraulic actuator.

Triplet tests typically experience a limited range of failure modes that primarily depend on the relative strengths of the bricks and mortar tested, as illustrated in figure 4.19c. Within this series of tests, failure mode *A/2* was predominantly observed accompanied by few *A/1* failures, indicating the brick-mortar interface was weaker than both the bricks and mortar.

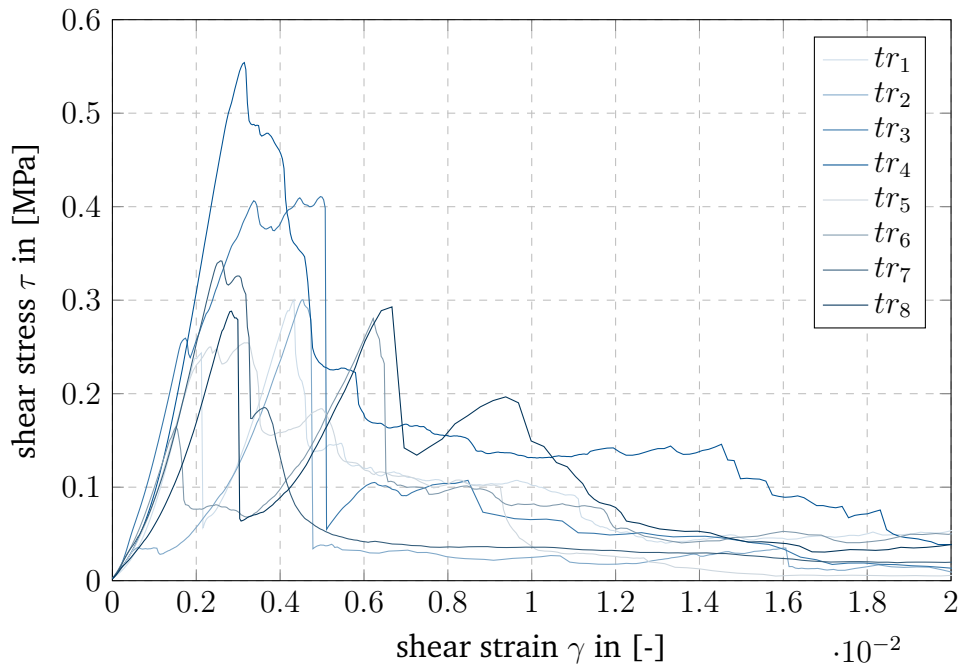


**Figure 4.20:** Triplet test shear stress-strain results.

According to DIN EN 1052-3 [80], the limit shear strength  $\tau$  is evaluated as:

$$f_{voi} = \frac{F_{i,max}}{2A_b} \quad (4.7)$$

where  $F$  is the applied force and  $A_b$  the area of each brick-mortar joint. The triplet test shear strain is evaluated with:  $\frac{u_{top}}{h}$  where  $u_{top}$  is the vertical machine displacement and  $h$  the height of the bricks. Employing the aforementioned relations, the shear stress-strain curves of the triplet shear tests are presented in figure 4.20. One may observe considerable variance between results which is attributed to premature small cracks developing in some of the specimens. This behavior is one of the primary distinctions of crack type  $A/2$ , where cracks develop through weaker areas, against crack type  $A/1$ , where the whole brick typically separates from the mortar. Additionally, the small number of bricks, small amount of mortar and limited failure planes of the triplet shear test promote result disparities due to the non-averaging of manufacturing and material defects (compared to larger scale tests where inhomogeneities are smeared).

The ultimate shear strengths  $f_{vo}$  of the triplet shear test are tabulated below:

	force $F$ in [kN]	shear strength $\tau$ in [MPa]
specimen 1	15.19	0.300
specimen 2	15.23	0.301
specimen 3	20.81	0.411
specimen 4	28.04	0.554
specimen 5	12.88	0.255
specimen 6	14.44	0.285
specimen 7	17.32	0.342
specimen 8	14.92	0.295
mean/ $f_{vo}$	17.35	0.343

**Macro scale shear tests:**

The macro-scale shear tests employed the numerically-justified specimen size to characterise the fully anisotropic in-plane elastic shear moduli  $G_{12}$  and  $G_{21}$  and produce a stair-like cracking shear failure as per figure 4.18.

To design an appropriate shear test setup of the macroscopic material properties, the mechanical expression of shear should be studied, which is outlined within figure 4.21. It shall be noted at this position that numerical studies do generally have more options than physical experiments, however, sometimes also limits within feasibilities do exist. Whereas it showed being rather straight forward to justify the specimen size via the simple shear criteria (c), this would not express the correct shear moduli. Accordingly, the aim is to activate a material response as per pure shear (a). To obtain this, it was chosen to not restrain the full top, rather than only a point close to the location of the load application. Around the support, the top line may rotate slightly to not put any further force in the specimen by compression or tension.

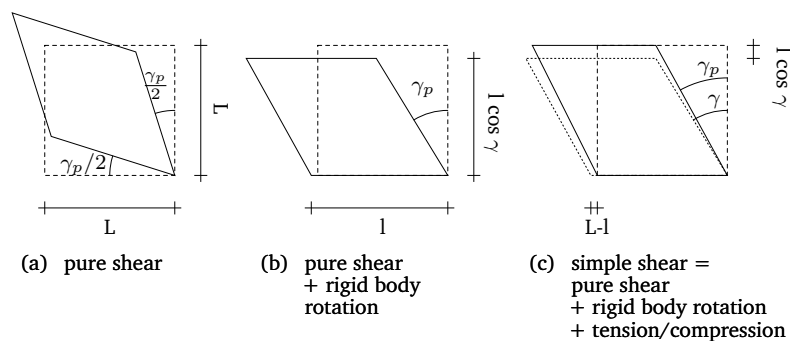


**Figure 4.21:** Decomposition of simple shear in pure shear, rigid body rotation and tension/compression parts (modified from [194]).

The test setup is illustrated in figure 4.22, in which the lower-left corner of the specimen is restrained against a mechanical stopper fixed to the strong floor. The lower and

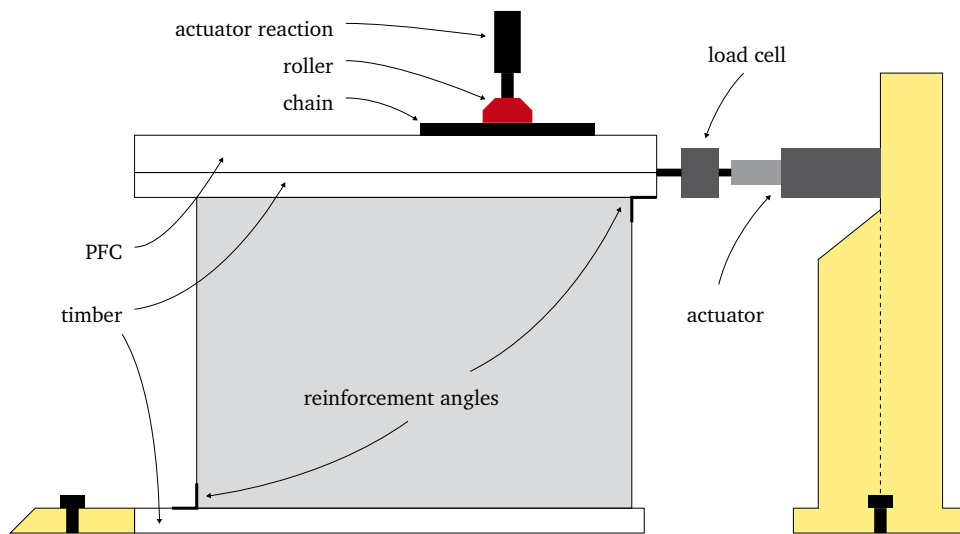


**Figure 4.22:** Shear test setup. The columns are only shown part wise. Both columns are fixed to the bottom and can be seen as rigid. The active actuator is connected to one of the columns. The reactionary actuator is connected to a connection bar between the to columns.

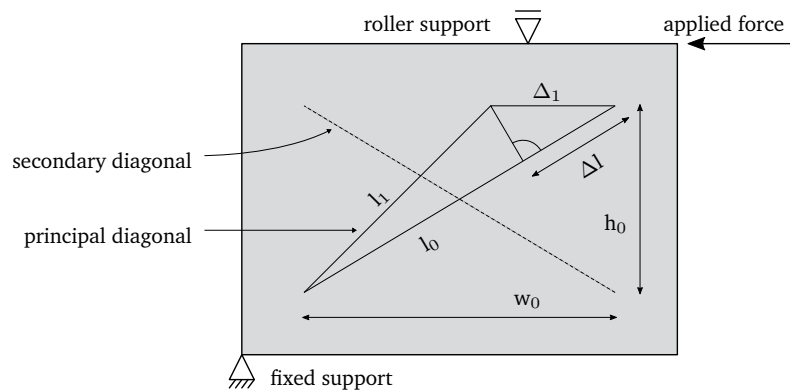


**Figure 4.23:** Analytical structural system of the shear tests.

top edge is adhesively bonded to timber studs, whereby the upper-right corner of the specimen is subject to an applied displacement (hydraulic actuator and forces measured through additional load cell) and the top is vertically restrained (hydraulic actuator containing a separate force and displacement measurement system) in displacement control to ensure pure shear behaviour and prevent overturning. To gain a deeper understanding of the setup, the corresponding analytical structural system of the test is presented in figure 4.23.

The measurements from the DIC system were taken from digital extensometers which produced the output variables  $w_0$ ,  $h_0$ ,  $l_0$  and  $\Delta l$  as defined in figure 4.23. Considering these output parameters,  $\Delta_1$  can be evaluated by the geometrical relation:

$$\frac{l_0}{w_0} \cdot \Delta l = \Delta_1 \quad (4.8)$$

from which  $\gamma_{12}$  may be determined according to equation 4.5 reproduced below:

$$\gamma_{12} = \frac{\Delta_1}{h_0} \quad (4.9)$$

The complementary shear  $\gamma_{21}$  is determined in an analogous manner.

### Macro shear tests in $e_1$ :

Figure 4.25a illustrates the shear stress-strain curves of the macro shear tests in  $e_1$  (determined along the principal diagonal illustrated in figure 4.23), while the limit strengths are tabulated below:

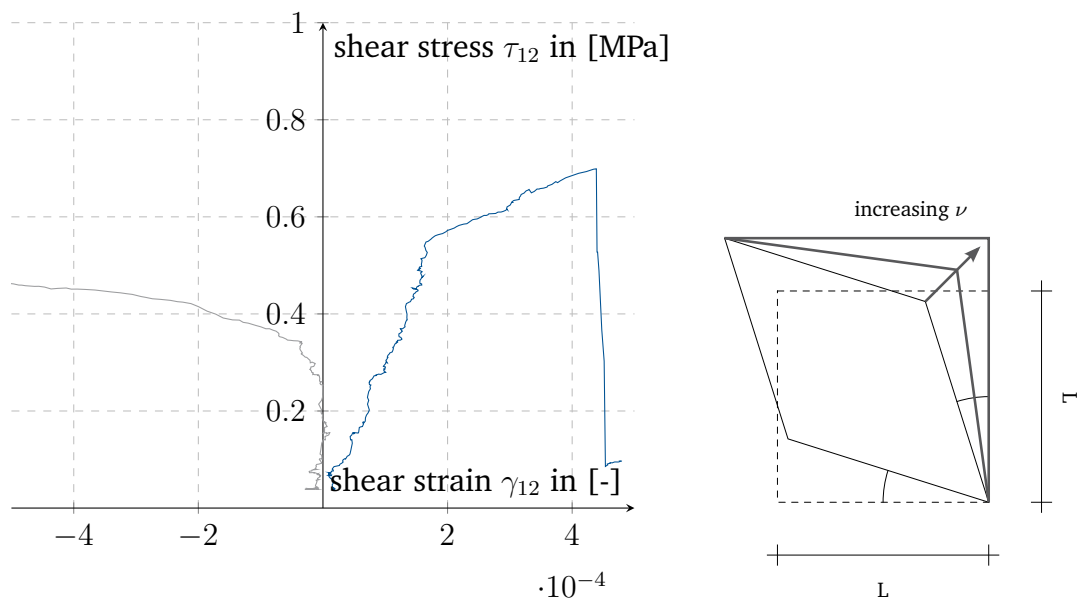
	force $F$ in [kN]	shear strength $\tau$ in [MPa]
specimen 1	52.44	0.679
specimen 2	53.42	0.685
specimen 3	66.21	0.860
specimen 4	53.91	0.699
mean	56.495	0.731

From the shear stress-strain curve (see figure 4.25a) the graphically averaged tangent shear modulus was considered to be  $G_{12} = 1.34 \times 10^3 \text{MPa}$ .

### Primary vs. secondary diagonal in $e_1$ :

Although the derivation of shear strains in equations 4.8 and 4.9 may conceptually be computed along either the principal or secondary diagonal in figure 4.23, it was found that only the primary diagonal yielded useful data. Specimen 4 shear stress-strain results computed along both diagonals are presented in Figure 4.24a, demonstrating remarkably different shear characterization.

The principal diagonal exhibits an approximately linear elastic range, from which it is possible to derive a shear modulus from, whereas the secondary diagonal suggests a clearly erroneous infinitely stiff elastic range followed by nearly fully plastic yielding.



(a) Shear stress - shear strain relation of specimen 4 measured in principal (blue) and secondary (grey) diagonal. (b) Influence of Poisson's ratio  $\nu$  on pure shear behaviour.

**Figure 4.24:** Primary vs. secondary diagonal in  $\mathbf{e}_1$ .

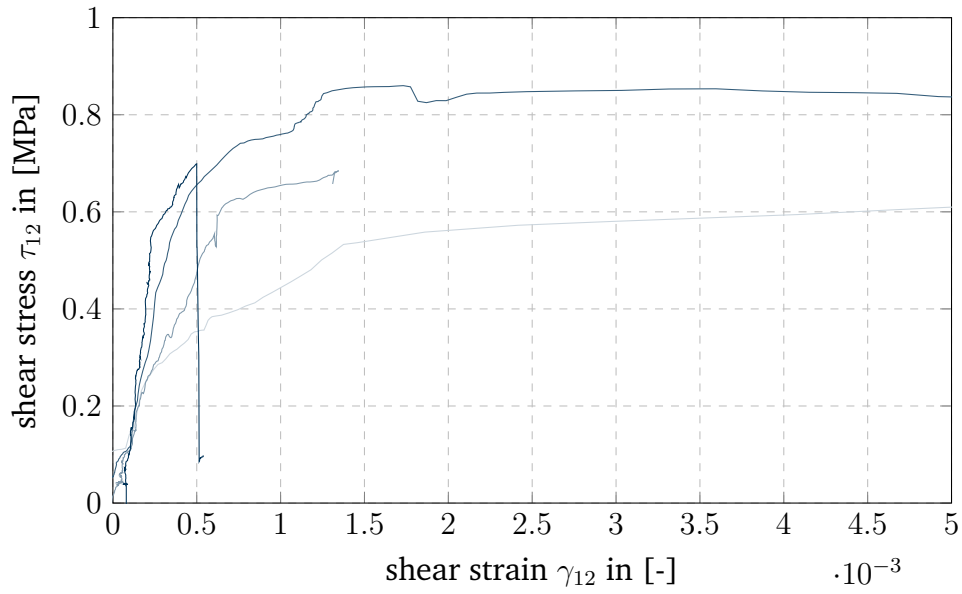
The reason for this discrepancy is intuitively illustrated in figure 4.26a where a staircase crack is apparent along the primary diagonal. Accordingly, measuring shear along the secondary diagonal amounts to incorrectly interpreting crack opening displacements with shear strains.

The apparent results additionally suggest, according to the expected deflections as per pure shear (see figure 4.24b), that the Poisson's ratio  $\nu$  is rather minor, which is expected for this modern masonry type, which contains large holes within the bricks.

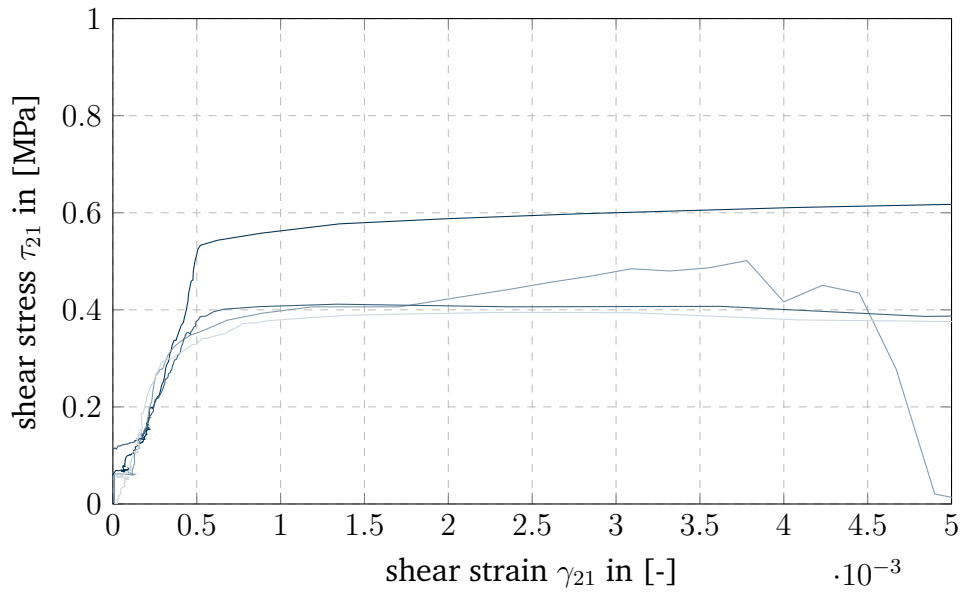
### Shear tests in $\mathbf{e}_2$ :

Figure 4.25b illustrates the shear stress-strain curves of the macro shear tests in  $\mathbf{e}_2$  (determined along the principal diagonal illustrated in figure 4.23), while the limit strengths are tabulated below:

	force $F$ in [kN]	shear strength $\tau$ in [MPa]
specimen 1	36.61	0.647
specimen 2	28.68	0.501
specimen 3	23.28	0.412
specimen 4	22.40	0.397
mean	27.74	0.489



(a) Direction  $e_1$ .



(b) Direction  $e_2$ .

**Figure 4.25:** Macro shear stress-strain curves.

From the shear stress-strain curve (see figure 4.25b) the graphically averaged shear modulus was considered to be  $G_{21} = 0.96 \times 10^3 \text{MPa}$ .

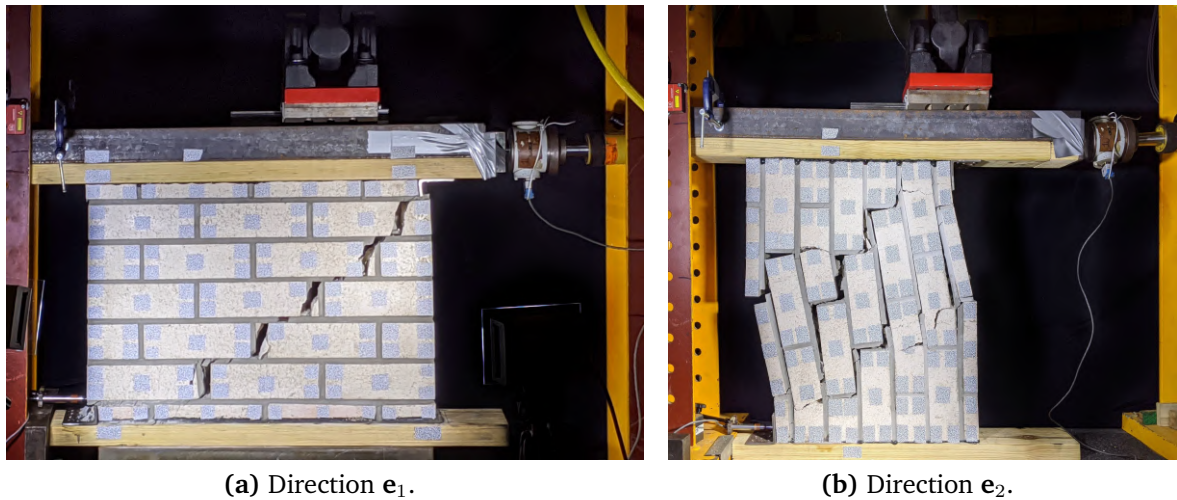


**Figure 4.26:** Shear failure of masonry in direction  $e_1$  and  $e_2$ .

### Shear damage:

Figures 4.26a and 4.26b illustrate the typical crack patterns that developed in each test orientation, confirming both exhibit the stair-like cracking motif. The horizontal  $e_1$  specimens displayed a faithful reproduction of the stair cracking pattern, with damage propagating almost exclusively along mortar lines. Furthermore, the cracks developed primarily on the brick-mortar interface, confirming that although the small scale triplet shear tests may not predict macro shear behaviour, they correctly predict local shear failure mechanisms that accrue to form emergent macro behaviour. Contrasting this singular damage propagation, the vertical  $e_2$  specimens appeared to initiate numerous stair cracking sites in parallel, each of which predominantly evolved along brick-mortar interfaces. Again, the small scale triplet shear tests accurately reflect the local brick-mortar interface dominated failure of the larger specimen, but naturally fails to predict the parallel damage evolution and resulting macro shear behaviour.

Furthermore, it can be noted according to the evaluation of the test results that the crack opening in direction  $e_2$  is much higher than in  $e_1$ , before losing the entire stiffness, resulting the fracture energy and the ductility is higher than in direction  $e_1$ .

### Comparison of triplet and macro-scale shear results:

The triplet shear test is a small-scale test method which provides the sliding shear strength of the masonry, while the custom macro scale test additionally provides the shear moduli and the different failure strengths. Nonetheless, it was demonstrated that the triplet shear tests predicted the local failure mode within the larger-scale tests,

but could not predict whether damage evolved in serial (horizontal  $\mathbf{e}_1$  macro-shear) or parallel (vertical  $\mathbf{e}_2$  macro-shear). Another feature of the triplet shear tests is that the prescribed DIN EN 1052-3 limit shear strength equation 4.7 assumes both bricks fail at the same time, which, due to material and manufacturing defects, is generally incorrect. Accounting for the fact that failure occurs along one weaker plane, the practical ultimate shear force may be expressed as:

$$f_{pi} = \frac{F_{i,max}}{A_b}, \quad (4.10)$$

which amounts to  $f_{pi} = 2f_{voi}$ . Thus, the mean practical ultimate shear strengths obtained from the triplet test is  $f_{po} = 2 \times 0.343 = 0.686\text{MPa}$ , which agrees well with the mean shear strength of the horizontal  $\mathbf{e}_1$  macro tests  $\tau = 0.731\text{MPa}$ . Contrasting this, the mean shear strength of the vertical  $\mathbf{e}_2$  macro specimen  $\tau = 0.489\text{MPa}$  was considerably lower. This is attributed to the parallel crack initiation, which subsequently propagates along the weakest of all manufacturing and material imperfections. Once propagating, this proto-crack serves to further weaken its immediate surroundings, promoting further crack initiation and growth.

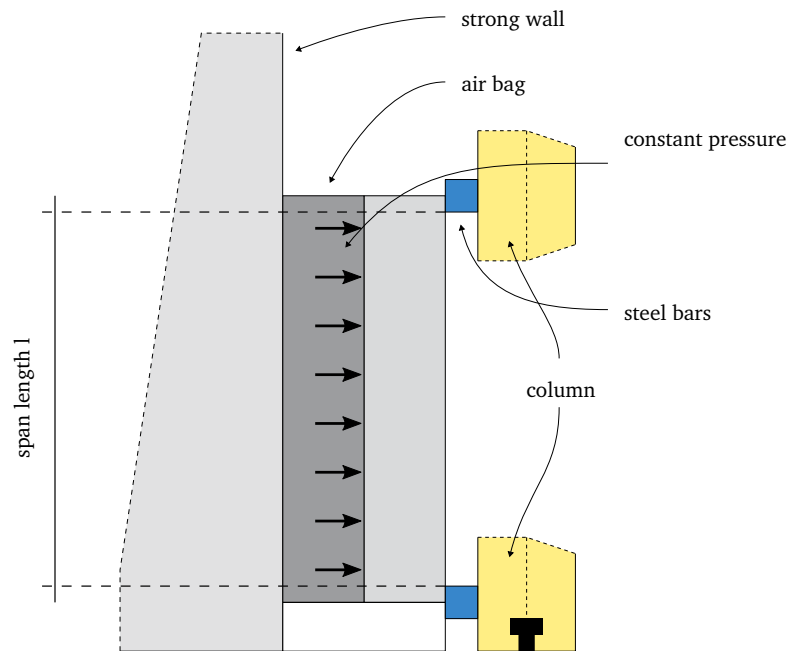
### 4.2.6 Bending tests

Static out-of-plane masonry behavior is an active research area [235, 94, 91] and is particularly relevant in preventing catastrophic failure during seismic events [85, 236, 127]. This study employs the numerically-justified specimen size to characterise the out-of-plane behaviour across horizontal and vertical orientations, particularly in terms of maximum moment capacity. Although some out-of-plane studies employ a 3-point bending arrangement, the brittle and imperfection-sensitive nature of masonry precludes this approach from meaningfully characterising the overall bulk out-of-plane behaviour of the masonry specimen. Therefore, an air bag driven testing apparatus illustrated in figure 4.27a was designed and constructed to properly examine the out-of-plane behaviour of the specimen.

The airbag was placed in-between the specimen and a strong wall and gradually pressurised during the test, thereby exerting a spatially constant pressure on one side of the specimen. Steel restraints against the horizontal translations were placed on both, the top and the bottom edges of the specimen. It must be noted that the assumption of constant pressure application is limited to small deflections and is not applicable after large deformation, especially including local damages of the masonry.

From the applied air bag pressure  $p$ , the resultant maximum moment in the specimen's vertical centre is determined by:

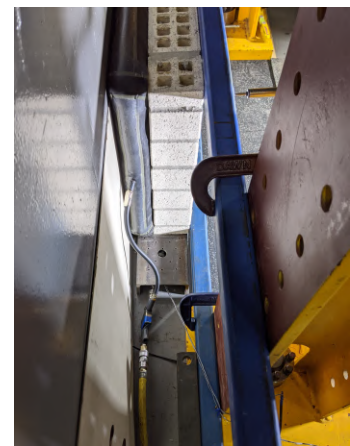
$$M_{max} = \frac{p \cdot l^2}{8}, \quad (4.11)$$



(a) Bending test setup side section. The columns (yellow) are only shown part wise. Two columns are fixed to the bottom and can be seen as rigid. Two steel bars (blue) connect the two columns and support the masonry sample on the top and the bottom to allow the bending in the middle. The air bag is put behind the specimen and shall apply a constant pressure load on the sample.



(b) Bending test setup with direction  $e_1$  masonry sample.



(c) Bending test setup with direction  $e_1$  masonry sample.

**Figure 4.27:** Bending test setup.

where  $l$  is the vertical span between supports running along the top and bottom edges of the specimen.

**Bending tests in  $e_1$ :**

The failure pressures and moments of the horizontal  $e_1$  specimens are tabulated below:

	$p$ in [kPa]	$M_{1,max}$ in [kNm]
specimen 1	46.927	1.296
specimen 2	33.566	0.927
specimen 3	25.343	0.699
mean	35.279	0.974

Note that bending stress-strain curves are not producible for either orientation due to the small out-of-plane deformations beyond the reliable limits of the DIC measurement system.

**Bending tests in  $e_2$ :**

The failure pressures and according moments of the vertical  $e_2$  specimens are tabulated below:

	$p$ in [kPa]	$M_{2,max}$ in [kNm]
specimen 1	40.219	2.124
specimen 2	42.745	2.257
specimen 3	51.970	2.745
specimen 4	41.612	2.198
mean	44.137	2.331

**Bending damage:**

Figures 4.28a and 4.28b illustrate the bending failures of the horizontal  $e_1$  and vertical  $e_2$  tests respectively. The horizontally  $e_1$  aligned specimens fully cracked and subsequently hinged along a vertically-centred horizontal mortar line. Furthermore, failure typically occurred along the brick-mortar interface. The relatively large spread of horizontal  $e_1$  results may be attributed to the focused nature of the fracture naturally magnifying manufacturing and material imperfection. The vertical  $e_2$  specimens fail predominantly via the same brick-mortar interface, however, brick fractures were also observed. This higher energy failure mode, in combination with the geometric strengthening (via crack propagation re-routing) of the brick-mortar interface failures, yielded greater moment capacities with less variability than the horizontal orientation.

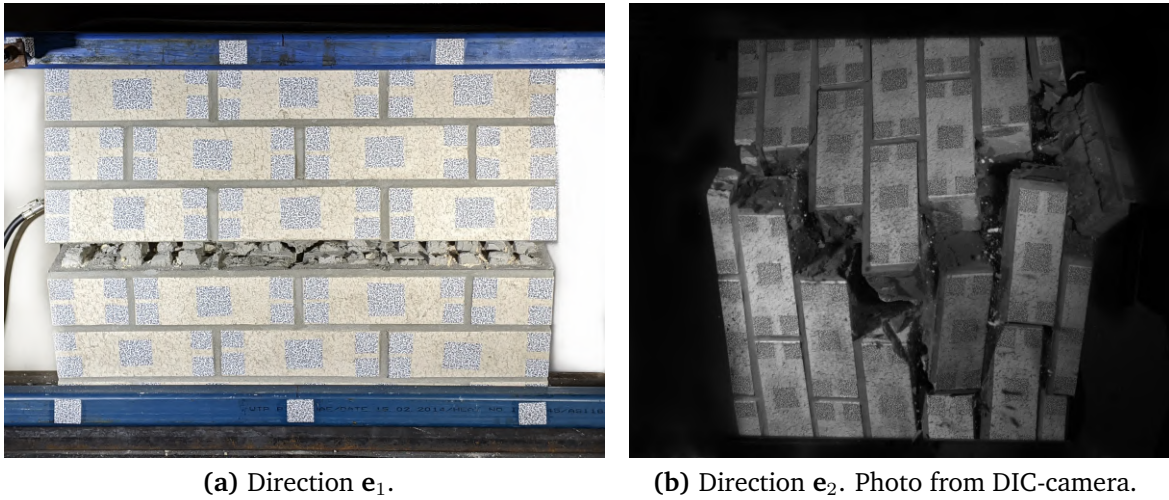


**Figure 4.28:** Bending failure in direction  $e_1$  and  $e_2$ .

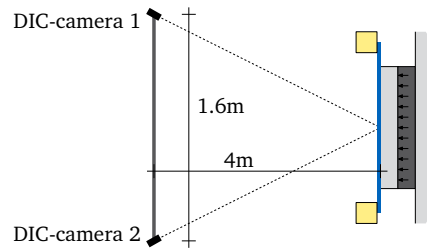


**Figure 4.29:** DIC-camera setup to measure out-of-plane behavior.

### Discussion of bending results:

The bending tests within this dissertation were performed to characterize the out-of-plane bending moment capacities of masonry across horizontal and vertical orientations. Initially, a secondary aim was to obtain shear parameters required to accurately model the out-of plane deflections within a shell formulation which includes shear (e.g. Reissner Mindlin). The accuracy of the DIC was not sufficient to measure bending or shear deflection within reliable parameters before the specimen experienced damage.

For this setup, 2 DIC cameras were taken with a distance between them of 1.6m and 4m to the specimen, as per figure 4.29.

Looking forward to future studies, it is expected that a larger specimen size may adequately magnify displacements to perceptible limits and/or a specialized sensitive measurement approach may provide sufficient results to obtain shear parameters relevant for shell type kinematics.

### 4.2.7 Summary of masonry macro material properties

The following table summarises the mean results of the preceding experimental program:

Test	$e_1$ orientation	$e_2$ orientation
Compression (section 4.2.3):		
$E$ [MPa]	5000	3100
$f_{c0}$ [MPa]	5.2	2.9
$f_c$ [MPa]	7.38	4.05
$f_{cr}$ [MPa]	1.3	0.0
$G_c$ [ $\frac{N}{mm}$ ]	1200	1100
Tension (section 4.2.4):		
$f_t$ [MPa]	0.091	0.272
$G_t$ [ $\frac{N}{mm}$ ]	15	60
Shear:		
Triplet shear (section 4.2.5):		
$f_{vo}$ [MPa]	0.343 (0.686*)	
Macro shear (section 4.2.5):		
$G_{12}$ [MPa]	1340	-
$G_{21}$ [MPa]	-	960
$\tau_{max}$ [MPa]	0.731	0.489
Bending (section 4.2.6):		
$M_{max}$ [kNm]	0.974	2.331

\* assuming imperfection-driven failure, refer section 4.2.5. Check figure 4.31 for the remaining parameter definitions.

Within this thesis, it shall be referred to the apparent material parameters with *Brisbane*-masonry.

### 4.2.8 Conclusion of material tests

The overall aim of this test series was to characterise the macro-scale orthotropic mechanical properties of masonry with experimental tests. However, the required experimental specimen size to avoid boundary and size effects is generally not obvious and usually not justified throughout literature. Therefore, an initial numerical study of the proposed experiment was conducted to determine the minimum specimen size free of scaling effects. Employing this numerically-justified specimen size, a comprehensive experimental program was conducted to determine macroscopic orthotropic masonry

material parameters across horizontal (direction  $\mathbf{e}_1$ ) and vertical (direction  $\mathbf{e}_2$ ) orientations. Following tests have been operated: compression, tension, triplet shear, macro shear, and out-of-plane bending.

Complementing this, several limitations of the current work may inform additional future research projects. One avenue is to revisit the out-of-plane bending tests with either larger specimen sizes or more sophisticated measuring techniques to derive additional material parameters. This is important to determine if Kirchhoff-Love or Reissner-Mindlin assumptions are valid. Another possible aspect would be extending the current bi-directional study to additional directions (such as [174, 70, 15]) facilitating full continuum simulations. Furthermore, bi-axial stiffness states are an essential quote of information for masonry. An additional major drawback is the missing bi-axial stiffness, which is another crucial parameter within the material properties [70].

### 4.3 Orthotropic damage model for masonry <sup>e</sup>

Continuum-based damage models define a conventional way to describe the structural properties of masonry buildings, specifically to express failures within the structures. Initially, one damage parameter was applied to describe the softening of the construction material [143]. Consequently, those damage parameters have been split into compression and tension damages to allow deeper insights in highly loading dependent materials [50, 84, 249]. Those concepts have been enhanced further with damage parameters per direction [33]. Other concepts do not make the damage split within the stress state but the direction [131] with inter-dependent damage parameters, which represent prevailing considerations but shapes up fairly complex and accordingly less appropriate for the apparent masonry properties. Following, within this dissertation, the focus shall be retained on two parameters  $d^+/d^-$ -damage models, as it contains less parameters and fewer internal dependencies.

The mentioned material models are adequate in the analysis of isotropic materials with sensible triggers for the softening zones. Thusly, in masonry, its applications are so-far mostly for the simulation within continuum-based micro models of bricks (without holes) and mortar. However, as the structural properties of masonry show significant correlating orthotropic behavior it is insufficient to fulfill the apparent direction-dependent estates. Rather than updating the yield surface with anisotropic surfaces as the Hill-type criterion [101, 100, 141] or Tsai-Wu [234] it is preferred to base upon a mapping from the real anisotropic space to an ideal mapped isotropic stress state, as this concept is generally simpler, with the possibility to keep former developments and mostly leaner computational costs. The concept of the implicit orthotropic yield criterion was initiated by [35] and later advanced by [172, 171]. Pelà et al. [180, 179] promoted those models to the simulation of masonry structures. The most significant

improvement from the macro model of Lourenço et al. [141] has been achieved by the split in compressive and tensile damages, which allowed to model an exceedingly vast amount of problems.

Subsequently, a model which merges the latest improvements of the relaxing behaviour from Petracca et al. [181] and Pelà et al. [179] into a novel material model, which adds better triggers in the softening within an appropriate orthotropic behavior is presented. Therefore, the isotropic model is presented in section 4.3.1, with the orthotropic mapping procedure in section 4.3.2.

#### 4.3.1 Continuum tension/compression damage model

Within this section the continuum based  $d^+/d^-$ -damage model from Petracca et al. [183, 182] shall be discussed with a focus on the applicability for the presented masonry. As the aim of this research is the simulation with thin walled shell-based formulations, the following relations are discussed in plane-stress state.

##### Constitutive relations:

The effective stresses  $\bar{\sigma}$  (with the notation  $\bar{\cdot}$  used to mark the effective state) are obtained from the elastic constitutive tensor  $C_{elastic}$  (for the apparent orthotropic plane stress problems see equation 4.1) and the actual strains  $\epsilon$ :

$$\bar{\sigma} = C_{elastic} : \epsilon \quad (4.12)$$

Similarly to [50, 84, 249], the effective stresses are split into the positive  $\bar{\sigma}^+$ -tensile and negative  $\bar{\sigma}^-$ -compressive constituents, while implying:

$$\bar{\sigma} = \bar{\sigma}^+ + \bar{\sigma}^- \quad (4.13)$$

The two parts can be computed as following:

$$\bar{\sigma}^+ = \sum_{i=1}^3 \langle \bar{\sigma}_i \rangle \cdot \mathbf{p}_i \otimes \mathbf{p}_i \quad \bar{\sigma}^- = \bar{\sigma} - \bar{\sigma}^+ \quad (4.14)$$

where,  $\sigma_i$  is the i-th principal stress, with the corresponding unitary eigenvector  $\mathbf{p}_i$ . The Macaulay brackets  $\langle \cdot \rangle$  selects the positive values, while being zero for negative  $\sigma_i$ .

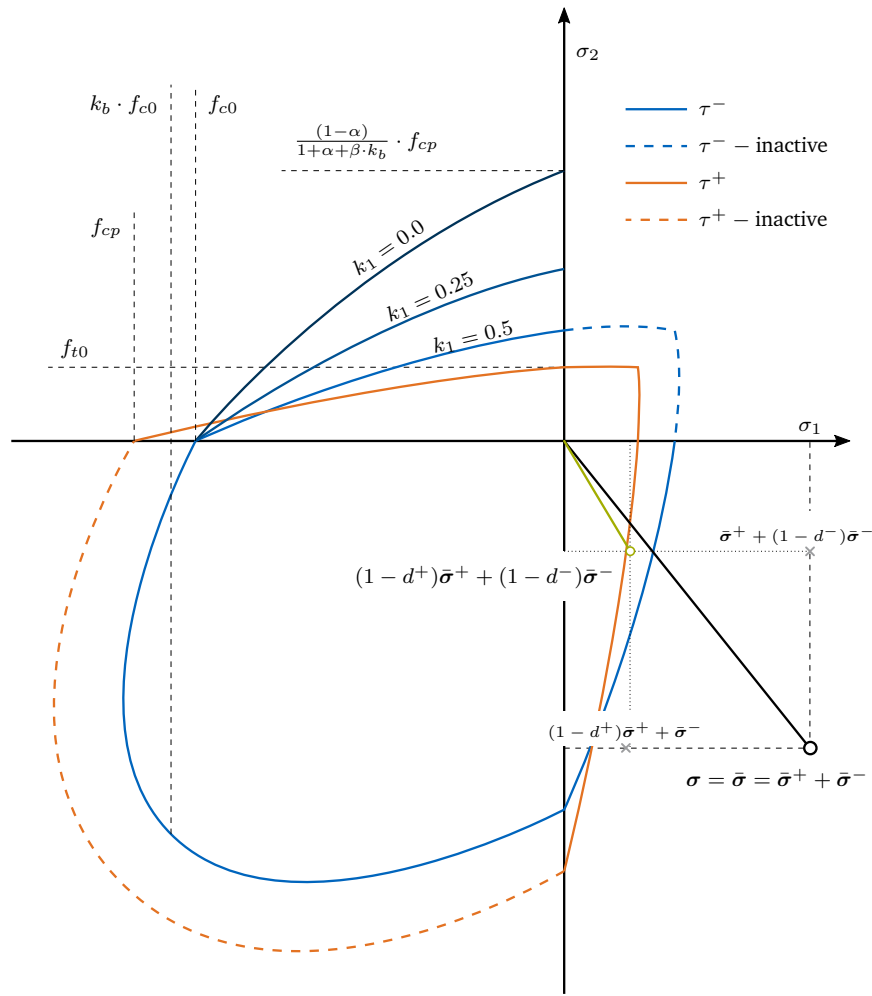


Figure 4.30: Compression and tension threshold surfaces (adapted from [181]).

### Equivalent stress threshold:

The stress thresholds  $r^+$  and  $r^-$  are the maximum uniaxial equivalent stresses which can be carried within a system. The applied threshold yield surface shall be based upon a Drucker-Prager criterion, enhanced by [143] and thoroughly defined by [182]. The two equivalent stress surfaces in tension  $\tau^-$  and compression  $\tau^+$ , are graphically displayed in Figure 4.30 and discussed in the following:

$$\tau^-(\bar{\sigma}) = H(-\bar{\sigma}_{min}) \left[ \frac{1}{1-\alpha} \left( \alpha \bar{I}_1 + \sqrt{3\bar{J}_2} + k_1 \beta \langle \bar{\sigma}_{max} \rangle \right) \right] \quad (4.15)$$

$$\tau^+(\bar{\sigma}) = H(\bar{\sigma}_{max}) \left[ \frac{1}{1-\alpha} \left( \alpha \bar{I}_1 + \sqrt{3\bar{J}_2} + \beta \langle \bar{\sigma}_{max} \rangle \right) \frac{f_t}{f_{cp}} \right] \quad (4.16)$$

with the scalars  $\alpha$  and  $\beta$  being used as subsequently:

$$\alpha = \frac{k_b - 1}{2k_b - 1} \quad \beta = \frac{f_{cp}}{f_t}(1 - \alpha) - (1 + \alpha) \quad (4.17)$$

Furthermore,  $\bar{I}_1$  is the first invariant of the effective stress tensor and  $\bar{J}_2$  the second invariant of the deviatoric stress tensor.  $\bar{\sigma}_{max}$  is used as the maximal principal effective stress, respectively  $\bar{\sigma}_{min}$  being the smallest principal effective stress. The shear reduction parameter  $k_1$  is introduced to control the compressive strength in the shear state, which properties are shown Figure 4.30. [181, 182] provide comprehensive studies on the structural effect of this parameter. Finally, the factor  $k_b$  is defined by the ratio from the biaxial strength of the applied material (see figure 4.30).

As the thresholds are defined for any stress state, in some cases it may happen that the damage surface advances for tension in uniaxial compression or in reverse. To avoid this, the Heavyside function  $H(x) = \begin{cases} 0 & \text{for } x \leq 0 \\ 1 & \text{for } x > 0 \end{cases}$  is used to ensure following criteria:

- tensile damage only evolves if at least one principal stress is positive,
- compressive damage only evolves if at least one principal stress is negative.

The effect of the applied Heavyside is deciphered in Figure 4.30 by the active and inactive threshold surfaces.

### Damage evolution:

The previously described uniaxial stresses shall be used as parameters for the irreversible damage evolution of the material. It is expected that the tensile softening is defined by the yield strength and the fracture energy with a non-linear softening, whereas the compression shows a more complex behavior with multiple inputs for the analysis (see Figure 4.31 for possible damaging zones).

The tensile damage growth is obtained by the subsequent equation:

$$d^+(r^+) = 1 - \frac{r_0^+}{r^+} \exp \left[ 2H_{dis} \left( \frac{r_0^+ - r^+}{r_0^+} \right) \right] \quad (4.18)$$

Where the thresholds are applied as  $r^+ = \max[r_0^+, \max(\tau^+)]$  with  $r_0^+ = f_{t0}$ . It shall be noted that always the maximal  $\tau^+$  should be considered, to avoid damage relaxation. The discrete softening parameter  $H_{dis}$  is defined as following:

$$H_{dis} = \frac{l_{ch}}{l_{mat} - l_{ch}} \quad \text{with} \quad l_{mat} = \frac{2EG_t}{f_{t0}^2} \quad (4.19)$$

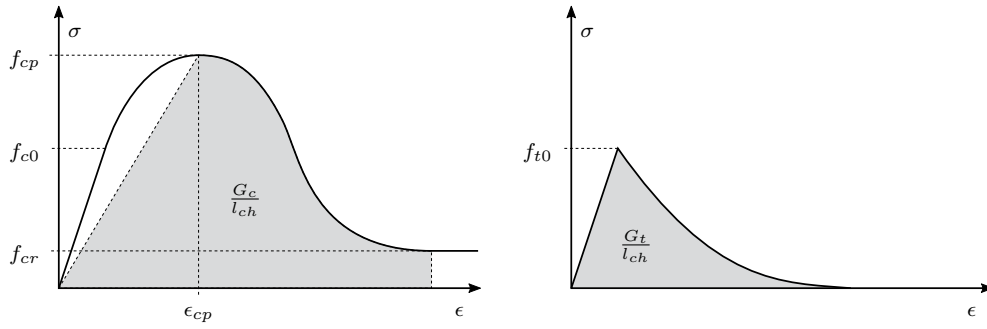


**Figure 4.31:** Compression and tension fracture zones.

The characteristic length  $l_{ch}$  is used to regularize the fracture zone and is dependent on the geometry of the finite element. Multiple approaches exist to approximate the characteristic length [28, 49, 29, 183]. It is possible to accurately calibrate the fracture dissipation length within structured quadrilaterals, however, more complex, non aligned geometries and high order geometries will typically produce discrepancies. Within appendix B is presented a study of possibilities for various length approximations, specifically with the focus on high order geometries.

As proposed by [182], the compression damage progression is analyzed on an ad hoc basis under a segmented Bézier curve, which is controlled by the elastic limit strength  $f_{c0}$ , the yield strength  $f_{cp}$ , its corresponding yield strain  $\epsilon_{cp}$  and the residual strength  $f_{cr}$ . The damage evolution is defined by the hardening variable  $\Sigma(\xi)$  with its strain-like counterpart  $\xi = \frac{r^-}{E}$  (follow appendix A for a detailed extraction of the Bézier curve):

$$d^-(r^-) = 1 - \frac{\Sigma(\xi)}{r^-}. \quad (4.20)$$

### Total stresses:

Including the convoluted damage parameters  $d^+/d^-$  the total stresses are defined by:

$$\boldsymbol{\sigma} = (1 - d^+) \bar{\boldsymbol{\sigma}}^+ + (1 - d^-) \bar{\boldsymbol{\sigma}}^- \quad (4.21)$$

### 4.3.2 Orthotropic damage model

In the following the recently described isotropic damage model shall be enhanced to enable orthotropic behaviours. Rather than updating the yield surface with anisotropic surfaces as the Hill type criterion [101, 100, 141] or Tsai-Wu [234] it is preferred to base upon a mapping from the real anisotropic space to an ideal mapped isotropic stress state [35, 172, 171], as this is the simpler and thusly computationally more efficient approach.

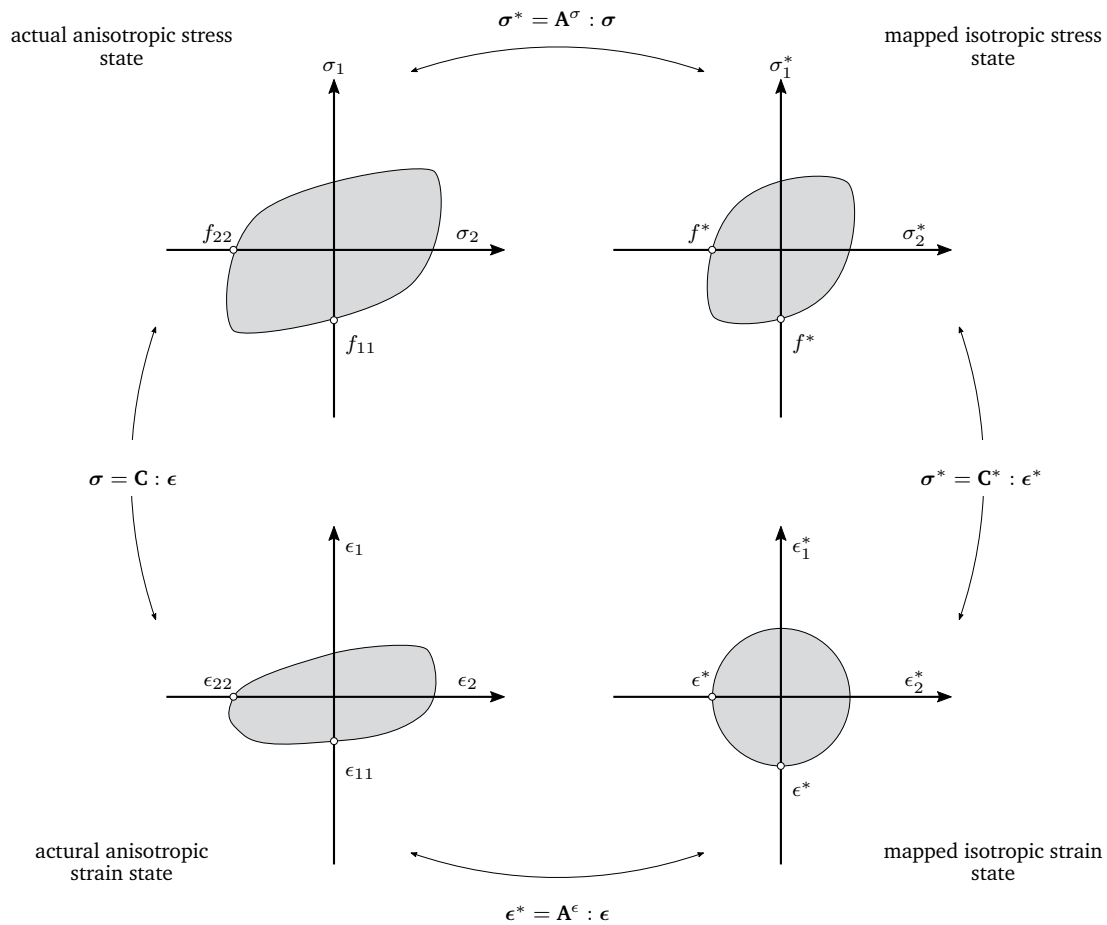


**Figure 4.32:** Mapping between actual anisotropic and isotropic space (adapted from [172]).

Furthermore, it allows the application of the more advanced threshold surfaces for isotropic materials, as e.g. the one discussed in the previous section 4.3.1.

**Transformation between actual orthotropic and mapped isotropic space:**

The concept of the implicit orthotropic yield criterion was initiated by [35] and lateron advanced by [172, 171]. By dividing the earlier constitutive models into compressive and tensile components, [180, 179] applied them to simulate masonry. The models are based upon a transformation between the actual anisotropic, or in this case orthotropic stress state to an arbitrary mapped isotropic space (notation  $(\cdot)^*$ ) and its corresponding strain-based reverse mapping, as shown in Figure 4.32.

The mapping from the actual stress state to the isotropic space is defined by the transformation tensor  $\mathbf{A}^\sigma$  is defined as following:

$$\bar{\sigma}^* = \mathbf{A}^\sigma : \bar{\sigma} \quad (4.22)$$

considering the split into tensile  $\sigma^+$  and compressive  $\sigma^-$  the mapping relations read:

$$\bar{\sigma}^{+*} = \mathbf{A}^{\sigma^+} : \bar{\sigma}^+ \quad \text{and} \quad \bar{\sigma}^{-*} = \mathbf{A}^{\sigma^-} : \bar{\sigma}^- \quad (4.23)$$

The transformation matrices  $\mathbf{A}^{\sigma^+}$  and  $\mathbf{A}^{\sigma^-}$ , which map from the actual orthotropic space and its actual limit strength to the mapped isotropic space. As the mapped isotropic space is a independent chosen space,  $f^{+*}$  and  $f^{-*}$  can be selected arbitrary, however, [180] suggests to use  $f^{\pm*} = f_1^\pm$  to simplify the transformation, which are defined by following matrices (see [172] for a detailed derivation of the constituents):

$$\mathbf{A}^{\sigma^+} = \begin{pmatrix} \frac{f^{+*}}{f_{t0,1}} & 0 & 0 \\ 0 & \frac{f^{+*}}{f_{t0,2}} & 0 \\ 0 & 0 & \frac{f_{t,12}^{+*}}{f_{t,12}} \end{pmatrix} \quad (4.24)$$

$$\mathbf{A}^{\sigma^-} = \begin{pmatrix} \frac{f^{-*}}{f_{cp,1}} & 0 & 0 \\ 0 & \frac{f^{-*}}{f_{cp,2}} & 0 \\ 0 & 0 & \frac{f_{12}^{-*}}{f_{c,12}} \end{pmatrix} \quad (4.25)$$

Additionally to  $f^{\pm*}$ , this model also requires  $f_{12}^{\pm*}$ , which shall impress the mapped space shear force, which itself is dependent on the isotropic mapping:  $f_{12}^{\pm*} = \frac{f^{+*}}{f_{t0,1}} f_{12}^\pm$ . Accordingly, the last entries of the mapping matrices shall devote the relation between the two shear strengths. <sup>a</sup> Considering equation 4.13, the stress split is still valid in the mapped isotropic space:

$$\bar{\sigma}^* = \bar{\sigma}^{+*} - \bar{\sigma}^{-*} \quad (4.26)$$

Proceeding, the uniaxial stresses can be computed with the mapped isotropic effective stresses by equations 4.15 and 4.16 and with those the damage parameters by equations 4.18 and 4.20. With the updated damage parameters the total stresses per loading are defined as following:

$$\sigma^{+*} = (1 - d^+) \bar{\sigma}^{+*} \quad \text{and} \quad \sigma^{-*} = (1 - d^-) \bar{\sigma}^{-*} \quad (4.27)$$

---

<sup>a</sup>[180] considers a Drucker-Prager damage surface, which itself modifies the threshold  $r_0^-$  with the biaxial strengths:  $r_0^{-*} = \frac{\sqrt{3}}{3}(k_b - \sqrt{2})f^{-*}$ . Whereby the Lubliner damage surface is reducing the uniaxial stress with the contribution of  $k_b$  (for definition see section 4.3.1). Accordingly, here the mapped shear forces are not affected, which makes the Lubliner surface simpler in the mapping between actual and mapped space and additionally maps the biaxial strengths correctly.

Those updated stresses are transformed back into the anisotropic space, where they yield with the appearing stress strain relation.

$$\boldsymbol{\sigma}^+ = \mathbf{A}^{\sigma^{+-1}} : \boldsymbol{\sigma}^{+*} \quad \text{and} \quad \boldsymbol{\sigma}^- = \mathbf{A}^{\sigma^{-1}} : \boldsymbol{\sigma}^{-*}. \quad (4.28)$$

In the actual anisotropic stress space, the stress split in total stresses is equivalent to the stress split with effective stresses, as per equation 4.13.

### Mapping of material properties:

The transformation towards a mapped isotropic stress state dependent on the chosen mapping limit strengths  $f^{\pm*}$  implies the dependency of the material lengths (see equation 4.19 for the computation of  $l_{mat}$ ):

$$l_{mat}^{\pm*} = l_{mat,1}^{\pm} = l_{mat,2}^{\pm} \quad \rightarrow \quad \frac{2E^*G_f^*}{f^{*2}} = \frac{2E_1G_{f,1}}{f_1^2} = \frac{2E_2G_{f,2}}{f_2^2} \quad (4.29)$$

this condition implies that the fracture energy in direction 1 and direction 2 is dependent upon following restriction:

$$G_{f,2}^{\pm} = \frac{(f_{22}^{\pm}/f_{11}^{\pm})^2}{E_2/E_1} G_{f,1}^{\pm} \quad (4.30)$$

To avoid this restriction, additional parameters will need a direction dependent mapping which is considering the angle to the main stress  $\theta$ <sup>b</sup>. The following equation can be used to interpolate the fractional energies:

$$\frac{1}{(l_{mat}^{\pm*})^2} = \frac{1}{(l_{mat,1}^{\pm})^2} \cos^2(\theta) + \frac{1}{(l_{mat,2}^{\pm})^2} \sin^2(\theta) \quad (4.32)$$

Similarly to  $f^{\pm*}$ ,  $E^*$  can be chosen arbitrarily, however it again simplifies the transformation operations significantly if it yields  $E^* = E_1$ , as otherwise this would imply an update of  $G_f^*$ , according to equation 4.29.

The tensile post crack behaviour is only dependent upon  $E$ ,  $G_t$  and  $f_{t0}$ , which are consistently mapped with equation 4.32. However, the applied compressive softening

<sup>b</sup>The angle to the main stress is being calculated as:

$$\theta = \begin{cases} \frac{1}{2} \arctan\left(\frac{2\tau_{12}}{\sigma_{11} - \sigma_{22}}\right) & \text{for } \sigma_{11} > \sigma_{22} \\ \frac{1}{2} \arctan\left(\frac{2\tau_{12}}{\sigma_{11} - \sigma_{22}}\right) + \frac{\pi}{2} & \text{for } \sigma_{11} \leq \sigma_{22} \end{cases} \quad (4.31)$$

is requiring additional parameters as  $f_{c0}$ ,  $f_{cr}$  and  $\epsilon_p$ . The stresses are within a direct interpolation of the mapped stresses accordingly:

$$f_{c0}^{-*} = \frac{f^{-*}}{f_{cp,1}^-} f_{c0,1}^- \cos^2(\theta) + \frac{f^{-*}}{f_{cp,2}^-} f_{c0,2}^- \sin^2(\theta) \quad (4.33)$$

$$f_{cr}^{-*} = \frac{f^{-*}}{f_{cp,1}^-} f_{cr,1}^- \cos^2(\theta) + \frac{f^{-*}}{f_{cp,2}^-} f_{cr,2}^- \sin^2(\theta) \quad (4.34)$$

The mapping of strain limit  $\epsilon_{cp}$  (see section 4.3.1 and appendix A) is mapped according to the reference states:

$$\hat{E}_1 = \frac{\sigma_{cp,1}}{\epsilon_{cp,1}} \quad \hat{E}^* = \frac{E^*}{E_1} \hat{E}_1 \quad (4.35)$$

$$\epsilon_{cp}^* = \frac{\epsilon_{cp,1}}{\frac{f^{-*}}{E^*}} \epsilon_{cp,1} \cos^2(\theta) + \frac{\epsilon_{cp,2}}{\frac{f^{-*}}{E^*}} \epsilon_{cp,2} \sin^2(\theta) \quad (4.36)$$

In the scenario that  $f^{-*} = f^{-1}$  and  $E^* = E^1$  follows that  $\frac{f^{-*}}{E^*} = \epsilon_{cp,1}$  and thusly equation 4.36 can be simplified to:

$$\epsilon_{cp}^* = \epsilon_{cp,1} \cos^2(\theta) + \frac{\frac{f^{-*}}{E^*}}{\frac{f^{-1}}{E^1}} \epsilon_{cp,2} \sin^2(\theta) \quad (4.37)$$

The Bézier-curve controllers (see appendix A) are mapped subsequently:

$$c_i^* = c_i \cos^2(\theta) + c_i \sin^2(\theta) \quad \text{for } i = 1, 2, 3. \quad (4.38)$$

## 4.4 Numerical discretization methods for masonry

Within this section a range of possible FEM discretization techniques for masonry are discussed. Secondly, the adoption towards different shapes and shape functions is outlined.

### 4.4.1 FEM approaches for masonry simulation

Throughout the recent years, various discretization techniques have been employed for the structural simulation of masonry. The most popular approaches are the classical FEM (linearized meshes), FE<sup>2</sup>, Discrete Element Method (DEM), among others. This can be discussed generally, independently of the considered scale. However, some methodologies are more suitable for certain scale considerations than others (see table 4.1). FEM is generally suitable to express each scale, while being very efficient for macro scale simulations by simulating the entire domain as a continuum. This can be

coped with constitutive models, such as the previously described one (see section 4.3). However, also the application of macro elements, such as e.g. springs can be seen as a macro scale simulation with FEM. Expression of micro scale mostly involves a combination of different continua (masonry and mortar) with contact elements in-between the constituents (e.g. see Lourenço et al.[139]). Meso scales models would incorporate the brick-mortar-brick with a contact formulation, while keeping the brick continuum (see Lourenço et al.[142] and Zhang et al. [255]).  $FE^2$  approaches compute the micro or meso scale behavior within the macro scale simulation. Thus, they can be seen as a combination between all scales. Finally, however, they express a certain macro scale. This means that typical micro scale phenomena, such as specific strain gaps are smeared throughout the macro model. In contrast, large deformations and complex contact behaviours at the interfaces makes the DEM a suitable numerical approach for meso-models [186, 187, 191], although material calibration and contact aspects are more sophisticated and sensitive in comparison to traditional continuum based finite element modelling approaches. In some scenarios, DEM may be employed as well for micro scale simulations. However, this can be computationally costly, while difficult to calibrate.

This research aims to facilitate simulations capable to express complex geometries and structures with justifiable computational costs with full scale buildings under consideration that the structural extend of the walls in two directions is comparatively large vs the third direction. Auxiliary elements and beams typically have increasingly challenges when modelling complex structures. Whereas, solid and particle based modeling allows almost infinite possibilities in the geometrical specification of constructions, typically the computational efforts prevent the application in structural analyses processes. Thus, within this chapter the focus shall be set on the description of surface based shell structures, which allow the expression of many geometrical shapes, under consideration of reasonable computation costs, as expressed within figure 1.1.

Within this contribution the analysis of masonry structures with CAD-integrated IGA shall be proposed, which poses within a similar range of applicability as FEM. It is capable to express the macro scale beneficially. However, due to the high order shape

scales	micro	simplified micro/ meso	macro
FEM	o	o	+
$FE^2$	-	-	+
DEM	o	+	-
IGA	-	-	+
MPM	-	-	o

-  $\hat{=}$  complex, with limitations; o  $\hat{=}$  possible, not optimal; +  $\hat{=}$  suitable

**Table 4.1:** Different FEM discretizations per scale.

functions and limited coupling facilities between the domains, modelling stress and specifically strain jumps between the materials is rather sophisticated, compared to the other methods. This makes the discretization less practical for micro and simplified micro/meso scale model approaches. However, considering shell-based simulations, IGA, fits greatly in the scope of masonry, while intrinsically enabling CAD-integrated analysis.

Within this work immersed methods for masonry have been reviewed (see section 3.6). Accordingly, an independent mesh or NURBS domain, which covers the entire structure would be considered. Within this, the constituents, namely brick, and mortar would be numerically embedded. The advantage would have been that one can adapt easily to varying patterns, or place irregular grids. However, it can be observed that the numerical estimated macro parameters from section 4.1 that rely entirely on the micro parameters, and the results of the experimentally tested macro parameters from section 4.2 vary significantly. This makes the approach of the immersed methods sophisticated, while already a certain correction would need to be applied to accurately represent the macro behaviour from the micro scale material parameters. Additionally, it evolved that the efforts of stabilizing the domains with varying stiffnesses are greater than its benefits. The respective regularization has to be employed per loading direction, which results in a complex procedure, while elements with high aspect ratios return questionable results. The consequence is that elements with multiple domains damage quicker than expected. The according result plots appear to be visually correct, however, the quantitative results are not reliable, due to the significantly faster release of the stiffness. Accordingly, the approach of embedding the different modulo of stiffness has not been considered further.

MPM was investigated to see if it was an appropriate approach for the apparent masonry structures (see section 3.7). This avenue was expected to provide more insights into damaging parts with larger deflections. While being a particle method, MPM still provides accurate continuum information for structural assessments. However, it turned out that MPM requires a lot of stabilization for being sufficiently reliable, due to e.g. cell crossing and numerical fracture. It shall be noted that this is not being considered a permanent limitation, but it requires additional investigations. Those are suggested for subsequent research.

Furthermore, masonry can be assessed within a multiphysics environment. Therefore, either different zones of the structure may be expressed by varying physics, while e.g. depending on if damages are expected or if not. This may resolve in a computationally accurate and highly efficient simulation. Alternatively, multiphysics can be used to express sophisticated boundary and load conditions, such as wind loads, shrinking foundations, or impacts. The according numerical fundamentals are provided within this dissertation in section 3.8. However, the focus is kept on the structural assessments

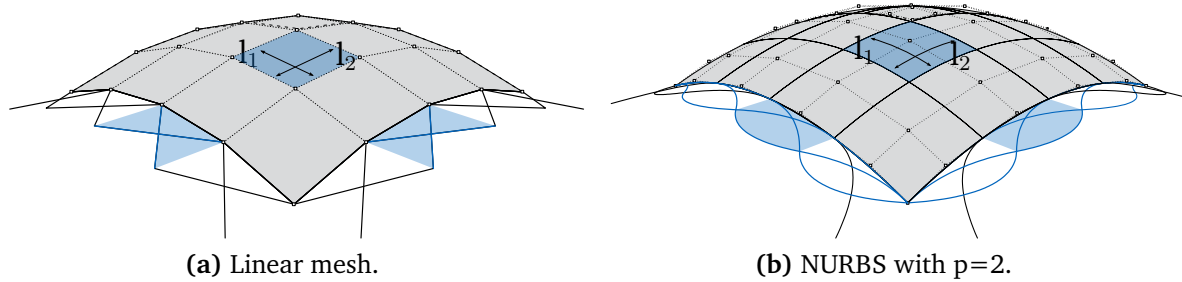


**Figure 4.33:** Regularization sizes.

and thusly the methods have not been employed further within the scope of masonry simulations.

#### 4.4.2 Stabilization to different shape descriptions <sup>f</sup>

From an implementation aspect, independent on the FEM discretization (FEM, IGA, or MPM), all integration points have a member of the constitutive law, containing all required historic variables, such as damage parameters. Considering a stress based formulation which contains multiple integration points in thickness, each thickness integration point carries its own representation of the model. In that way a consistent loading and damaging can be guaranteed.

In material modeling with local constitutive laws, the regularization by the element size plays a crucial role in the quantitative solutions. The regularization controls the amount of energy which is dissipated within a specific element (for further information about regularization see Bažant et al. [28]). The system is controlled by the characteristic length (see equation 4.19). Initial constitutive models for concrete and masonry have considered fixed mesh sizes and have employed scaling factors (see Scotta et al. [209] and Berto et al. [32]), which are directly dependent on the mesh sizes. While considering the length in the model, the aim to achieve a mesh in-dependency can be addressed. Perfectly formed quadrilaterals, with linear shape functions can be stabilized easily by considering the lengths of each side. However, element geometries with higher aspect ratios will always appear with a slight mesh dependency and will make simulations difficult.

Within IGA and NURBS, the specific element, or characteristic length extensions are typically not determined perfectly. Therefore, a good representation may be a knot span (see figure 4.33). However, with higher polynomial degrees than  $p=1$ , the respective influence zone is non-local and thus the characteristic length is becoming larger (refer to the blue-marked shape functions in figure 4.33b). It shall be mentioned that this is up-to

date an open research question. However, an empirical estimation of the characteristic length for varying polynomial degrees is presented within appendix B.

The characteristic length is estimated at each integration point. Furthermore, it is dependent on the mean stress direction, which becomes significant while aspect ratios are unequal to 1. Within the orthotropic mapping, the material length is computed per direction and mapped accordingly. This form already contains the relevant geometrical length in the stress direction dependent mapping. The examples from section 5.4 and from section 5.6 show cases of mesh refinement, while the results seem stabilized significantly.

## 5 Examples and Investigations <sup>e</sup> and <sup>f</sup>

Consequently are discussed some of the previously introduced numerical approaches from section 3 in combination with the constitutive model and material parameters from the masonry study from section 4.

Primarily, in-plane problems are discussed. The directional properties from the uniaxial tests as per section 4 shall be examined by the introduced constitutive material model. Consequently, the behaviour of the shear wall tests from [241] with varying pre-compression and different geometrical shapes (full and with window) shall be examined. This example includes most of the dominant in-plane characteristics and failure modes of masonry.

Consequently, out-of-plane studies are processed. Initially, air-bag loaded masonry walls (experimentally tested by [94]) are presented. Those reflect geometrically structural members of most masonry buildings. The study is proceeded by more complex shapes. Therefore, a circular arch (experimentally tested by [240] and [147]) is tested under asymmetric and symmetric loading until failure. Consequently, a masonry cross vault, tested by [81] is examined numerically.

Finally, predictive studies are presented with a masonry church roof and a masonry building. It shall give a presentation of the possibilities of the introduced approaches within more complex problems. Subsequently, a numerical study with a masonry building is presented. Hereby, the focus is put on the presentation of the parametric CAD-integrated workflow.

### 5.1 Uniaxial numerical tests of *Brisbane* masonry

In this study, the uniaxial behaviours within both directions shall be examined with the apparent material model, including a perspective to the damage growth. This is conducted to prove that the orthotropic mapping is working properly, with a focus on the variated strengths within compression and tension. Within figure 5.1 are summarized the material properties, with the additional Bézier curve parameters, as per appendix A. The corresponding numerical test setup is shown within figure 5.2, defining

## 5 Examples and Investigations

Elastic and tension properties:

$E$ [MPa]	$\nu$ [-]	$G$ [MPa]	$G_t$ [N/mm]	$f_{t0}$ [MPa]
5000	0.0	1340	$1.5 \times 10^{-3}$	0.091
3100	0.0	960	$4.5 \times 10^{-3}$	0.272

Compression properties:

$G_c$ [N/mm]	$f_{c0}$ [MPa]	$f_{cp}$ [MPa]	$\epsilon_r$ [-]	$f_{cr}$ [MPa]
1.2	5.2	7.38	0.0018	1.3
1.1	2.9	4.05	0.002	0.0

Bézier curve parameters:

$c_1$ [-]	$c_2$ [-]	$c_3$ [-]
0.65	0.8	1.2
0.65	0.5	1.5

**Figure 5.1:** Summary of masonry material properties from experimental tests as per section 4, including the required specific constitutive model parameters.

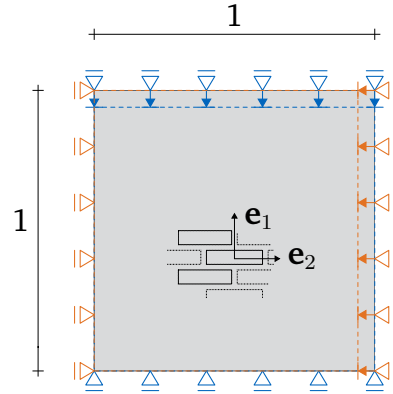
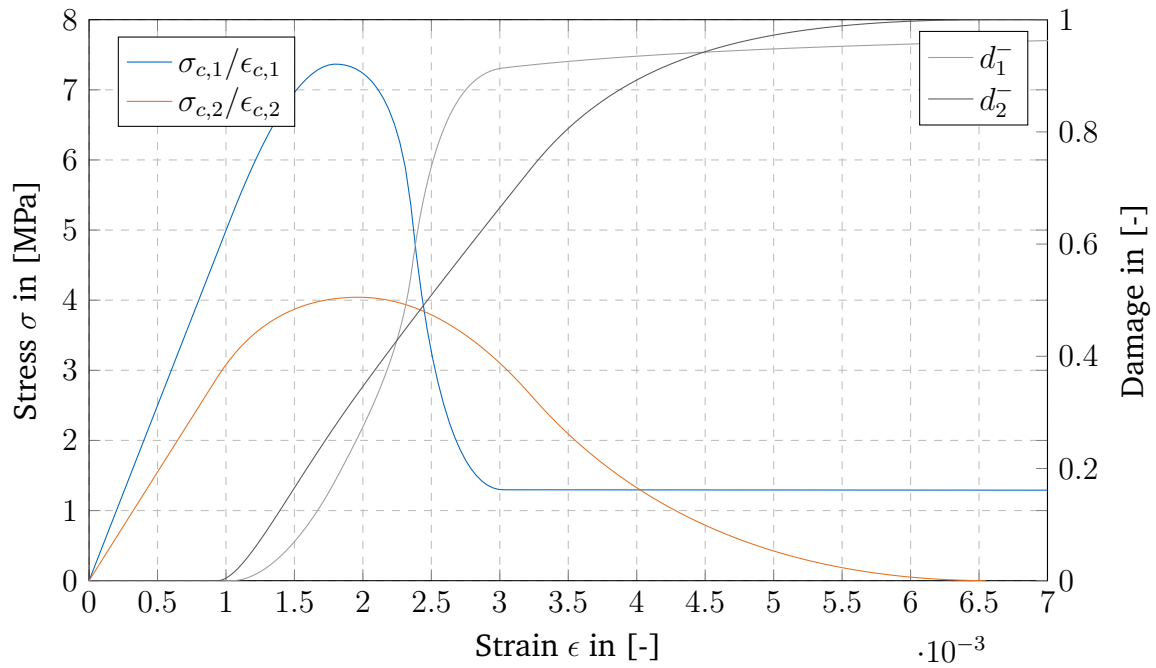


**Figure 5.2:** Numerical test setup within both directions.

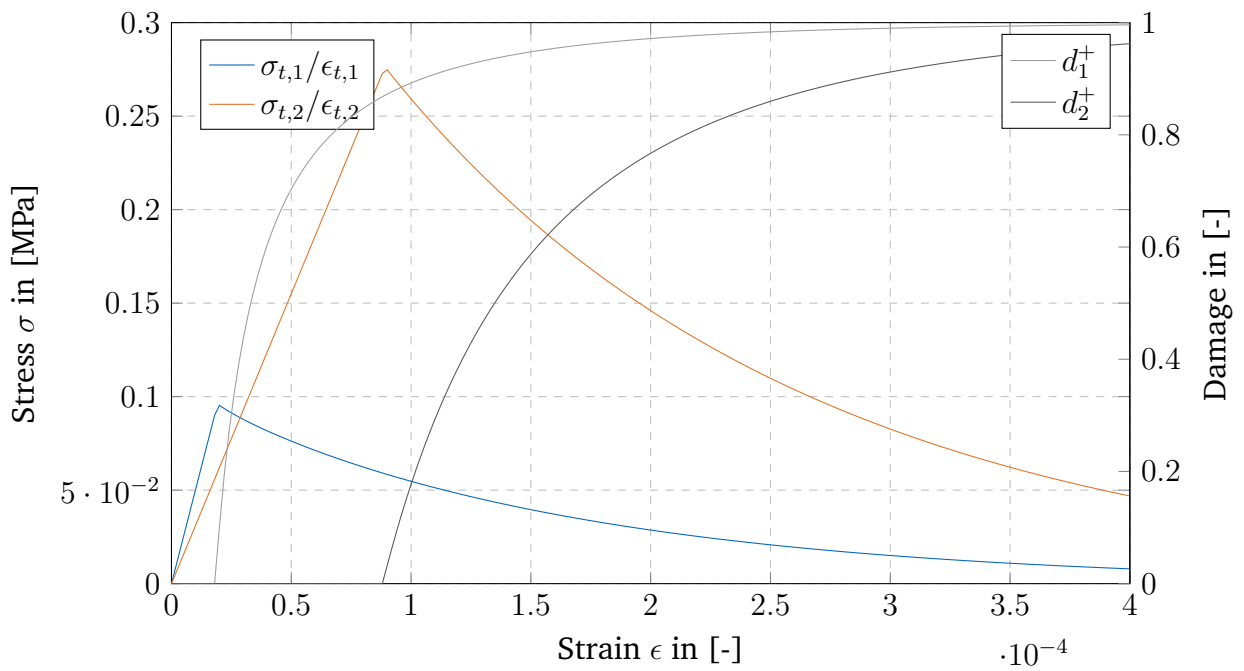
the parameter direction and the distinct tests, which are displayed in compression direction.

The obtained results for compression and tension are presented within figure 5.3. It shows that both directions can be expressed appropriately and that all control parameters are mapped consistently between the apparent spaces. The additionally presented damage growth shall communicate the reader an impression of how the material model is operating.

## 5.1 Uniaxial numerical tests of *Brisbane* masonry



(a) Compressive damage.



(b) Tensile damage.

**Figure 5.3:** Stress-strain relation of compression and tension tests in two directions and according damage parameter growth for the apparent properties of section 4.

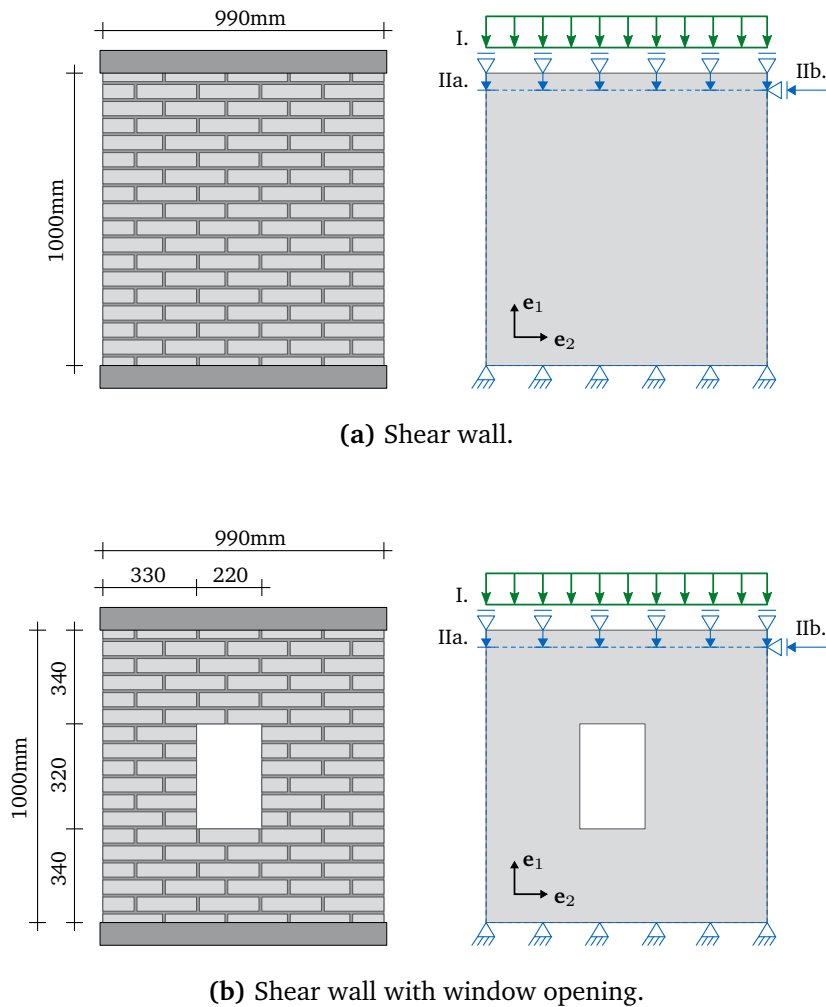


**Figure 5.4:** [241] shear walls. The experimental program is split into 2 phases, the pre-compression and the fixing at this deflection and shearing.

## 5.2 Shear wall

This study considers a masonry wall which is first subjected to a vertical load (I.) at different magnitudes. In a second step it is fixed vertically at this deformation (IIa.) and sheared horizontally (IIb.). Geometrically this problem appears within two different variations: once as a whole wall (see figure 5.4a) and once with a window opening (see figure 5.4b). Both walls have a dimension of 1x0.99m.

This example is well known in literature, among others shall be mentioned:

- Lourenço [139]: Micro and macro models

Elastic, tension, biaxial, and shear parameters:

$E$ [MPa]	$\nu$ [-]	$G$ [MPa]	$f_{t0}$ [MPa]	$G_t$ [N/mm]	$k_b$ [-]	$k_1$ [-]	$\frac{f_{t,12}}{f_{t,21}}$ [-]	$\frac{f_{c,12}}{f_{c,21}}$ [-]
${}^t7520$	${}^{s,[141]}0.09$	${}^t1460$	${}^t0.30$	${}^t5e \times 10^{-3}$	${}^s1.2$	${}^s0.16$	${}^s1$	${}^s1$
${}^t3960$	${}^{s,[179]}0.05$	${}^t1460$	${}^{s,[179]}0.25$	${}^{s,[179]}4.8 \times 10^{-3}$	${}^s1.2$	${}^s0.16$	${}^s1$	${}^s1$

Compression and Bézier curve parameters:

$f_{c0}$ [MPa]	$f_{cp}$ [MPa]	$\epsilon_r$ [-]	$f_{cr}$ [MPa]	$G_c$ [N/mm]	$c_1$ [-]	$c_2$ [-]	$c_3$ [-]
${}^s6.8$	${}^t10$	${}^s0.002$	${}^s2.3$	${}^s2.0$	${}^s0.65$	${}^s0.5$	${}^s1.5$
${}^s5.2$	${}^t8.8$	${}^s0.002$	${}^s3.0$	${}^s1.96$	${}^s0.65$	${}^s0.5$	${}^s1.5$

**Table 5.1:** Masonry material properties from experimental tests [241] or evaluated and introduced within [141, 179, 87].

- Lourenço et al. [142]: Meta models
- Pela et al. [179]: orthotropic mapping damage model
- Petracca et al. [183]: FE<sup>2</sup> model
- Fu et al. [87]: orthotropic plastic damage model
- Abdulla et al. [2]: simplified micro model

Due to the high amount of references, the example delivers great possibilities for comparisons and thus, it appears as a good benchmark. Most of the in-plane masonry phenomena are apparent: significant orthotropic material, shear failure and biaxial stiffness effects. This helps to justify if the model is suitable to express the major in-plane masonry characteristics.

It shall be noted that the apparent literature, typically focuses on either of the geometrical options: full wall or wall with window. This shows that covering this example entirely remains challenging.

The material properties of the tests are summarized in table 5.1. Some of the macro scale parameters are known directly from test data  ${}^t(\cdot)$  by [241], some are obtained by micro scale analyses from [139], whereas some are obtained by speculation  ${}^s(\cdot)$  and reverse engineering, from either author or completed with the apparent requirements. It must be noted that some speculated values are varying throughout distinct publications as the applied models slightly adjust and apply parameters in a different manner. Unfortunately, not sufficient experimental data is available to mechanically justify either of the selected parameters. Additionally, various parameter sets could be valid for the apparent model. As a further challenge shall be noted that the material parameters seem to vary significantly between various tests. However, within this numerical study only one parameter set shall be considered. This may show larger discrepancies compared to some test results, but should be a step towards a homogenization which would allow predictions and not purely a result fitting by calibration.

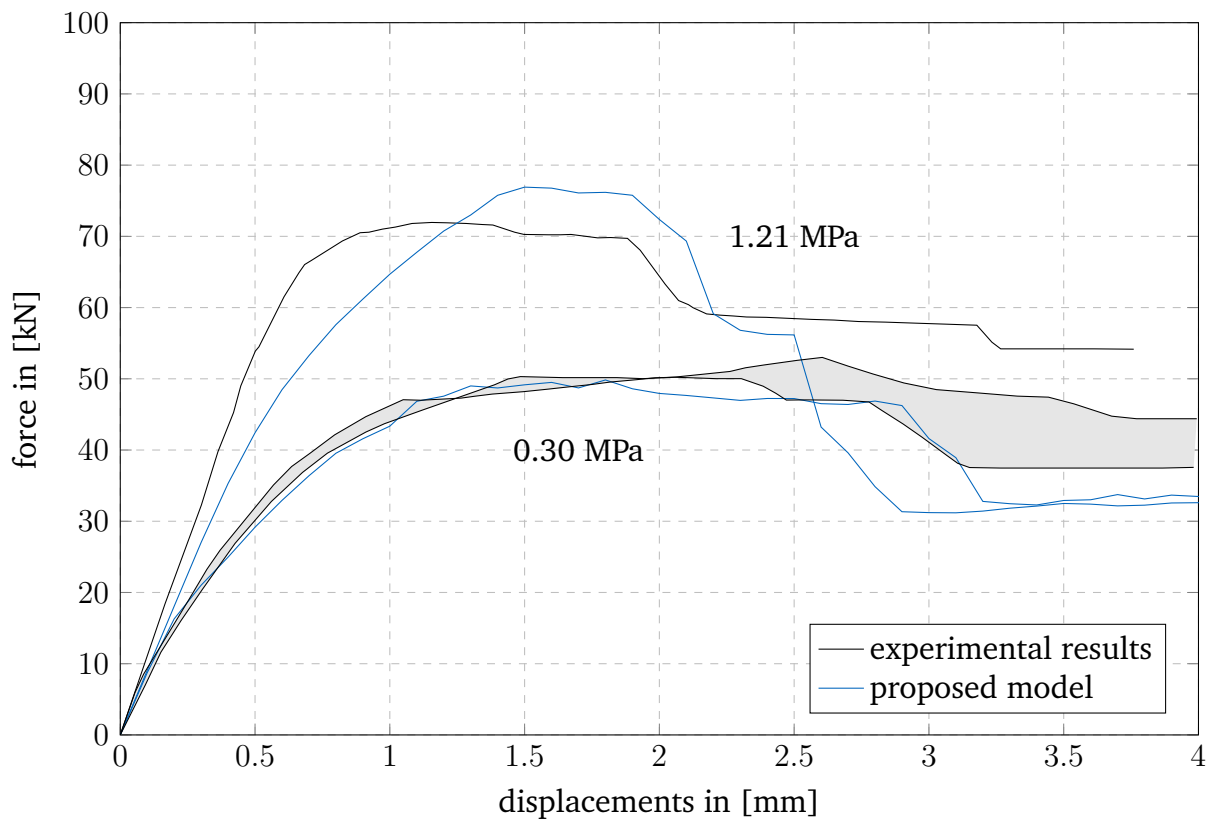


**Figure 5.5:** Shear wall from [241]. Computed with  $p=1$  and  $50 \times 50$  elements.

### 5.2.1 Wall with varying pre-pressure

The initial example is considering the wall without window, as per figure 5.4a. The experiments are analyzed with 2 different pre-compression loadings: 0.3MPa and 1.21MPa. As per Vermeltfoort et al. [241] the pre-loading with 0.3MPa appears in 2 repeated experimental tests. It is an important numerical study as it investigates the capability of expressing varying biaxial strengths of a material.

The stress strain relations of this example are presented within figure 5.5. The strengths of the 0.3MPa pre-loading examples are expressed greatly. However, the remaining tests are slightly underestimated. The 1.21MPa experimental test denotes that already significant different material properties are apparent as the elastic zone appears already stiffer than within the other examples. In both test setups, the softening of the specimen seems to be faster and more significant in the numerical tests than in the experimental tests. The results of the experimental study shows that the overall material behaviour can be estimated correctly. With an increased pre-loading the maximum resistance increases. The tendencies of the response of the numerical model appears to be cor-

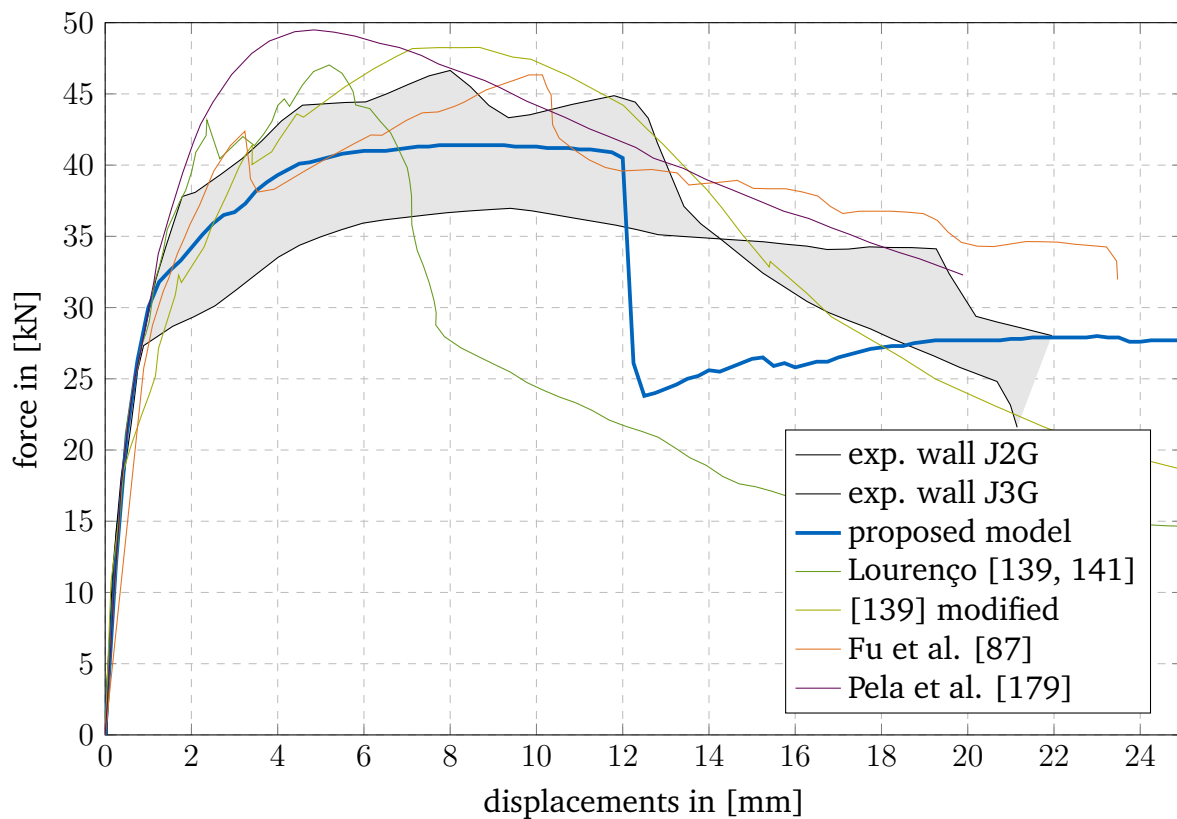


**Figure 5.6:** Shear wall from [241] with window. Computed with  $p=1$  and  $50 \times 50$  elements.

rect, while at the same time overestimating the final strength slightly for the larger pre-compression.

### 5.2.2 Wall with window opening

The second example deals with the same wall dimensions as the previous specimen, while having a window opening with the extensions of  $320 \times 220$  mm (see figure 5.4b). With this example shall be investigated if the model is capable to deal with different shapes. The same material parameters are considered.

The stress-strain relation of the problem is shown within figure 5.6. The results are compared to the experimental data, and the solutions of other literature [141, 179, 87]. The softening curve of the proposed model shows good agreement between both test results. The initial damaging is covered in a suitable manner, however, the first significant damaging and softening appears to be overestimated by this model.

In comparison to the other tests, it notes that either of the models has difficulties in expressing some parts. The micro model of Lourenço et al. [139] matches the behaviour greatly, however, shows a significant early softening. This test has applied the material parameters as known from experimental studies, with few additional estimations. Within, [139]-*modified*, the material parameters have been calibrated to obtain a better match with the softening of *Wall J2G*. The 2 macro models from Pelà et al. [179] and Fu et al. [87] show a good agreement with the test results, mostly with *Wall J2G*. However, both models rely as well on speculated input parameters, whereby some are in a disagreement with the other literature.

Within figure 5.7 are shown the respective displacements, once in reference to the aimed current displacements and once with respect to the total displacements. Furthermore are provided the von Mises stresses and the tensile damage of the digital model. The evolving damage-results from figure 5.7 denote a crack initiation at the corners of the windows that are opening towards the supports of the walls amid increasing displacements. At the top left and basal right part of the specimen is shown a damage which is not displayed within the referenced crack pattern. This is showing a separation of the specimen from the concrete top and bottom bars, which can also be observed within the experimental results. Furthermore, in the damage patterns can be seen that in both, the experimental tests and the numerical model, a crack happens in the left upper third and right bottom third. This proves quite effectively that a certain trust can be given to the macroscopic models and that not only micro models would display this local phenomena. Finally, the cracks which initiate at the corners of the windows do not go towards the corners of the specimen, but towards a close point at top or bottom. The reason of this is that most of the forces, which are supplied from top to bottom go through the parts left and right of the window. Accordingly those areas are under compression and thusly do not fail by tensile forces. This explanation can be supported by the plots of the von Mises stresses.

The tensile damage indicates good agreement with the reference solutions, see figure 5.8, which displays the test results within the solutions from the numerical experiment at a displacement of 20mm. It shows thin crack lines where only single cracks appear (top third left and bottom third right). At the zones of multiple crack lines, the model shows damage zones instead of thin cracks (corners of the window towards the boundaries of the specimen).

Within the von Mises plots can be observed that the numerical model develops a stress distribution, where most of the energy distributes around the window. The areas of the cracks do not carry any load and split the masonry wall into some structural pieces. This is a significant result of such a damage analysis, as the force rearrangement might give suggestions about remaining resistances of a damaged structure. Additionally, it may indicate that other parts of the remaining undamaged structure or supports might get high stresses, which could lead towards a failure of connected parts or supports.

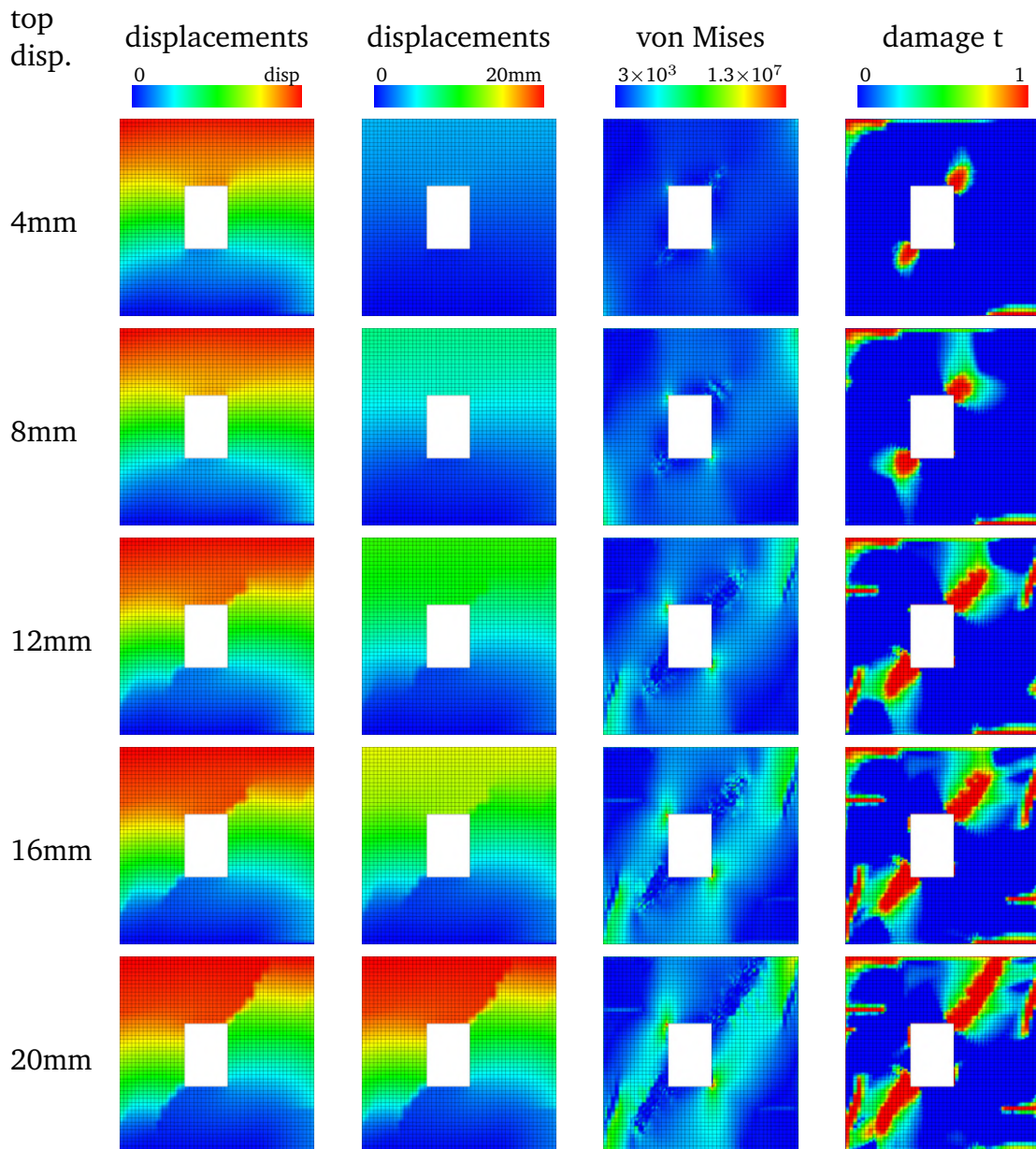


**Figure 5.7:** Observed damage at [241]-wall tests with varying polynomial degrees of the background shape descriptions. Computed with  $50 \times 50$  elements and a polynomial degree of  $p=1$ .

This would be undetected in geometrically non-linear analyses which only considers the limit stresses.

Finally, the observed displacements show that the expected separation into two main pieces, with some additional local failures is happening. After a final crack opening those pieces would mostly have a rigid body movement with a remaining sliding resistance.

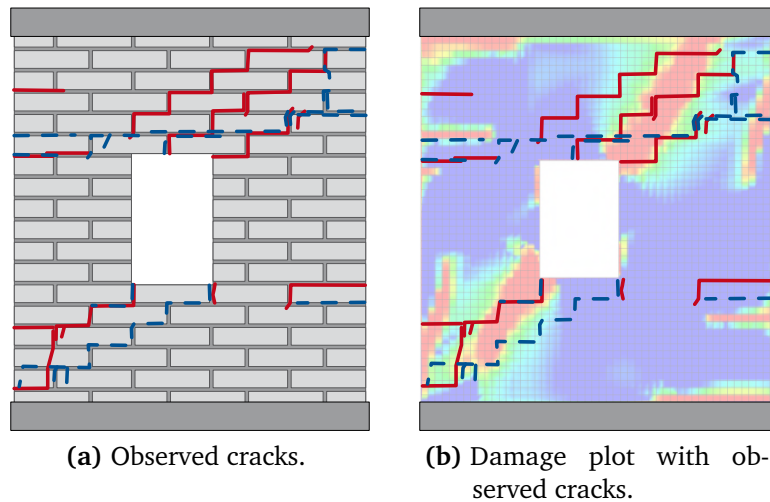


**Figure 5.8:** Observed damage at experimental tests of [241]-wall with window in comparison to the numerical solutions. The red lines mark the cracks from the first experimental test, blue from the second.

One of the dominant properties of IGA is that NURBS habitually come along with higher order shape functions. The damage regularization within those has been arisen as a significant challenge as shown in appendix A. Accordingly, this test case shall be studied additionally with a varying order of shape function. Figure 5.9 shows the damage zones with an evolving top displacement for background shape functions of polynomial degrees of  $p=1$ ,  $p=2$  and  $p=3$ . The 3 examples have been evaluated with  $30 \times 30$  elements, namely knot spans in the context of IGA. The regularization achieves to align the stress-strain relation. However, within the simulated damage patterns can be observed a significant difference. Within higher order shape functions, the crack opening would directly influence neighboring elements and the damage zones would thusly appear much thicker. The cracks, which appear at the top third left and bottom third right show effectively that for the order of  $p=1$ , only one element would show a damage. The higher the polynomial degrees becomes, the more neighboring elements would be involved in the crack opening. This effect is driven by the non-locality of the basis functions. Furthermore, the high order shape function do appear to have increasing problems around the corners of the window. Thin cracks would be expected in those zones, however, it appears as rather large and thick damage areas. However, multiple reasons may thrive this. First, it shall be noted that in the experimental crack pattern not a single line, but multiple crack lines spread from the window to the bottom of the specimen. Second, a fracture that is distributed diagonally cannot be supported perfectly by the aligned knot span mesh of the NURBS. As a result, cracks always have a zone that is certainly thicker. This is a permanent consequence of using NURBS

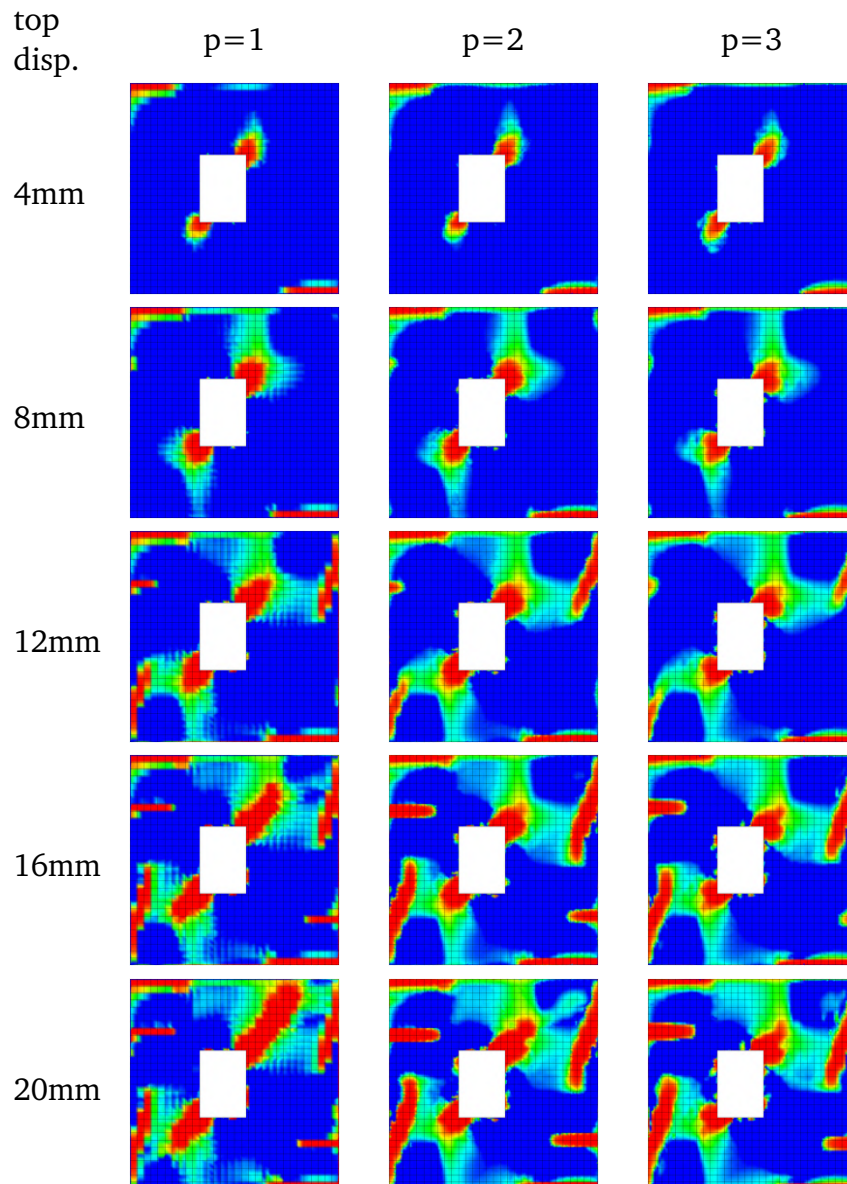


**Figure 5.9:** Observed damage at [241]-wall with window tests with varying polynomial degrees of the background shape descriptions. Computed with 30x30 knot spans. The color plot is ranging from no damage: 0 (blue) to fully damaged: 1 (red).

because of its tensor product-like characteristic, which might result in mistakes in certain circumstances.

As for most numerical simulations, apart from the polynomial degree the number and size of applied elements denote important parameters in the accurateness of the models. Accordingly, a mesh refinement study is presented within figure 5.10 for  $p=1$  and

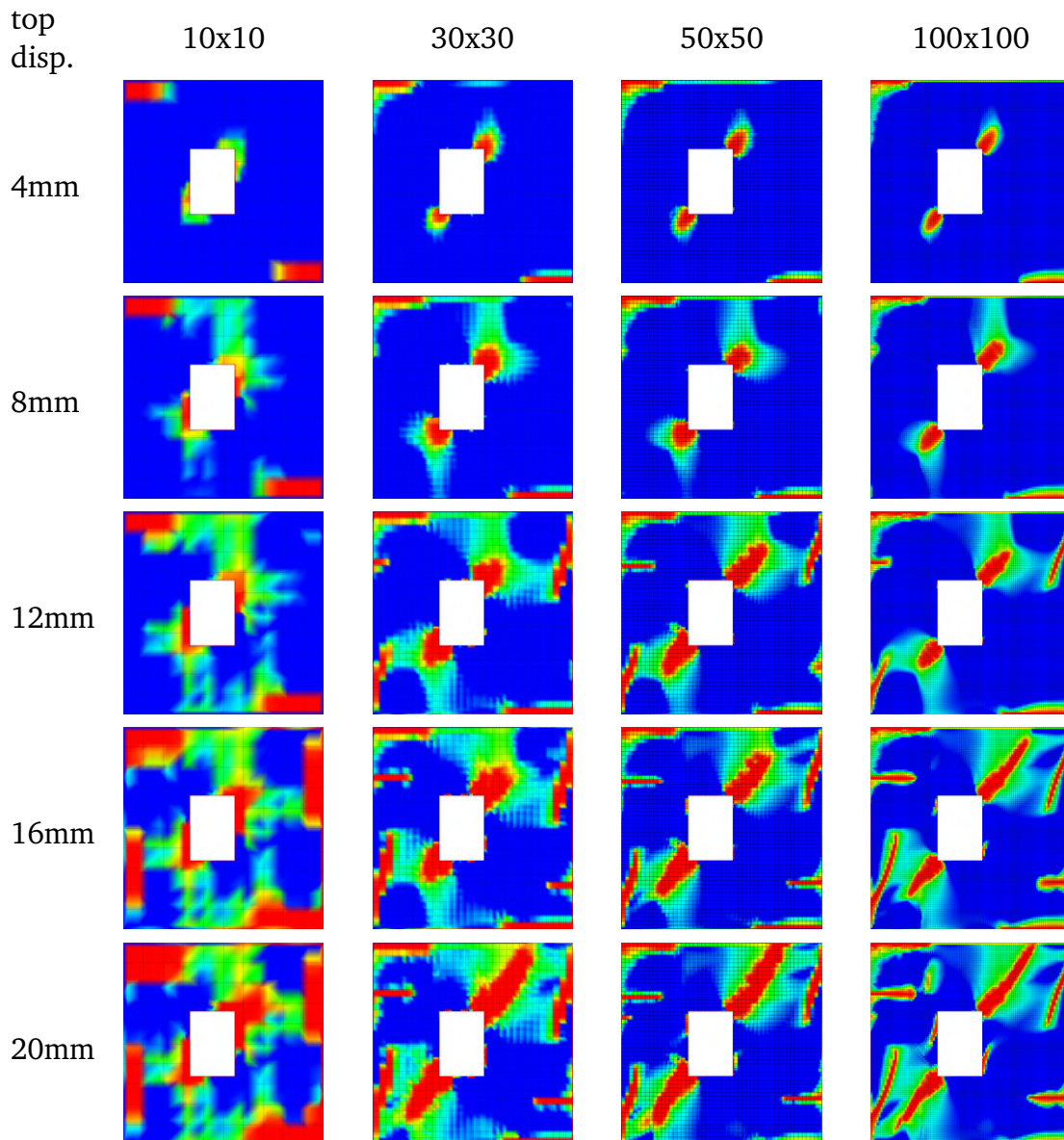


**Figure 5.10:** Observed damage at [241]-wall with window tests with varying a polynomial degree  $p=1$  and mesh refinement from 10x10, towards 100x100 knot spans.

within figure 5.11 for  $p=2$ . With increased refinement the appearing crack zones shrink, which is towards the expectations as the cracks are actually not zones but thin lines. Additionally, certain cracks cannot be displayed in the coarse mesh as e.g. in the 10x10 mesh the middle cracks on both edges are not apparent.

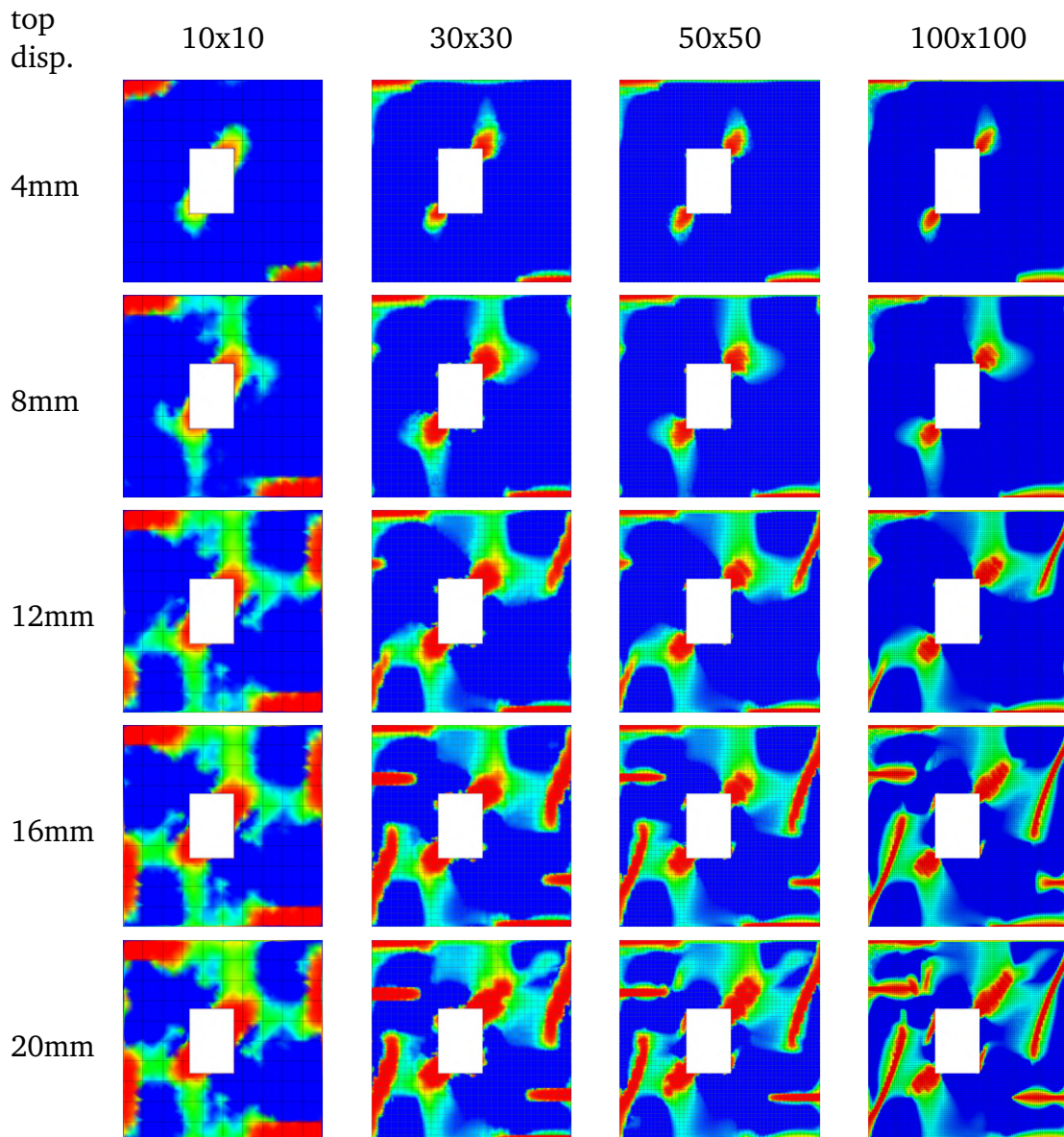


**Figure 5.11:** Observed damage at [241]-wall with window tests with varying a polynomial degree  $p=2$  and mesh refinement from 10x10, towards 100x100 knot spans.

### 5.2.3 Discussion of results and methodology

A simplified typical shear behaviour of masonry is outlined in figure 5.12. After the elastic zone, the resistance of the structures is mainly influenced by the tensile strength, which is benefited by the biaxial loading, whereby the experimental results are giving evidence about this part. After full delamination of the constituents, the wall is carrying loads only through the shear resistance between separated pieces. The experimental

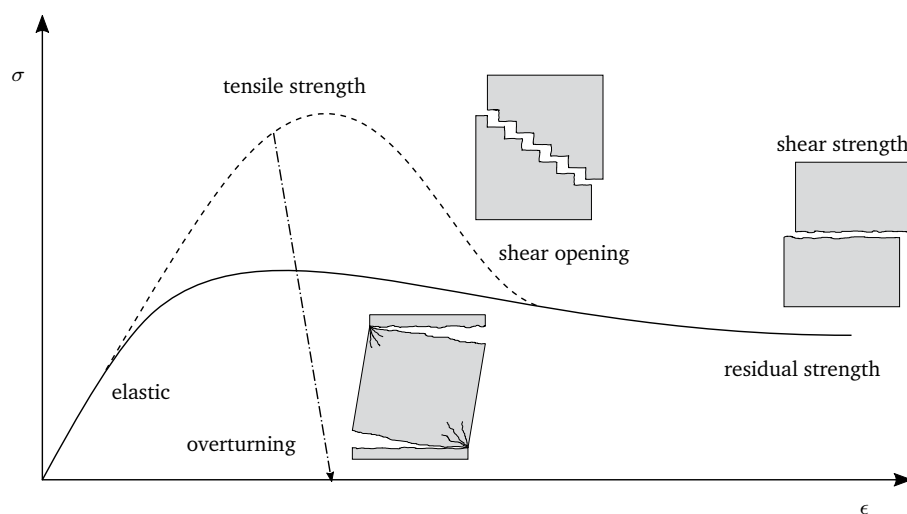


**Figure 5.12:** Simplified typical behaviour of masonry walls subjected to shear.

results show that the described effects are significantly apparent and can be represented by the proposed numerical counterpart. The elastic part is mainly sensitive to the shear modulus  $G_{12}$ , whereby the post elastic part is being controlled by the tensile strengths, the factor  $k_1$  and the biaxial multiplier  $k_b$ . The latter is specifically relevant if pre-load is supplied to the system.

One of the major improvements of the proposed model is the capability to cover the biaxial stress states and the resulting internal forces in an orthotropic manner, which allows the analysis of masonry in different pre-loading scenarios. Furthermore, the model has a large bandwidth of possibilities to trigger the stress strain behaviour, which brings stability within the simulation if the material response is known. As contrast, comparatively many parameters need to be obtained, which is up-to date infrequent, as typically only few parameters are studied within a series of experimental tests. Thus, it has to be noted that a large amount of material properties needed to speculated as not sufficient test data was provided. Seeing the performance of the constitutive law within a fully comprehensive test setup would be required to specify the generality of the model.

It can be noted that the suggested developments of this research enable the use of masonry simulations with NURBS. This has a significant advantage in CAD-integrated simulations where the user has little control over the polynomial degree that is provided. However, for fast and accurate simulations lower polynomial degrees do typically provide better results.

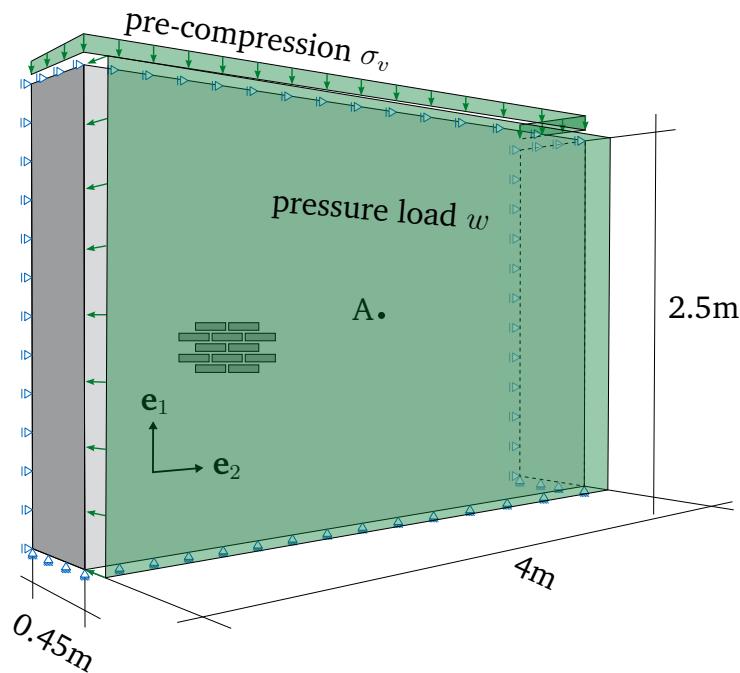


Figure 5.13: Dimensions of masonry wall from Griffith et al. [94].

### 5.3 Out-of-plane strength of unreinforced masonry wall

To better understand the behaviour of unreinforced masonry walls by earthquake loading, Griffith et al. [94] have tested a series of masonry walls subjected to out-of-plane loads by the application of air bags. The study has later been enhanced to cover the cyclic response of similar walls [95]. Additionally, comparable walls have been tested within a shaketable setup to assess seismic responses [236]. However, cyclic and seismic effects shall not be considered within the presented numerical study.

An analytical macro element model to assess the out-of-plane load-displacement relations has been proposed by the authors of the tests within [235]. The model provides, mechanically proven insights in the limit strengths and the failure modes of two-way spanned masonry walls.

Structurally, the experimental study covers a range of masonry phenomena, such as bending, limit stresses and failure modes. Accordingly, it has gained the attention of some researchers in the development of numerical models:

- Petracca et al. [182]:  $FE^2$  multiscale model
- Abdulla et al. [2]: simplified micro model
- Noor-E-Khuda et al. [166]: explicit macro model
- Noor-E-Khuda et al. [165]: explicit macro model with continuum shell elements

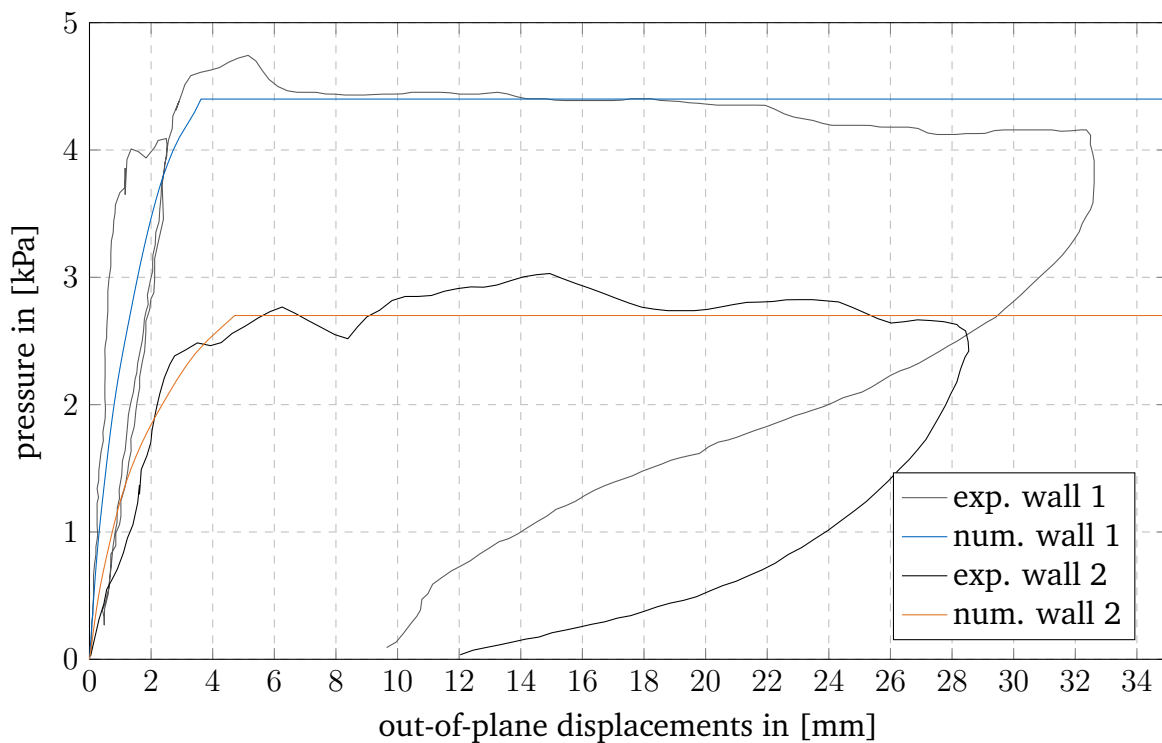


**Figure 5.14:** Out-of-plane displacements at point A (see figure 5.13).

The problem description can be found in figure 5.13. The wall is supported by two wall sections that should resemble a clamping. Within the simulations, these supports will be treated as independent patches connected by a geometric  $G1$  continuity at a  $90^\circ$  angle. Thus, in total 3 untrimmed patches are considered for the analyses. Within this study, two configurations are tested: once with a vertical pre-compression of  $\sigma_v = 0.1\text{MPa}$  (wall 1) and once without pre-compression (wall 2). It needs to be noted that, as per Griffith et al. [94], both tests have employed significantly different masonry properties ( $E_{wall1} = 3188\text{MPa}$  vs.  $E_{wall2} = 2240\text{MPa}$ ). Material properties of both tests are presented within tables 5.2 and 5.3. Accordingly, a quantitative structural comparison cannot be processed. However, the varying failure modes shall be discussed.

The experimental and corresponding numerical results are presented within figure 5.14. The numerical simulations match the experimental result. As the numerical analyses are run in load control, the respective load decrease is not covered and analyses stop at failure states.

Within figure 5.15a and 5.15b are displayed the experimental failure patterns. Both patterns show significant diagonal cracking. However, the non-compressed wall 2 exhibits additionally a horizontal crack band at the center of the specimen. This is driven due to the lack of lateral pre-compression. The crack is separating the specimen into 2 main pieces. The same phenomena can also be observed within the numerical damage

## 5.3 Out-of-plane strength of unreinforced masonry wall

Elastic and tension properties:

$E$ [MPa]	$\nu$ [-]	$G$ [MPa]	$G_t$ [N/mm]	$f_{t0}$ [MPa]
3200	0.05	1600	$7 \times 10^{-3}$	0.07
2200	0.05	1600	$20 \times 10^{-3}$	0.2

Compression properties:

$G_c$ [N/mm]	$f_{c0}$ [MPa]	$f_{cp}$ [MPa]	$\epsilon_r$ [-]	$f_{cr}$ [MPa]
2	8.0	13.5	0.003	3.0
2	8.0	13.5	0.003	3.0

Bézier curve parameters:

$c_1$ [-]	$c_2$ [-]	$c_3$ [-]
0.65	0.5	1.5
0.65	0.5	1.5

**Table 5.2:** Wall 1.

Elastic and tension properties:

$E$ [MPa]	$\nu$ [-]	$G$ [MPa]	$G_t$ [N/mm]	$f_{t0}$ [MPa]
2240	0.05	1000	$10 \times 10^{-3}$	0.05
1600	0.05	1000	$6.5 \times 10^{-3}$	0.15

Compression properties:

$G_c$ [N/mm]	$f_{c0}$ [MPa]	$f_{cp}$ [MPa]	$\epsilon_r$ [-]	$f_{cr}$ [MPa]
2	8.0	13.5	0.003	3.0
2	8.0	13.5	0.003	3.0

Bézier curve parameters:

$c_1$ [-]	$c_2$ [-]	$c_3$ [-]
0.65	0.5	1.5
0.65	0.5	1.5

**Table 5.3:** Wall 2.

patterns, which are compared within figures 5.15c and 5.15a. It can be noted that the major failure in wall 2 is the horizontal crack, whereby wall 1 experiences the diagonal cracking stronger.

It can be noted that the diagonal cracking is displayed thin within the numerical analyses. However, the diagonal cracks are significant large zones. Part of the argumentation are the higher order shape functions of  $p=2$ . Additionally, the structured grid carries a strong mesh dependency.

### 5.3.1 Variation of pre-compression

The previous tests have already intended to study various pre-compression scenarios. However, due to the varying stiffnesses it is not possible to dictate a precise relation. Thus, a study has been operated which studies numerically the relation between the final strength under the variation of pre-compression. For this test hypothetical material properties are considered.

The stress strain relations of the varying tests are presented within figure 5.16. One major observable characteristic is, that tests with a small pre-compression exhibit a more ductile damaging until failure. Tests with a high pre-compression seem to act elastically until a brittle failure.

All failure loads are compared to pre-compression, including corresponding displacements at failure and presented within figure 5.17. It denotes that the maximal out-of-plane load capacity for this example is in the range of 0.25-2MPa, while higher and lower pre-compression loads lead to an earlier failure.

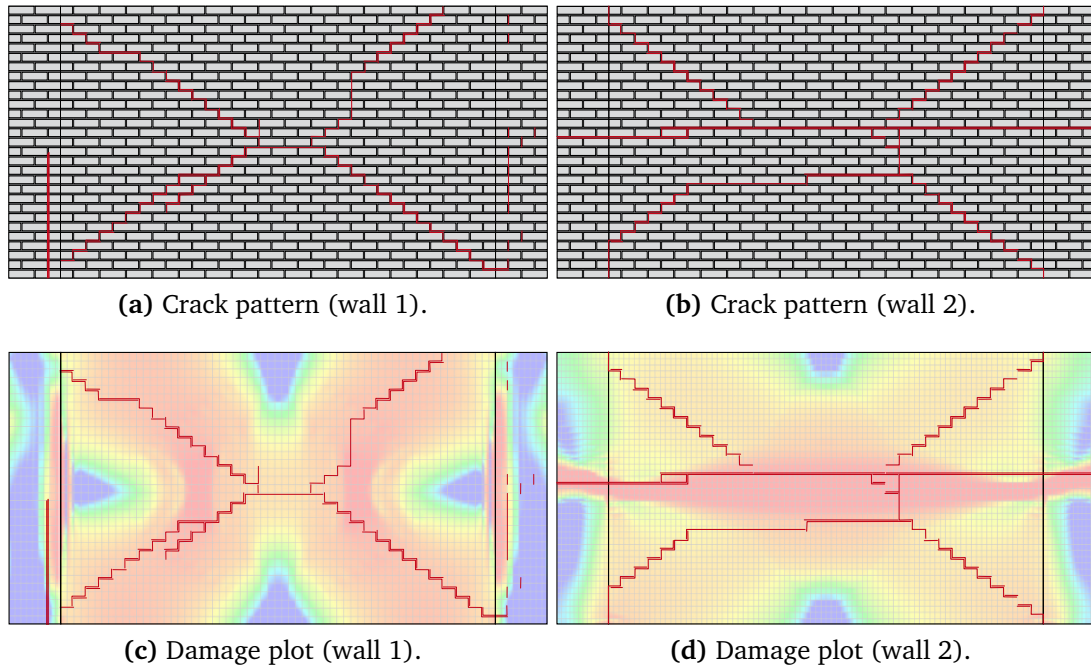


Figure 5.15: Damage patterns.

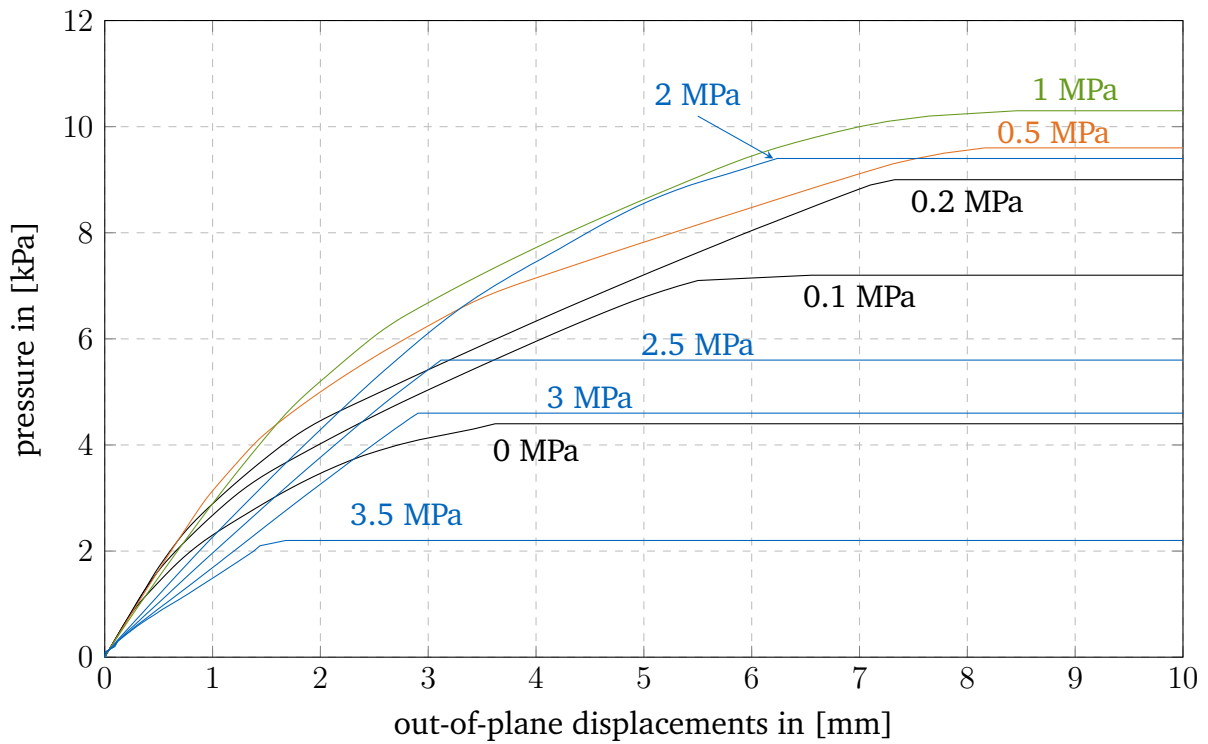
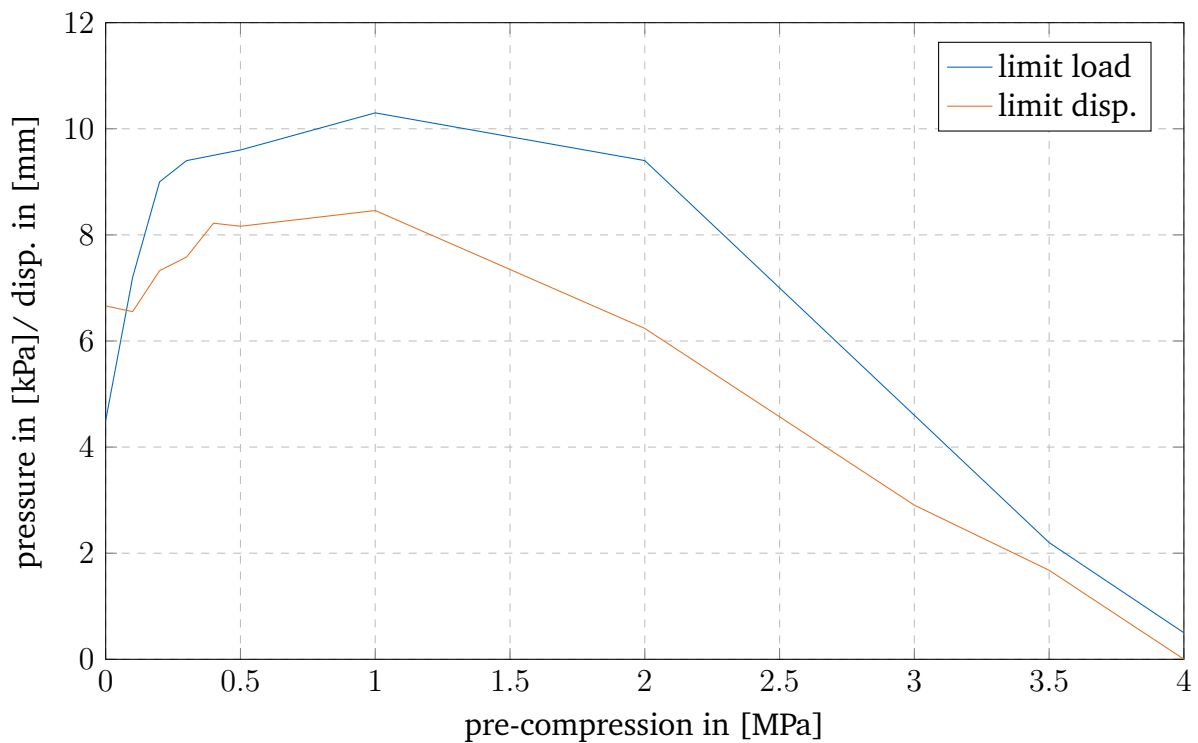


Figure 5.16: Out-of-plane displacements at point A (see figure 5.13) with varying pre-compression.



**Figure 5.17:** Limit states at point A (see figure 5.13) with varying pre-compression.

Additionally, shall be discussed the progressing failure patterns. Within figure 5.18 are presented some of the damage plots shortly before failure of the structures. It can be seen that initially, the failure pattern is exhibiting the horizontal crack, while higher pre-compressions show the diagonal crack patterns.

### 5.3.2 Discussion of results and methodology

The numerical test have been processed with pure load-control. To better estimate the relaxation of the post crack zone, alternatives would be required, such as the arc-length approach. The goal of this study was to calculate accurate loading toward failure and failure loads. Load control can sufficiently express this.

The numerical results are mostly studied at the center point of the specimen (point A, figure 5.13). This may be accurate for many scenarios. However, calibrating the model to fit this behaviour is many times facilitated. It would be important to have multiple test points within the specimen to check if the shell behaviour is sufficient to accurately express the complex behaviour of the masonry walls. The model can be calibrated to fit either shell theory, Reissner-Mindlin or Kirchhoff-Love. Thus, with the limited provided

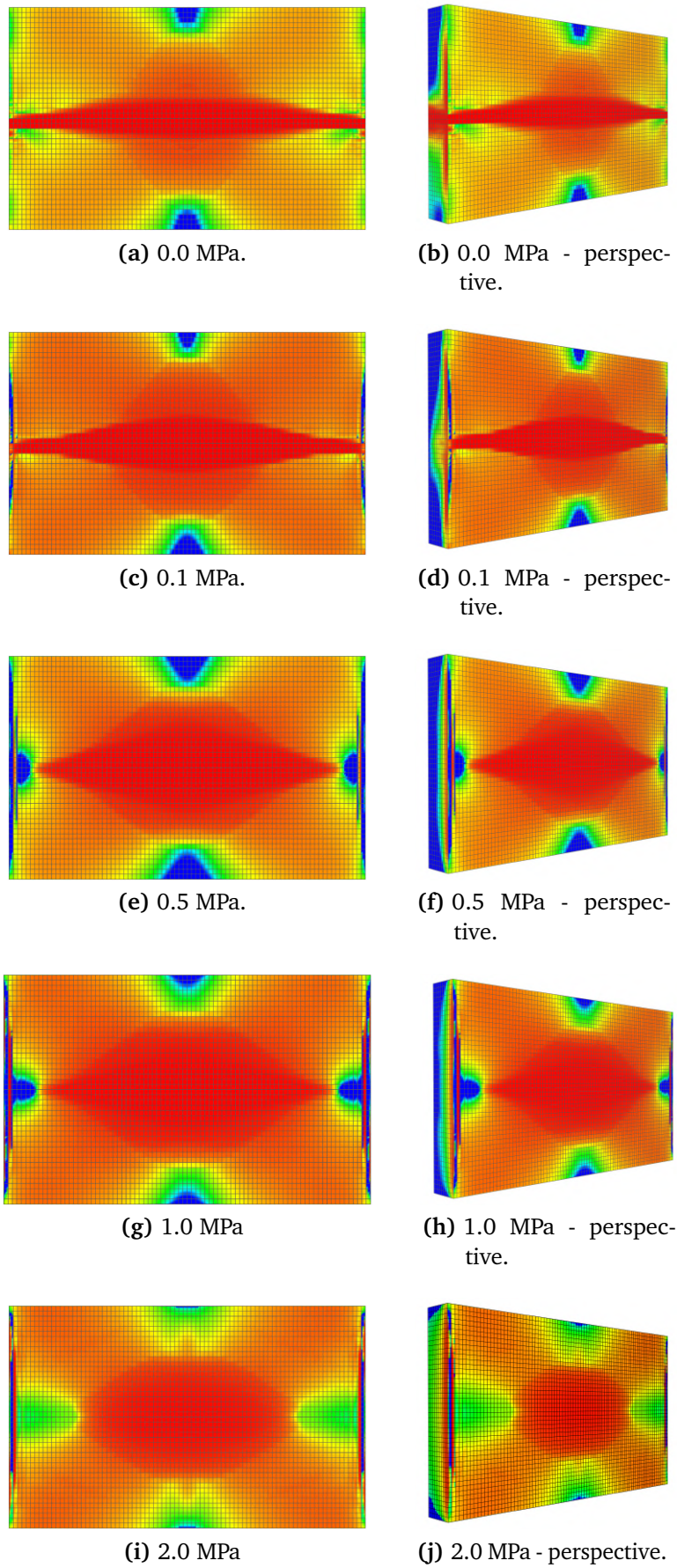


Figure 5.18: Damage of varying pre-compression.

material parameters and corresponding results, it cannot be securely said if the model expresses all zones accurately.

Petracca et al. [182] have simulated the same wall with a FE<sup>2</sup> approach. They have considered half of the wall and have employed symmetry conditions. The suggested IGA manner would thereby bring the boundary shape functions into the measuring spectrum. This would affect the size dependent material detrimentally. Additionally, enforcing clamping at the boundary would either require the bending strip approach [119], or the weak application of the clamping. This would be dependent on a penalty factor, which would introduce a model error and thus corrupt the results. Thus, it was chosen to simulate the entire wall. From a computational aspect the proposed methodologies are still faster than the approach from [182]. It has been mentioned that the coarsest configuration has taken 07:12[hh:mm] for the micro scale simulation and 04:54[hh:mm] for the corresponding FE<sup>2</sup> approach. The here proposed simulation endured 00:21[hh:mm]. Those results cannot be compared one by one as the software has advanced since then and different machines have been employed. It might, however, offer a comparison of magnitudes.

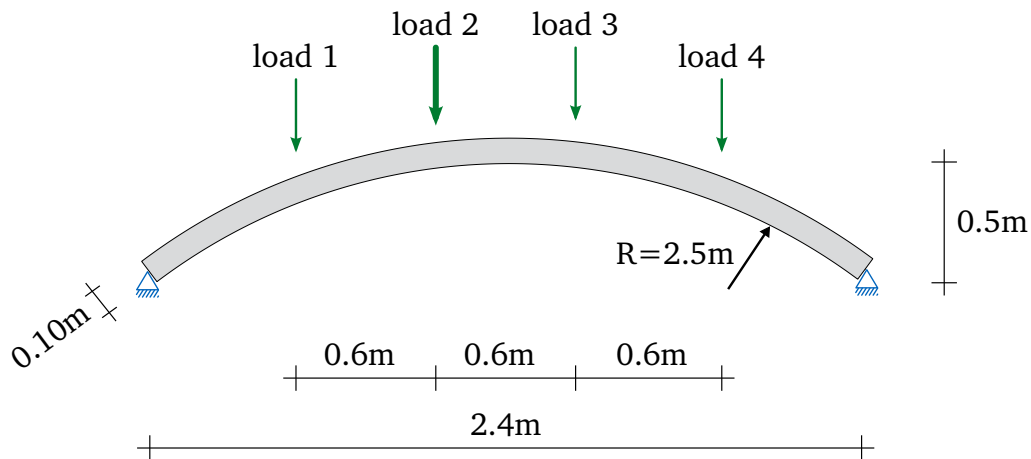


Figure 5.19: Dimensions of masonry arch from [240].

## 5.4 Masonry arch

Masonry arches are a well known and frequently applied structural form, mostly defined by a curved rigid span between two supports [14]. A very common analysis method to estimate the static strength of masonry arches is the thrust method. Therefore, the eccentricity between moments and normal forces are considered to estimate if moments become too strong and would cause the failure of the structure. The approach dates back some centuries [7, 42] and is yet, still frequently applied within the structural assessment of historical and modern arches [37]. In contrast to the classical approaches, the proposed numerical methods shall be exploited within this section to see if the classical form of masonry arches can be assessed properly.

### 5.4.1 Asymmetric loaded masonry arch

This problem deals with the analysis of a masonry arch with a circular shape which was tested by Vermeltfoort [240]. The example has been considered within:

- E. Milani et al. [151]: numerical limit analysis
- G. Milani et al. [154]: meso-macro model
- Chiozzi et al. [54, 53]: kinematic limit analysis

The dimensions of the arch are provided within figure 5.19. It is built with a single layer of bricks, which results in an arch thickness of 100mm, equals the brick thickness. The mortar layer is around 12mm. The inner radius of the arch is 2.5m with a clear span of 3m and a sagitta of 0.5m. The width is 1.25m. Within table 5.4 are referenced the relevant material parameters. It shall be mentioned that the example does not consider

Elastic, tension, biaxial, and shear parameters:

$E$ [MPa]	$\nu$ [-]	$G$ [MPa]	$f_{t0}$ [MPa]	$G_t$ [N/mm]	$k_b$ [-]	$k_1$ [-]	$\frac{f_{t,12}}{f_{t,21}}$ [-]	$\frac{f_{c,12}}{f_{c,21}}$
$^t3000$	$^s0.1$	$^s1500$	$^s0.90$	$^s3e \times 10^{-2}$	$^s1.15$	$^s0.13$	$^s1$	$^s1$

Compression and Bézier curve parameters:

$f_{c0}$ [MPa]	$f_{cp}$ [MPa]	$\epsilon_r$ [-]	$f_{cr}$ [MPa]	$G_c$ [N/mm]	$c_1$ [-]	$c_2$ [-]	$c_3$ [-]
$^s8$	$^s13.6$	$^s0.003$	$^s3.0$	$^s2.0$	$^s0.65$	$^s0.5$	$^s1.5$

**Table 5.4:** Material properties of masonry arch. The characteristics are regarded isotropic as this example is structurally one-dimensional.  $^t(\cdot)$  is known from experimental data and  $^s(\cdot)$  is obtained by calibration and speculation.

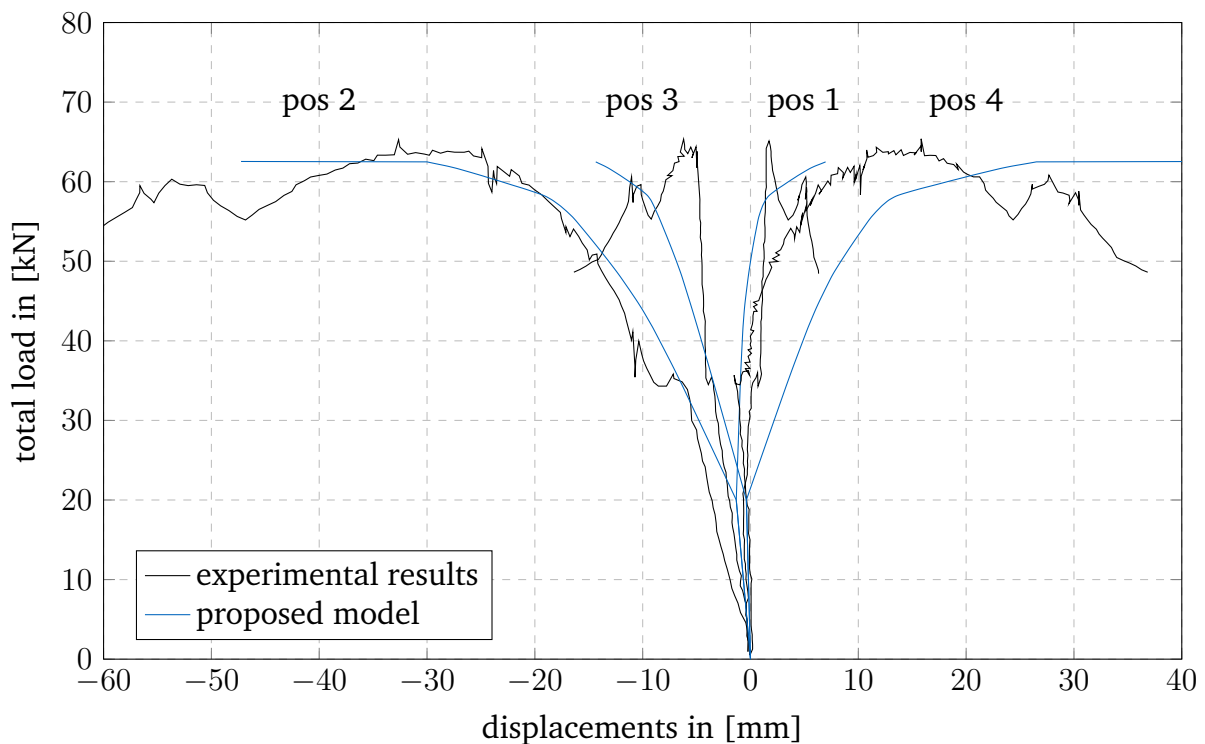


**Figure 5.20:** Vertical displacements - total load of masonry arch.

any compressive damage, as this is far off the range. Furthermore, as the example is rather 2-dimensional no specific orthotropy needs to be considered, which reduced the parameter set significantly.

A stress-based Kirchhoff-Love shell has been employed with 5 integration points per thickness. The total model employed 200x20 knot spans with polynomial degrees of 2x2. Few material information has been provided, thus, the properties have been estimated from the different tests.

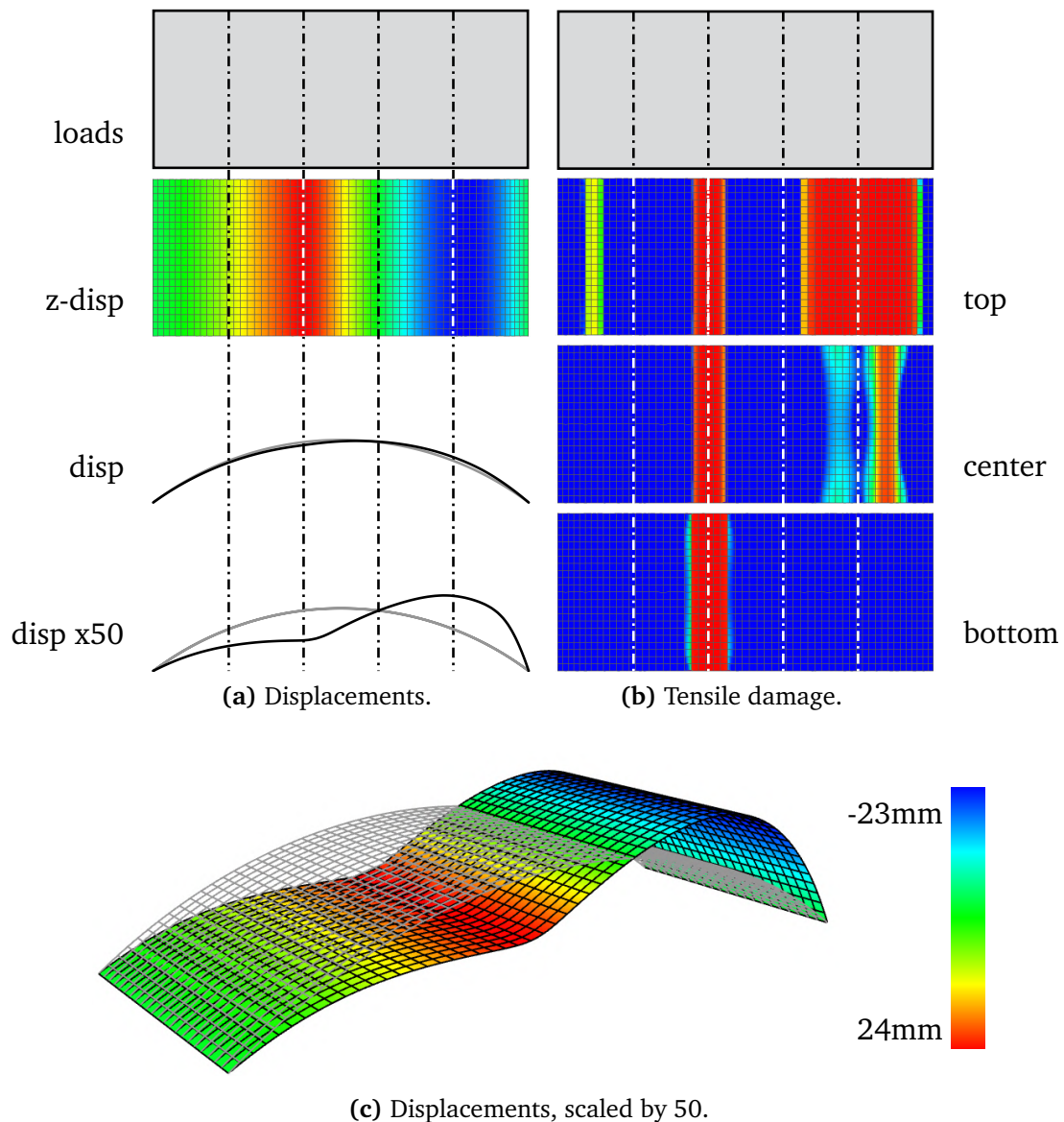


**Figure 5.21:** Post-Processing of masonry arch as experimentally tested by [240].

All four positions are loaded equally until they individually reach 5kN (20kN total). From this stage on, solely the load at position 2 is raised until the arch fails. The corresponding outcomes of this investigation are shown in figure 5.20. It can be seen that the displacements remain symmetric until 20kN is attained. Then, the loading becomes unsymmetrical and the movements go towards different locations. The authors of [240] note that the test setup had some problems in the preciseness of the load control, which shall describe some discrepancies between the model and the experimental results. However, it can be seen that the ultimate loads are close to the experimentally estimated results.

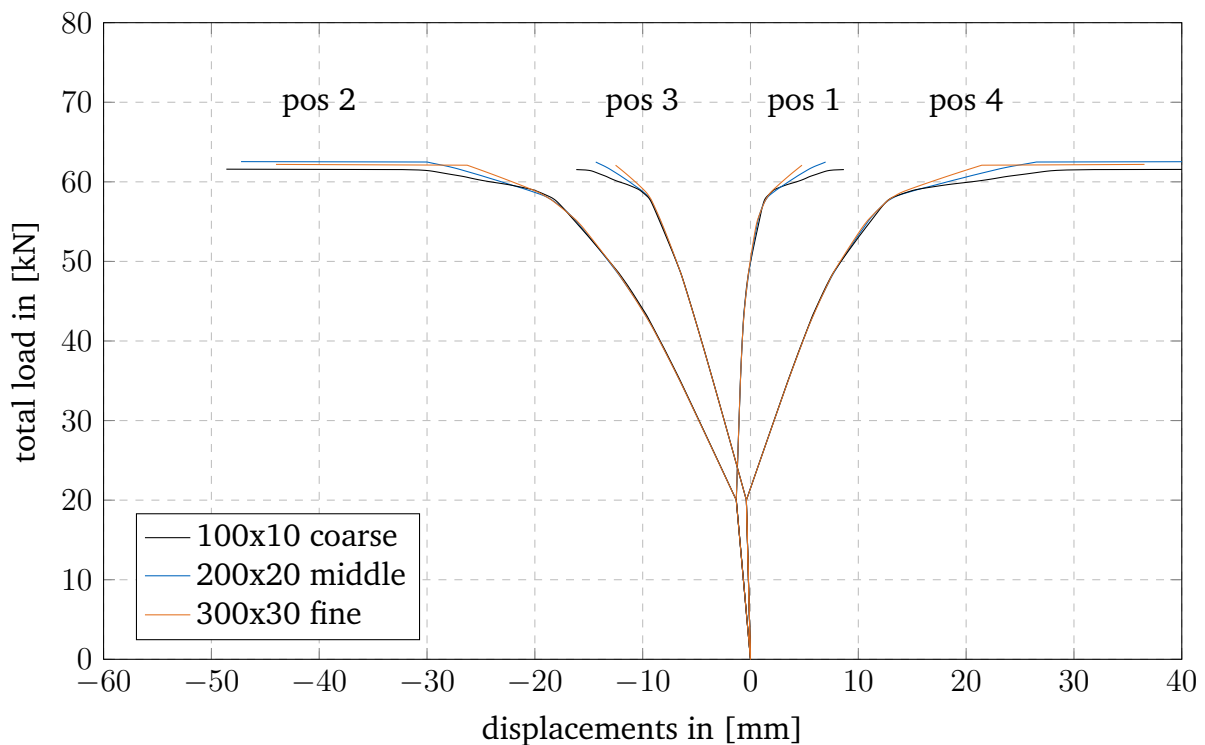


**Figure 5.22:** Vertical displacements - total load of masonry arch - refinement.

The post-processing of the arch example is presented within figure 5.21. The deflections of this problem are presented within figure 5.21a. It shows that the failure mechanism exhibits 3 sub parts, with the highest downwards displacements at the position of the increasing load. In contrast, an uplift can be observed on the opposite side where only the initial loads are applied. Figure 5.21b supports the separation within the 3 sub-modules. The failure mode is similar to the classic 4 hinge mechanism (the same failure pattern has been observed by [151]). It can be seen that the major crack appears at the load application position. This crack dissipates through the whole thickness and is finally crucially decisive for the failure of the structure. However, additional cracks can be observed within the arch. Those do not go through the entire thickness and thus do not lead to failure at this stage. [240] is noting that a minor crack is appearing on the top part of the structure, left of load position 1 (ca. 60mm left of it). As per figure 5.21b, top, the crack initiation is also presented in the digital twin.

To study the insensitivity of the refinement, the example is processed within 3 different refinement configurations. Once with 10x10, 20x20, and 30x30 knot spans. The results are displayed within figure 5.22. It must be noted that there keeps being a slight mesh dependency within the ultimate strength of the respective failing pattern. A slight

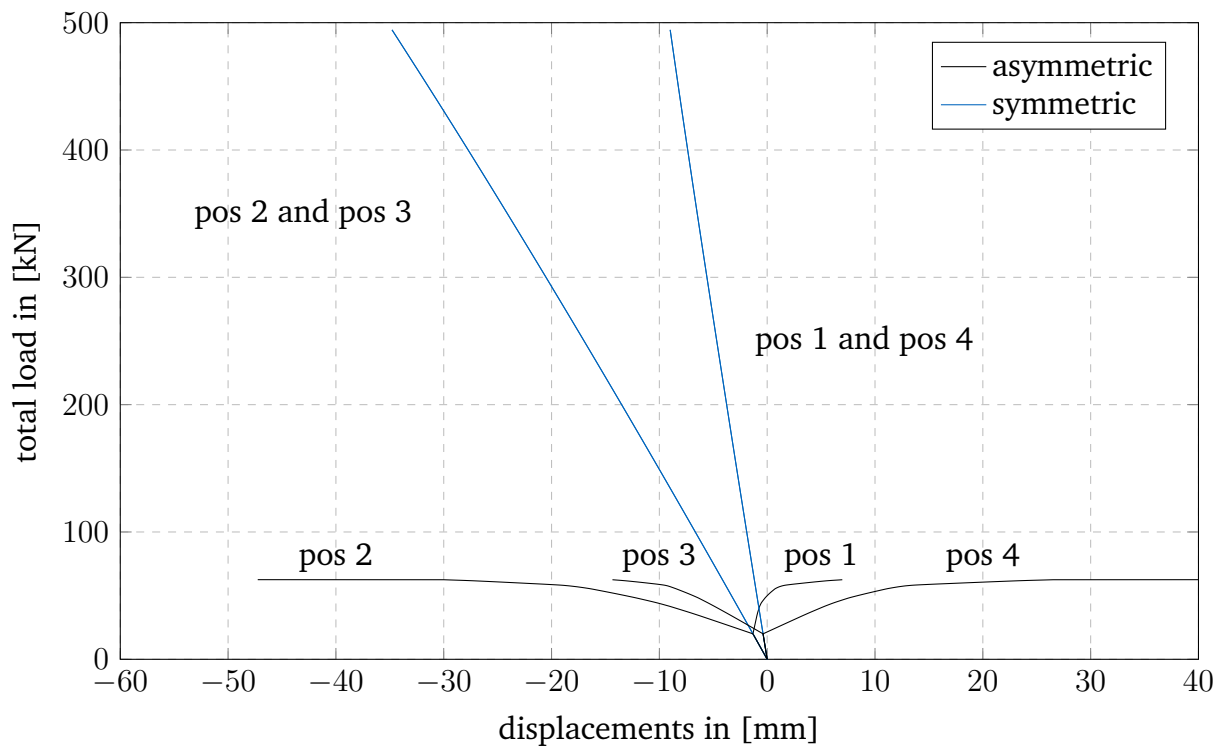


**Figure 5.23:** Vertical displacements - total load of masonry arch - symmetric loading.

variation of the deflections can be observed close to the failure load. However, it can be seen that those variations seem to be within a reasonable range.

#### 5.4.2 Symmetric loading

The same arch is now loaded with similarly increasing loads at all positions. Thus, it is now containing a symmetric loading. This is significantly more beneficial for the carrying behaviour of arches. Within figure 5.23 are compared the numerical results of the symmetric and asymmetric loading cases. It significantly denotes a difference of the loading capacity being around 8 times higher than in the asymmetric loading condition. There is no apparent relaxation and softening phase. Once failure happens, an immediate snap through of the structure can be observed. Accordingly, damages are small shortly before the failure (see figure 5.24). Main damages do not occur at the load application positions, but in-between them.

This examples shows why many masonry arches are actually employed within bridges, where a filler between arch and pavement ensures almost symmetric and even more

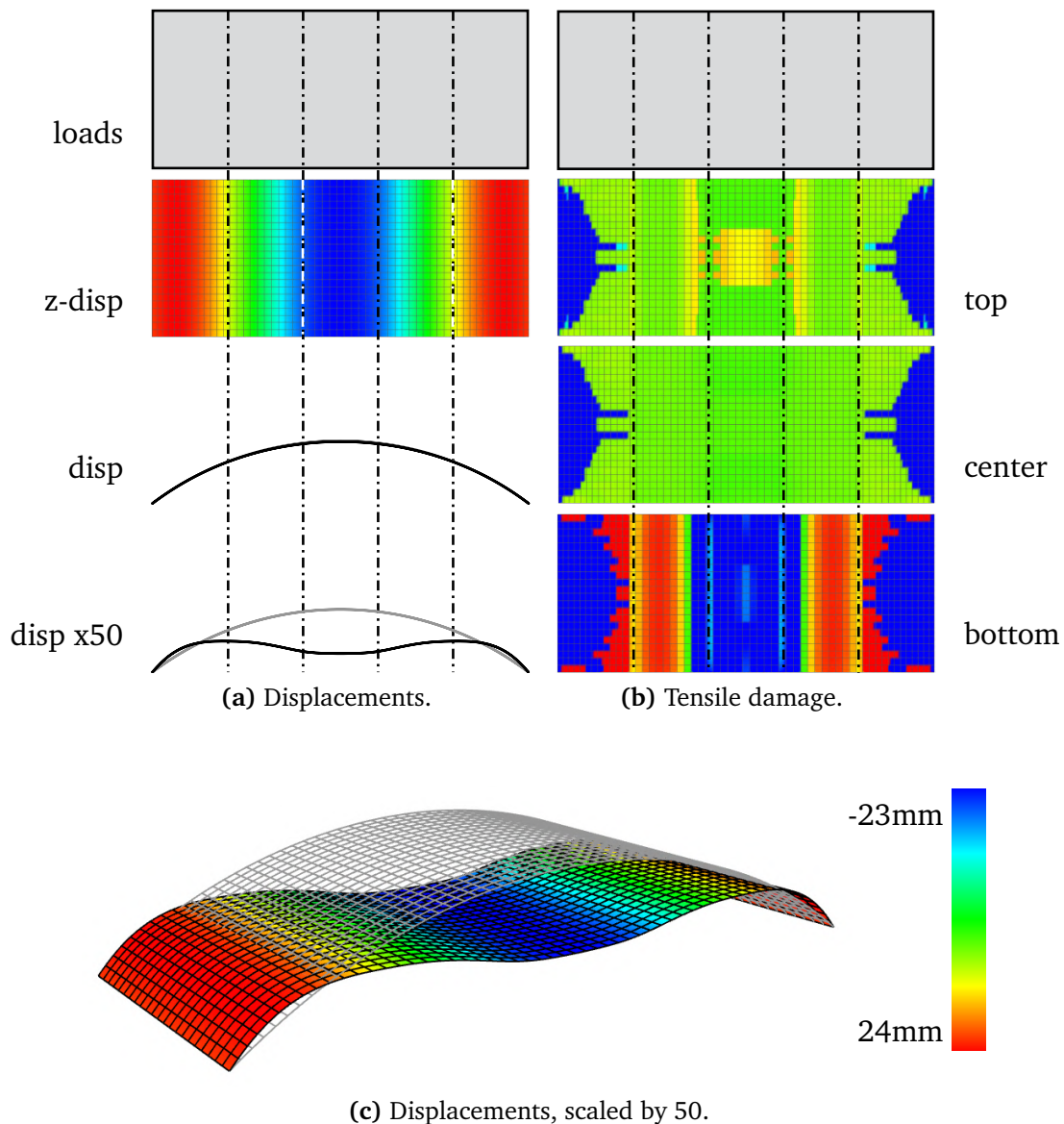


**Figure 5.24:** Post-processing of masonry arch with symmetric loading.

beneficial constant loading [156]. In this way more of the carrying capacity of this structural member can be activated.

### 5.4.3 Thick arch

Another arch example shall be examined within this study which considers a thicker structure, built of two brick layers within the thickness. The arch has been tested by Melbourne et al. [147]. The study considers a series of arches with varying thicknesses

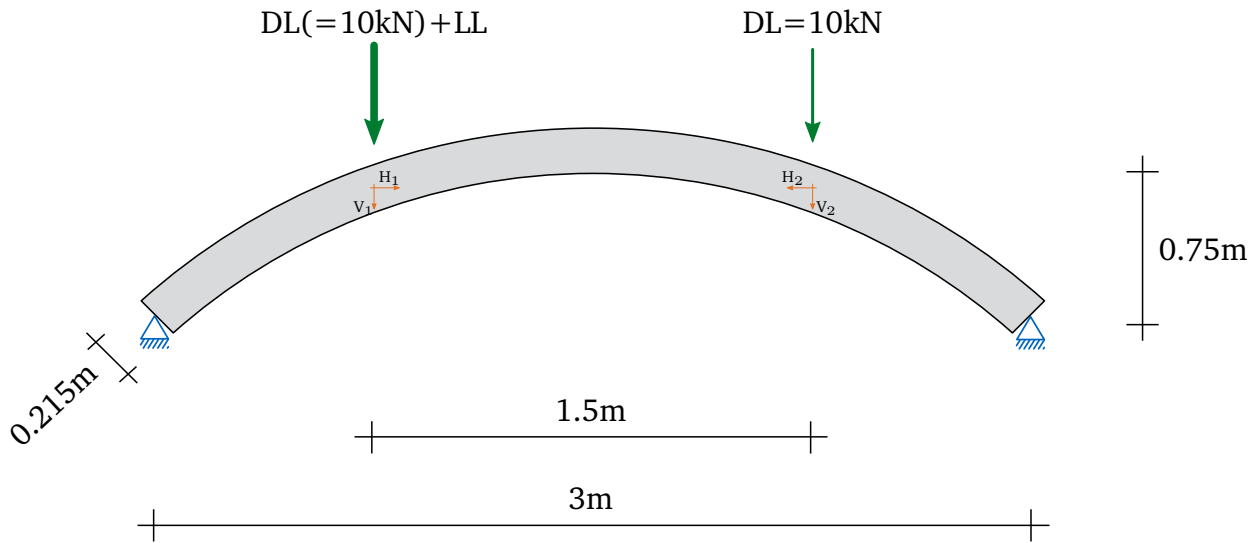


**Figure 5.25:** Dimensions of masonry Arch G from [147].

Elastic, tension, biaxial, and shear parameters:

$E$ [MPa]	$\nu$ [-]	$G$ [MPa]	$f_{t0}$ [MPa]	$G_t$ [N/mm]	$k_b$ [-]	$k_1$ [-]	$\frac{f_{t,12}}{f_{t,21}}$ [-]	$\frac{f_{c,12}}{f_{c,21}}$
$^s2200$	$^s0.05$	$^s900$	$^s0.23$	$^s2.8e \times 10^{-2}$	$^s1.15$	$^s0.13$	$^s1$	$^s1$

Compression and Bézier curve parameters:

$f_{c0}$ [MPa]	$f_{cp}$ [MPa]	$\epsilon_r$ [-]	$f_{cr}$ [MPa]	$G_c$ [N/mm]	$c_1$ [-]	$c_2$ [-]	$c_3$ [-]
$^s8$	$^s13.6$	$^s0.003$	$^s3.0$	$^s2.0$	$^s0.65$	$^s0.5$	$^s1.5$

**Table 5.5:** Material properties of masonry arch. Properties are considered isotropic as this example is structurally 1-dimensional.

and shapes. Within this example it shall be referred to *Arch G*. The dimensioning and problem setup of this arch is presented within figure 5.25. The arch is loaded with 2 symmetrically applied dead loads (DL) of 10kN each. Then, the live load (LL) is increased steadily until failure of the arch. The original study lacks of detailed material properties, thus, those needed to be obtained mostly from calibration (see table 5.5).

This study has previously been considered by Zhang et al. [255] within a partitioned mesoscale analysis. The research shows good match with the tests, while investigating a range of possible material variations.

Within the present research this example shall be used to show the effects of different shell formulations. Therefor, the study is primarily employed with the hierarchic Reissner-Mindlin(RM) (see section 3.3.2) formulation. Furthermore, the results are compared towards the Kirchhoff-Love(KL) shell which is applied mostly throughout this dissertation. The constitutive law from section 4.3 is introduced in a plane stress formulation and therefor would require additional efforts to consistently enable the shear deflections from RM. Therefor, the original isotropic formulation is considered for

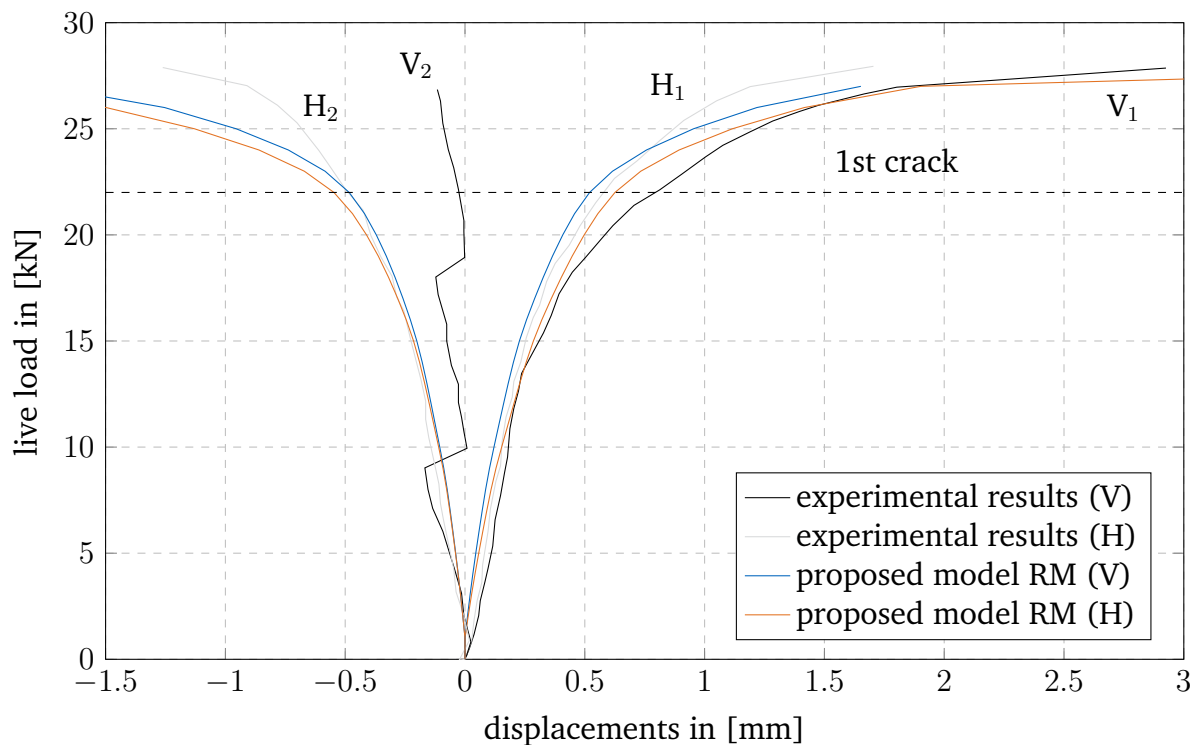


**Figure 5.26:** Vertical displacements - total load of masonry arch.

this example. This assumption is valid as this example is structurally 1-dimensional, as the width direction is continuous.

The numerical results and the experimental references are presented within figure 5.26. It appears that the experimental measurement of  $V_2$  did not work thoroughly, however, this shall not be considered consequently. The results seem to match with the experimental measurements in the remaining positions. Within the numerical solutions, the softening (from around 22kN) is underestimated, expressing the structure stiffer than it actually is. While reaching the same ultimate strength of 28kN it can be noted that the numerical approach is well suitable to express the structural behaviour of the arch.

Consequently, the two shell formulations: KL and RM shall be compared to themselves. The results of this study is presented within figure 5.27. It shows that the arch behaves slightly stiffer with the KL formulation in the elastic zone. This is expected according to the theories of the kinematic formulations. However, thereafter the KL stiffness relaxes significantly faster than the RM counter part. RM shells allow an additional deflection in the shear direction, which makes it deflecting faster in the initial elastic zone. It is expected that the restriction of this deflection within the KL-shell theory resolves in a faster increase of the damage and therefor a faster softening and lower limit load. However, this theorem is not proven and requires additional research. Furthermore, a

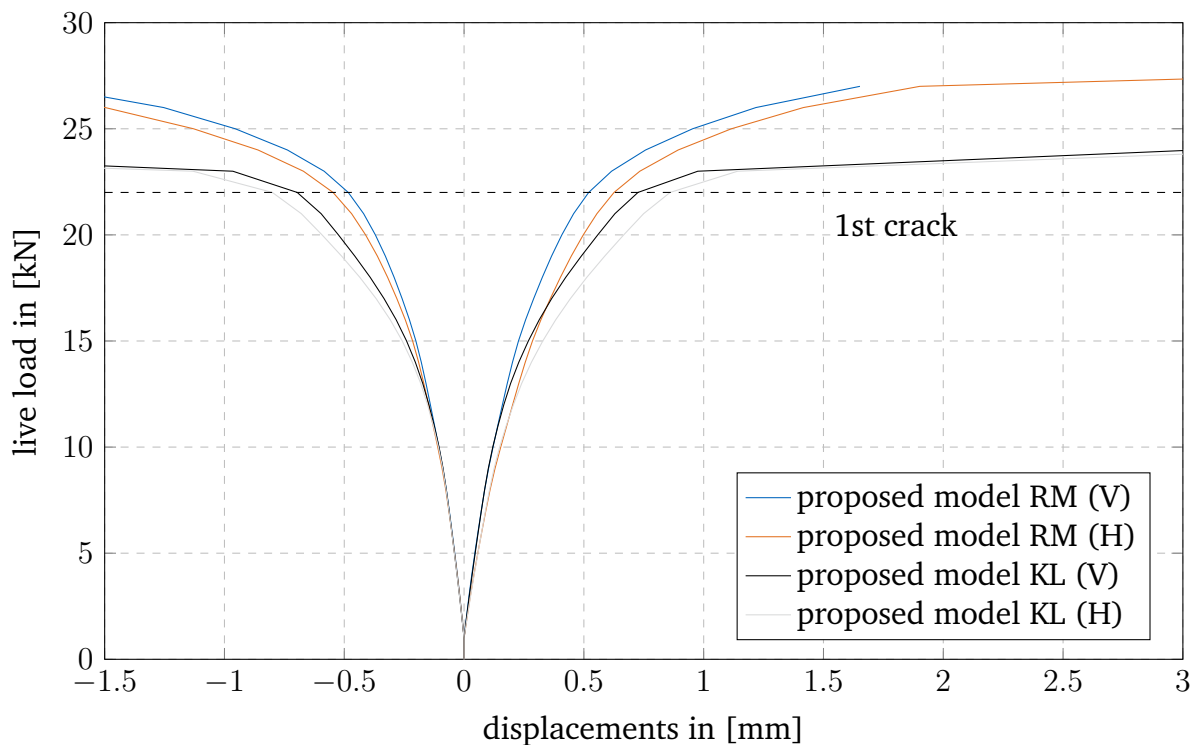
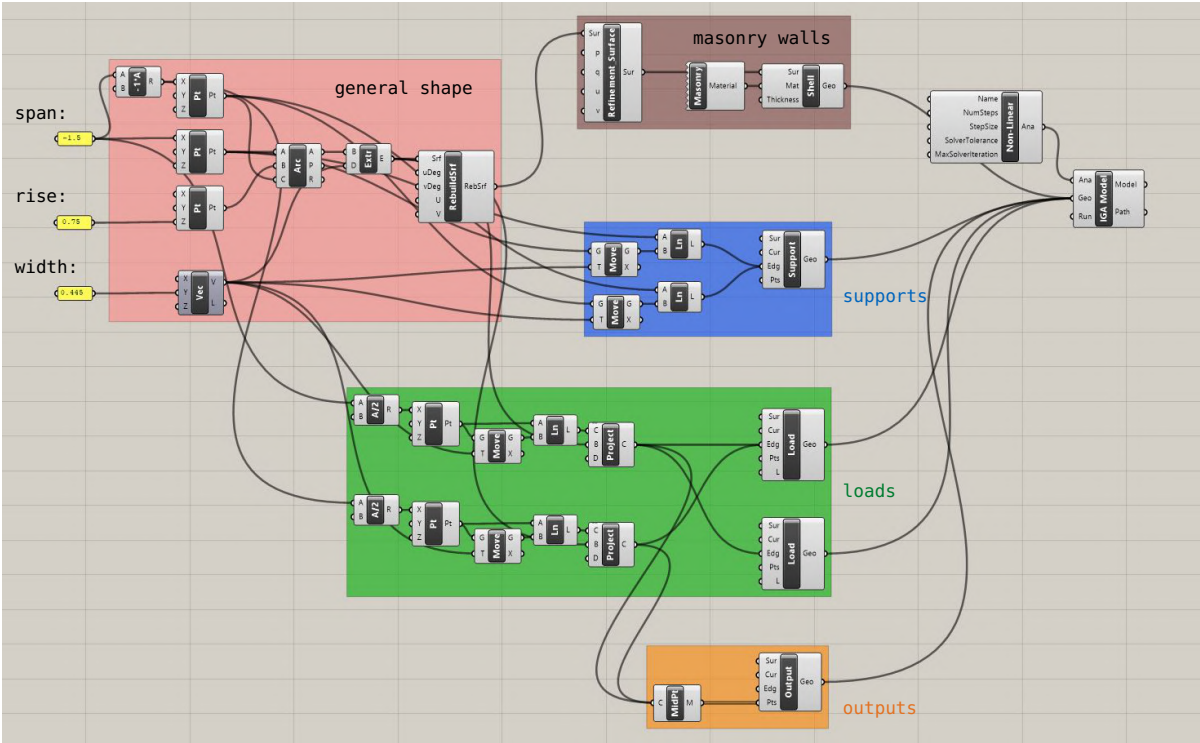


**Figure 5.27:** Vertical displacements - total load of masonry arch.

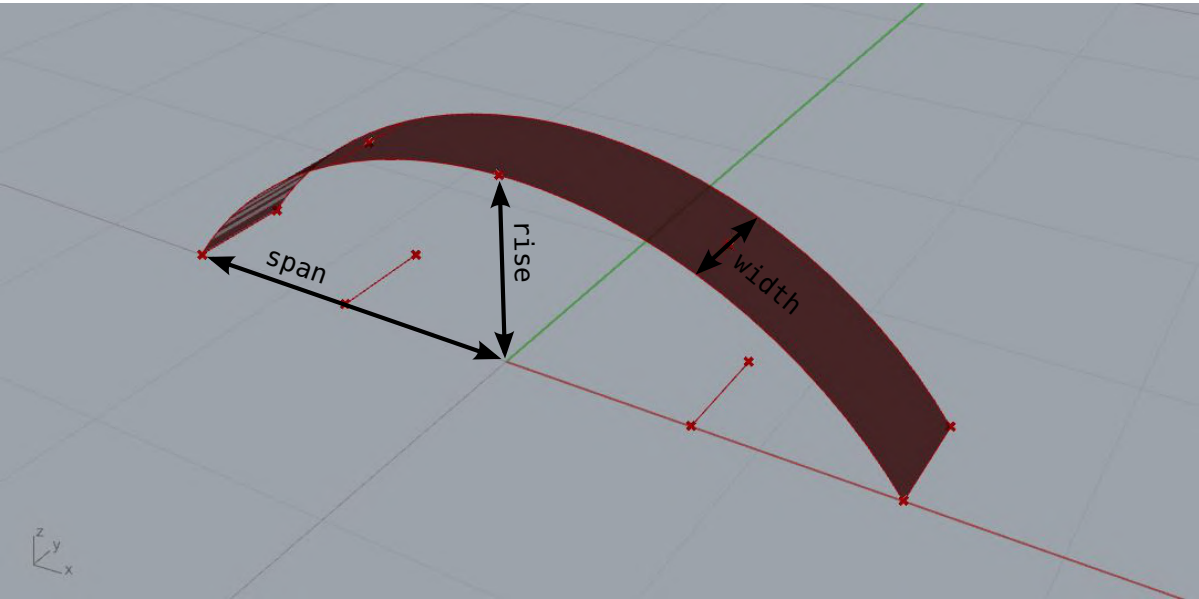
quantitative study including all relevant micro scale tests would be required to enable a calibration-free simulation and therefore proof which kinematic theory is more accurate for this structural problem.

#### 5.4.4 Parametric arch model

One of the fundamental aspects of this research has been the incorporation of numerical techniques into a parametric CAD-integrated environment. As a result, the necessary modeling efforts are greatly facilitated. This section discusses the two previously mentioned arch constructions that have been examined by distinct researchers. It was able to develop a single parametric model that could be used to model both problems adequately. The respective grasshopper model is presented within figure 5.28a. The corresponding shapes are shown within figure 5.28b. By modifying the parameters of: span, rise, and width the shapes of both models can be generated (see figure 5.28b). The positioning of loads is more involved. Therefore, additional shapes are created, which are again dependent on the previous parameters, such as  $\frac{1}{3}$ , or  $\frac{1}{4}$  of the span. Finally, parameters as the specific material properties or the desired thickness of the



(a) Grasshopper model.



(b) Shapes and parameter definition.

Figure 5.28: Parametric model of both masonry arches which have been discussed within this section.

shell need to be adopted. This example shows fundamentally that it is possible to reduce the workload significantly, while relying on a parametric CAD-integrated analysis.

#### 5.4.5 Discussion of results and methodology

Typically, the failure of arches is associated with [147]:

- Hinge mechanism (mostly triggered by tensile strength).
- Snap through.
- Crushing failure (mostly triggered by compressive strength).

A set of possible failure forms are possible, whereby some are presented within figure 5.29.

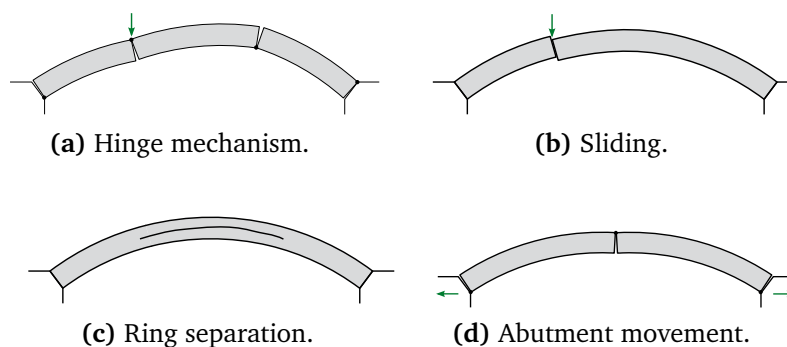


**Figure 5.29:** Typical arch failure modes (inspired by [147]).

It shall be noted that the apparent modeling avenue with the stress-based Kirchhoff-Love shell is able to detect eventual failure modes of the hinge mechanisms, the snap through and the crushing failures. To detect sliding failure, higher parameter shell formulations, such as Reissner-Mindlin shells would be able to present the arch behaviour to a deeper extend. For the analysis of ring separation, classical shells are probably not suitable. To simulate the abutment movement, additional support formulations would need to be modeled into the system.

The presented approach, by using IGA is capable to adequately simulate limit states of arches. However, it needs to be mentioned that the nature of the high order background shape functions is in controversy to crack opening and the according allowance of large deflections. Similarly to the previous examples the damage zones of the cracks would appear wider than expected and kinks are rather smooth (see figure 5.21).

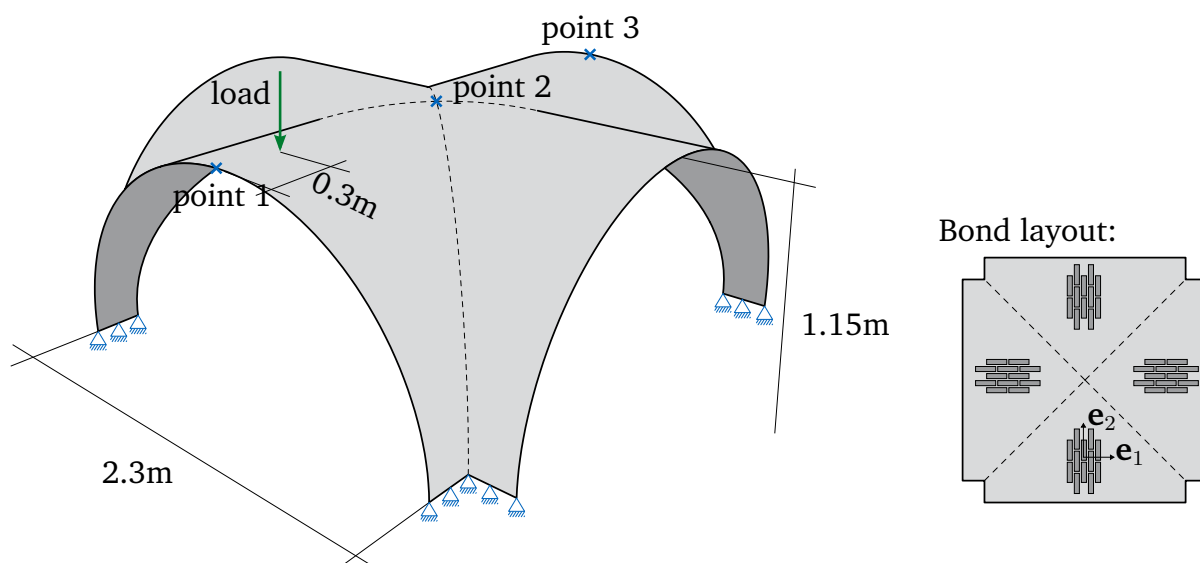


Figure 5.30: Dimensions of masonry cross vault from [81].

## 5.5 Masonry cross vault

Within the history of Europe, the first known masonry cross vaults date back to the Roman empire [88]. Later it was heavily used in the construction of halls and churches. The structural member is able to carry high loads, due to its geometrical properties. However, with the improvements in materials the highly efficient structure lost attraction throughout recent years. While most historic structures have been designed by rule of thumbs and trial-and-error, the correct and quantitative assessment of such structures has since been an open research question. Within the 18th century first known analysis methods have been applied [88]. Within the 19th century, the thrust network or thrust line analysis, known from the analysis of masonry arches has found its application as well in the assessment of masonry vaults. Those, however, have appeared with the following assumptions [106]:

- No tensile strength.
- Unlimited compressive strength.
- No sliding failure between joints.

This is limited in accurateness and can hardly express complex structures. Accordingly, with the introduction of finite element methods, more possibilities have arisen in the correct simulation of those masonry structures. Still, the structural analyses of masonry cross vaults keeps being an open research topic which has gained more and more attention within the last years [153, 34]. Known references mostly focus on the following approaches [34]:

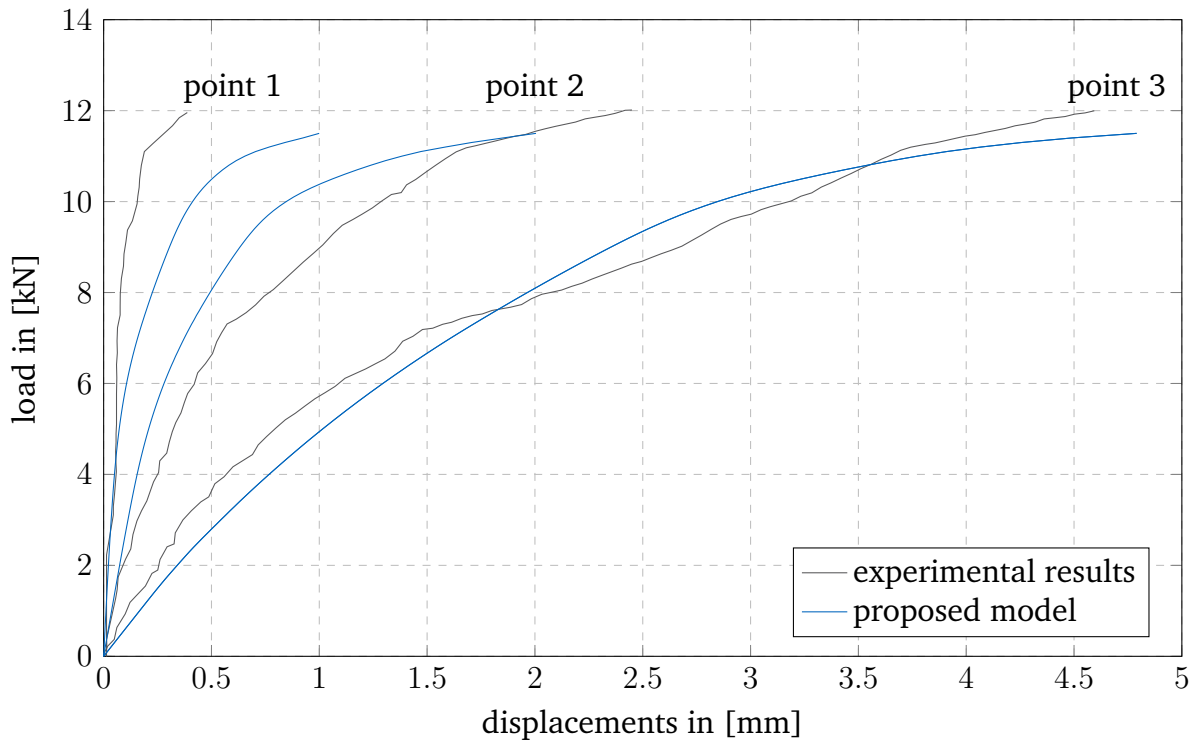


**Figure 5.31:** Displacements - load of cross vault.

- Continuum-based (Creazza et al. [64], Theodossopoulos et al. [231], G.Milani et al. [154])
- Limit state analysis strategies (E.Milani et al. [151], Chiozzi et al. [54])
- Discrete Element Method (DEM) (Lengyel et al. [135, 134])

Of the proposed avenues, typically the continuum-based approaches provide the most comprehensive insights in the buildings. This involves e.g. precise load-displacement relations and accurate stress plots. The other approaches, however, give very fast estimations of the limit loads of the structures. Thusly, the here presented continuum-based approach aligns within the other proposed avenues. In addition to the greatly matching results from Creazza et al. [64], the proposed avenue contains orthotropic behaviour, which allows continuing studies.

### 5.5.1 Masonry cross vault from Faccio et al. [81]

The subsequent example is a masonry cross vault, which has been experimentally tested by Faccio et al. [81]. The cross vault has previously been evaluated in a variety of numerical models:

- Creazza et al. [64] have shown the applicability of continuum based concrete damage models for masonry structures.
- E. Milani et al. [151] have considered the example as part of a limit stress analysis study. In 2017, this study has been proceeded by Chiozzi et al. [54] with a NURBS-based kinematic limit analysis.
- G. Milani et al. [154] present the apparent problem by a meso-macro model. Furthermore, various macro models are tested and compared.

The geometrical sizes of this problem are presented within figure 5.30. Unfortunately, the original authors did not give many geometrical expansions. The vault contains of 4 cut barrels. Its feet are supported strongly in all directions. One load is applied at 0.3m to the edge of one barrel. The resultant displacements are measured at points 1, 2, and 3.

A CAD model has been created, which contains of 4 trimmed B-Spline patches with a polynomial degree of 2x2. NURBS are avoided, despite the fact that they would accurately reflect the geometry. Instead, approximating B-Splines are used. NURBS would contain a knot duplicity at the top line of the structure and would introduce an unintended discontinuity in  $G^1$  (see section 3.5.3 for further information). This would introduce errors at a very important and sensitive position.

The qualitative results of this study, right before failure, are presented within figure 5.32. Failure, within this structure is driven by the delamination of the middle top line and a crack at each side of the loaded barrel. This failure mode is known to the failure of arches with similar bonds. This can be observed in the damage patterns from figures 5.32c-5.32h. The brick layout is providing a failure mode, which induces only limited failure in the non-loaded barrels. A similar failure mode has been documented by [154]. The limit load of the numerical analysis is with 11.5kN slightly lower than the experimental limit load, being 12kN. This proves the applicability of the proposed numerical analysis with being slightly on the safe side. The load-displacement comparison of test vs. numerical results are presented within figure 5.31. It shows a sufficient agreement between model and tests, specifically at point 3. The deflections at point 2 are slightly under, while at point 1 slightly over estimated. The explanation of the discrepancy may involve that the numerical model does not contain the ribs of the cross vault, as those are not specified within the experimental description. Furthermore, the experimental program is not fully outlined and some dimension required speculation.

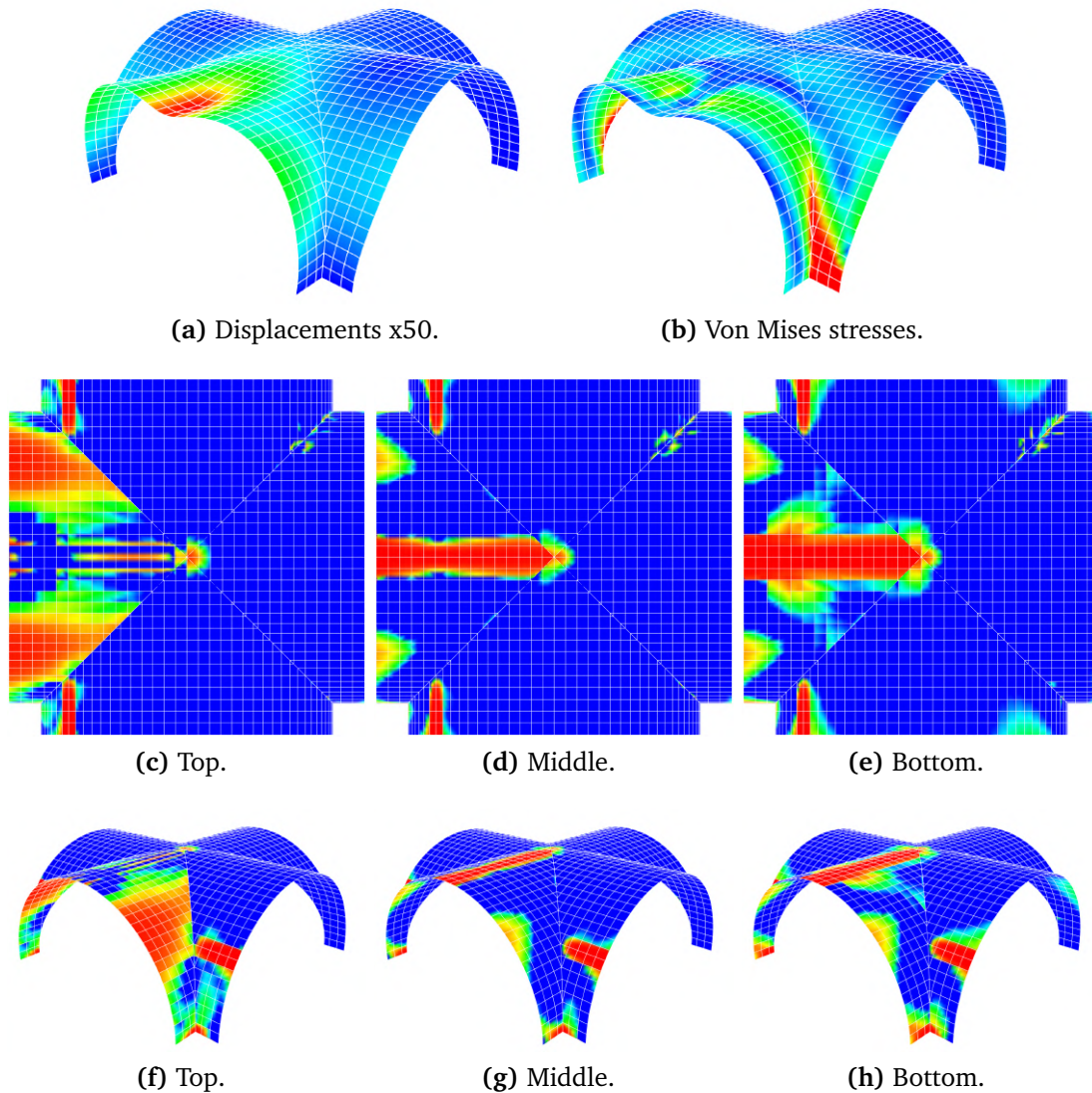


**Figure 5.32:** Results for masonry cross vault.

Material parameters were extrapolated using a variety of tests and relationships discovered by the experimental program that was suggested in section 4.2. The numeric values have been summarized within table 5.6. Most parameters have been obtained from Creazza et al. [64] and G.Milani et al. [154]. It should be emphasized that this example is more sensitive to the material's tensile attributes than its compressive characteristics. This is according to historical presumptions that gave masonry an innumerable compressive strength.

In the following the results shall be compared with available literature. The known references are plotted within figure 5.33. Creazza et al. [64] seem to match the limit stress and the deflections fairly well. The analysis has been processed by a calibrated

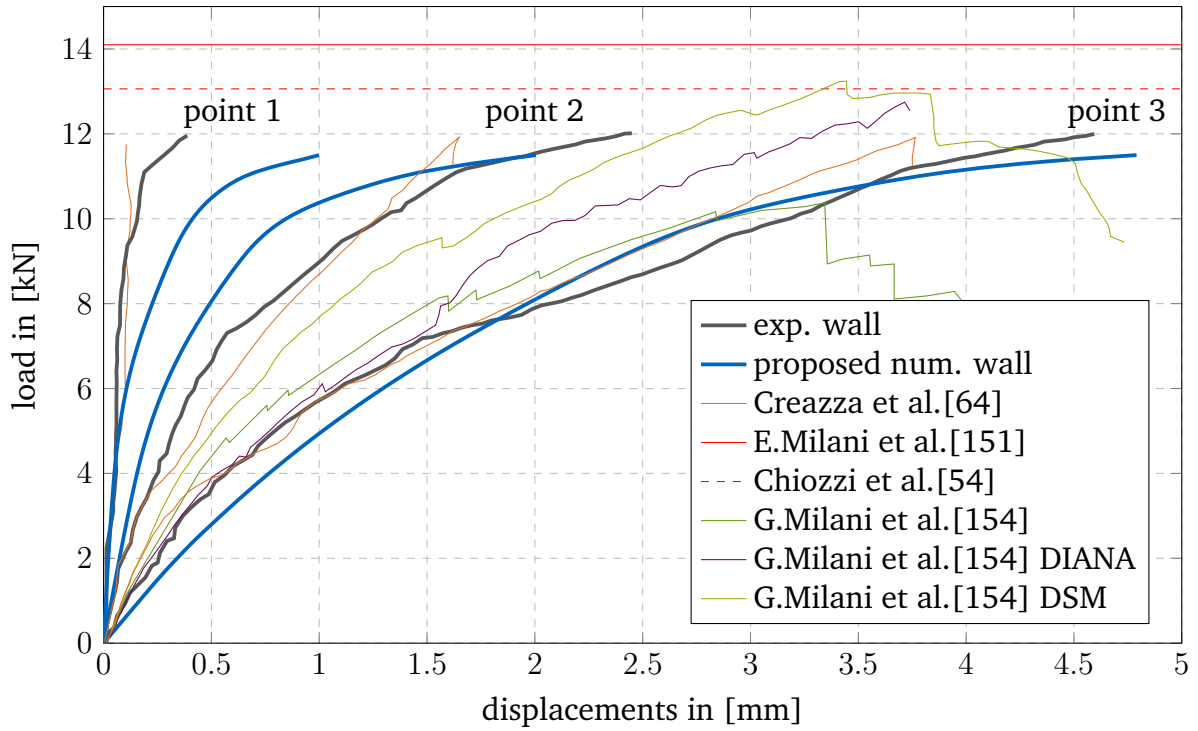


**Figure 5.33:** Displacements - load of cross vault comparison to references from various literature.

Elastic, tension, biaxial and shear parameters:

$E$ [MPa]	$\nu$ [-]	$G$ [MPa]	$f_{t0}$ [MPa]	$G_t$ [N/mm]	$k_b$ [-]	$k_1$ [-]	$\frac{f_{t,12}}{f_{t,21}}$ [-]	$\frac{f_{c,12}}{f_{c,21}}$ [-]
1100	0.1	400	0.1	$6.5e \times 10^{-3}$	1.15	0.13	1	1
800	0.1	400	0.25	$20 \times 10^{-3}$	1.15	0.13	1	1

Compression and Bézier curve parameters:

$f_{c0}$ [MPa]	$f_{cp}$ [MPa]	$\epsilon_r$ [-]	$f_{cr}$ [MPa]	$G_c$ [N/mm]	$c_1$ [-]	$c_2$ [-]	$c_3$ [-]
6	10	0.003	3	2.0	0.65	0.5	1.5
6	10	0.002	3	2.0	0.65	0.5	1.5

**Table 5.6:** Cross vault masonry material properties.

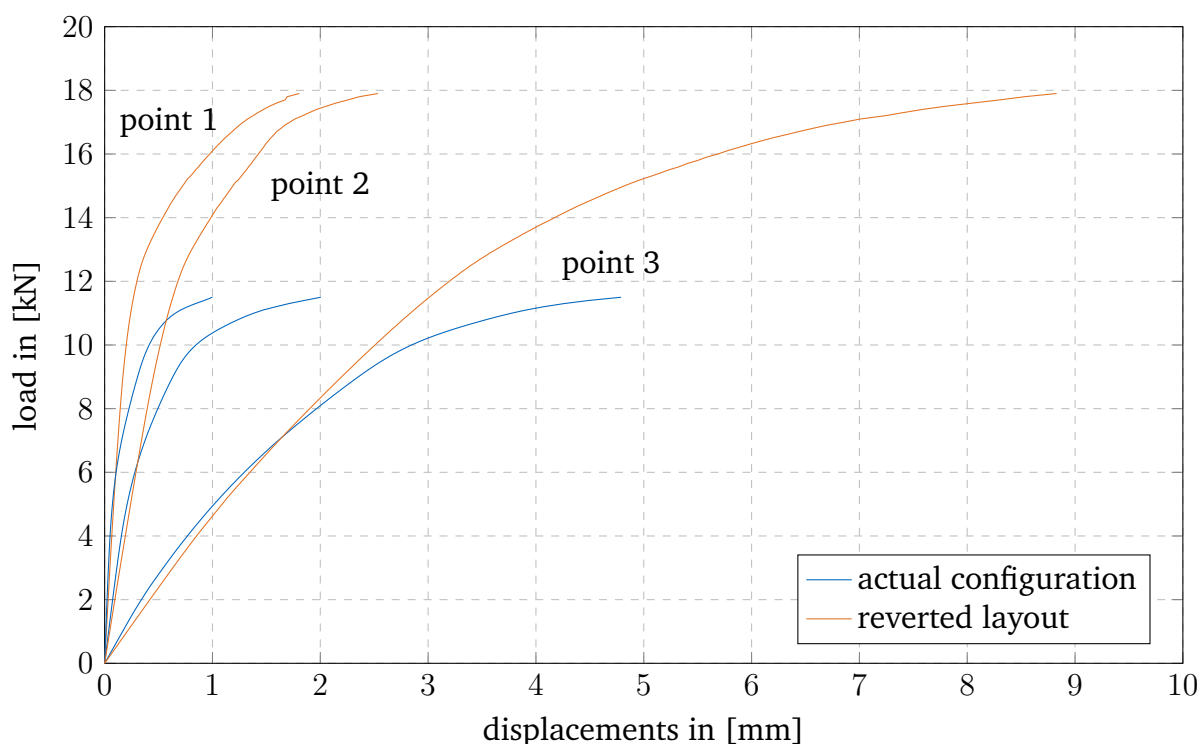


**Figure 5.34:** Displacements - load of cross vault and cross vault with reverted bonds.

isotropic damage model, known from concrete simulations. The authors note that a major problem in the simulations have been the correct calibration of the material parameters. The limit analysis from E.Milani et al. [151] shows off as being slightly over estimated. G.Milani et al [152] propose a meta-macro model and compare their results to 2 different macro models. The 2 macro models processed by DIANA [71] and Deteriorating Simplified Model (DSM) [152, 154] present the characteristics of the structure, however, slightly over estimate the limit stress. The meta-macro model expresses the structure reasonably well, while underestimating the limit state. For all 3 models only deflections at point 3 are provided.

### 5.5.2 Turned masonry bond layout

This study has been extended by a numerical investigation of the bond layout. Therefore the direction of the bonds has been swapped. Thus, bricks are laying now horizontally to the edges of the barrels.

The turned layout shows a significant increase of the final stiffness by around 1.5 (11.5kN vs 17.9kN). Furthermore, another failure mode can be observed. As figure 5.34

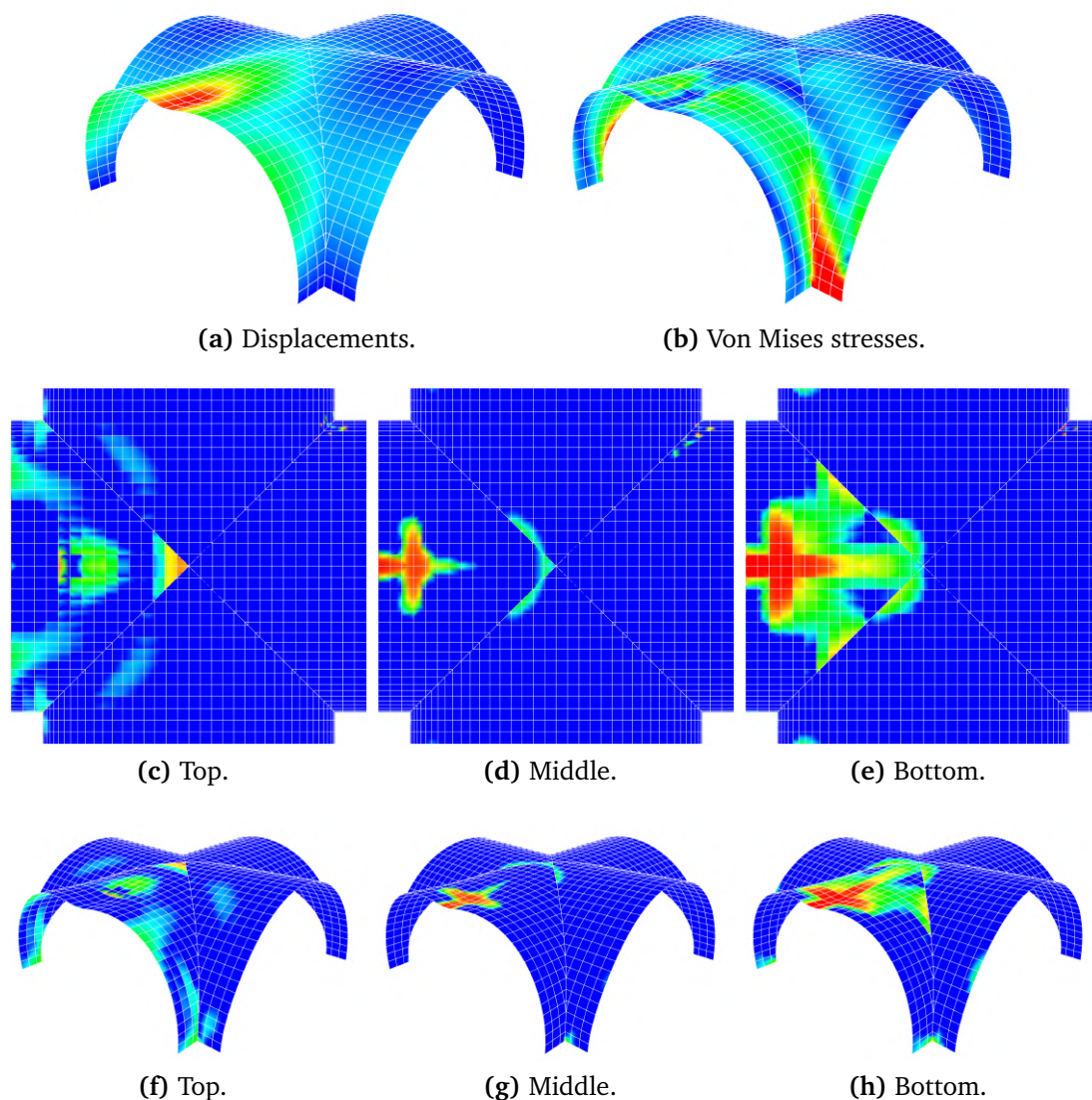


**Figure 5.35:** Results for masonry cross vault with reverted bond layout at 12kN.

shows, the structure initially behaves softer, due to the reduced Young's modulus in  $\mathbf{e}_2$ . However, the failure is later, which can be related to the higher tensile strength. The major crack line is not going directly to the center. The cracks are separating a piece of the structure close to the edges (see figure 5.36e). The same failure mode has been presented within [151], where the same bond direction has been considered.

Although, the structure seem to carry more, it shall be noted that turning the brick layout shall not be put as a general suggestion. The employed load case may be more beneficial for one brick layout, where a different load case may result in conflicting suggestions. E.g. a continuous load would carry more in the original layout.

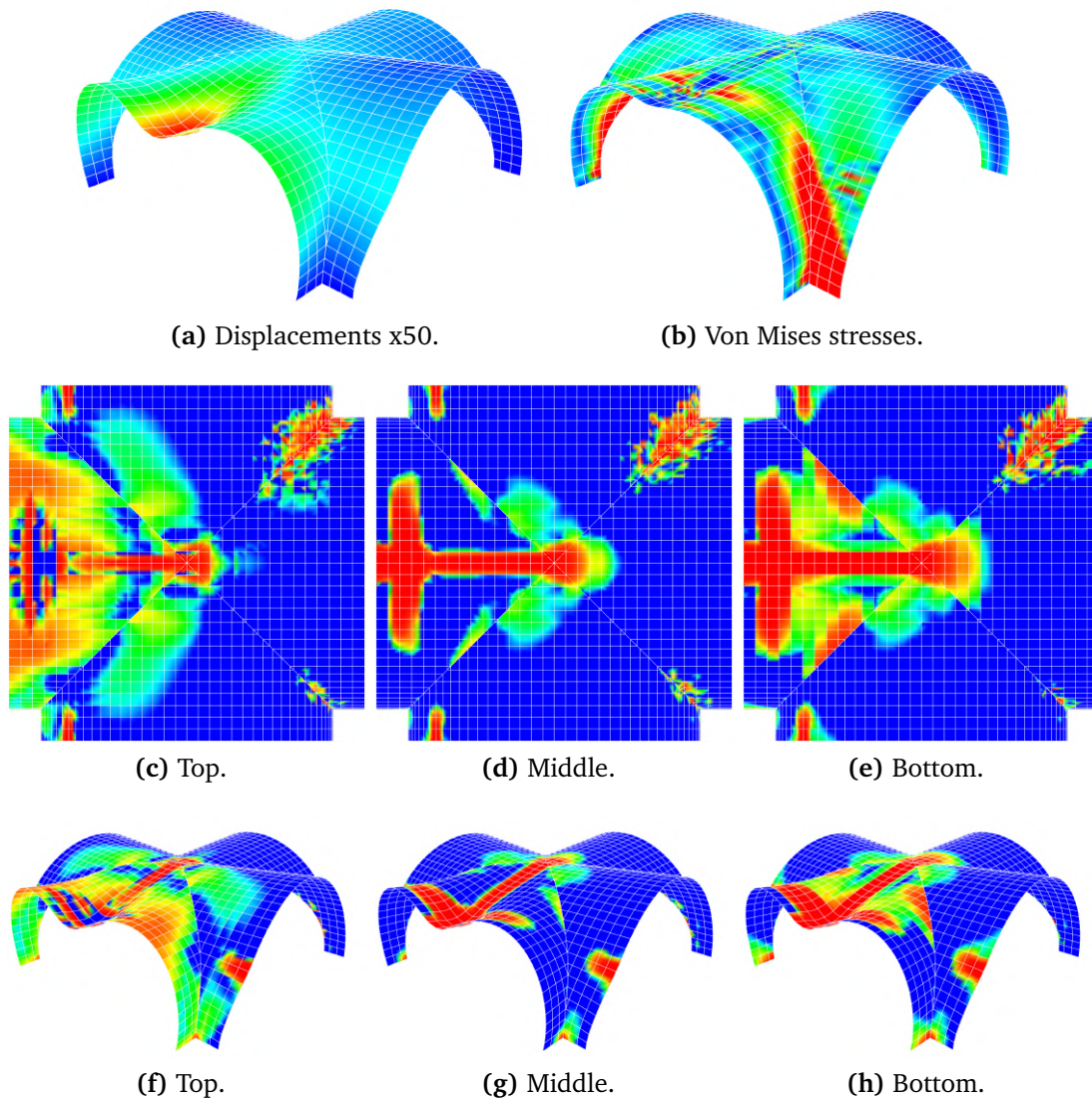


**Figure 5.36:** Results for masonry cross vault with reverted bond layout at limit strength.

### 5.5.3 Discussion of results and methodology

The results show a suitable match with the experiments and previous numerical studies. However, one aspect shall be discussed from the characteristics of IGA: at the connections between the patches, disturbances can be observed within the damage patterns. This is significantly observable within the reverted analysis (see figure 5.36). This peculiar effect is triggered by the trimmed knot spans in combination with the penalty coupling of the patches. Furthermore, the slightest error within the tolerances in the coupling integration may cause significant disturbances. However, for the apparent problem this is not affecting the results.



Figure 5.37: Exemplary roof.

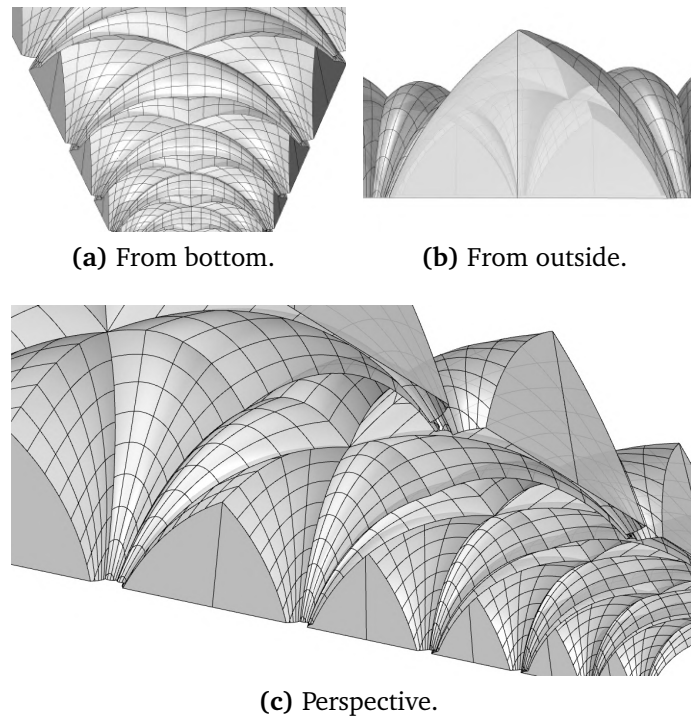


Figure 5.38: NURBS-based CAD model.

## 5.6 Church roof

The consequent example is inspired by a domed vault church roof, which has been constructed in the 14th century and is made of masonry. The shape of the roof has been re-modeled within CAD, and will consequently be analyzed within the framework of IGA, by applying non-linear shell kinematics.

The shape of the structure is shown within figure 5.38. The entire roof is based upon a row of repeating members. Each arch has a longitudinal length of 18m and a width of 10m. For efficiency, only one part will be considered for the subsequent structural studies. This piece is placed between a set of symmetry support conditions and subjected to a progressing dead load on the surface. The structural counter-part including its dimensions are displayed within figure 5.39. The thickness of the roof is considered with 0.2 m and the surface shapes are modeled with a Kirchoff-Love shell [118]. The initial part of this study has been processed by a cutting force based shell to put a focus on the membrane effects of the carrying structure. This has been enhanced by a study comparing those results with the stress based KL formulation. The CAD model consists of 2 trimmed coupled NURBS-surfaces. The symmetry and wall supports are discretized in a strong form by enforcing the support at the nodes. This is possible as those edges

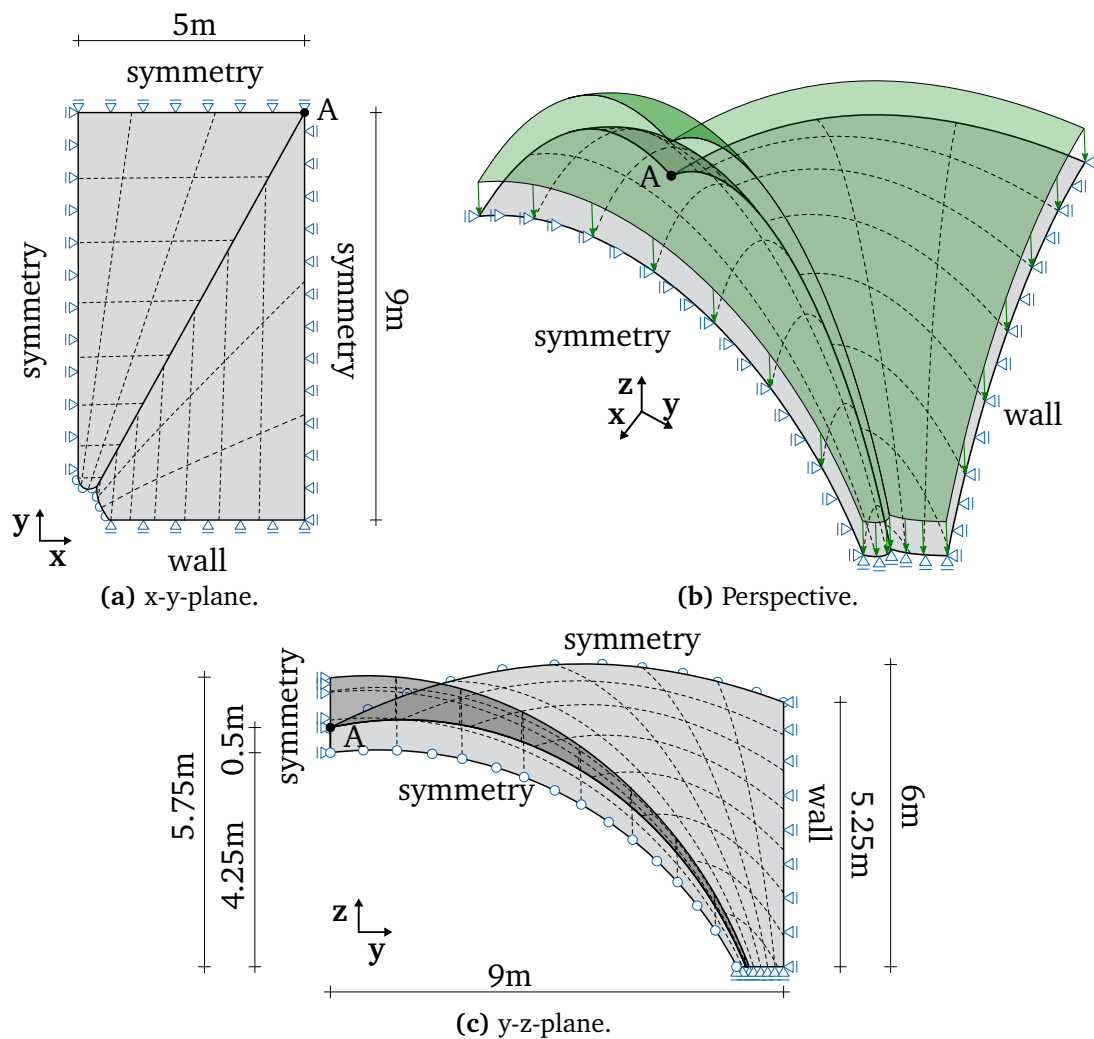
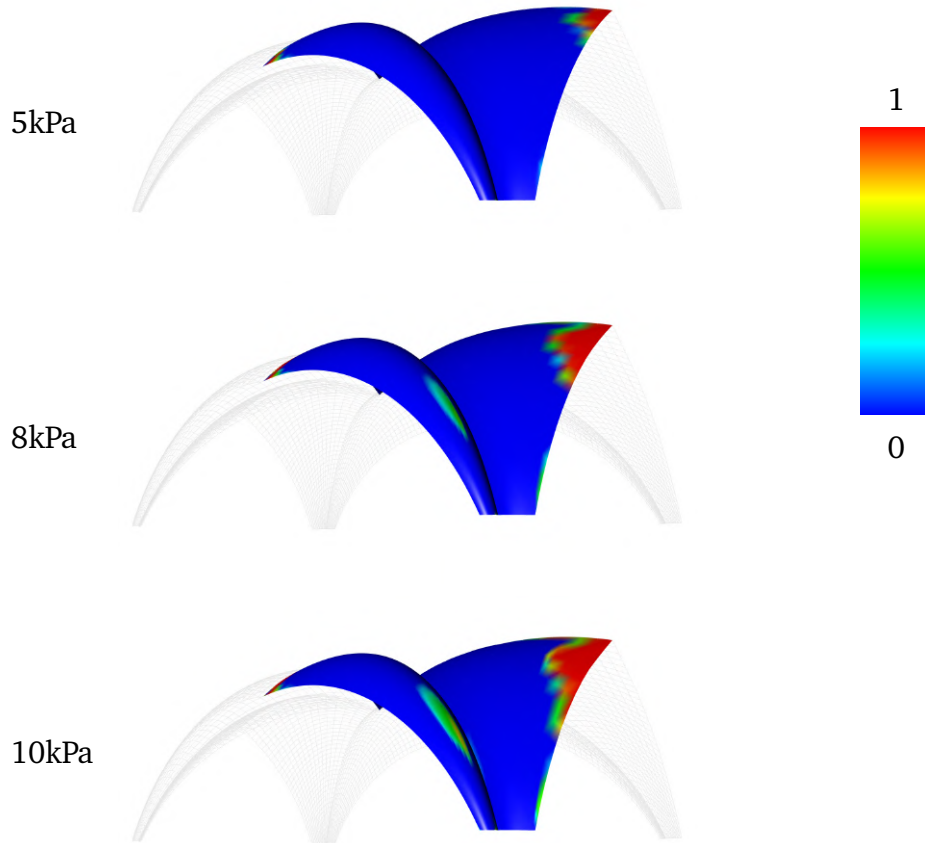


Figure 5.39: Structural model of church roof.

are non-trimmed. For the vertical supports at the position of the columns is applied a penalty support, as those are placed at a trimmed edge.

Initially, the tensile damage evolution amid increasing dead load shall be observed visually, which is displayed within figure 5.40. The compression damage is negligible within this example as almost no damage is occurring with the applied load. It shows that most damages are located around the upper right support of the roof structure. This is as expected from observations of the church, where a noticeable gap can be seen in this part of the structure towards the supporting wall. Two additional damage zones appear, whereby one is at a center location and at the lower left corner of the middle support, which is enforced due to symmetry condition. The damage within the middle of the hull structure suggests that not the optimal shape has been used for this roof as this damage may have been avoided by successful optimization techniques. The other

damage seems to happen due to a slight kink in the shape. Its effects do not significantly corrupt the results and shall thusly not be discussed further.



**Figure 5.40:** Evolving tensile damage.

From the visual observations of the structural damages shall now be considered a more quantitative study of the support forces from the right side of the structure. The roof is modeled once with a damage model and once with linear elastic behavior. The respective results are presented within figure 5.41. The outcome shows clearly that the applied damage model prevents tensile forces which are bigger than the tensile limit strength. The tensile-force peak is going downwards, amid increasing load. Compared to the simulation, which is not considering damage, the compressive forces are slightly higher. This is an important outcome, as it suggests that due to the damage a different load flow happens within the structure. This is an important observation which displays the possibilities for structural engineering with such damage models.

An additional aspect which shall be considered by this example are the deflections within the model. Those are presented in figure 5.42. Here, the absolute- and the y-displacements from the geometrically non-linear and damage model are compared. It

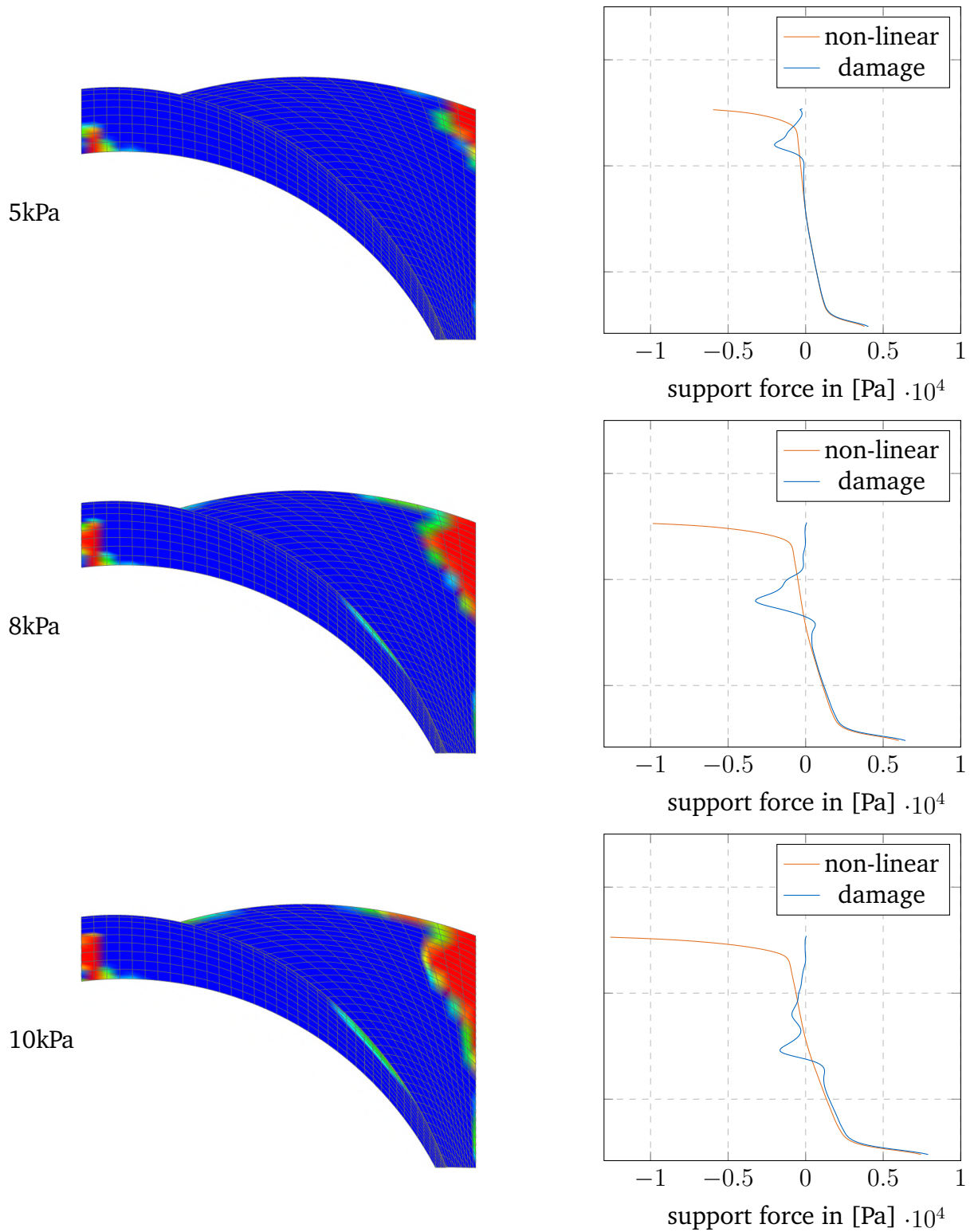
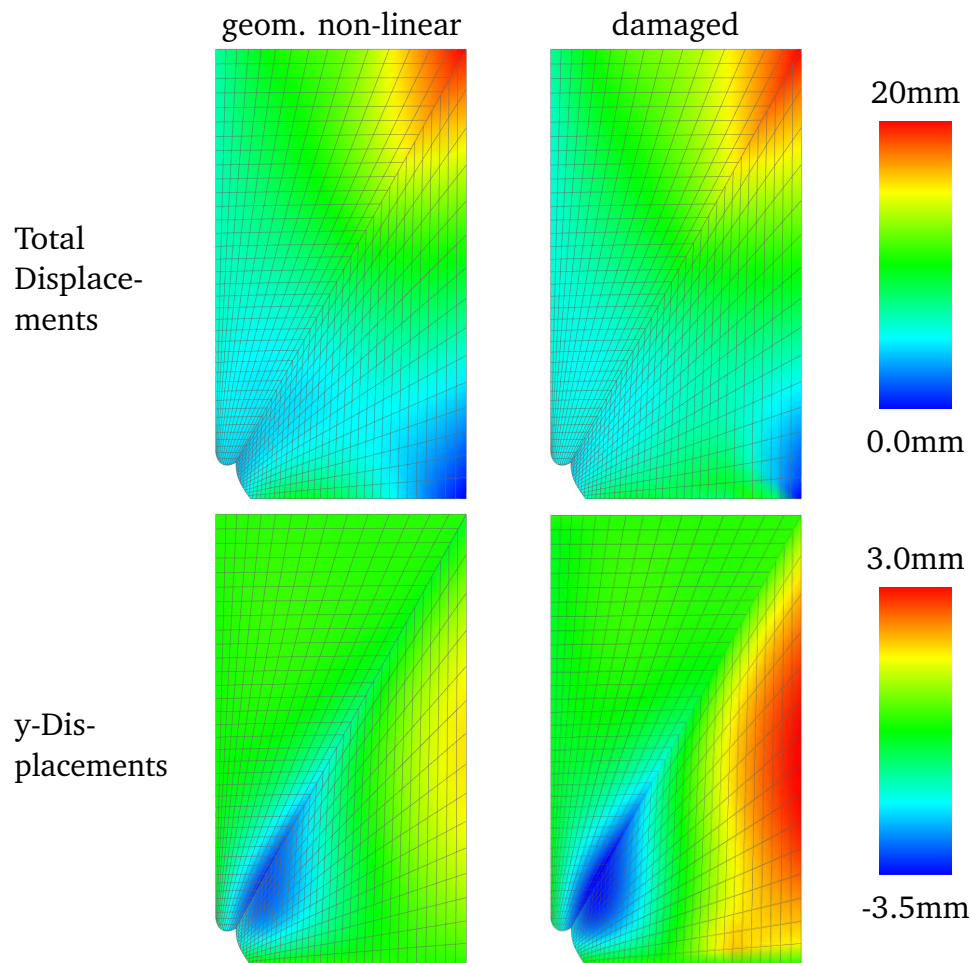


Figure 5.41: Qualitative support force amid evolving tensile damage.



**Figure 5.42:** Displacements of the church roof with the geometrically non-linear and the damage model from top x-y-view.

can be noticed that there is a significant movement in y-direction close to the damaging support. Still, the largest deflections occur at the center point (point A, see figure 5.39) of the vault. Hence, the displacements at this point are studied and displayed within figure 5.43.

The church roof is analyzed in 4 different configurations: the proposed damage model, once cutting force-based and once stress-based, the linear elastic geometrically non-linear, and the geometrically linear configuration. The load is gradually increased until failure i.e. the solution cannot be solved anymore. The results show that the geometrically non-linear simulation does not vary significantly to the geometrically linear solution. However, the non-linear effects present an expected slight softening behavior of the roof. In comparison to this, the roof behavior, which is considering the damage is significantly softer with much higher observed limit deflections. Finally the stress based (s-b) formulation notes the earliest failure. This is expected as the cutting

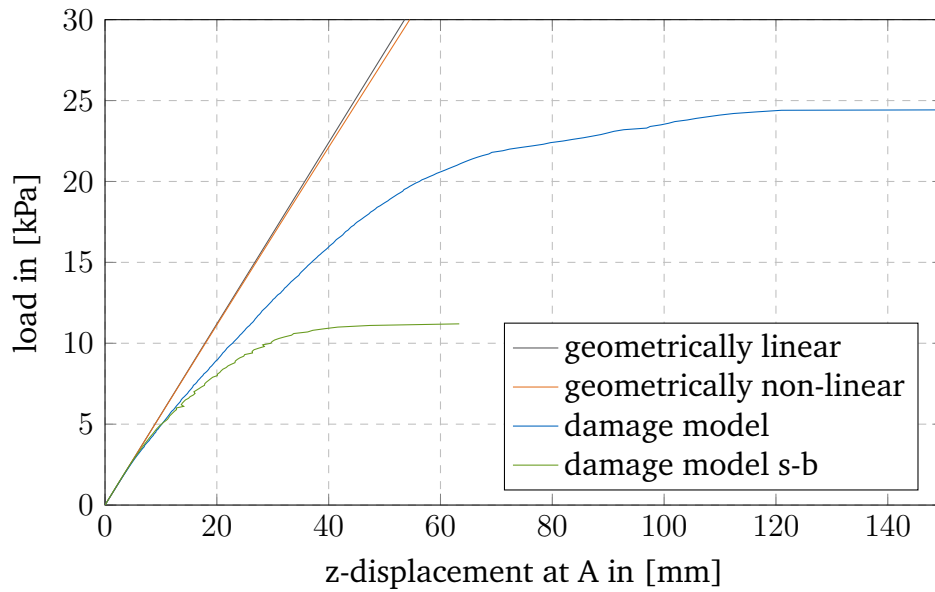


**Figure 5.43:** Displacements from geometrically linear, geometrically non-linear and damage model at Point A (see figure 5.39).

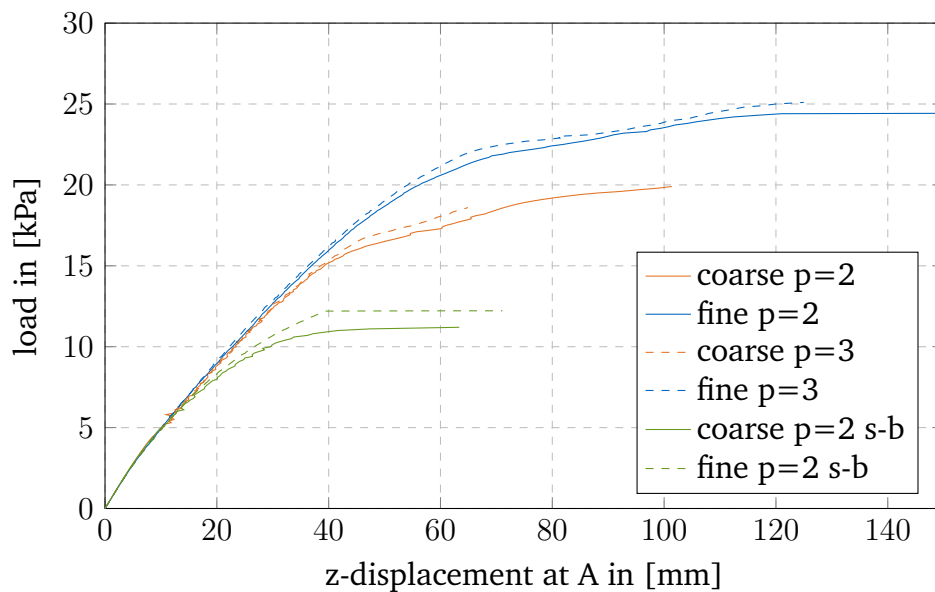


**Figure 5.44:** Comparison of refinement and polynomial degree.

force based formulation is only sensitive to membrane forces, whereby, the stress-based formulation can also consider bending failures.

Additionally, the sensitivity to the polynomial degree and refinement is studied and presented within figure 5.44. It notes that while having the same refinement level, the variation of polynomial degree is rather insensitive. However, the resolvability stops

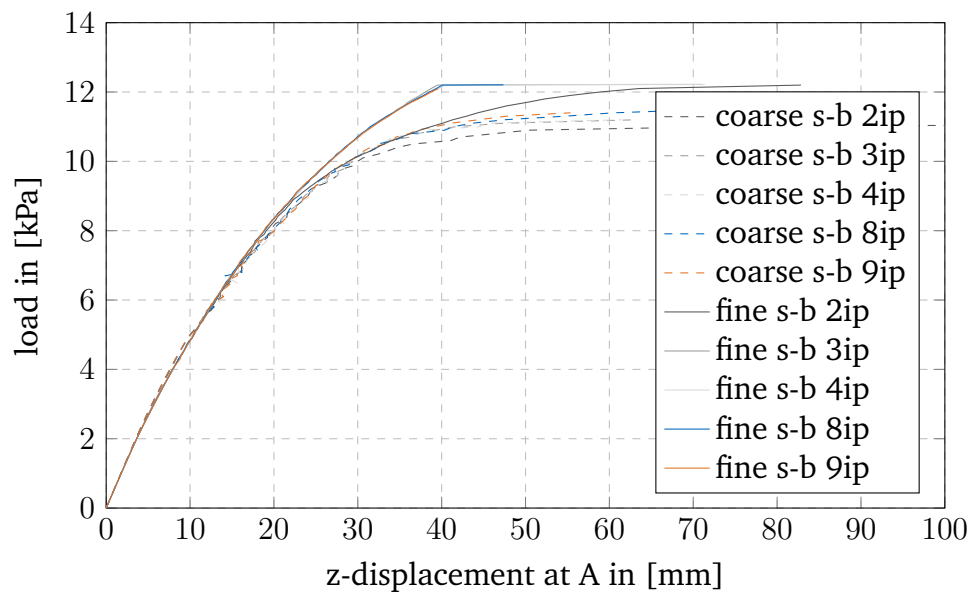


**Figure 5.45:** Stress-based (s-b) shell displacements at point A (see figure 5.39) with varying thickness integration points (ip).

earlier with a polynomial degree of  $p=3$ , while  $p=2$  can solve additional solution steps. This can be described by the cut offs which appear within the relaxation curves from appendix B. The refinement level appears to have a more significant impact on the solutions and the final failure. Even though the variation is not immense, it shows that there keeps being a mesh dependency.

The same refinement study has been processed for the stress-based shell formulation (see figure 5.45). It can be seen that here the differences between the two different meshes seem to vanish slightly. The study has been enhanced to investigate the influence of the number of integration points in thickness direction. It can be noted that the differences are not significant, while no convergence towards any result is observed for the coarse scenario. The variation within the refined structure seem vary only for 2 integration points from the other solutions. The results suggest that 2 integration points per thickness provide the smoothest and at the same time softest lightening of the structure.

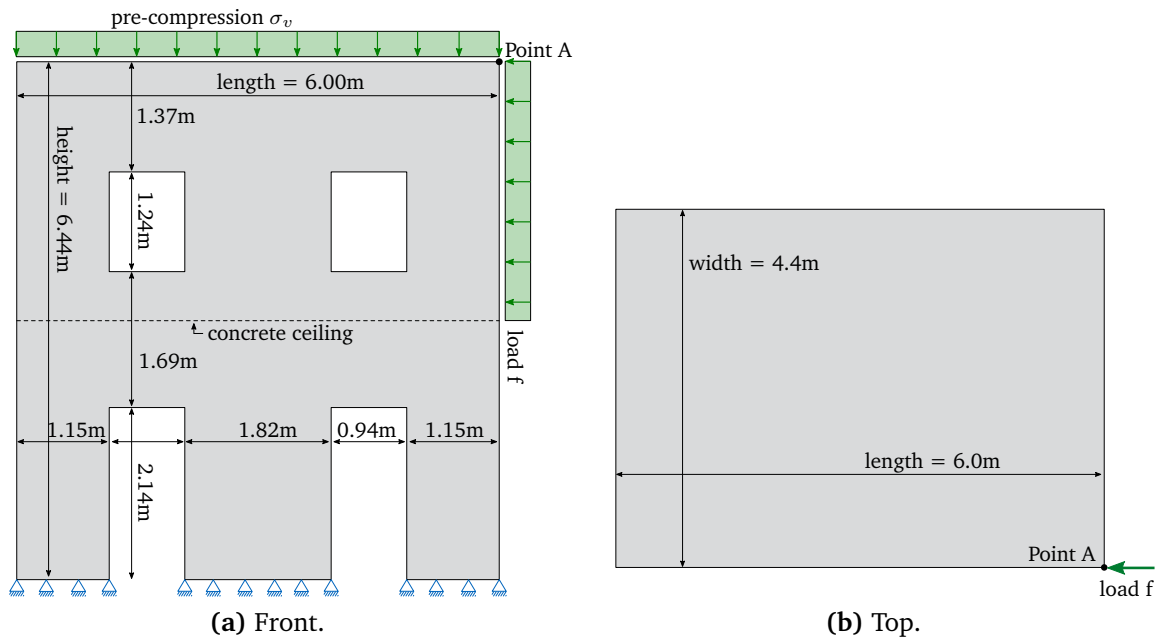


**Figure 5.46:** Model of masonry house from Cannizzaro et al. [45].

## 5.7 Masonry house

The subsequent masonry house is inspired by a set of benchmark studies of masonry houses: see D'Altri et al. [68] for various boundary conditions, Cannizzaro et al. [45] for the study of different material models and Cattari et al. [47] for a general summary of the goals for benchmarks of masonry buildings. Those examples have been created to estimate the strength of buildings under horizontal loadings, which is specifically critical with seismic earthquake impacts. Those research projects have been initiated after the 2016 earthquakes in central Italy.

This example is a 2-story building with a concrete floor in-between. The material properties from example 5.3 have been employed for the masonry walls. It is inspired by the architecture from various central Italy buildings.

The structure itself is simple, however, applied within multiple buildings and is mostly varying throughout them only from the selection of dimensioning parameters. Thus, it is perfectly suitable to be designed from a parametric model. Accordingly, the major purpose of the presented numerical example is the explanation of the analysis of masonry structures in a parametric modeling environment, while triggering few parameters. This would specifically enable a fast analysis of many buildings and perfectly shows the benefit of the application of the proposed parametric CAD-integrated IGA workflow.

Within figure 5.47 is presented the grasshopper model of the masonry building, along with the analytical enhancements. The model displays how deep the geometrical design

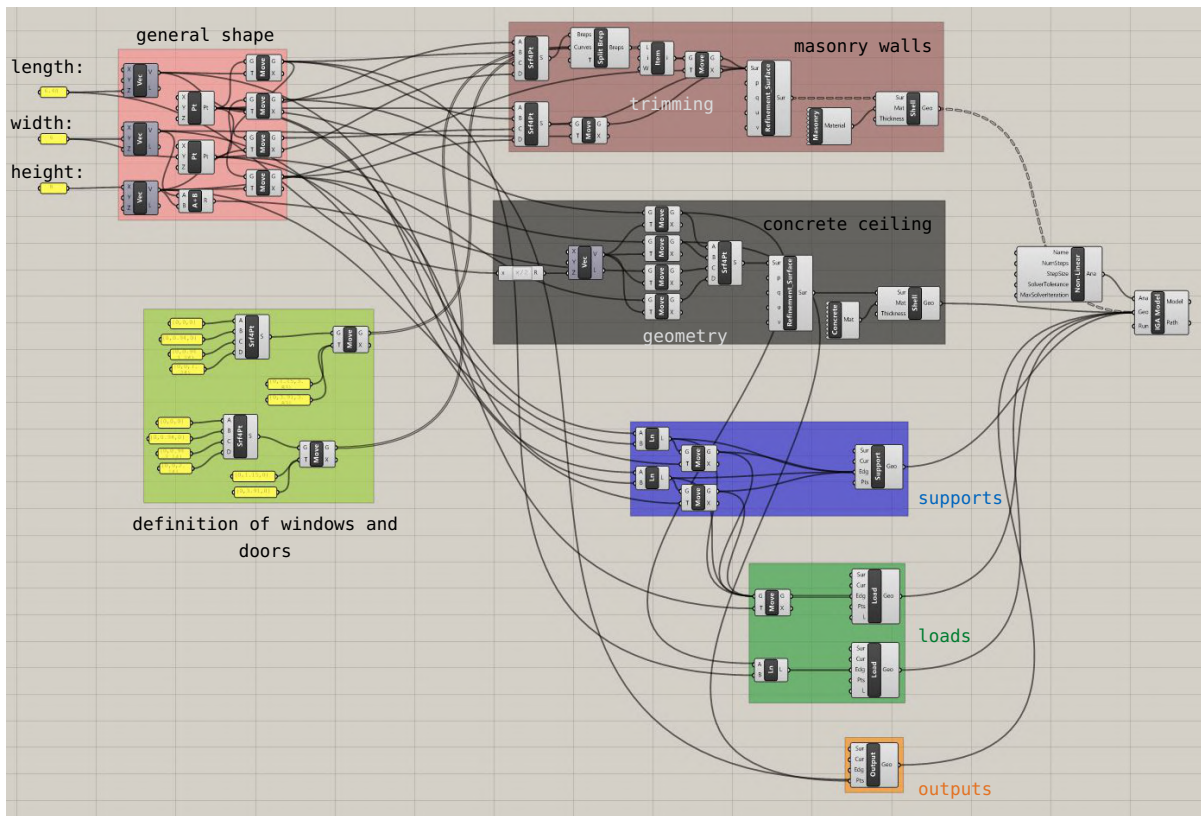


Figure 5.47: Parametric model of a generic masonry house.

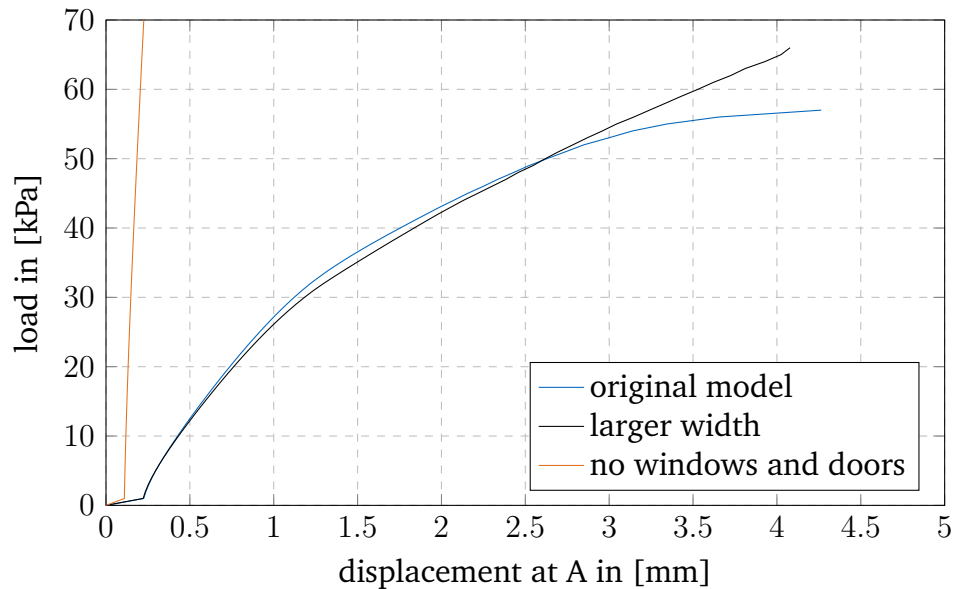
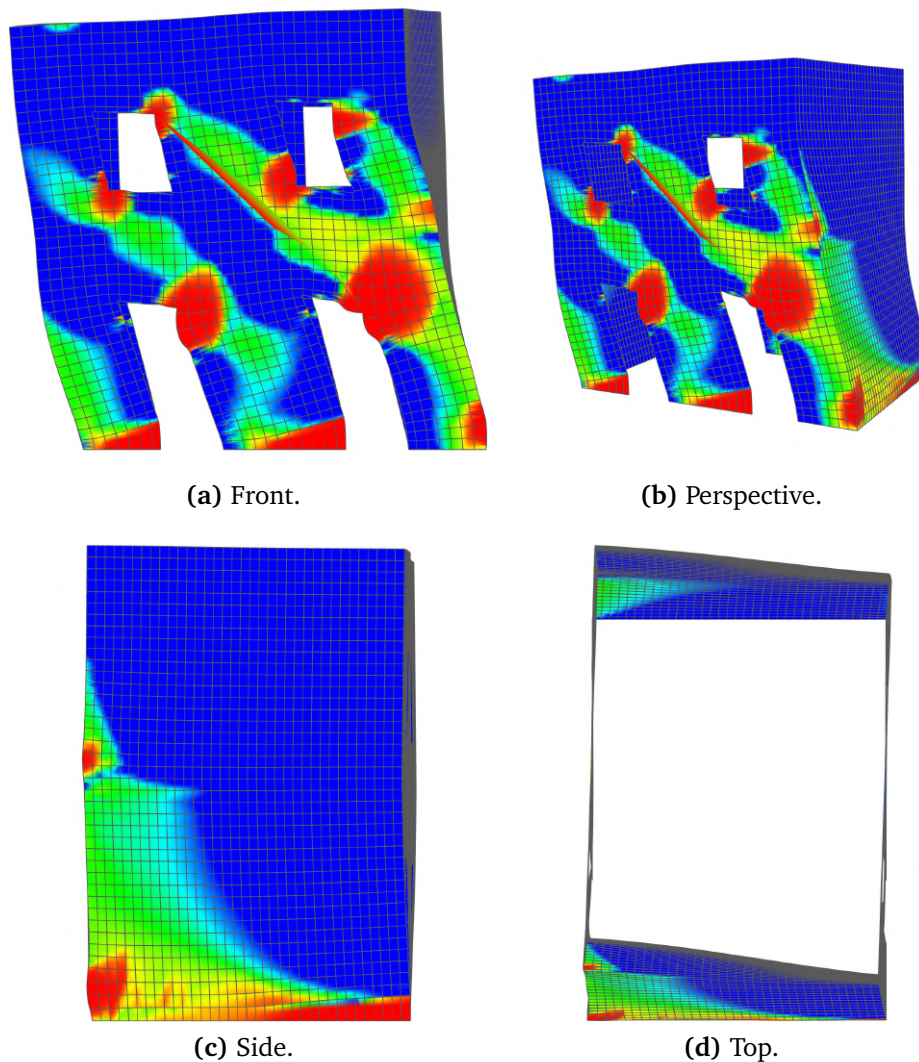


Figure 5.48: Displacements at point A (see figure 5.46).



**Figure 5.49:** Damage results for masonry house. Damage reaches from blue 0 to red 1. Displacements are scaled  $\times 200$ .

interacts with the physical enhancements. Geometrically, the model is mostly dependent on the 3 lengths of the house: the length, the width and the height. It additionally contains a trimming loop for the embodiment of windows and doors. The resulting geometrical forms are directly connected to the numerical element formulations. Additional geometrical entities of any kind can be constructed for specific formulations. This is mostly applied for supports, loads and measurements. The design and analysis model may be created by linking, disconnecting, or choosing values. This is displayed in the following by simulating 3 different options: the original design (inspired by [45]), a larger width, and no windows and doors.

The displacements amid increasing loads are presented within figure 5.48. It can be seen that the model which has a larger width is showing a slight larger final stiffness than the corresponding model with the original width. However, at lower loads it deforms more significantly than its counter model. On the other end, the model without openings performs much stronger with a significant increase of the final stiffness (larger than 1MPa). Those, results seem to be expected, however, with standard methods it may be hard to find a quantitative comparison. Figure 5.49 is presenting the corresponding damage patterns in a scaled deformed configuration. The results seem correct with a general engineering understanding and seem to match with the results from Cannizzaro et al. [45]. It shows that the loaded part of the building is deflecting significantly more than the other side and that in total a slight torsion of the structure is visible.

There is no experimental comparison for this example, which makes it complex to quantify the results. However, this study shows the great potentials which arise with the application of the proposed CAD-integrated approach. Complex geometrical operations, which would require a complete remodeling of the analysis part can be processed easily by only changing the corresponding parameters. Thus, it may facilitate to study different configurations and therefore optimizes the design processes.



# 6 Computer Aided Engineering (CAE) Workflow

To embed the recent developments in existent multiphysics software frameworks, novel software architecture and algorithms were developed, which shall be presented within this chapter. Initially, the aimed CAE workflow is enciphered (see section 6.1), followed by the integration of CAD utilities with a secluded CAD-kernel (see section 6.2.2) including essential generalized communication interfaces (see section 6.3) and the FEM-generalized quadrature point based geometries (see section 6.5), allowing to unify different finite element physics and procedures for multiphysics coupling (see section 6.5.3).

CAE stands for the broad union of computer based techniques and software to solve engineering based problems, whereby it refers to design, analysis and synthesis and their interaction. Typically, CAE comes along with the application of various Finite Element Analyses (FEA), reaching from e.g. structural analyses, computational fluid dynamics (CFD) and optimization of products or processes. Those CAE blocks are broadly grouped in three main fields: design, and pre-processing, analyses, and post-processing.

The software developments, which are discussed within this section are published in the open source project *Kratos* [126]. To facilitate future researchers a better understanding of the apparent code, this section mostly relies on the *Kratos* syntax. However, most of the section is intended to be generic to point out the generality of the proposed software architecture avenues.

## 6.1 FEM-based CAE workflow

Considering common work environments for bigger engineering projects, typically the initial phase starts with the planning and visualization of ideas. By advancing the handwritten notebook, CAD presents the optimal facilities for creation and parametric modeling of complex objects. However, from CAD to an eventual simulation it is frequently a more involved procedure, evolving from the different perspectives, being: fast visualization versus engineering correctness on the other side.

Figure 6.1 summarizes the main required steps towards a fully CAD-integrated simulation by application of classic FEM procedure.

Often the export and respective import of CAD files into pre-processing software is possible, however, the geometrical information might not be suitable for simulation. Accordingly, an involved preparation of the model is required, including a restructuring of shapes into new forms, whereby in many cases it is just more beneficial to completely redraw the model such that it is optimized for analyses. It shall be noted that in most cases those operations are non-reversible and the designer or creator of the CAD model will not benefit from the updates, which might run into problems in an iterative procedure. Those geometrical forms, either imported or remodeled are in an additional step transformed towards a FEM-analysis suitable mesh. This step habitually requires a certain simulation engineering understanding about the numerical properties for the correct adjustment of refinement to avoid e.g. eventual singularities. Additionally, within the pre-processing stage the user is required to connect a geometry selection with the corresponding kinematic formulations, internals, and boundary conditions. The numerical parameters including chosen physics and materials is exported along with the geometrical mesh towards a FEM-solver. In some cases the pre-processing might be within the same framework, however, mostly internal interfaces between the solving capabilities exist. Even though that data may be transferred easier, the data at the interface in an embedded pre-processing and analyses are typically similar to external codes.

The FEM-solver itself can be structured within 3 main stages, the initialization, the solving and the finalization (see figure 6.1). Each stage is discussed consequently and it shall be referred to algorithm 6.1 for a procedural overview. (*Kratos* [126] syntax is used to allow a better understanding of the applied code for future researchers):

**Initialization** responsible for reading in all required data and information. Geometrical forms are imported and being related to materials, physics, and the respective solver properties. This stage is used to apply mesh refinements and other model preparations, if required. Furthermore, it deals mostly with initialization of the required objects of the simulation.

**Solving** is the main stage of the analysis. Here, an iterative loop is executed until a certain breaking criteria is reached, either defined by a convergence or a user defined step or time. Within each iteration, apart from some eventual preparations, first the linear equation system is assembled, considering the elements and conditions of the solver. This is consequently solved. If a non-linear simulation is considered, the assembly and solved is repeated until a desired convergence criteria is reached or until a defined break point, which is typically seen as the failure of a simulation. After having reached the convergence, the solutions are prepared for the next iteration step and for an eventual output.

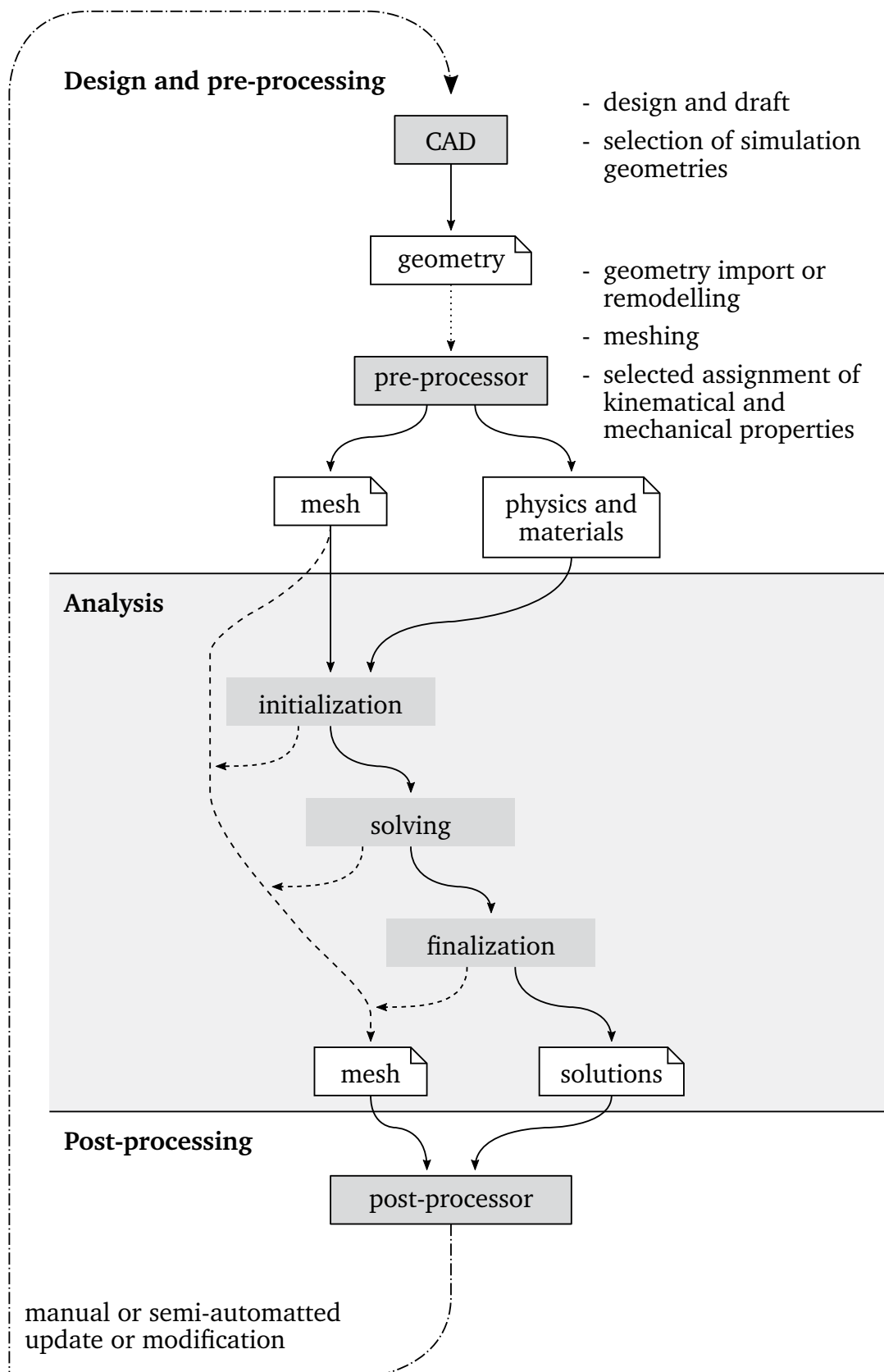


Figure 6.1: Classic FEM-based CAE workflow.

**Finalization** is often used for a post-processing of results and a separate output, which could contain an updated mesh or purely results per nodes, degrees of freedom and per elements. It shall be noted that many simulation do not consider this step at all, as output is already done after each iteration.

```
1 # Imports mesh and prepares memory and simulation
2 Analysis.Initialize()
3     Solver.ImportModelPart()
4     Solver.Initialize()
5 # Run the solution loop
6 Analysis.Solve()
7     while time < end_time
8         InitializeSolutionStep()
9         while not converged
10            Solver.SolveSolutionStep()
11            FinalizeSolutionStep()
12            OutputSolutionStep()
13 # Prepares internals for correct output
14 Analysis.Finalize()
```

**Algorithm 6.1:** Classical FEM solver procedure. *Kratos* [126] syntax is used for a comparison to the available code.

Finally, after having resolved the numerical problem, the results are taken back to the pre-processor, or a separate post-processor and are typically visualized or distinctly analyzed there. From here, it typically requires human interaction to either terminate the process or in many cases update the initial CAD model which could resolve into an iterative optimization process until a suitable design is found. This process would include many involved interfaces from CAD to pre-processing and analysis and from post-processing to CAD. Accordingly, it shall be addressed to advance this process by the continuous integration of IBRA as shown in the consequent section.

## 6.2 CAD-based CAE workflow

To avoid the difficulties arising from the conversion between the different discretizations from CAD and FEM, a workflow considering solver-integrated CAD utilities shall be presented. This involves a direct simulation based upon IBRA (see section 3.4), or can be e.g. a workaround including its own meshing, which however still keeps the connectivities to the original CAD model.

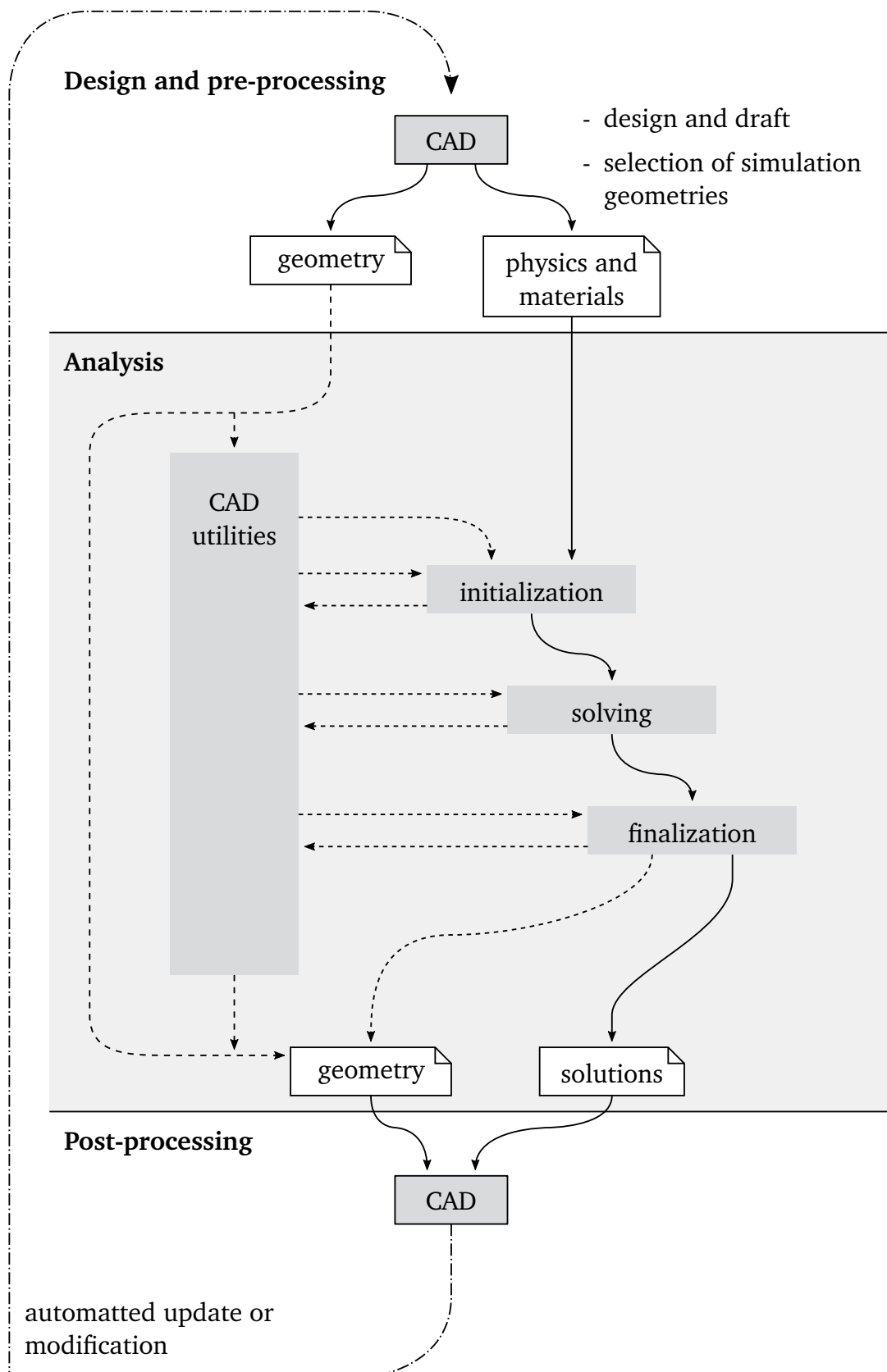


Figure 6.2: CAE workflow with integrated CAD kernel.

Initially the CAD model needs to be prepared and enhanced with physical information as suggested in section 2.3. This information is later-on being exported within two groups, the geometry, which is containing pure geometrical model data (see [222] for a comprehensive explanation and a possible format for this exchange) and a physics and materials section connecting the geometrical attributes to mechanical properties.

Those information shall be the input of the respective solver, whereby, the typical phases defined within algorithm 6.1 shall be kept. The initialization stage of the analysis shall be used to import the CAD-geometries, consequent by an eventual refinement and finally a discretization into a feasible integration domain, which shall be taken and reformed into elements. A alternative of directly using the provided geometry description, is by meshing or tessellating the latter to run classical FEM simulations. Hereby, it may help significantly to have the exact geometry description, as then, simulation demanded refinements can be operated without leaving the solver with user involved updates.

Consequently the procedures are theoretically identical to the classical FEM based CAE workflow (see section 6.1), with the difference that the CAD-based simulation can continuously communicate with the CAD geometries by eventual geometrical updates, refinements or eventual reflection and analyses of results on the geometries, including outputs upon the CAD model [27].

### 6.2.1 Interface between CAD and IBRA solver

Different stages can be enciphered between the CAD model and an analysis suitable model, whereby figure 6.3) is summarizing the required pre-processing steps for a classic IBRA analysis, as per section 3.4, in comparison to the FEM procedures with a geometry meshing. Whereby, some solvers do provide a vast amount of geometric operations, some others do not any, or provide only few. Accordingly, the differences and requirements shall be discussed.

From figure 6.3d no additional complexity is required, as standard FEM-solvers should be able to cope with this information. Accordingly, information for all integration points, including evaluated shape functions (a suggested internal data structure for FEM-codes is outlined within section 6.5) is provided from the external input. This is a important interface, which facilitates the non-invasive use of many FEM codes, however, considering the requirement of some derivatives, this interface might be very heavy. Still, considering the workflow from section 6.2 this might be the exchange between CAD-utilities and solver.

To reduce the amount of exchange information, figure 6.3c, provides only the location of the integration points within the respective domains, which requires the facilities to evaluate NURBS for the assessment of shape functions. Within [222] is proposed

a possible format for an exchange at this step. As described per section 3.4, the operations to reach this information might be methodologically deeply involved within the IBRA simulation, especially as various inputs and geometry descriptions might require very flexible treatments to achieve a robust procedure, specially mentioning the evaluation of trimmed domains, or detection of continuity information might require sophisticated knowledge. Accordingly, as this interface is a great combination between required developments within the solver with manageable exchange information, some commercial products currently rely on it (as up-to date LS Dyna [133]). The transition from CAD-geometries to a feasible integration domain can either be evaluated within separate tools or can directly be evaluated within CAD, which itself frequently provides essential mathematical functions for an eased implementation. As comparison, within classic FEM procedures, at this stage the location of quadrature points is defined according to the chosen integration rule.

The exchange from figure 6.3b is a rather theoretical exchange. However, it shall be noted within some code environments, the separation towards knot spans is known as elements, as all quadrature points within a single knot span would share the same non-zero control points. Accordingly, some software would require specifically the relation towards the groups where it belongs to.

Another essential step, which typically is the first geometry preparation step, is the refinement of geometries, as per figure 6.3a. It shall be noted that CAD-software can typically cope with those mathematically quite complex operations fairly well, which makes many solver developers rely on it. However, it shall be noted that the exchange information might be significantly different and additionally, certain mesh refinement operations are a useful tool within the simulation, which increases the flexibility of the software. This step can be somehow compared to the classic meshing per defined accuracy, as drafted by figure 6.31. This operation may happen in a dedicated pre-processor, however, can also be executed by a specific solver, with the given CAD-raw content. It shall be mentioned that within IBRA, further refinements are still possible without additional loss of quality, whereas once meshed, further refinements will not better approximate the exact geometry. While keeping the CAD model within the solver environment, re-meshing may be done upon the original shape, resulting in a better shape quality.

It shall be noted that for many purposes, as e.g. contact or solver induced meshing an interface no later than figure 6.3a would be required as later stages do not necessarily have a link back to the geometries itself which may carry the essential information.

To summarize, the whole spectrum of depicted interfaces between CAD and a solver is possible and in general it holds: A solver which is close to CAD needs a very high level of CAD functionalities and only a little amount of (complex) CAD data, whereas solvers without any dedicated build-in CAD functions require a big amount of rather basic data [222].

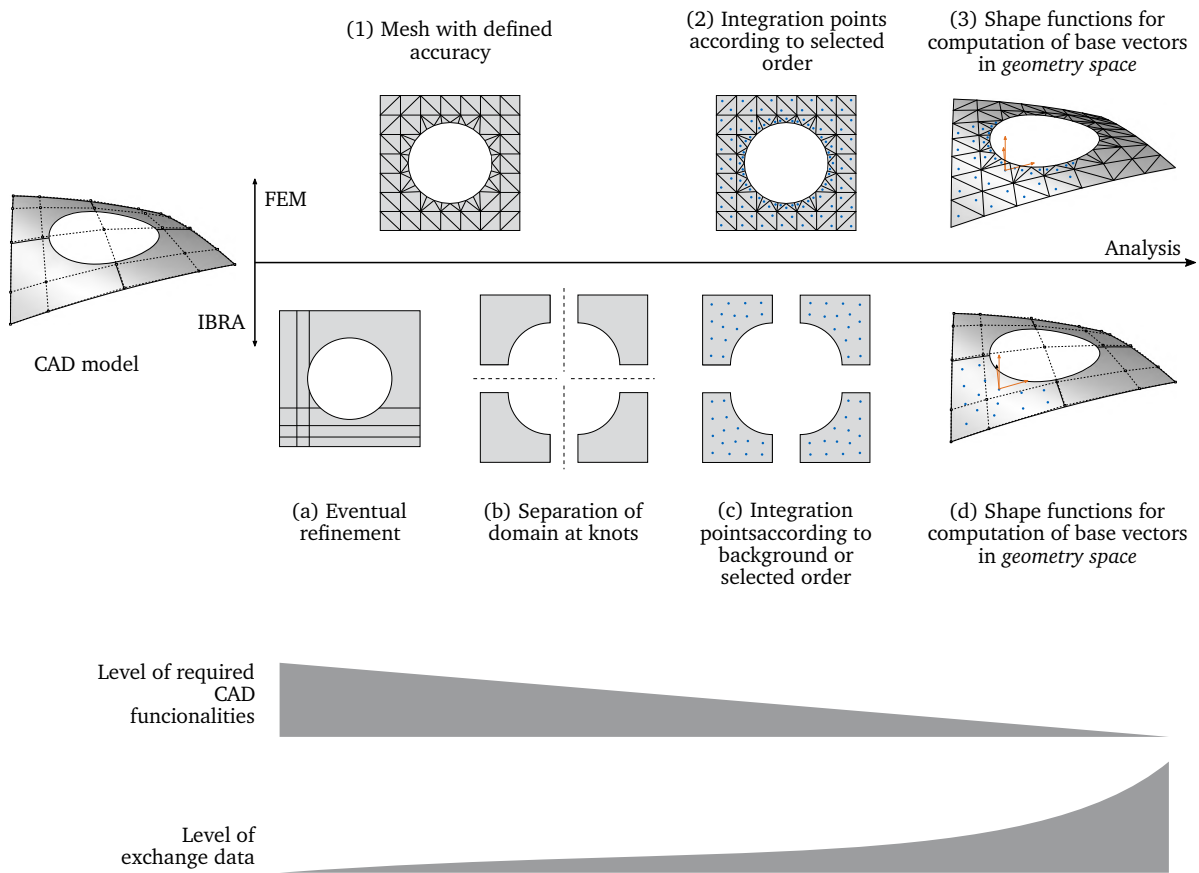


**Figure 6.3:** Selected interfaces from CAD model to analysis, including classical FEM meshing and isogeometric B-Rep analysis based approaches (modified from [222]).

### 6.2.2 Solver-integrated CAD geometry kernel

The integration of CAD facilities require a comprehensive incorporation of advanced geometries, capable to fulfill the demands from both the design and the analyses, whereby it showed up that the required geometries can be grouped in 3 types (see Figure 6.4).

The first group contains of untrimmed geometries, containing the complete description of the shape. As within this scope mainly NURBS geometries are considered this group is mainly being either NURBS solids, NURBS surfaces or NURBS curves. Nevertheless, any type of geometry is eligible to be part of this group, e.g. standard triangles, quads or lines can be used similarly, as all those geometries are standalone geometries, meaning that those are containing all relevant information and do not have any dependency to other geometries.

Some special geometries within this group are ones which are described within the parameter space of different geometries, whereby with the here described problems, those are mainly curves on surfaces, however, also e.g. surfaces within solids or curves within solids are being studied. The curve on surface is behaving as a curve considering its dimensional coordinates, however, the curve description is defined in the local space of the surface which has its own specific shape (see section 3.1.3). Considering certain mappings, first the curve shape is being evaluated, second the mapping towards global space is applied. To cope with the need of generality, those geometries form a single object, which relies itself on two or more geometries.

Secondly, the group of B-Rep geometries unites a set of sub geometries. Where NURBS geometries contain of their mathematical description, B-Rep geometries have additional boundary delineations. For a curve this is start and end point, for a surface these are the boundary curves (see section 2.1). Exemplary, a B-Rep curve on surface is incorporating a NURBS surface described in 3D with an embedded NURBS curve described in the two parameter dimensions of the surface. An important remark at this stage is that the

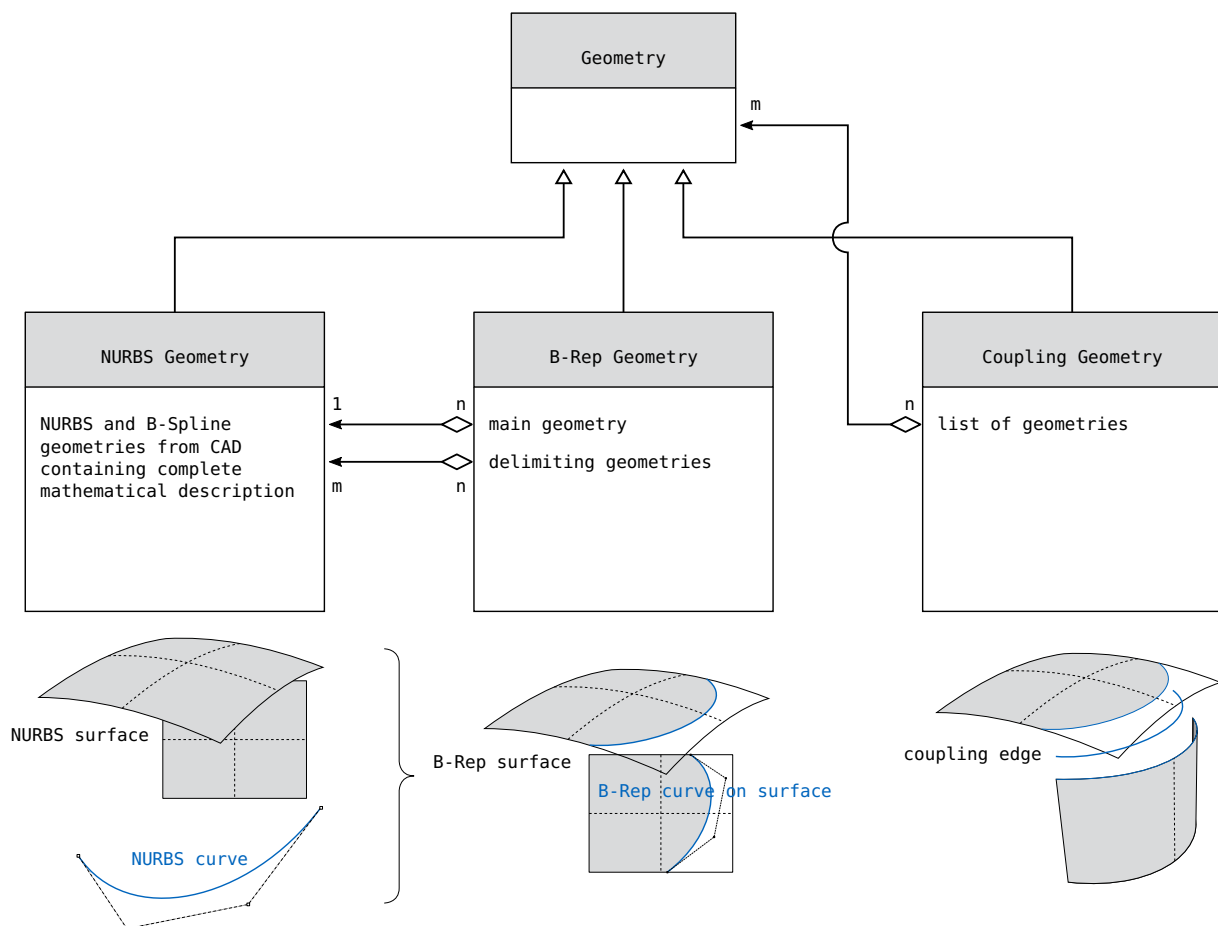


Figure 6.4: Geometry groups of CAD-described models.

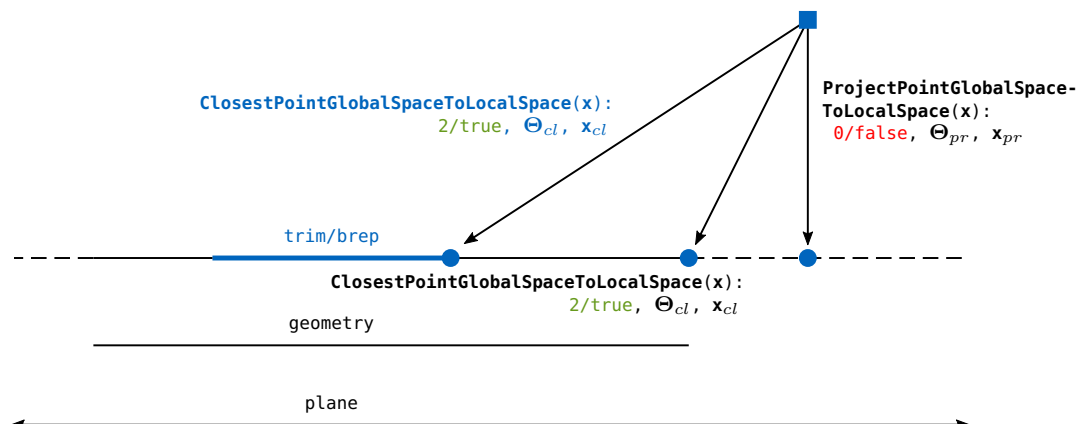
background geometry contains the control points with degrees of freedom, whereby the embedded curve might exclusively rely on the spatial position of the control points, which means that different node containers may be applied within the B-Rep geometry for efficiency. Additionally to the shape, it embraces the information of the reversal of the curve direction and the delimiting start and end points.

The third group are the coupling geometries, which contain a set of sub-geometries, combined without a predefined order, nevertheless certain dependencies need to be fulfilled to succeed water-tightness of the model. Coupling geometries are essential for the simulation with CAD-based models, as it is a tool to preserve the continuity within the sub-domains or patches within structural model. Those can be exerted to either apply pure  $C^0$  continuity of dofs between the spatial discretizations, dependent on the underlying kinematic formulation peculiar conditions as the curvature enforcement, namely  $G^1$ , is within its scope and also special contact formulation can be applied on those boundaries (More generally spoken, coupling geometries are mainly used as interface containing all required information and connection for the operations described within section 3.8.1). Because those interfaces are unimportant for CAD visualization, many systems either have difficulty detecting the coupling interfaces appropriately or disregard them completely. As a result, to ensure correct detection and description of the coupling geometries, additional efforts must often be processed, either in the CAD-API or the corresponding solver integrated CAD utilities (see section 3.5.3).

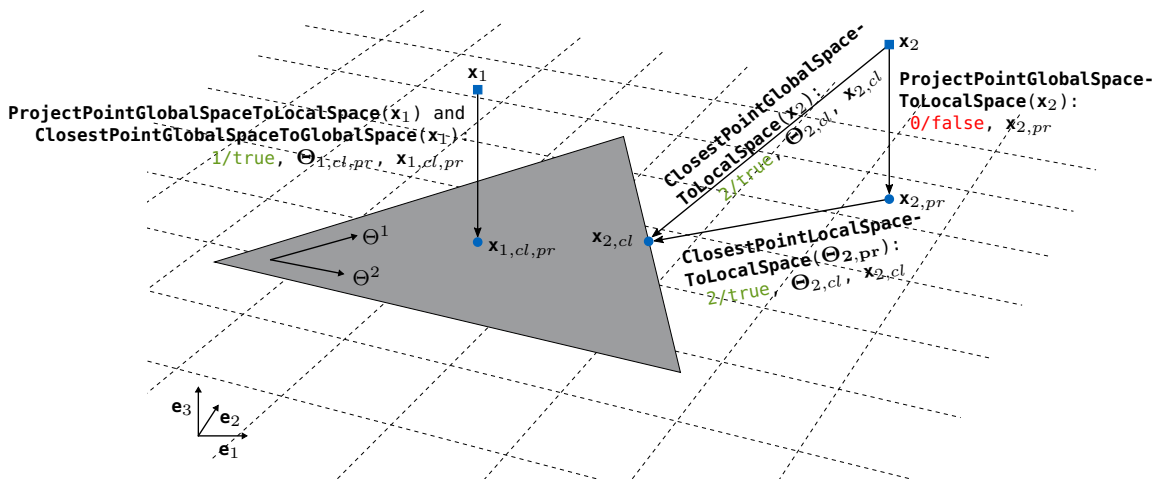
### 6.3 Geometrical interfaces

This section shall discuss some avenues to generically interact with all types geometries within a given solver environment. Initially, it shall be discussed a way to generify geometrical interfaces with the specific needs and specification from CAD-geometries. Furthermore, a standard is introduced which covers the interaction with CAD-models, feasible integration geometries and meshes.

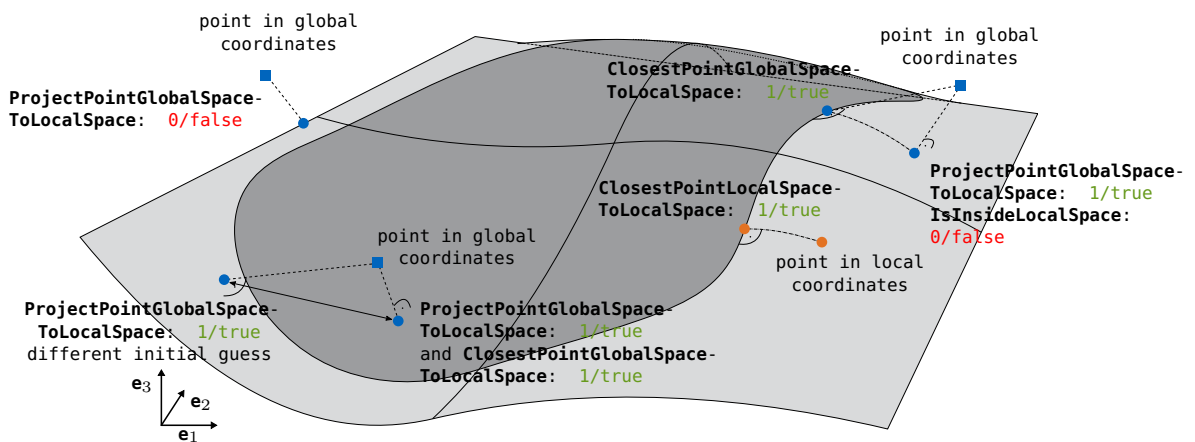
To substantially integrate NURBS and B-Rep forms within the geometrical procedures of any software framework, interfaces need to be standardized to distinguish different scenarios for algorithms, such as meshing, integration, search or intersection detection. Within different stages, certain additional information might be provided. Projection cases may be a sophisticated and often very costly operations, while sometimes those require many iterations to find the optimal position. Furthermore, closest point detections are having mostly saddle point problems and thus the convergence may not be guaranteed for a random starting point. This may make it essential to obtain a proper initial guess, whereby those may come from a closest point in a point cloud of a discrete form of the geometry. This point cloud is dependent upon the deflections of the shape and thusly might be updated continuously. This may not be a crucial issue as it is



(a) 1D line projections. Operations on the trim/ brep forms are labelled in blue, operations on the untrimmed geometry are displayed in black.



(b) 2D triangle projections.



(c) Trimmed NURBS surface projections.

Figure 6.5: Projection scenarios for different geometrical forms with according interfaces and their responses.

dependent on the amount of points and the complexity of the shape. Thus, sometimes it may be less involved to recompute the point cloud, rather than keeping the memory of storing it. However, creating the point cloud within every search may result into a computational overkill. Following, it may be helpful to group certain operations to improve the computational efficiency in highly optimized operations.

The efficiency can be optimized significantly for some use case, as sometimes certain information might be already available from the calling utilities. To make advantage of this, interfaces are split up within distinct complexities: the **ProjectPoint**, the **IsInside** and the **ClosestPoint** functions.

**ProjectPoint** is meant to directly apply mathematical projection functionalities, such as a Newton-Raphson search. Those methods are usually heavily dependent on the initial guess (see figure 6.5c) and some convergence parameters. It is specified that this interface does not make any complex advanced estimations to ensure a solution quality. Instead, it follows the mathematical algorithms for the provided input parameters. Accordingly, by using different initial guesses as input, the outcome of the interface might change. This is required because of computational efficiency and allows a user control as e.g. sometimes different contact points might be triggered due to distinct initial guesses.

**ProjectPointGlobalSpaceToLocalSpace** maps globally defined points into the local space of the plane or shape spanned by the respective geometry.

**ProjectPointLocalSpaceToLocalSpace** if point is not inside the physical domain it maps locally defined points onto the trimming, or natural boundary within the local space of the respective geometry.

**IsInside** Even though that this interface is mostly applied for checks if e.g. projections have succeeded, it may be a computationally costly operation and thusly requires a specific investigation. If the reference point is provided in global coordinate system, the method requires a projection in the local space, which may be processed through **ProjectPointGlobalSpaceToLocalSpace**. Secondly, the method checks if the local coordinates are within the bounds of the geometries. This may be accessed through the **IsInsideLocalSpace**.

**IsInsideLocalSpace** checks whether locally defined points are within the trimming, or if not applicable, the natural boundaries of the geometry in its plane. For most primitive shapes, this is a reasonably cheap operation. However, for NURBS-based trimmed surfaces this may be computationally involved. A standard operation to process the test is by creating a tessellation of the trimming curves and then making an inside outside check from the obtained polygon, which is a fairly fast algorithm and accurate within the chordal error tolerance of the tessellation. Dependent on the amount of calls, both

recreating or storing the tessellation may be applicable and thusly should be decided carefully.

**ClosestPoint** is a deeper level of the interfaces, which processes, additionally to the mathematical projection, a initial guess search for the projections which is crucial from some projection scenarios. Furthermore **ClosestPoint** ensures the **IsInside** criteria. As discussed previously, the initial guess search might be very involved and thusly computationally costly, e.g. once point clouds needs to be created. Accordingly, if applicable it would be more efficient to directly use the **Projection-Point**.

**ClosestPointLocalSpaceToLocalSpace** considering a projection was successful, however, the mapped point does not lay within the physical domain, i.e. the trimmed domain, this function provides methodologies to obtain the closest boundary of the respective geometry to obtain a point which is inside. In a 1D cases this would be the delimiter of the curve which is closest to the local coordinate, in 2D cases this mapping would be more sophisticated, considering a projection to the boundary curves.

**ClosestPointGlobalSpaceToLocalSpace** is the most comprehensive interface and accordingly computationally most costliest. In a generic implementation it may rely directly on the previous methods. In contrast, there the local coordinates are already provided, whereby here the closest point computation will require to obtain those first. Accordingly, it does a search of appropriate initial guesses for the projection, ensuring that the global minimum instead of a local optimum is found, which in some cases might lead to multiple calls of the projection function. After getting the projected point, it is checked whether the resulting point lays within the physical domain, which would lead to the call of the **ClosestPointLocalSpaceToLocalSpace** function.

## 6.4 Analysis embedded Modelers and Processes

The introduction of the CAD-kernel within the analysis process (see algorithm 6.1) with all required preparations and interfaces suggests that specific stages will need to be defined, to continuously embed novel procedures without modification of existent sequences.

In the proceeding, modelers shall be the communicators with the geometry/ internal CAD models, whereby communications can be i.e. inputs, discretizations, meshing or tessellations, spatial delimitations for contacts or boundary conditions. Respectively, solvers handle and communicate with the computation models, which includes for example the handling of nodes with dofs, assembly of linear equation system and its

solve. Finally, processes deal with the initiated geometries, or models and accordingly are initiated, only after the solvers and modelers. After the initialize phase, processes deal with the entire communication between solvers and the geometry models, as those provide interface in-between all solver based calls.

It shall be noted that all instances are embedded within a dynamic memory list, accordingly are named in plural within this section, allowing to easily vary the number of used modelers, solvers and processes by the use case and example.

To cover all tasks and to avoid conflicts, the calls are embedded and structured within the initialize of the analysis with the respective sequences as shown in algorithm 6.2.

```
1 Analysis.Initialize()
2   # Import CAD and geometry models
3   Modelers.SetupGeometryModel()
4   # Update and prepare geometry models
5   Modelers.PrepareGeometryModel()
6   # Set up computation ready models
7   Modelers.SetupComputationModel()

9   # Import computation data
10  Solvers.ImportComputationModel()
11  # Prepare computation models before analysis
12  Solvers.Initialize()

14  # Prepare computation models before analysis
15  Processes.Initialize()
```

**Algorithm 6.2:** Usage of **Modelers**, **Solvers** and **Processes**.

Referring to CAD-integrated simulations, the first stage, the *SetupGeometryModel* is mainly used for rawly importing geometries coming from CAD. This is consequent by the preparation of the entities within *PrepareGeometryModel*, being for example a eventual refinement (see section 6.4). Other possible operations within this stage could include a meshing or tessellation of the pure geometries, towards a eventual classical FEM simulation. The last geometry model oriented step, is the *SetupComputationModel*, which respectively shall be responsible for creating a analysis suitable model, accordingly is e.g. evaluating the integration domain for IBRA and creating the elements and conditions.

Within IBRA, the processes might be used for assigning the correct values of load and boundary conditions. However, various preparations are happening within this phase.

By following clearly defined interfaces, e.g. as from section 6.3, those modelers and processes can be generalized and can be used for an efficient simulation with either classical FEM, IBRA, or more sophisticated approaches involving coupled simulations.

## 6.5 Quadrature point geometry based unified FEM simulations

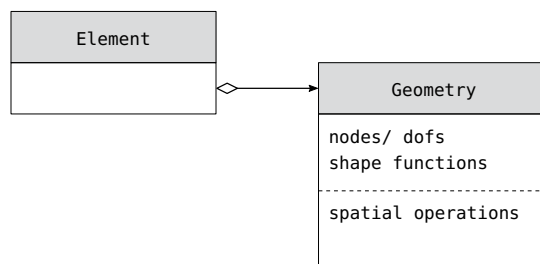
Within classic FEM software architecture geometrical information are generally decoupled from the kinematic element formulation, to allow a seamless inter-exchange without repetition of code. Each element formulation typically contains an access to property information such as constitutive laws, material properties and physical properties and a corresponding geometrical object. From this information it shall be capable of defining the kinematic formulation, resulting into local stiffness matrices and load vectors.

The geometry itself provides all information required for numerical continuum mechanics as the spacial location of integration points, its corresponding shape functions, evaluations of base vectors and more. However, geometries require to deal with more as the same set of data may additionally be used for operations as e.g. contact checks and geometrical delineations. This provides an additional advantage of the separation between element and geometry.

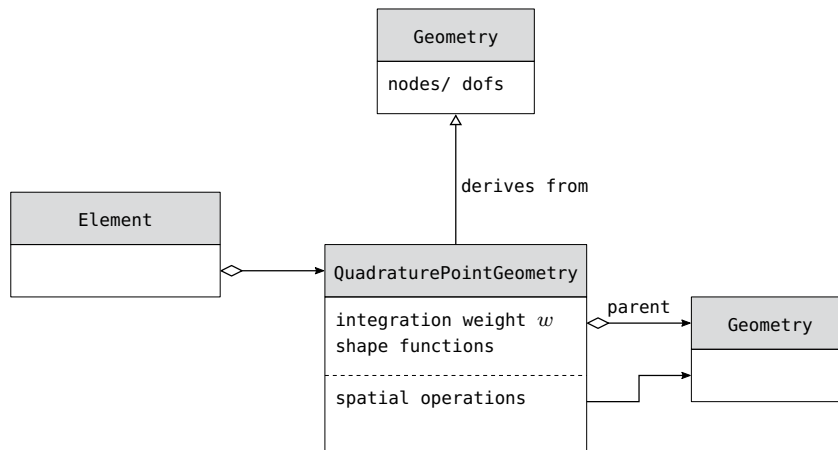
As the geometry is part of the element, the relation linking element and geometry can be seen as an aggregation, rather than a composition (see figure 6.6a). The geometry can exist and act independently, which is a characteristic typically exploited by the CAD-kernel when the geometries are meant to serve several functions rather than just completing one part.

To avoid extensive reimplementations a replacement structure has to be found which fulfills all requirements from eventual element formulations and seamlessly mimics the behavior of various geometrical objects which itself do not satisfy those conditions.

In accordance to achieve this, it was chosen to take the lowest level of a geometry, the integration point and create geometries which similarly act as an independent geometry, however, do contain only the information that a integration point needs as the integration weight (corresponding to equation 3.11) its degrees of freedom, namely the nodes and a pre-evaluated amount of shape functions and derivatives (see figure 6.6b). To make it inter-exchangeable with other geometries, it is a derivation from the geometry base class, which interfaces and functionalities still deal with accessing the respective nodes.



(a) Classic architecture.



(b) Novel proposed alternative using *QuadraturePointGeometries*.

**Figure 6.6:** Aggregation between Element and Geometry in numerical analyses software architectures.

With this novel geometry, the majority of tasks within a numerical simulation can be achieved, however, some operations require a larger bandwidth of information, as maybe a differential variation, a neighbor or contact search or many more. In order to provide this additional information, it is essential to keep the respective geometry, which the quadrature point is part of, as a parent, through which, almost all function as specifically spatial operations can be accessed.

Amid being developed for the seamless and efficient integration of IBRA (see consequent section 6.5.1) in an existent software environment, it showed off as a powerful tool, coping with much more, as e.g an efficient implementation of MPM including some unique methodological modifications (see section 6.5.2) and as a novel implementation technique for many more numerical approaches, being either particle or continuum based. It provides unique opportunities for novel developments as it allows a low level interaction for comprehensive problems, which would otherwise require an own framework. Additionally, it provides data exchange-abilities and interface connections between various physics, as of the lowest level it can directly interact with most methodologies (see section 6.5.3).

As drawback of the *quadrature point geometries* shall be mentioned that for many scenarios, it may be more memory involved as a separate implementation. However, this is many times outweighed by the fact that it can be relying on deeply optimized and largely tested implementations and developments, which would need to be redeveloped otherwise. To slightly optimize the procedures with *quadrature point geometries*, for some scenarios it is suggested to modify the new geometries in such a way that it may contain multiple integration points, being related to the same degrees of freedom, which could improve memory consumption and facilitates in some cases the assembly process.

### Remark 6.5.1: Memory of pre-evaluated shape functions in *Kratos Multiphysics*

Geometries in *Kratos* have access to a static container through which the shape function values at Gauss point locations can be accessed, where those are pre-evaluated once and are valid for all geometries of the same type. This helps reducing repetitive shape function evaluations and minimizing memory due to the static container. Additionally, respective interfaces do not need any derivation and are thusly non-virtual functions of the geometry base class as the structure and access is given through the container, which itself is provided by each geometry type. Accordingly, memory and computation costs are optimized for finite element simulations, involving standard geometry entities.

However, for special geometry types it means that those very essential interfaces cannot be overridden. To cope with this, the quadrature point geometries, mimic this container with a non-static container being carried by the respective object, which allows to use the optimized interfaces. The shape function container can be updated throughout runtime, however, it cannot be updated or computed while needed, which means on the other hand that all shape functions are required to be pre-evaluated and stored, which involves an inevitable additional use of memory.

### 6.5.1 IBRA simulation with CAD-based geometries

Both, NURBS and B-Rep geometries (see section 6.2.2) would contain sufficient information to be directly enhanced as geometries to element and condition formulations (see figure 6.6a), additionally those provide full facilities for spatial operations. However, it showed up as unfeasible to directly rely on those entities as of following reasons, being mainly related to software architecture issues.

Primitives, typically used for CAD to usually have a small amount of nodes and quadrature points, e.g. a triangle has 3 nodes and 1 quadrature point, for the lowest order integration. However, as contrast NURBS-based geometries may have endless amount of nodes, namely control points and even a higher amount of quadrature points, whereby

those are respectively typically not interfered by all control points of the geometry. The outcome is that for keeping existent implemented formulations, very large shape function vectors, containing many zeros would need to be stored and passed to the elements. This would result in additional computational overhead including a unnecessary memory consumption.

Moreover, by keeping the integration together with the full geometry objects, parallelization could not be executed within the element layer, however would need to be handled within the element itself, which could run into thread control problems with blocking waiting times.

It shall be noted that by implementing corresponding element formulations to the novel geometries, those issues could be minimized, however, bringing this together with existing code does not provide a possible design. To cope with those issues, the quadrature point geometries, as per section 6.5 were introduced. Those are initiated in the beginning from the CAD NURBS geometries. The procedures described within section 3.4 are processed and for each found quadrature point is created a new geometry and respectively element. Those quadrature point geometries, do only have the respective non-zero control points and are accordingly more efficient. Additionally, they have their own shape function container, which facilitates the memory access and accordingly the parallelization.

The initial process of detecting integration points, which might be quite involved within a trimmed domain is executed only once, which may also increase the efficiency of the entire simulation, which as controversy would be resolved at every access through the B-Rep or NURBS geometry.

### 6.5.2 The MPM as extension of FEM

Material points, are particles described within a mesh, which is principally similar to a finite element piece with a single integration point. Accordingly, quadrature point geometries shape the ideal geometrical counterpart for material point elements.

It results that by using an updated Lagrangian element, which refers to figure 3.24a, the particle based steps figure 3.24b-c can be applied by processes being executed at the beginning of each time step. Theoretically, also the end would be feasible, however, then the degrees of freedoms would be reset which would mean that own output processes would need to be created, as otherwise, internals can be evaluated by the same known form from the original implementation.

By keeping the background grid as parent of the quadrature point geometry, the search can be facilitated significantly by first checking if the material point lays still within the

same geometry and if not new location can be found easily by recursively searching within the neighboring forms.

Following the previous suggestions, the numerical procedure can be summarized by enhancing algorithm 6.1, resulting into algorithm 6.3.

```

1  # Imports mesh and prepares memory and simulation
2  Analysis.Initialize()
3      Solver.ImportModelPart()
4      Solver.Initialize()
5  # Run the solution loop
6  Analysis.Solve()
7      while time < end_time
8          Processes.BeforeInitializeSolutionStep()
9              # (b) - interpolate from background grid to internals
10             # (c) - reset grid
11             # (d) - extrapolate internals to the background grid
12             InitializeSolutionStep()
13             while not converged
14                 # (a) - Lagrangian perspective
15                 Solver.SolveSolutionStep()
16             FinalizeSolutionStep()
17             OutputSolutionStep()
18 # Prepares internals for correct output
19 Analysis.Finalize()

```

**Algorithm 6.3:** Classical FEM solver procedure, using *Kratos* [126] syntax for a better comparison.

Finally, it can be summarized that by using the recent developments for the implementation of MPM a vast re-usability of existent code structures becomes applicable, which typically implies a highly tested code, with often optimized algorithms. For the apparent case it means that the updated Lagrangian element from classical finite element structural formulations is being reused.

By combining (b)-(d) within a single function, the memory consumption can be reduced drastically, as herewith no additional memory needs to be allocated permanently. This is achieved as the relevant information can be computed in the old configuration and then transferred within the same function to the reset configuration.

Additionally, by keeping the close connection between classical FEM procedures and MPM, both, a non-continuous threshold driven update or a continuous update, known from classic MPM is similarly possible. Therefore, the process being responsible for the

particle based perspective is triggering the update only once certain criteria are met, as a number of steps or a defined stress limit. By reducing the amount of updates the accuracy of the simulation can be improved as per remark 3.7.2, including also a more reduced amount of cell crossings keep stability within the simulation and additionally the computational efficiency can be improved significantly.

### 6.5.3 Unifying inter physic coupling

As previously described, the usage of quadrature point geometries allows an unidentified coupled simulation, being on the chosen physic and geometrical description. In that manner, many numerical approaches can be streamlined by having common interfaces resulting in a unified data exchange, involving closest neighbor, closest element/condition towards Mortar-based information transformation.

Algorithm 6.4 is describing the procedure which shall be aimed for by the continuous integration of coupled multiphysics simulations. 2 independently described analysis are taken into account, being **Analysis1** and **Analysis2**. It shall be noted that those do not necessarily need to be within the same code environment, which is an essential feature considering that mostly, different tools come along with advanced implementations in varying fields.

Within the simulation, the communication between the procedures are happening either before or after running a dedicated solution loop. Depending on the physics, the desired accuracy and the wanted information exchange, the complexity of the interfacial operations between the analyses may vary largely. Starting from user defined connections and exchange relations up to interface formulations, many avenues different are applicable. However, it showed that for most cases standardized relations may be formulated. Accordingly, the need of a mapper, which independently detects interfaces raised. Hereby, again different complexities can be triggered:

**closest node** maps solution step results from a node on one side to the closest node on the other domain. It shall be noted that the solution quality may shrink drastically once nodes are not placed closely between the two domains.

**closest element/condition** brings information from dedicated elements or conditions, which typically unifies multiple nodes towards. Sufficient for many discretization, this exchange brings in inequalities if the geometries itself are not related tightly.

**Mortar-based mapping** geometrically resolves the interface (see Wilson et al. [246]). It is the most involved mapper, with typically the best accuracy for the interface equilibrium.

```

1  CoupledAnalysis.Initialize()
2      Analysis1.Initialize()
3      Analysis2.Initialize()

5      Mapper.SetUpMappingMatrix()

7  # Run the solution loop
8  CoupledAnalysis.Solve()
9      while time < end_time
10         while not converged or number of iterations
11             # number of iterations = 1 for weak and for FETI

13             Analysis1.InitializeSolutionStep()
14             while not converged
15                 Analysis1.Solver.SolveSolutionStep()
16                 Analysis1.FinalizeSolutionStep()
17                 Mapper.MapFrom1to2()

19             Analysis2.InitializeSolutionStep()
20             while not converged
21                 Analysis2.Solver.SolveSolutionStep()
22                 Analysis2.FinalizeSolutionStep()
23                 Mapper.MapFrom2to1()

25         if needed
26             Mapper.UpdateMappingMatrix()

28         Analysis1.OutputSolutionStep()
29         Analysis2.OutputSolutionStep()
30 # Prepares internals for correct output
31 CoupledAnalysis.Finalize()

```

**Algorithm 6.4:** Coupled FEM procedure, using *Kratos* [126] syntax for a better cross comparison.

Depending on the problem and the applied adjustments, the mapping information needs to be updated after or before each time step, which is mostly the case once the interface is changing largely, as e.g. in contact simulations.

Accordingly, the mapper itself has three major tasks: creating and keeping the mapping matrix which defines the relation of the two domains, finding the geometrical relation

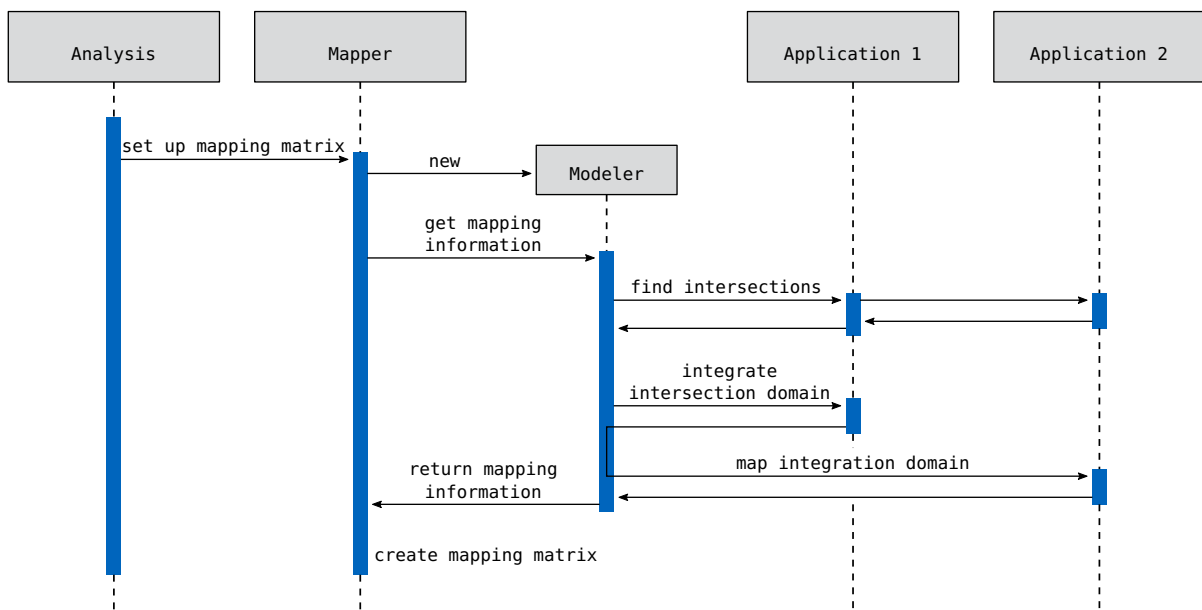


**Figure 6.7:** Sequence diagram for the creation of the mapping matrix between two independent domains from the applications 1 and 2, under consideration of a *Modeler* unit.

and exchanging the information. Whereby, keeping the first and latter are problem independent procedures, finding the geometrical relation might be involved and highly varying upon the chosen descriptions (e.g. as per section 3.4.3). To cope with this problematic, the specific operations are once again out-sourced from the original mapper and applied within modelers (similar to section 6.4). This facilitates to create mappings between domains of major complexities. However, to deal with the resulting information a standardized data management is required, which consequently is achieved through a combination of quadrature point geometries, within coupling geometries. Accordingly, the modelers create this type of information resulting from the geometrical identities of the physics. The modeler itself uses this information and assembles a mapping matrix, which is used for the information exchange.

The modeler embedded mapper sequence to create the exchange information between two independent sub-domains is graphically enciphered within figure 6.7. It shall be noted that the shown procedures from the modeler may be provided by pre processing or is detected in a different way. Accordingly, the here provided suggestions are mainly valid for the within this thesis discussed approaches, namely classical FEM, IGA/IBRA and MPM.

## 6.6 Cocodrilo: Pre- and post-processing<sup>d</sup>

The Rhino [193] plugin Cocodrilo [224] has been developed as part of this dissertation, which copes with the data collection and respective data processing towards solver interaction. Its contemporary design has been IGA, however, it grew towards a platform for parametric multiphysics problems, as it is enhanced to parametrically create inputs for classical FEM, DEM and MPM. It does furthermore provide possibilities for the post-processing of results. This covers the visualization of deformed geometries, contour plots, the position of integration points, array plots of internals, and more. The plugin works seamlessly with Kratos multiphysics [126], however, not limited.

The tool has been successfully employed in research, teaching, and industry. It is frequently exercised within the courses "Membrane workshop" and "Shell structures".

This section presents the design of the plugin. Further information can be found within [223].

### 6.6.1 Interaction with the CAD-data

Generally, multiple avenues exist for the user interaction with a CAD model, which are also dependent upon when the interaction with the models happen. Most script-based CAD software would allow to genuinely add the entities within the geometry creation process, as the user data enhancement can happen at the same time. Most systems rely on a graphical interface and do not provide access to their internal data management for the user. Additional procedures have to be incorporated. Within this publication three possible ways shall be outlined and discussed: the command-based, the GUI-based and the visual-programming-induced process.

#### **Command-based enhancements:**

Commands are the least complex interaction possibility. Each command is implemented in such a form that it consequently demands certain input, as e.g. the selection of specific geometry objects of defined types, or simpler inputs as strings or numbers. The output is either saved as a user data enrichment of the geometrical entities or as a general data collection at the plugin level.

Commands are typically interesting once few operations need to be processed, however, they might appear heavy and blocking if much information needs to be collected. Additionally, an overview of all conducted steps and the supplied information is not available without additional data visualization in the viewport or reporting commands, which is generally no blocker, however it lacks a bit in overview.

### **GUI-based enhancements:**

A GUI shall help the user to quickly get an overview of the available options and modification parameters. This allows a fairly easy introduction in a novel software, helps the unlearned user and should also reduce possible misunderstanding within the modeling process. An example of a GUI for the structural analysis with thin-walled structures is presented in figure 6.8a.

Within Rhino, it turned out that having a hybrid format between the GUI and the commands result in a very efficient work flow. Accordingly, the button of the GUI would call certain commands and provide selected properties, which were provided in the GUI. The command collects the missing information by letting the user select the respective geometrical items.

### **Visual programming-based enhancements:**

Lately, parametric design has evolved significantly allowing to make models dependent upon defined parameters [196, 162]. This allows to easily adapt to changing needs throughout the design process. Consequently, it helps to streamline certain drafts by defining the relevant sizes as parameters and later on only adjust those parameters for an automatic update without having to manually redraw the entire structure.

A prominent parametric design tools is the Grasshopper plugin [93], belonging to Rhino [193]. It comes along with a so-called visual programming platform, which allows to include various components, being e.g. geometrical entities or physical properties. It is upon the user to connect those, by developer defined interfaces, without, or with barely interacting with the source code, which gives simplified but enormous possibilities.

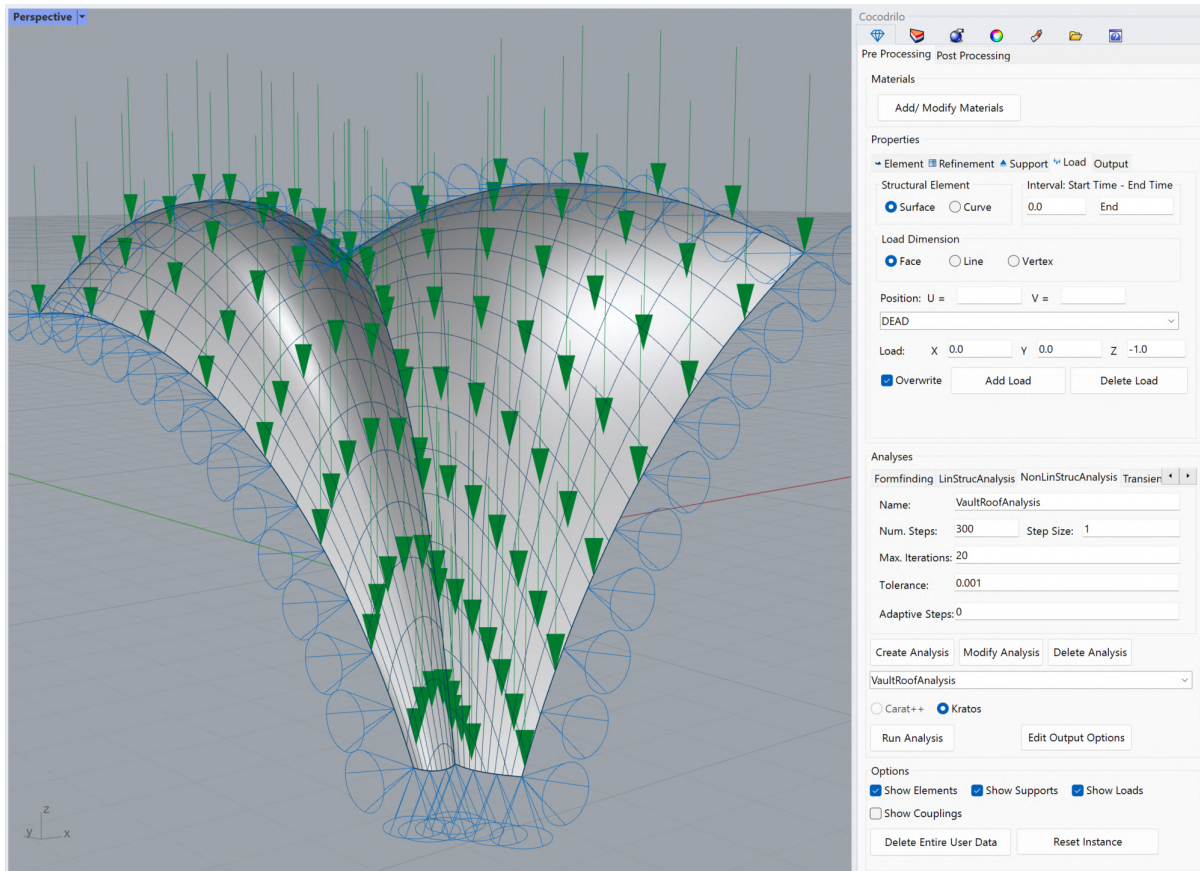
Within the scope of Grasshopper-based CAE, there already exist many structural analysis tools such as Kangaroo [116], Karamba [117] and kiwi!3d [120]<sup>a</sup>, whereby the latter is also based upon IGA. Within architecture and some fields of engineering those plugins have been established as essential parts within the design process.

Within the scope of visual programming, the previously discussed commands are exchanged by objects. Those take certain geometrical entities as inputs and pass them along with the physical enrichments. Finally all data is collected within a model object, where all entities are combined and an exchange with the solver may be processed.

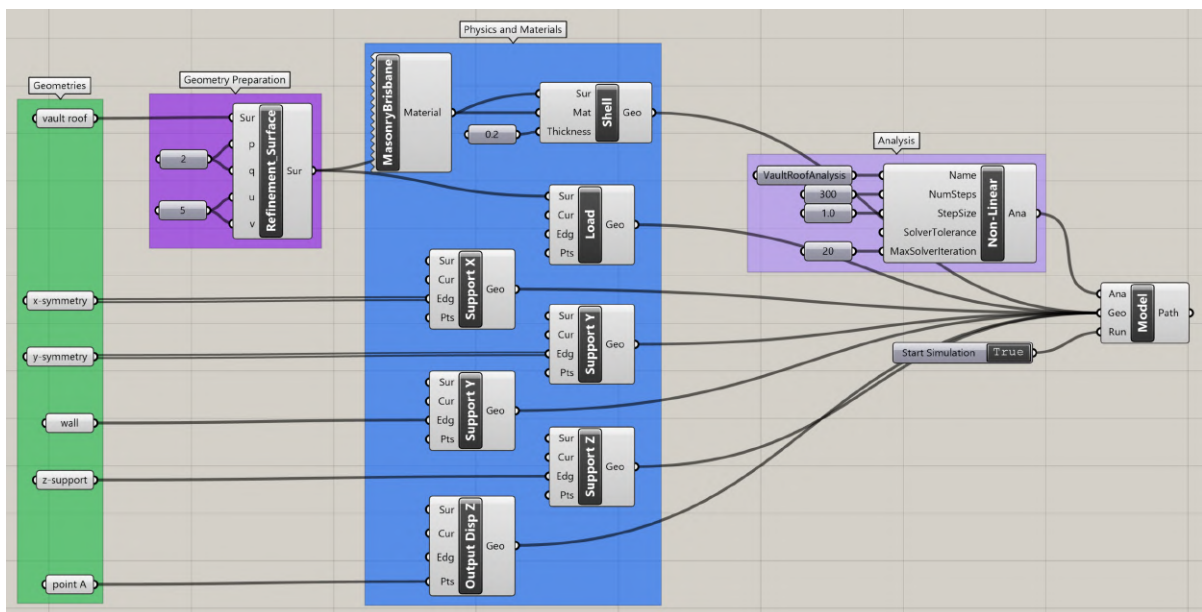
---

<sup>a</sup>kiwi!3d is based upon a similar Rhino-plugin concept as Cocodrilo and was designed and optimized to work seamlessly with Carat++ [46], whereby Cocodrilo relies on the application of KratosMulti-physics.

## 6.6 Cocodrilo: Pre- and post-processing



(a) GUI-based.



(b) Visual programming-based.

**Figure 6.8:** User interaction avenues within the pre-processing for church vault roof from section 5.6.

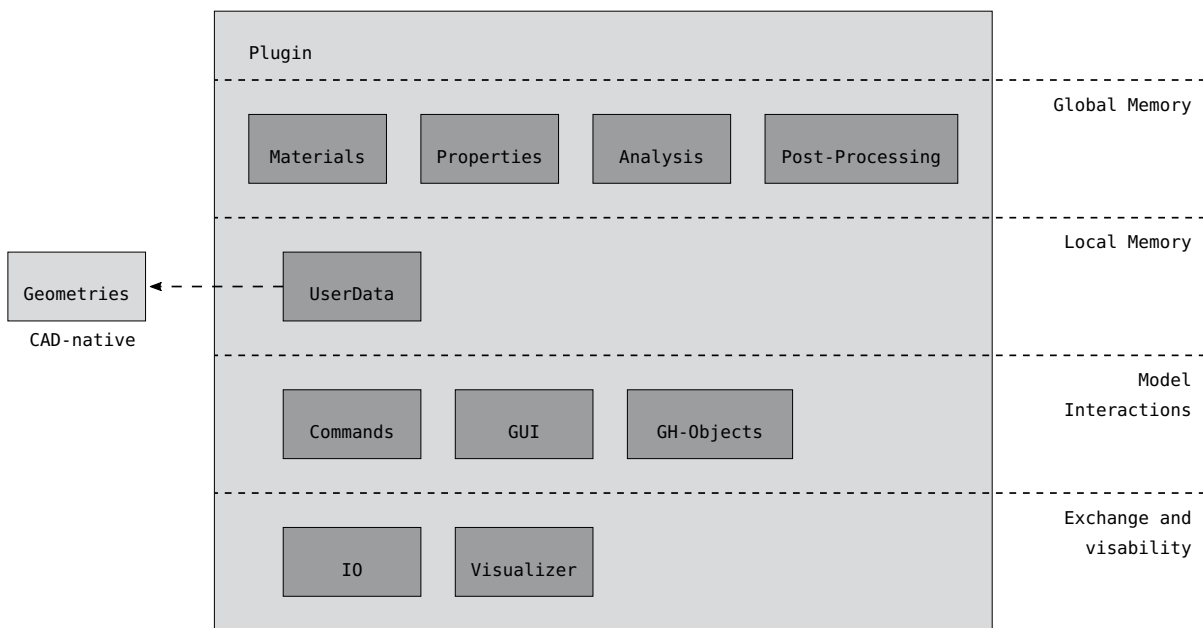


**Figure 6.9:** Software architecture of *Cocodrilo* (Modified from [228])

### Discussion about the various interaction processes:

It shall be noted that either of the previously mentioned procedures has its advantages and accordingly, use cases. The command and GUI-based approaches are typically essential once the design of the CAD model has been completed and is only imported and processed for the analysis model. In that scenario, selecting the according geometries is pretty simplified and fast for untrained users.

On the other end, once the analysis shall be included within the design process and the model variations are more than moving some control points, the visual programming shows off as the most efficient way. Specifically, once topology is changed, Rhino might have issues in keeping the correct data in place. In contrast, Grasshopper rebuilds the whole analysis model from the changed parameters. This is possible since the relation between the geometries and physics is not stored with respect to an object id but as a function of the geometric input.

### 6.6.2 Software architecture

The discussed groups are presented within figure 6.9. They are classed among the global memory, which is accessible from any place, the local memory, which is attached to specific entities and the model interactions, which describe the possibilities to enhance, or modify data trees. Those class groups shall be outlined within the following:

**Plugin** The plugin is the namespace and place of the entire code, which shall be discussed here. Additionally, it is the address for global memory, which is accessible from any instance. Some of its entities are attached to specific geometries, however, some data is not specific for an individual geometry object but appears multiple times. In order to avoid unnecessary large exchange file sizes due to data duplicates, it is beneficial to store the information once in the global memory and access it by pointers. This is e.g. the case for *Materials* and *Properties*.

**Properties** Those contain the kinematic formulations and their respective characteristics. Furthermore, the properties might also indicate global solver attributes, as e.g. required types of degrees of freedom, post-processing values, linear-solver suggestions and compatibilities, and more.

**Materials** Within the finite element software, those are often not copied but passed as reference to all elements, because depending on the chosen constitutive law this might contain many parameters. Accordingly, the plugin also tries to reduce the amount of copied information by referencing it at the geometry level and storing it globally to avoid redundancies.

**Analysis** Defines the selected analysis type, e.g. structural analyses, transient analyses, and optimizations or form-finding.

**Post-Processing** The post-processing can generally be implemented either within the local memory and attached to the respective geometries or it can be collected at global memory level and then be distributed once specific options are selected. Within the presented implementation, it was chosen to use the global memory, as it turned out as less complicated to structure the available post-processing options for the user. This avoids large lists of possible post-processing options that are only partially filled by the respective analysis. This becomes especially useful when the initial analysis set-up, i.e. the pre-processing, is not available in order to filter the options.

The post-processing operations are typically quite heavy objects since those may contain the result information of the whole model with a large set of control points, or evaluation points.

**User Data** Directly connects *Materials*, *Properties* and additional geometrical information with the respective geometry items<sup>b</sup>. Furthermore, it may be used to attach

---

<sup>b</sup>It shall be noted that within certain transform operations, as copies up to trimmings in some cases the user data might get lost. Stable copy constructor operations are required. Within Cocodrilo this is processed within the *EventWatcher* class as *onReplaceObject*.

additional, mostly embedded entities, as points or curves. It is also used to provide identical identifiers to the objects which is for example beneficial to obtain consistent coupling information.

**Commands** Are designed with the respective needs of the corresponding CAD program and should follow the suggestions from section 6.6.1.

**GUI** The *GUI* should be adapted according to the respective use case as described in section 6.6.1. Within Cocodrilo in Rhino, it is a Windows form providing all features. Essential for a seamless work is a guidance through *Delegates* which keeps all GUI-forms up-to date after data updates.

**GH-Objects** The grasshopper objects are a generalization of the previously defined *Commands*, which take inputs and allow outputs. In that way, a complete simulation with pre- and post-processing can be established. Accordingly, it allows a great flexibility with still a reliable and greatly observable frame.

**IO** The IO functions are the main function for the interfaces with the solvers. Those transfer the previously collected data into appropriate input files. Accordingly, once multiple solvers would be required, those can be enhanced by implementing an additional IO-class.

**Visualizer** The visualizer shows entities as element formulations, supports, loads or other features in order to have an visual impression of the selected options and conducted assignments. This happens within the display conduit and does not add geometries to the document but only adds them to the view port, to avoid problems with the user interaction.

### 6.6.3 Data preparation algorithms

Within this section and figure 6.10, some of the most crucial steps towards a creation of feasible input files, which require additional attention, shall be briefly discussed.

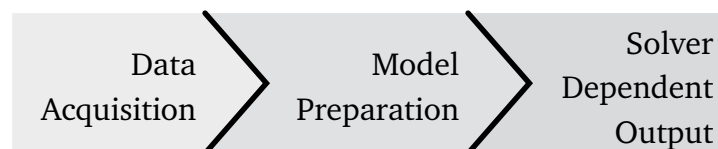


**Figure 6.10:** Steps towards an output/solver exchange

### Data Acquisition:

One of the major challenges within the pre- and post-processing is the data acquisition, which is one of the biggest differences between the Rhino-based commands and GUI and the Grasshopper induced GH-objects. Within the Rhino-based plugin, the geometrical data can be obtained from the active document. The geometries contain the user data with all required information. On the other side, within Grasshopper, it turned out as feasible to collect all simulation-relevant geometries within a final *Model* GH-object. This collection may then be processed with the same procedures as the active document collected selection.

### Model Preparation:

Some of the essential model preparation issues are mentioned within section 2.3, whereby it shall be noted that some of the discussed points may be resolved, whereas others remain limitations within CAD-integrated analysis.

The input within this operation is typically a list of B-Reps, containing mostly single or connected faces, curves and points. At this stage, it is recommended to provide unique identifiers to all entities <sup>c</sup>. This is essential to consistently store and transfer all information, including topology, to the solver.

This step is accompanied by the detection of additional coupling cases, as described in section 3.5.3. It shall be noted that there are significant differences between the Rhino- and the Grasshopper-based approaches. Whereas, within Rhino most of the connection cases may have been provided already, within Grasshopper those may often be undetected. In Grasshopper, it is possible to join geometries, similarly to Rhino. However, it is fairly difficult to select embedded or trim geometries, as those can only be selected by index. This index may not be determined in the beginning, or may change through eventual joins or when iteratively running the system with slightly changed parameters. This implies difficulties for the user. Since information is stored on separate geometries and not attached to the same objects using e.g. edge properties, the connectivity between geometries have to be found in an additional step. Accordingly, the number of intersection scenarios within the Grasshopper implementation are often more extensive. However, due to differences within the needs of visual connectivity and physical connections, it is still inevitable to do checks if geometries are intersecting, also for the Rhino path.

---

<sup>c</sup>It has been investigated to provide identifiers at the geometry construction stage, or once user data is defined and enhanced. Keeping the information consistent during the pure design process is rather complex since even simple operations as e.g. move, scale would recreate such a user data and would consequently disturb the system.

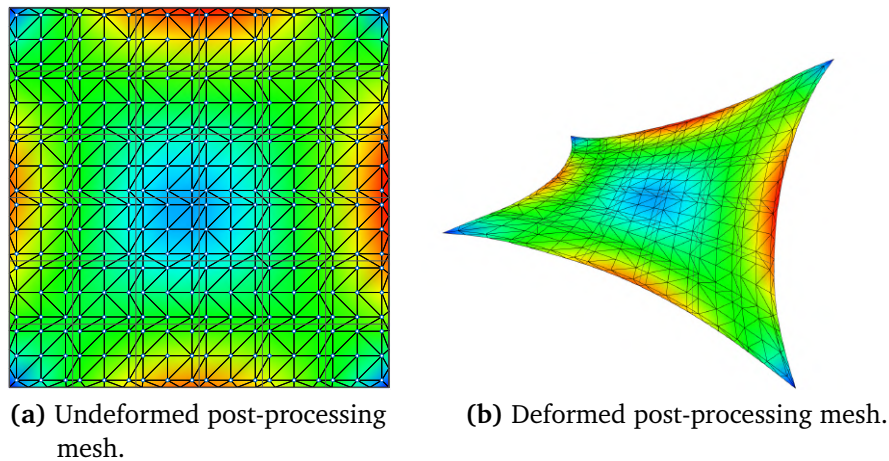


**Figure 6.11:** Post-processing mesh.

### Solver-dependent Output:

Once the data is collected and the model is prepared, the output may be processed in a solver specific way. However, a possible standardized implementation for the essentially required geometrical information is shown in [222].

#### 6.6.4 Post-processing

The aim of the proposed CAD-integrated analysis environment is a visualization upon the initial and the deformed geometries. The general shapes may be expressed by applying the resulting displacements on the control points. Furthermore, to express the magnitudes of the results a color plot shall be introduced. This contour plot is constructed by a mesh to have a fast and continuous visualization, similar to the rendering. This mesh is connected to the integration points of the simulation. Those points are often not defined upon the borders since it is not required for the integration of a surface using Gauss interpolation. Thus to complete the mesh further points need to be introduced at the borders of the shapes (Ideally, those additional points are generated by the solver and stocked with respective results to avoid a necessary extrapolation of information). With this set of points a meshing operation is processed. The possible outcome is displayed in figure 6.11a and in figure 6.11b.

This post-processing mesh may be used for nodal and integration point variables. The nodal variables are interpolated to the respective locations, whereas integration point variables can be applied directly from the post-processing of the elements. Generating a direct mesh of the integration point variables turned out as more beneficial than mapping analysis results to the program inherent visualization mesh since costly search operations can be omitted.

# 7 Summary and Outlook

The aim of this dissertation is the development of a data consistent CAD-integrated simulation of various structural scenarios for the assessment of masonry. As the CAD-integrated analysis is discussed more generically within this scope, the two key topics shall be examined separately.

## 7.1 Summary of simulation of masonry

A range of masonry structures are presented within section 5. Those cover a variety of structural elements and loadings, which are apparent within various infrastructures, buildings, and monuments. This involves in-plane compression and shear tests, and out-of-plane loaded walls, single curved arches, and cross vaults. Most masonry structures, like houses, churches or bridges are built of those components. It was possible to show, that the apparent methodologies are capable to express the typical behaviour of those structures. However, it needs to be noted that all models have required an extensive study of masonry material parameters to obtain the correct response from the digital twin. Those have been captured from various literature or have been calibrated until match throughout a series of simulations. As the studied models from available references are distinct, frequently, the respectively employed parameters do not match across those for the same examples. Another uncertainty within the simulations remains the mesh/knot span refinement. As shown within appendix B, the general response may be regularized. However, this is the specific case for perfectly aligned and quadratic quads. Once the aspect ratios become larger and the mesh becomes distorted, the regularization can only be achieved within a certain range. This effect can be identified within the church example from section 5.6, where a mesh refinement has been processed and the results are varying within a reasonable range. Additionally, according to the test series of the shear wall example (see section 5.2), varying refinement degrees would enable different failure modes. This concludes, that as part of the calibration, the mesh and its refinement enacts a significant role. Thus, as most available large-scale tests, do not provide a comprehensive amount of micro scale material parameter tests, the correctness of the numerical results cannot be verified completely, as it is not known if the matching results are achieved by calibration or by

the correct estimation of the model. Predicting the behaviour of a completely different structure with another material keeps being complex.

This problem has been used as the basis to propose a combination of tests, which need to be processed to revert the apparent controversy and enable a prediction of the large scale behaviour, while knowing the small scale parameters. Yet, it is not possible to generically prove this theory as no large scale tests with the employed material have been processed. However, the out-of-plane unreinforced masonry wall tests from section 5.3 have been constructed with a very similar masonry type. Here, the knowledge from the tests was used to facilitate the calibration of the remaining, not provided parameters. It is not seldom to find some of the micro scale experiments in specific scenarios and references. However, the combination of all is remain rare.

Another difficulty in the accurate prediction of the structural behaviour is that the tested micro scale parameter may not be equal to the corresponding parameters from the numerical material model. This parameter fluctuation is discussed for the compressive strength within various studies [230, 1]. Codes provide correction factors for the result variation, e.g. the AS 3700 [13], the CSA S304.1 [66], and the ASTM C1314 [16]. However, those correction factors do not coincide. Thus, the correction factor for each material parameter is only valid throughout the respective standard and cannot be transferred without additional manipulation. The same problematic accounts for the presented masonry analysis framework. A study has been employed to verify the specimen size, such that minimal size effects are apparent. However, it shall be mentioned that for some of the employed tests this specimen size might not be sufficient. While calibrating the model to the material test, this would not affect the results. Accordingly, this avenue would allow a prediction of structures without knowing the large scale behavior.

To summarize this section: analysis of various structures is possible. However, prediction is yet limited by parameter calibration. Accordingly, an experimental test series, fitting to the constitutive model approach is presented. This methodology is proposed, however, for its verification, the apparent masonry would need to be studied in large scale structures. It has been employed by literature results which contain very similar, but not identical material properties.

The CAD-integrated analysis, with the inclusion of a parametric design environment, has been proven as an efficient and fast tool for pre- and post-processing. It easily reacts to model changes, while keeping a consistent and correct analysis environment. IGA has brought challenges, such as the size effect of high order shape functions. However, those may have been resolved by additional regularizations. With the examples of section 5, it has been shown that most apparent effects of masonry buildings can be expressed properly by the employed methods.

Thus, for the immediate future work it is proposed to verify the presented prediction framework towards safe design guidelines. To address an even larger community and to place the methodologies in design codes, material parameters of the most common masonries and brick mortar combinations may be obtained by industry and be tabulated. Under the presumption of having those, many masonry types can be estimated accurately.

## 7.2 Summary of CAD-integrated analysis methodologies

The CAD-integrated analysis of masonry structures has been the core purpose of the processed developments. However, the methods have been employed in a generic way, which enables them to simulate a much larger variety of problems (some of the applications are presented within [226, 205, 51, 246, 149]). To successfully achieve this, the principles of the isogeometric analysis for thin-walled structures have been implemented and enhanced by novel developments, which shall be summarized consequently:

- A thorough workflow for CAD integrated analysis and design-through analysis has been established by defining required interfaces between CAD and solvers. Additionally, bottlenecks within possible models have been identified for which some solutions have been proposed (see section 3.5).
- Various element formulations (e.g. hierarchic RM shell, 3d shell, director-based RM shell) have been brought from IGA towards IBRA for the usage within a broad range of applications with the scope on thin-walled structures.
- Discretization techniques have been generalized in a form that the initial CAD-geometries are possibly used towards other physics such as MPM (see section 6.5.2). In this form a special focus has been put on the exchange ability between either of the eventually chosen numerical approaches, whereby geometrical methodologies and mathematical couplings have been adapted.
- Innovative software architecture has been proposed to achieve a non-invasive non-repetitive implementation of the required features within the open source multiphysics software *Kratos* [126]. This approach allows to geometrically deal with a large variety of combinations between different shape descriptions and kinematic element formulations.
- A Rhino/Grasshopper plugin for the CAD-integrated pre- and post-processing and the consistent data exchange has been developed, discussed, and published [223] as part of this work (see section 6.6). The developments cover conventional design flows and the setup of parametric, for geometrical and physical parameters,

models. The proposed tool has been used within research, teaching and industry and is available under open-source license [224]. With this development, not only academic examples can be set up, but also larger industry scale problems. All introduced developments can be accessed and controlled from this plugin. See [225] for modular construction design applications of this parametric design tool.

At the stage of this work, one of the major limitations of CAD-integrated analysis has been the restriction towards 2D descriptions. Accordingly, some immediate future research is suggested to investigate avenues to enable a direct CAD-integrated analysis for 3D-solid models (see [149] for a three dimensional analysis of B-Rep-described solids).

# A Uniaxial compression Bézier-curve based relaxation

Within this appendix, the uniaxial compression Bézier-curve based relaxation introduced by [182], which is shown within figure A.1 shall be deciphered. The model itself requires as input  $E$ ,  $f_{c0}$ ,  $f_{cp}$ ,  $\epsilon_{cp}$  and  $f_{cr}$ . Furthermore, the locations of the remaining required stress/strains can be controlled by a set of scalars, namely the Bézier controllers  $c_1$ ,  $c_2$ , and  $c_3$ . However, if preferred, the input can also contain the full set of stresses and strains, rather than controllers, also different controller definitions are eligible.

With the input of the Bézier controller inputs, the complete set of initial control parameters shall be defined as following:

$$\sigma_j = f_{c0}, \quad \sigma_i = \sigma_p = \sigma_j = f_{cp}, \quad \sigma_u = \sigma_r = f_{cr}, \quad (\text{A.1})$$

$$\epsilon_p = \epsilon_{cp}, \quad \epsilon_0 = \frac{\sigma_0}{E}, \quad \epsilon_i = \frac{\sigma_p}{E}, \quad (\text{A.2})$$

$$\hat{\epsilon}_j = \epsilon_p + \alpha \cdot c_2, \quad \hat{\epsilon}_k = \hat{\epsilon}_j + \alpha \cdot (1 - c_2), \quad (\text{A.3})$$

$$\text{with: } \alpha = 2\left(\epsilon_p - \frac{\sigma_r}{E}\right),$$

$$\sigma_k = \sigma_r + (\sigma_p - \sigma_r) \cdot c_1, \quad (\text{A.4})$$

$$\hat{\epsilon}_u = \frac{(\hat{\epsilon}_k - \hat{\epsilon}_j)}{(\sigma_p - \sigma_k)}(\sigma_p - \sigma_r) + \hat{\epsilon}_j, \quad \hat{\epsilon}_r = \hat{\epsilon}_u \cdot c_3. \quad (\text{A.5})$$

Within the damage model the strain-like counterpart shall be tracked as following:

$$\xi = \frac{r^-}{E}. \quad (\text{A.6})$$

which is the basis for the evaluation of the hardening variable  $\Sigma(\xi)$ :

$$\Sigma(\xi) = \begin{cases} 0 & \text{for } \xi \leq \epsilon_0 \\ \mathcal{B}(\xi, \epsilon_0, \epsilon_i, \epsilon_p, \sigma_0, \sigma_i, \sigma_p) & \text{for } \epsilon_0 < \xi \leq \epsilon_p \\ \mathcal{B}(\xi, \epsilon_p, \epsilon_j, \epsilon_k, \sigma_p, \sigma_j, \sigma_k) & \text{for } \epsilon_p < \xi \leq \epsilon_k \\ \mathcal{B}(\xi, \epsilon_k, \epsilon_u, \epsilon_r, \sigma_k, \sigma_u, \sigma_r) & \text{for } \epsilon_k < \xi \leq \epsilon_r \\ \sigma_u & \text{for } \epsilon_r < \xi \end{cases} \quad (\text{A.7})$$

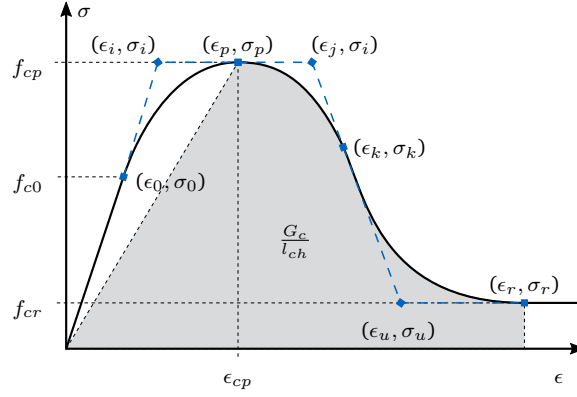


**Figure A.1:** Uniaxial compression segmented Bézier-curve based relaxation (adapted from [182]).

whereby, each Bézier curve segment is defined as following:

$$\mathcal{B}(X, x_1, x_2, x_3, y_1, y_2, y_3) = (y_1 - 2y_2 + y_3) \cdot t^2 + 2(y_2 - y_1) \cdot t + y_1 \quad (\text{A.8})$$

including the the parameters:

$$\begin{aligned} A &= x_1 - 2x_2 + x_3, & B &= 2(x_2 - x_1) \\ C &= x_1 - X, & D &= B^2 - 4AC \\ t &= \frac{-B + \sqrt{D}}{2A}. \end{aligned} \quad (\text{A.9})$$

Furthermore, the fracture energy  $G_c$ , which is the shaded area under the Bézier curve (see figure A.1) can be computed as following:

$$\begin{aligned} G_c &= G_{c,1} + G_{c,2} + G_{c,3}, & (\text{A.10}) \\ G_{c,1} &= \frac{\sigma_p \epsilon_p}{2}, & G_{c,2} &= \mathcal{A}(\epsilon_p, \epsilon_j, \epsilon_k, \sigma_p, \sigma_j, \sigma_k), & G_{c,3} &= \mathcal{A}(\epsilon_k, \epsilon_u, \epsilon_r, \sigma_k, \sigma_u, \sigma_r). \end{aligned}$$

whereby  $\mathcal{A}$  is the respective area under the Bézier curve:

$$\mathcal{A}(x_1, x_2, x_3, y_1, y_2, y_3) = \frac{x_2 y_1}{3} + \frac{x_3 y_1}{6} - \frac{x_2 y_3}{3} + \frac{x_3 y_2}{3} + \frac{x_3 y_3}{2} - x_1 \left( \frac{y_1}{2} + \frac{y_2}{3} + \frac{y_3}{6} \right). \quad (\text{A.11})$$

Considering that the explained model is an ad hoc formulation,  $G_c$  is not the total area as it will need to be regularized to comply with the grey shaded area, being  $\frac{G_c}{l_{dis}}$  (see figure A.1). The regularization is applied with a stretching factor  $\mathcal{S}$ , defined subsequently:

$$\mathcal{S} = \frac{G_c - G_{c,1}}{G_c - G_{c,1}} - 1. \quad (\text{A.12})$$

---

The stretching factor  $\mathcal{S}$  is applied on the constituents  $\epsilon_j, \epsilon_k, \epsilon_u$  and  $\epsilon_r$ :

$$\epsilon_n = \hat{\epsilon}_n + \mathcal{S}(\hat{\epsilon}_n - \epsilon_p) \quad \text{for} \quad n = j, k, u, \text{ and } r \quad (\text{A.13})$$

It shall be noted that the stretching factor should not be lower than -1, which would otherwise lead into snap back and accordingly a discontinuity in the softening. To avoid  $\mathcal{S} < -1$ , the dissipated length should be smaller than the respective plastic material length:

$$l_{dis} < l_{mat} \quad \text{where} \quad l_{mat} = \frac{2E_p G_c}{f_{cp}^2} = \frac{2G_c}{\sigma_p \epsilon_p}. \quad (\text{A.14})$$



## B Regularization

Locally delineated material models are highly dependent upon the chosen geometrical entities, whereby, the areal domain denotes how much energy can be dissipated within a single element. Accordingly, to control the relaxation of the brittle material, the geometrical extensions need to be considered to achieve appropriate mesh independent results. As trigger, the characteristic dissipation length  $l_{dis}$ , applied per equation A.12 is being used. Within this appendix, regularization shall be studied with the material properties from section 4.2.3, figure 4.12b within direction 2 are considered.

A unitless square, as per figure B.1 is consequently considered for all tests. It shall be noted that the number of elements/knot spans are counted and mentioned per test direction, even though that refinement is performed uniformly in both directions. Consequently, the gray-marked area under the relaxation curve, defined by equation A.10, is computed as the integral  $A_f$ . The reference solution is  $G_f = 1.1^4$  and the discussed error is applied as  $\epsilon = \frac{G_f - A_f}{G_f}$ .

Initially, not considering the dissipation length for the problem, for a single element is expressed by figure B.2. Here,  $l_{dis}$  is set manually to 0.5, 1, 2, and 4. The estimated errors are:

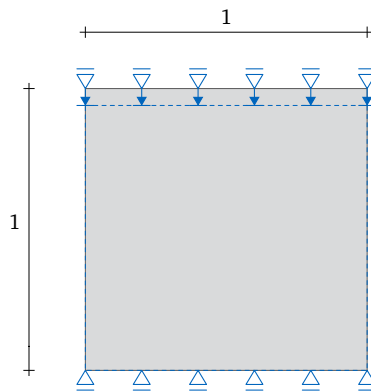


**Figure B.1:** Unite square test for regularization.

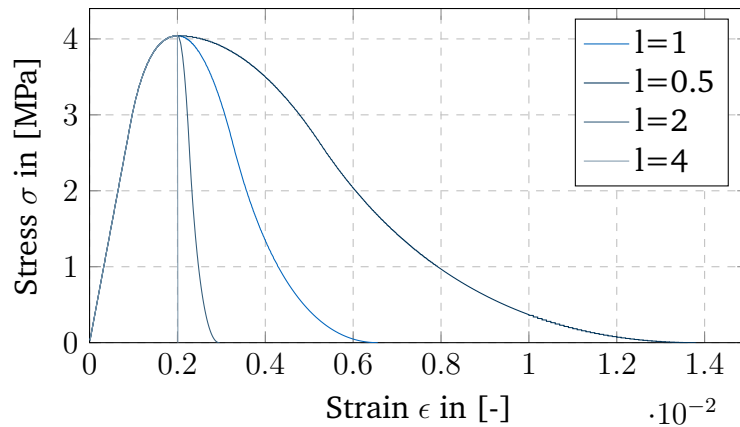


**Figure B.2:** Relaxation with fixed characteristic lengths.

element length in [-]	percentage error in [%]
0.5	95.78%
1	0.18%
2	-50.18%
4	-63.25%

Considering the possibilities in the integration the value for the regularization length 1 can be considered as exact, however, all other values do show severe discrepancies. It results that even by refining with double the elements, which results in a halved length, the model would not be usable.

Consequently,  $l_{dis}$  is set to the initial length of each element (see figure B.3a) and to the current length (see figure B.3b). It notes that both regularizations bring stability in the system. The areal errors  $\epsilon$  vary between:

number of elements [-]	initial lengths - error in [%]	current lengths - error in [%]
1	-0.18%	0.23%
10	-4.41%	-4.7%
25	-5.98%	-6.44%
100	-11.58%	-40.67%

Generally, the fracture energies are either underestimated for the utilization of initial lengths and overestimated for current lengthens. Even though the spectrum of possible simulations may have been increased significantly with this type of regularization, it still shows that for a large refinement the accurateness may not be sufficient for many scenarios.

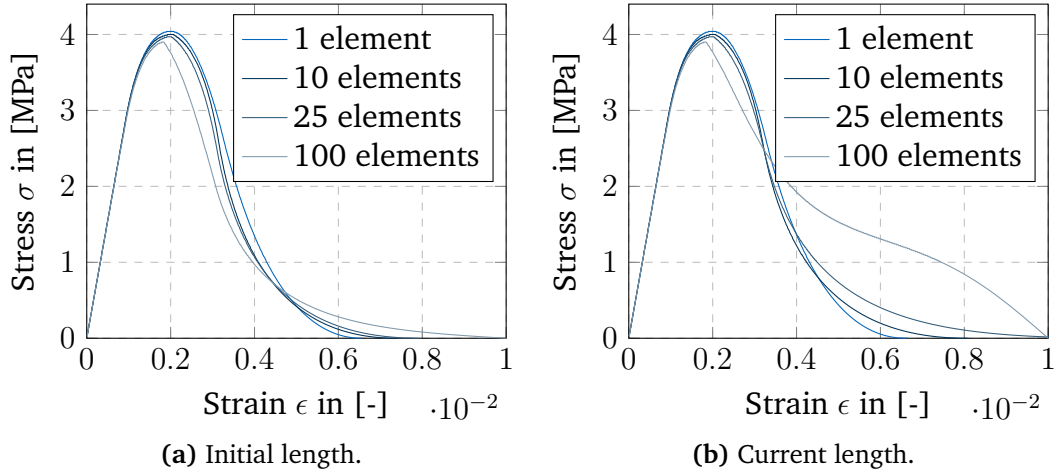


**Figure B.3:** Relaxation with initial length and current length.

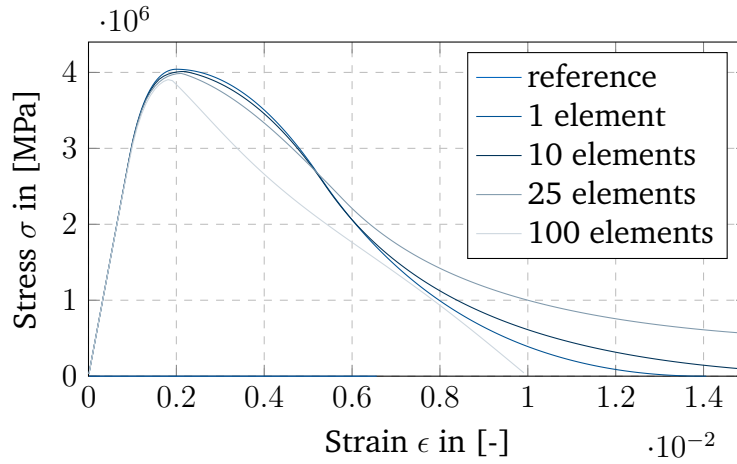


**Figure B.4:** Relaxation by consideration of integration weight.

On the further end it shall be noted that it yields, as per equation A.14 that a maximum feasible element length is delineated through the fracture energy. Specifically saying that if the element is too large in comparison to the available fracture energy, the specific element is not capable of dissipating that much energy and accordingly the regularization is not possible anymore.

Another common avenue for the approximation of the characteristic length for a respective integration point  $i$  is by considering the square root of the integration area, as this is misunderstood as the respective area and accordingly wrongly dissipation zone of the integration point:

$$l_{char,i} = \sqrt{w_i \cdot J_{2,i}}. \quad (\text{B.1})$$

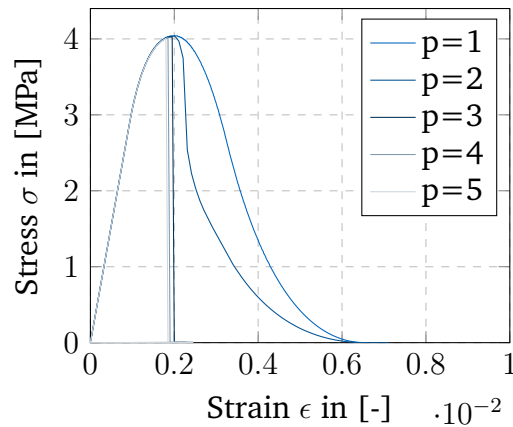


**Figure B.5:** Varying polynomial degree with initial length  $L$ .

This approach gained much attention within MPM, where generally, the integration is locally through the weight of the particles, with sometimes limited knowledge about the retaining element. However, it notes that this approach is highly dependent on the integration rule and thusly not generically suitable. The relaxation curves with this approach are presented within figure B.4, with the respective errors being:

number of elements in [-]	percentage error in [%]
1	99.69%
10	99.79%
25	240.38%
100	65.97%

Considering those results, it notes that estimating the geometrical length of the element is requiring different approaches. Additionally, this approach is dependent upon the integration rule. Accordingly, it is rather unsuitable for a stable solution.

The previous observations suggest that using the characteristic length as per element extension provides feasible results. However, this reaches limits once non-local high order shape functions are being considered, as e.g. NURBS. This is mostly required within the scope of IGA (see section 3.4).

Within NURBS the natural element boundaries are not clearly defined. Accordingly, in this scope those shall be considered as the respective lengthens of the underlying not spans.

Within figure B.5 are shown the respective results, whereby the areal errors are summarized as:

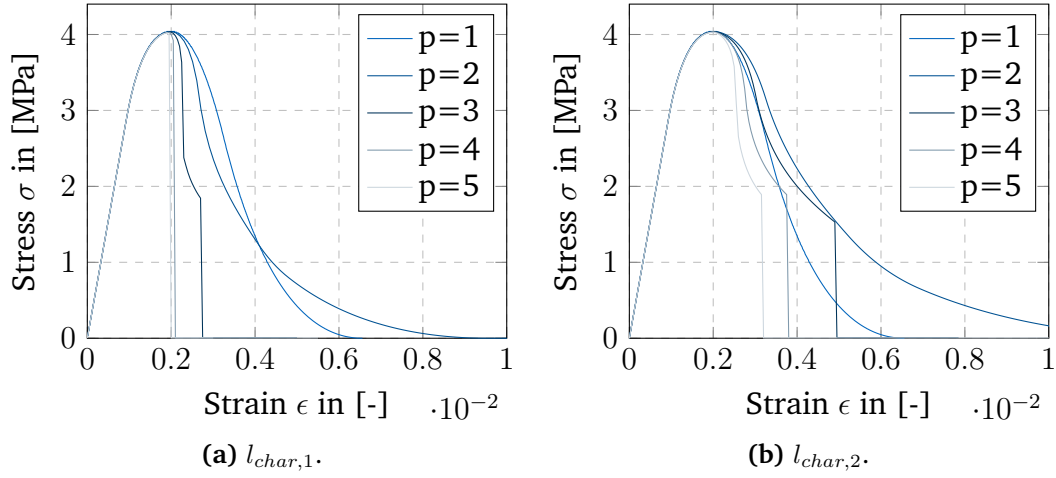


**Figure B.6:** Varying polynomial degree with  $l_{char,1}$  and  $l_{char,2}$ .

polynomial degree [-]	percentage error in [%]
1	-0.18%
2	-28.44%
3	-62.27%
4	-64.90%
5	-65.92%

As those results are not sufficiently close to get reliable results, 2 possible regularization avenues shall be studied, which consider the polynomial degree of the background shape functions:

$$l_{char,1} = \frac{l_{char}}{\sqrt{p}}, \quad (\text{B.2})$$

$$l_{char,2} = \frac{l_{char}}{p}. \quad (\text{B.3})$$

polynomial degree [-]	$l_{char,1}$ - error in [%]	$l_{char,2}$ - error in [%]
1	-0.18%	-0.18%
2	-1.51%	43.51%
3	-45.61%	8.27%
4	-58.36%	-15.89%
5	-61.89%	-30.53%

It denotes that the primary approach provides better results for a polynomial degree of  $p=2$ , whereas with larger polynomial degrees the latter avenue becomes more accurate.

## B Regularization

---

The approach provides a much larger feasibility range than not considering the respective polynomial degrees. However, it shall be noted that further research is required to find more accurate regularization techniques for NURBS forms. Future investigations may involve the stress measures in large strain regimes, as presented for various material models within [204].

# Bibliography

- [1] Ali Abasi, Reza Hassanli, Thomas Vincent, and Allan Manalo. “Influence of prism geometry on the compressive strength of concrete masonry.” In: *Construction and Building Materials* 264 (2020), p. 120182. ISSN: 0950-0618. DOI: <https://doi.org/10.1016/j.conbuildmat.2020.120182> (cit. on pp. 65, 186).
- [2] Kurdo F. Abdulla, Lee S. Cunningham, and Martin Gillie. “Simulating masonry wall behaviour using a simplified micro-model approach.” In: *Engineering Structures* 151 (2017), pp. 349–365. ISSN: 0141-0296. DOI: <https://doi.org/10.1016/j.engstruct.2017.08.021> (cit. on pp. 107, 117).
- [3] Shreeram S. Abhyankar and Chanderjit Bajaj. “Automatic parameterization of rational curves and surfaces 1: conics and conicoids.” In: *Computer-Aided Design* 19.1 (1987), pp. 11–14. ISSN: 0010-4485. DOI: [https://doi.org/10.1016/0010-4485\(87\)90147-3](https://doi.org/10.1016/0010-4485(87)90147-3) (cit. on p. 29).
- [4] abuildersperspective. *History of Structural Analysis*. 2011. URL: <https://abuildersperspective.wordpress.com/2011/09/16/history-of-structural-analysis/> (cit. on p. 1).
- [5] Daniela Addressi and Elio Sacco. “A multi-scale enriched model for the analysis of masonry panels.” In: *International Journal of Solids and Structures* 49.6 (2012), pp. 865–880. ISSN: 0020-7683. DOI: <https://doi.org/10.1016/j.ijsolstr.2011.12.004> (cit. on p. 60).
- [6] Aegion, Tyfo WS. Accessed: 2021-01-23. URL: <https://www.aegion.com/about/resources/fyfecatalog/epoxies-coatings/epoxies/tyfo-ws> (cit. on p. 68).
- [7] Alessio Ageno, Andrea Bernabò, Federico Foce, and Anna Sinopoli. “THEORY AND HISTORY OF THE THRUST LINE FOR MASONRY ARCHES. A BRIEF ACCOUNT (ARCH '04).” In: Nov. 2004 (cit. on p. 124).
- [8] Valerio Alecci, Mario Fagone, Tommaso Rotunno, and Mario De Stefano. “Shear strength of brick masonry walls assembled with different types of mortar.” In: *Construction and Building Materials* 40 (2013). Special Section on Recycling Wastes for Use as Construction Materials, pp. 1038–1045. ISSN: 0950-0618. DOI: <https://doi.org/10.1016/j.conbuildmat.2012.11.107> (cit. on pp. 76, 77).

- [9] Francisco P.A. Almeida and Paulo B. Lourenço. “Three-dimensional elastic properties of masonry by mechanics of structure gene.” In: *International Journal of Solids and Structures* 191-192 (2020), pp. 202–211. ISSN: 0020-7683. DOI: <https://doi.org/10.1016/j.ijsolstr.2019.12.009> (cit. on p. 60).
- [10] A. Anthoine. “Derivation of the in-plane elastic characteristics of masonry through homogenization theory.” In: *International Journal of Solids and Structures* 32.2 (1995), pp. 137–163. ISSN: 0020-7683. DOI: [https://doi.org/10.1016/0020-7683\(94\)00140-R](https://doi.org/10.1016/0020-7683(94)00140-R) (cit. on pp. 60, 65).
- [11] A. Apostolatos, R. Schmidt, R. Wüchner, and K.-U. Bletzinger. “A Nitsche-type formulation and comparison of the most common domain decomposition methods in isogeometric analysis.” en. In: *International Journal for Numerical Methods in Engineering* 97.7 (Feb. 2014), pp. 473–504. DOI: [10.1002/nme.4568](https://doi.org/10.1002/nme.4568) (cit. on pp. 28, 42, 50, 51).
- [12] Andreas Apostolatos. “Isogeometric Analysis of Thin-Walled Structures on Multipatch Surfaces in Fluid-Structure Interaction.” Dissertation. München: Technische Universität München, 2019. ISBN: 978-3-943683-51-6. URL: <http://mediatum.ub.tum.de/?id=1453663> (cit. on p. 41).
- [13] *AS 3700:18. Australian Standards for Masonry Structures*. 2018 (cit. on pp. 65, 186).
- [14] National Concrete Masonry Association. *Concrete Masonry Arches, TEK 14-14*. 2014. URL: <https://ncma.org/resource/concrete-masonry-arches/> (cit. on p. 124).
- [15] Panagiotis Asteris and Vagelis Plevris. “Anisotropic Masonry Failure Criterion Using Artificial Neural Networks.” In: *Neural Computing and Applications* 28 (Aug. 2017). DOI: [10.1007/s00521-016-2181-3](https://doi.org/10.1007/s00521-016-2181-3) (cit. on p. 90).
- [16] *ASTM C1314-21. Standard Test Method for Compressive Strength of Masonry Prisms*. 2021 (cit. on pp. 65, 186).
- [17] *ASTM C1717-19. Standard Test Methods for Conducting Strength Tests of Masonry Wall Panels*. 2019 (cit. on p. 65).
- [18] *Austral Bricks Commons*. Accessed: 2021-02-23. URL: <https://australbricks.com.au/qld/product/commons/> (cit. on p. 68).
- [19] Ivo Babuška, Joseph E. Flaherty, John E. Hopcroft, William D. Henshaw, Joseph E. Oliger, and Tayfun E. Tezduyar, eds. *Modeling, Mesh Generation, and Adaptive Numerical Methods for Partial Differential Equations*. Springer-Verlag, New York, 1995 (cit. on p. 2).
- [20] Claudius Barbosa, Paulo Lourenco, and João Hanai. “On the compressive strength prediction for concrete masonry prisms.” In: *Materials and Structures/Materiaux et Constructions* 43 (Apr. 2010), pp. 331–344. DOI: [10.1617/s11527-009-9492-0](https://doi.org/10.1617/s11527-009-9492-0) (cit. on p. 65).

- [21] Yavuz Basar and Wilfried B. Krätzig. *Mechanik der Flächentragwerke*. 1985. ISBN: 978-3-322-93983-8. DOI: <https://link.springer.com/book/10.1007%2F978-3-322-93983-8> (cit. on p. 15).
- [22] Klaus-Jürgen Bathe. *Finite element procedures*. Boston, Mass.: Bathe, 2006. ISBN: 9780979004902 (cit. on p. 2).
- [23] A. M. Bauer, M. Breitenberger, B. Philipp, R. Wüchner, and K. -U Bletzinger. “Embedded structural entities in NURBS-based isogeometric analysis.” In: *Computer Methods in Applied Mechanics and Engineering* 325 (2017), pp. 198–218. ISSN: 0045-7825. DOI: [10.1016/j.cma.2017.07.010](https://doi.org/10.1016/j.cma.2017.07.010) (cit. on p. 42).
- [24] A. M. Bauer, M. Breitenberger, B. Philipp, R. Wüchner, and K.-U. Bletzinger. “Nonlinear isogeometric spatial Bernoulli beam.” In: *Computer Methods in Applied Mechanics and Engineering* 303 (2016), pp. 101–127. ISSN: 00457825. DOI: [10.1016/j.cma.2015.12.027](https://doi.org/10.1016/j.cma.2015.12.027) (cit. on pp. 28, 35, 38).
- [25] A. M. Bauer, R. Wüchner, and K. -U Bletzinger. “Weak coupling of nonlinear isogeometric spatial Bernoulli beams.” In: *Computer Methods in Applied Mechanics and Engineering* 361 (2020), p. 112747. ISSN: 0045-7825. DOI: [10.1016/j.cma.2019.112747](https://doi.org/10.1016/j.cma.2019.112747) (cit. on pp. 38, 52).
- [26] Anna Maria Bauer. “CAD-integrated Isogeometric Analysis and Design of Lightweight Structures.” Dissertation. München: Technische Universität München, 2020. ISBN: 978-3-943683-54-7. URL: <http://mediatum.ub.tum.de/?id=1540855> (cit. on pp. 39, 43, 52).
- [27] Daniel Baumgärtner. “On the grid-based shape optimization of structures with internal flow and the feedback of shape changes into a CAD model.” Dissertation. München: Technische Universität München, 2020 (cit. on p. 160).
- [28] Zdenek Bažant and Byung Oh. “Crack Band Theory for Fracture of Concrete.” In: *Matériaux et Constructions* 16 (May 1983), pp. 155–177. DOI: [10.1007/BF02486267](https://doi.org/10.1007/BF02486267) (cit. on pp. 94, 101).
- [29] Zdenek Bažant and Jaime Planas. *Fracture and Size Effect in Concrete and Other Quasibrittle Materials*. Mar. 2019. ISBN: 9780203756799. DOI: [10.1201/9780203756799](https://doi.org/10.1201/9780203756799) (cit. on p. 94).
- [30] Y. Bazilevs, V. M. Calo, J. A. Cottrell, J. A. Evans, T.J.R. Hughes, S. Lipton, M. A. Scott, and T. W. Sederberg. “Isogeometric analysis using T-splines.” In: *Computer Methods in Applied Mechanics and Engineering* 199.5 (2010), pp. 229–263. ISSN: 0045-7825. DOI: [10.1016/j.cma.2009.02.036](https://doi.org/10.1016/j.cma.2009.02.036) (cit. on p. 22).
- [31] D.J. Benson, Y. Bazilevs, M.C. Hsu, and T.J.R. Hughes. “Isogeometric shell analysis: The Reissner–Mindlin shell.” In: *Computer Methods in Applied Mechanics and Engineering* 199.5 (2010). Computational Geometry and Analysis, pp. 276–289. ISSN: 0045-7825. DOI: <https://doi.org/10.1016/j.cma.2009.05.011> (cit. on p. 23).

- [32] L. Berto, A. Saetta, R. Scotta, and R. Vitaliani. “Failure mechanism of masonry prism loaded in axial compression: Computational aspects.” In: *Materials and Structures/Materiaux et Constructions* 38.276 (2005). Cited by: 26, pp. 249–256. DOI: [10.1617/14096](https://doi.org/10.1617/14096) (cit. on p. 101).
- [33] Luisa Berto, Anna Saetta, Roberto Scotta, and Renato Vitaliani. “An orthotropic damage model for masonry structures.” In: *International Journal for Numerical Methods in Engineering* 55.2 (2002), pp. 127–157. DOI: <https://doi.org/10.1002/nme.495> (cit. on p. 90).
- [34] Elisa Bertolesi, Jose M. Adam, Paula Rinaudo, and Pedro A. Calderón. “Research and practice on masonry cross vaults – A review.” In: *Engineering Structures* 180 (2019), pp. 67–88. ISSN: 0141-0296. DOI: <https://doi.org/10.1016/j.engstruct.2018.10.085> (cit. on p. 135).
- [35] Josef Betten. “Applications of tensor functions to the formulation of yield criteria for anisotropic materials.” In: *International Journal of Plasticity* 4.1 (1988), pp. 29–46. ISSN: 0749-6419. DOI: [https://doi.org/10.1016/0749-6419\(88\)90003-4](https://doi.org/10.1016/0749-6419(88)90003-4) (cit. on pp. 90, 94, 95).
- [36] Kai-Uwe Bletzinger. “Formoptimierung von Flächentragwerken.” PhD thesis. Universität Stuttgart, 1990 (cit. on p. 41).
- [37] P. Block and J. Ochsendorf. “Thrust network analysis: A new methodology for three-dimensional equilibrium.” In: *Journal of the International Association for Shell and Spatial Structures* 48.155 (2007), pp. 167–173 (cit. on p. 124).
- [38] Carl de Boor. “On calculating with B-splines.” In: *Journal of Approximation Theory* 6.1 (1972), pp. 50–62. ISSN: 0021-9045. DOI: [10.1016/0021-9045\(72\)90080-9](https://doi.org/10.1016/0021-9045(72)90080-9) (cit. on p. 20).
- [39] Andre Borrmann, Markus König, Christian Koch, Jakob Beetz, Frank Petzold, Andreas Hild, Christoph Langenhan, and Henrik Thomä. *Building Information Modeling Technologische Grundlagen und industrielle Praxis*. Aug. 2015. ISBN: 978-3-658-05606-3. DOI: [10.1007/978-3-658-05606-3](https://doi.org/10.1007/978-3-658-05606-3) (cit. on p. 7).
- [40] M. Breitenberger, A. Apostolatos, B. Philipp, R. Wüchner, and K.-U. Bletzinger. “Analysis in computer aided design: Nonlinear isogeometric B-Rep analysis of shell structures.” In: *Computer Methods in Applied Mechanics and Engineering* 284 (2015). Isogeometric Analysis Special Issue, pp. 401–457. ISSN: 0045-7825. DOI: <http://dx.doi.org/10.1016/j.cma.2014.09.033> (cit. on pp. 2, 28, 29, 31, 39, 41, 42, 51).
- [41] Michael Breitenberger. “CAD-Integrated Design and Analysis of Shell Structures.” Dissertation. München: Technische Universität München, 2016 (cit. on pp. 19, 29, 39, 41, 42).

- [42] Antonio Brencich and Renata Morbiducci. “Masonry Arches: Historical Rules and Modern Mechanics.” In: *International Journal of Architectural Heritage* 1.2 (2007), pp. 165–189. DOI: [10.1080/15583050701312926](https://doi.org/10.1080/15583050701312926) (cit. on p. 124).
- [43] Ericka Brivadis, Annalisa Buffa, Barbara Wohlmuth, and Linus Wunderlich. “Isogeometric mortar methods.” In: *Computer Methods in Applied Mechanics and Engineering* 284 (2015), pp. 292–319. ISSN: 0045-7825. DOI: [10.1016/j.cma.2014.09.012](https://doi.org/10.1016/j.cma.2014.09.012) (cit. on p. 50).
- [44] C. J. Burgoyne and M. A. Crisfield. “Numerical integration strategy for plates and shells.” In: *International Journal for Numerical Methods in Engineering* 29.1 (1990), pp. 105–121. DOI: <https://doi.org/10.1002/nme.1620290108> (cit. on p. 27).
- [45] Francesco Cannizzaro, Giovanni Castellazzi, Nicola Grillanda, Bartolomeo Pantò, and Massimo Petracca. “Modelling the nonlinear static response of a 2-storey URM benchmark case study: comparison among different modelling strategies using two- and three-dimensional elements.” In: *Bulletin of Earthquake Engineering* 20.4 (2022), pp. 2085–2114. DOI: [10.1007/s10518-021-01183-0](https://doi.org/10.1007/s10518-021-01183-0) (cit. on pp. 150, 152, 153).
- [46] Carat++. URL: [www.cee.ed.tum.de/en/st/software/research/carat/](http://www.cee.ed.tum.de/en/st/software/research/carat/) (cit. on p. 178).
- [47] Serena Cattari and Guido Magenes. “Benchmarking the software packages to model and assess the seismic response of unreinforced masonry existing buildings through nonlinear static analyses.” In: *Bulletin of Earthquake Engineering* 20.4 (2022), pp. 1901–1936. DOI: [10.1007/s10518-021-01078-0](https://doi.org/10.1007/s10518-021-01078-0) (cit. on p. 150).
- [48] N. Cavalagli, F. Cluni, and V. Gusella. “Evaluation of a Statistically Equivalent Periodic Unit Cell for a quasi-periodic masonry.” In: *International Journal of Solids and Structures* 50.25 (2013), pp. 4226–4240. ISSN: 0020-7683. DOI: <https://doi.org/10.1016/j.ijsolstr.2013.08.027> (cit. on p. 60).
- [49] M. Cervera, E. Hinton, and O. Hassan. “Nonlinear analysis of reinforced concrete plate and shell structures using 20-noded isoparametric brick elements.” In: *Computers & Structures* 25.6 (1987), pp. 845–869. ISSN: 0045-7949. DOI: [https://doi.org/10.1016/0045-7949\(87\)90200-8](https://doi.org/10.1016/0045-7949(87)90200-8) (cit. on p. 94).
- [50] Miguel Cervera, Javier Oliver, and Rui Faria. “Seismic evaluation of concrete dams via continuum damage models.” In: *Earthquake Engineering & Structural Dynamics* 24.9 (1995), pp. 1225–1245. DOI: <https://doi.org/10.1002/eqe.4290240905> (cit. on pp. 90, 91).

- [51] Bodhinanda Chandra, Veronika Singer, Tobias Teschemacher, Roland Wüchner, and Antonia Lares. “Nonconforming Dirichlet boundary conditions in implicit material point method by means of penalty augmentation.” en. In: *Acta Geotechnica* (2021). DOI: [10.1007/s11440-020-01123-3](https://doi.org/10.1007/s11440-020-01123-3) (cit. on pp. 3, 187).
- [52] Margarit Chasapi, Leonie Mester, Bernd Simeon, and Sven Klinkel. “Isogeometric analysis of 3D solids in boundary representation for problems in nonlinear solid mechanics and structural dynamics.” In: *International Journal for Numerical Methods in Engineering* (). DOI: <https://doi.org/10.1002/nme.6893> (cit. on p. 35).
- [53] Andrea Chiozzi, Gabriele Milani, and Antonio Tralli. “A Genetic Algorithm NURBS-based new approach for fast kinematic limit analysis of masonry vaults.” In: *Computers & Structures* 182 (2017), pp. 187–204. ISSN: 0045-7949. DOI: <https://doi.org/10.1016/j.compstruc.2016.11.003> (cit. on p. 124).
- [54] Andrea Chiozzi, Gabriele Milani, and Antonio Tralli. “Fast Kinematic Limit Analysis of FRP-Reinforced Masonry Vaults. II: Numerical Simulations.” In: *Journal of Engineering Mechanics* 143.9 (2017), p. 04017072. DOI: [10.1061/\(ASCE\)EM.1943-7889.0001268](https://doi.org/10.1061/(ASCE)EM.1943-7889.0001268) (cit. on pp. 124, 136, 137, 139).
- [55] Corrado Chisari, Lorenzo Macorini, Claudio Amadio, and Bassam A. Izzuddin. “Identification of mesoscale model parameters for brick-masonry.” In: *International Journal of Solids and Structures* 146 (2018), pp. 224–240. ISSN: 0020-7683. DOI: <https://doi.org/10.1016/j.ijsolstr.2018.04.003> (cit. on p. 57).
- [56] F. Cirak, M. Ortiz, and P. Schröder. “Subdivision surfaces: a new paradigm for thin-shell finite-element analysis.” In: *International Journal for Numerical Methods in Engineering* 47 (2000), pp. 2039–2072. ISSN: 00295981 (cit. on p. 22).
- [57] Alain Combescure and Anthony Gravouil. “A numerical scheme to couple subdomains with different time-steps for predominantly linear transient analysis.” In: *Computer Methods in Applied Mechanics and Engineering* 191.11 (2002), pp. 1129–1157. ISSN: 0045-7825. DOI: [https://doi.org/10.1016/S0045-7825\(01\)00190-6](https://doi.org/10.1016/S0045-7825(01)00190-6) (cit. on p. 56).
- [58] “Computers in Manufacturing.” In: *Computer Aided Design and Manufacturing*. 2020. Chap. 1, pp. 1–33. ISBN: 9781119667889. DOI: <https://doi.org/10.1002/9781119667889.ch1> (cit. on p. 9).
- [59] Luca Coradello, Davide D’Angella, Massimo Carraturo, Josef Kiendl, Stefan Kollmannsberger, Ernst Rank, and Alessandro Reali. “Hierarchically refined isogeometric analysis of trimmed shells.” In: *Computational Mechanics* 66.2 (2020), pp. 431–447. DOI: [10.1007/s00466-020-01858-6](https://doi.org/10.1007/s00466-020-01858-6) (cit. on p. 22).

- [60] Luca Coradello, Josef Kiendl, and Annalisa Buffa. “Coupling of non-conforming trimmed isogeometric Kirchhoff–Love shells via a projected super-penalty approach.” In: *Computer Methods in Applied Mechanics and Engineering* 387 (2021), p. 114187. ISSN: 0045-7825. DOI: <https://doi.org/10.1016/j.cma.2021.114187> (cit. on p. 41).
- [61] Marco Corradi, Antonio Borri, and Andrea Vignoli. “Experimental study on the determination of strength of masonry walls.” In: *Construction and Building Materials* 17 (July 2003), pp. 325–337. DOI: [10.1016/S0950-0618\(03\)00007-2](https://doi.org/10.1016/S0950-0618(03)00007-2) (cit. on pp. 59, 76).
- [62] J. Austin Cottrell, Thomas J. R. Hughes, and Yuri Bazilevs. *Isogeometric Analysis: Toward Integration of CAD and FEA*. 1st. John Wiley & Sons, Ltd, 2009. ISBN: 9780470748732. DOI: <https://doi.org/10.1002/9780470749081> (cit. on p. 29).
- [63] M. G. COX. “The Numerical Evaluation of B-Splines.” In: *IMA Journal of Applied Mathematics* 10.2 (1972), pp. 134–149. ISSN: 0272-4960. DOI: [10.1093/imamat/10.2.134](https://doi.org/10.1093/imamat/10.2.134) (cit. on p. 20).
- [64] Giuseppe Creazza, Renato Matteazzi, Anna Saetta, and Renato Vitaliani. “Analyses of Masonry Vaults: A Macro Approach based on Three-Dimensional Damage Model.” In: *Journal of Structural Engineering* 128.5 (2002), pp. 646–654. DOI: [10.1061/\(ASCE\)0733-9445\(2002\)128:5\(646\)](https://doi.org/10.1061/(ASCE)0733-9445(2002)128:5(646)) (cit. on pp. 136–139).
- [65] Ray Crotty. “The Impact of Building Information Modeling. Transforming Construction.” In: *The Impact of Building Information Modelling: Transforming Construction* (Mar. 2013), pp. 1–216. DOI: [10.4324/9780203836019](https://doi.org/10.4324/9780203836019) (cit. on p. 7).
- [66] CSA, S304-14 (R2019). *Design of masonry structures*. 2019 (cit. on pp. 65, 186).
- [67] Davide D. Angella, Stefan Kollmannsberger, Ernst Rank, and Alessandro Reali. “Multi-level Bézier extraction for hierarchical local refinement of Isogeometric Analysis.” In: *Computer Methods in Applied Mechanics and Engineering* 328 (2018), pp. 147–174. ISSN: 0045-7825. DOI: <https://doi.org/10.1016/j.cma.2017.08.017> (cit. on p. 22).
- [68] Antonio Maria D’Altri, Francesco Cannizzaro, Massimo Petracca, and Diego Alejandro Talledo. “Nonlinear modelling of the seismic response of masonry structures: Calibration strategies.” In: *Bulletin of Earthquake Engineering* 20.4 (2022), pp. 1999–2043. DOI: [10.1007/s10518-021-01104-1](https://doi.org/10.1007/s10518-021-01104-1) (cit. on p. 150).
- [69] Daniel Baumgärtner, Johannes Wolf, Riccardo Rossi, Pooyan Dadvand, and Roland Wüchner. “A robust algorithm for implicit description of immersed geometries within a background mesh.” In: *Advanced Modeling and Simulation in Engineering Sciences* 5.1 (2018), pp. 1–40. ISSN: 2213-7467. DOI: [10.1186/s40323-018-0113-8](https://doi.org/10.1186/s40323-018-0113-8) (cit. on p. 42).

- [70] Manicka Dhanasekar, Peter Kleeman, and Adrian Page. “Biaxial Stress-strain Relations for Brick Masonry.” In: *Journal of Structural Engineering-asce - J STRUCT ENG-ASCE* 111 (May 1985). DOI: [10.1061/\(ASCE\)0733-9445\(1985\)111:5\(1085\)](https://doi.org/10.1061/(ASCE)0733-9445(1985)111:5(1085)) (cit. on p. 90).
- [71] *DIANA 9.3 version User’s Manual*. 2008 (cit. on p. 140).
- [72] W. Dornisch, S. Klinkel, and B. Simeon. “Isogeometric Reissner–Mindlin shell analysis with exactly calculated director vectors.” In: *Computer Methods in Applied Mechanics and Engineering* 253 (2013), pp. 491–504. ISSN: 0045-7825. DOI: <https://doi.org/10.1016/j.cma.2012.09.010> (cit. on p. 23).
- [73] W. Dornisch, R. Müller, and S. Klinkel. “An efficient and robust rotational formulation for isogeometric Reissner–Mindlin shell elements.” In: *Computer Methods in Applied Mechanics and Engineering* 303 (2016), pp. 1–34. ISSN: 0045-7825. DOI: <https://doi.org/10.1016/j.cma.2016.01.018> (cit. on p. 23).
- [74] Anastasios Drougkas, Pere Roca, and Climent Molins. “Nonlinear micro-mechanical analysis of masonry periodic unit cells.” In: *International Journal of Solids and Structures* 80 (2016), pp. 193–211. ISSN: 0020-7683. DOI: <https://doi.org/10.1016/j.ijsolstr.2015.11.004> (cit. on pp. 57, 60).
- [75] A. Düster, J. Parvizian, Z. Yang, and Ernst Rank. “The finite cell method for three-dimensional problems of solid mechanics.” In: *Computer Methods in Applied Mechanics and Engineering* 197.45-48 (2008), pp. 3768–3782. ISSN: 00457825. DOI: [10.1016/j.cma.2008.02.036](https://doi.org/10.1016/j.cma.2008.02.036) (cit. on p. 35).
- [76] R. Echter, B. Oesterle, and M. Bischoff. “A hierarchic family of isogeometric shell finite elements.” In: *Computer Methods in Applied Mechanics and Engineering* 254 (2013), pp. 170–180. ISSN: 0045-7825. DOI: [10.1016/j.cma.2012.10.018](https://doi.org/10.1016/j.cma.2012.10.018) (cit. on pp. 23, 24, 35).
- [77] Ralph Echter and Manfred Bischoff. “Numerical efficiency, locking and unlocking of NURBS finite elements.” In: *Computer Methods in Applied Mechanics and Engineering* 199.5 (2010), pp. 374–382. ISSN: 0045-7825. DOI: [10.1016/j.cma.2009.02.035](https://doi.org/10.1016/j.cma.2009.02.035) (cit. on p. 24).
- [78] Mohamed Elhaddad, Nils Zander, Tino Bog, László Kudela, Stefan Kollmannsberger, Jan Kirschke, Thomas Baum, Martin Ruess, and Ernst Rank. “Multi-level hp-finite cell method for embedded interface problems with application in biomechanics.” In: *International Journal for Numerical Methods in Biomedical Engineering* 34.4 (2018). e2951 cnm.2951, e2951. DOI: <https://doi.org/10.1002/cnm.2951> (cit. on p. 49).
- [79] *EN 1052-1. Methods of test for masonry. Part 1: Determination of compressive strength*. 1998 (cit. on pp. 64, 65).
- [80] *EN 1052-3. Methods of test for masonry. Part 3: Determination of initial shear strength*. 2007 (cit. on pp. 76–78).

- [81] P. Faccio, P. Foraboschi, and E. Siviero. “Masonry vaults reinforced with FPR strips [In Italian: Volte in muratura con rinforzi in FRP].” In: *L’Edilizia* 7-8.8 (1999), pp. 44–50 (cit. on pp. 103, 135, 137).
- [82] Charbel Farhat, Po-Shu Chen, and Jan Mandel. “A scalable Lagrange multiplier based domain decomposition method for time-dependent problems.” In: *International Journal for Numerical Methods in Engineering* 38.22 (1995), pp. 3831–3853 (cit. on p. 56).
- [83] Charbel Farhat and Francois-Xavier Roux. “A method of finite element tearing and interconnecting and its parallel solution algorithm.” In: *International Journal for Numerical Methods in Engineering* 32.6 (1991), pp. 1205–1227. DOI: [10.1002/nme.1620320604](https://doi.org/10.1002/nme.1620320604) (cit. on p. 56).
- [84] R. Faria, J. Oliver, and M. Cervera. “A strain-based plastic viscous-damage model for massive concrete structures.” In: *International Journal of Solids and Structures* 35.14 (1998), pp. 1533–1558. ISSN: 0020-7683. DOI: [https://doi.org/10.1016/S0020-7683\(97\)00119-4](https://doi.org/10.1016/S0020-7683(97)00119-4) (cit. on pp. 90, 91).
- [85] Gianmarco Felice and Renato Giannini. “Out-of-plane seismic resistance of masonry walls.” In: *JOURNAL OF EARTHQUAKE ENGINEERING* 5 (Apr. 2001), pp. 253–271. DOI: [10.1080/13632460109350394](https://doi.org/10.1080/13632460109350394) (cit. on p. 85).
- [86] C. A. Felippa. “Introduction to Finite Element Methods: Appendix O.” Manuscript. Boulder: University of Colorado Boulder, 2015. URL: <http://www.colorado.edu/engineering/CAS/courses.d/IFEM.d/IFEM.AppO.d/IFEM.AppO.index.html> (cit. on p. 2).
- [87] Qiu Fu, Jiang Qian, and Dimitri Beskos. “Inelastic anisotropic constitutive models based on evolutionary linear transformations on stress tensors with application to masonry.” In: *Acta Mechanica* 229 (Feb. 2018). DOI: [10.1007/s00707-017-1995-0](https://doi.org/10.1007/s00707-017-1995-0) (cit. on pp. 107, 109, 110).
- [88] Angelo Gaetani, Giorgio Monti, Paulo B. Lourenço, and Giancarlo Marcari. “Design and Analysis of Cross Vaults Along History.” In: *International Journal of Architectural Heritage* 10.7 (2016), pp. 841–856. DOI: [10.1080/15583058.2015.1132020](https://doi.org/10.1080/15583058.2015.1132020) (cit. on p. 135).
- [89] Wei Gao, Jiawen Wang, Shuohui Yin, and Y.T. Feng. “A coupled 3D isogeometric and discrete element approach for modeling interactions between structures and granular matters.” In: *Computer Methods in Applied Mechanics and Engineering* 354 (2019), pp. 441–463. ISSN: 0045-7825. DOI: <https://doi.org/10.1016/j.cma.2019.05.043> (cit. on p. 3).
- [90] *Gartner’s Top 10 Strategic Technology Trends for 2017*. Accessed: 2021-08-24. URL: <https://www.gartner.com/smarterwithgartner/gartners-top-10-technology-trends-2017/> (cit. on p. 13).

- [91] Natalino Gattesco and Ingrid Boem. “Out-of-plane behavior of reinforced masonry walls: Experimental and numerical study.” In: *Composites Part B: Engineering* 128 (2017), pp. 39–52. ISSN: 1359-8368. DOI: <https://doi.org/10.1016/j.compositesb.2017.07.006> (cit. on p. 85).
- [92] Bahman Ghiassi and Gabriele Milani. *Numerical Modeling of Masonry and Historical Structures*. 1st. Elsevier, 2019. ISBN: 978-0-08-102439-3. DOI: <https://doi.org/10.1016/C2017-0-01579-3> (cit. on p. 57).
- [93] Grasshopper. URL: [www.grasshopper3d.com](http://www.grasshopper3d.com) (cit. on p. 178).
- [94] M. Griffith and Jaroslav Vaculik. “Out-of-Plane Flexural Strength of Unreinforced Clay Brick Masonry Walls.” In: *TMS Journal* 25 (Sept. 2007), pp. 53–68 (cit. on pp. 85, 103, 117, 118).
- [95] M. C. Griffith, J. Vaculik, N. T. K. Lam, J. Wilson, and E. Lumantarna. “Cyclic testing of unreinforced masonry walls in two-way bending.” In: *Earthquake Engineering & Structural Dynamics* 36.6 (2007), pp. 801–821. DOI: <https://doi.org/10.1002/eqe.654> (cit. on p. 117).
- [96] James Edward Guilkey and Jeffrey A Weiss. “Implicit time integration for the material point method: Quantitative and algorithmic comparisons with the finite element method.” In: *International Journal for Numerical Methods in Engineering* 57.9 (2003), pp. 1323–1338. ISSN: 0029-5981 (cit. on p. 47).
- [97] Qi Guo, Xuchen Han, Chuyuan Fu, Theodore Gast, Rasmus Tamstorf, and Joseph Teran. “A Material Point Method for Thin Shells with Frictional Contact.” In: *ACM Trans. Graph.* 37.4 (2018). ISSN: 0730-0301. DOI: [10.1145/3197517.3201346](https://doi.org/10.1145/3197517.3201346) (cit. on p. 48).
- [98] Yujie Guo and Martin Ruess. “Nitsche’s method for a coupling of isogeometric thin shells and blended shell structures.” In: *Computer Methods in Applied Mechanics and Engineering* 284 (2015), pp. 881–905. ISSN: 00457825. DOI: [10.1016/j.cma.2014.11.014](https://doi.org/10.1016/j.cma.2014.11.014) (cit. on p. 42).
- [99] Austin J. Herrema, Emily L. Johnson, Davide Proserpio, Michael C.H. Wu, Josef Kiendl, and Ming-Chen Hsu. “Penalty coupling of non-matching isogeometric Kirchhoff–Love shell patches with application to composite wind turbine blades.” In: *Computer Methods in Applied Mechanics and Engineering* 346 (2019), pp. 810–840. ISSN: 0045-7825. DOI: <https://doi.org/10.1016/j.cma.2018.08.038> (cit. on p. 38).
- [100] R. Hill. “Constitutive modelling of orthotropic plasticity in sheet metals.” In: *Journal of the Mechanics and Physics of Solids* 38.3 (1990), pp. 405–417. ISSN: 0022-5096. DOI: [https://doi.org/10.1016/0022-5096\(90\)90006-P](https://doi.org/10.1016/0022-5096(90)90006-P) (cit. on pp. 90, 94).

- [101] Rodney Hill and Egon Orowan. “A theory of the yielding and plastic flow of anisotropic metals.” In: *Proceedings of the Royal Society of London. Series A. Mathematical and Physical Sciences* 193.1033 (1948), pp. 281–297. DOI: [10.1098/rspa.1948.0045](https://doi.org/10.1098/rspa.1948.0045) (cit. on pp. 90, 94).
- [102] T. Hirschler, R. Bouclier, A. Duval, T. Elguedj, and J. Morlier. “The embedded isogeometric Kirchhoff–Love shell: From design to shape optimization of non-conforming stiffened multipatch structures.” In: *Computer Methods in Applied Mechanics and Engineering* 349 (2019), pp. 774–797. ISSN: 0045-7825. DOI: [10.1016/j.cma.2019.02.042](https://doi.org/10.1016/j.cma.2019.02.042) (cit. on pp. 38, 43).
- [103] Klaus Höllig, Christian Apprich, and Anja Streit. “Introduction to the Web-method and its applications.” In: *Advances in Computational Mathematics* 23.1-2 (2005), pp. 215–237. DOI: [10.1007/s10444-004-1811-y](https://doi.org/10.1007/s10444-004-1811-y) (cit. on pp. 29, 41).
- [104] Thomas Horger, Stefan Kollmannsberger, Felix Frischmann, Ernst Rank, and Barbara Wohlmuth. “A new mortar formulation for modeling elastomer bedded structures with modal-analysis in 3D.” In: *Advanced Modeling and Simulation in Engineering Sciences* 1.1 (2014). DOI: [10.1186/s40323-014-0018-0](https://doi.org/10.1186/s40323-014-0018-0) (cit. on p. 36).
- [105] Simeon Hubrich, Paolo Di Stolfo, László Kudela, Stefan Kollmannsberger, Ernst Rank, Andreas Schröder, and Alexander Düster. “Numerical integration of discontinuous functions: moment fitting and smart octree.” In: *Computational Mechanics* 60.5 (2017), pp. 863–881. DOI: [10.1007/s00466-017-1441-0](https://doi.org/10.1007/s00466-017-1441-0) (cit. on p. 31).
- [106] Santiago Huerta. “The Debate about the Structural Behaviour of Gothic Vaults: From Viollet-le-Duc to Heyman.” In: May 2009. ISBN: 978-3-936033-31-1 (cit. on p. 135).
- [107] T.J.R. Hughes, J.A. Cottrell, and Y. Bazilevs. “Isogeometric analysis: CAD, finite elements, NURBS, exact geometry and mesh refinement.” In: *Computer Methods in Applied Mechanics and Engineering* 194.39–41 (2005), pp. 4135–4195. ISSN: 0045-7825. DOI: <http://dx.doi.org/10.1016/j.cma.2004.10.008> (cit. on pp. 2, 21, 29).
- [108] Thomas J. R. Hughes, A. Reali, and Giancarlo Sangalli. “Efficient quadrature for NURBS-based isogeometric analysis.” In: *Computer Methods in Applied Mechanics and Engineering* 199.5-8 (2010), pp. 301–313. ISSN: 00457825. DOI: [10.1016/j.cma.2008.12.004](https://doi.org/10.1016/j.cma.2008.12.004) (cit. on pp. 29, 31).
- [109] S. R. Idelsohn, F. Del Pin, R. Rossi, and E. Oñate. “Fluid–structure interaction problems with strong added-mass effect.” In: *International Journal for Numerical Methods in Engineering* 80.10 (2009), pp. 1261–1294. DOI: <https://doi.org/10.1002/nme.2659> (cit. on p. 3).

- [110] “Immersed b-spline (i-spline) finite element method for geometrically complex domains.” In: *Computer Methods in Applied Mechanics and Engineering* 200.13 (2011), pp. 1432–1445. ISSN: 0045-7825. DOI: <https://doi.org/10.1016/j.cma.2010.12.008> (cit. on p. 41).
- [111] *Initial Graphics Exchange Specification (IGES), NBSIR 80-1978, Digital Representation for Communication of Product Definition Data*. U.S. National Bureau of Standards (cit. on p. 13).
- [112] Chenfanfu Jiang, Theodore Gast, and Joseph Teran. “Anisotropic Elastoplasticity for Cloth, Knit and Hair Frictional Contact.” In: *ACM Trans. Graph.* 36.4 (2017). ISSN: 0730-0301. DOI: [10.1145/3072959.3073623](https://doi.org/10.1145/3072959.3073623) (cit. on p. 48).
- [113] John F. Abel and Mark S. Shephard. “An algorithm for multipoint constraints in finite element analysis.” In: *International Journal for Numerical Methods in Engineering* 14.3 (1979), pp. 464–467. ISSN: 1097-0207. DOI: [10.1002/nme.1620140312](https://doi.org/10.1002/nme.1620140312) (cit. on p. 50).
- [114] J.N. Jomo, F. de Prenter, M. Elhaddad, D. D’Angella, C.V. Verhoosel, S. Kollmannsberger, J.S. Kirschke, V. Nübel, E.H. van Brummelen, and E. Rank. “Robust and parallel scalable iterative solutions for large-scale finite cell analyses.” In: *Finite Elements in Analysis and Design* 163 (2019), pp. 14–30. ISSN: 0168-874X. DOI: <https://doi.org/10.1016/j.finel.2019.01.009> (cit. on p. 41).
- [115] Joseph Jordan. “Effiziente Simulation großer Mauerwerksstrukturen mit diskreten Rissmodellen.” PhD thesis. Technische Universität München, Lehrstuhl für Statik, 2011 (cit. on p. 57).
- [116] Kangaroo3d. URL: [kangaroo3d.com](http://kangaroo3d.com) (cit. on p. 178).
- [117] Karamba3D. URL: [www.karamba3d.com](http://www.karamba3d.com) (cit. on p. 178).
- [118] J. Kiendl, K.-U. Bletzinger, J. Linhard, and R. Wüchner. “Isogeometric shell analysis with Kirchhoff–Love elements.” In: *Computer Methods in Applied Mechanics and Engineering* 198.49 (2009), pp. 3902–3914. ISSN: 0045-7825. DOI: [10.1016/j.cma.2009.08.013](https://doi.org/10.1016/j.cma.2009.08.013) (cit. on pp. 23, 27, 35, 38, 143).
- [119] Josef M. Kiendl, Yuri Bazilevs, M.-C Hsu, Roland Wüchner, and Kai-Uwe Bletzinger. “The bending strip method for isogeometric analysis of Kirchhoff–Love shell structures comprised of multiple patches.” In: *Computer Methods in Applied Mechanics and Engineering* 199.37-40 (2010), pp. 2403–2416. ISSN: 00457825. DOI: [10.1016/j.cma.2010.03.029](https://doi.org/10.1016/j.cma.2010.03.029) (cit. on pp. 39, 123).
- [120] kiwi!3d. URL: [www.kiwi3d.com](http://www.kiwi3d.com) (cit. on p. 178).
- [121] Richard E. Klingner. *Masonry Structural Design*. 2010 (cit. on p. 57).

- [122] S. Klinkel, L. Chen, and W. Dornisch. “A NURBS based hybrid collocation–Galerkin method for the analysis of boundary represented solids.” In: *Computer Methods in Applied Mechanics and Engineering* 284 (2015). Isogeometric Analysis Special Issue, pp. 689–711. ISSN: 0045-7825. DOI: <https://doi.org/10.1016/j.cma.2014.10.029> (cit. on p. 35).
- [123] Sven Klinkel and Margarita Chasapi. “Isogeometric Analysis of Solids in Boundary Representation.” In: *Novel Finite Element Technologies for Solids and Structures*. Ed. by Jörg Schröder and Paulo de Mattos Pimenta. Cham: Springer International Publishing, 2020, pp. 153–197. ISBN: 978-3-030-33520-5. DOI: [10.1007/978-3-030-33520-5\\_6](https://doi.org/10.1007/978-3-030-33520-5_6) (cit. on p. 35).
- [124] Patrick Knupp and Stanly Steinberg. “The Fundamentals of Grid Generation.” In: 3 (Jan. 1993) (cit. on p. 2).
- [125] S. Kollmannsberger, A. Özcan, J. Baiges, M. Ruess, E. Rank, and A. Reali. “Parameter-free, weak imposition of Dirichlet boundary conditions and coupling of trimmed and non-conforming patches.” In: *International Journal for Numerical Methods in Engineering* 101.9 (2015), pp. 670–699. DOI: [10.1002/nme.4817](https://doi.org/10.1002/nme.4817) (cit. on p. 49).
- [126] KratosMultiphysics. URL: [github.com/KratosMultiphysics](https://github.com/KratosMultiphysics) (cit. on pp. 155, 156, 158, 173, 175, 177, 187).
- [127] Lidija Krstevska, Željana Nikolić, and Mladen Kustura. “Shake Table Testing of Two Historical Masonry Structures for Estimation of Their Seismic Stability.” In: *International Journal of Architectural Heritage* (June 2020), pp. 1–19. DOI: [10.1080/15583058.2020.1779870](https://doi.org/10.1080/15583058.2020.1779870) (cit. on p. 85).
- [128] László Kudela, Stefan Kollmannsberger, Umut Almac, and Ernst Rank. “Direct structural analysis of domains defined by point clouds.” In: *Computer Methods in Applied Mechanics and Engineering* 358 (2020), p. 112581. ISSN: 0045-7825. DOI: <https://doi.org/10.1016/j.cma.2019.112581> (cit. on p. 35).
- [129] Bimal Kumar. *A Practical Guide to Adopting BIM in Construction Projects*. Nov. 2015. ISBN: 978-1-84995-146-3 (cit. on p. 7).
- [130] Lambros Rorris and Attila Nagy and Stefan Hartmann and Ioannis Chalkidis and Anastasios Vafeidis. *The ANSA / LS-DYNA approach for Isogeometric Analysis Simulations*. Ed. by 8th BEFORE REALITY Conference (cit. on p. 42).
- [131] Ireneusz Lapczyk and Juan A. Hurtado. “Progressive damage modeling in fiber-reinforced materials.” In: *Composites Part A: Applied Science and Manufacturing* 38.11 (2007). CompTest 2006, pp. 2333–2341. ISSN: 1359-835X. DOI: <https://doi.org/10.1016/j.compositesa.2007.01.017> (cit. on p. 90).

- [132] Karl Larsson, Stefan Kollmannsberger, Ernst Rank, and Mats G. Larson. “The finite cell method with least squares stabilized Nitsche boundary conditions.” In: *Computer Methods in Applied Mechanics and Engineering* 393 (2022), p. 114792. ISSN: 0045-7825. DOI: <https://doi.org/10.1016/j.cma.2022.114792> (cit. on p. 41).
- [133] L. F. Leidinger, M. Breitenberger, A. M. Bauer, S. Hartmann, R. Wüchner, K.-U. Bletzinger, F. Duddeck, and L. Song. “Explicit dynamic isogeometric B-Rep analysis of penalty-coupled trimmed NURBS shells.” In: *Computer Methods in Applied Mechanics and Engineering* 351 (2019), pp. 891–927. ISSN: 0045-7825. DOI: [10.1016/j.cma.2019.04.016](https://doi.org/10.1016/j.cma.2019.04.016) (cit. on pp. 29, 41, 161).
- [134] G. Lengyel. “Discrete element analysis of gothic masonry vaults for self-weight and horizontal support displacement.” In: *Engineering Structures* 148 (2017), pp. 195–209. ISSN: 0141-0296. DOI: <https://doi.org/10.1016/j.engstruct.2017.06.014> (cit. on p. 136).
- [135] G. Lengyel and K. Bagi. “Numerical analysis of the mechanical role of the ribs in groin vaults.” In: *Computers & Structures* 158 (2015), pp. 42–60. ISSN: 0045-7949. DOI: <https://doi.org/10.1016/j.compstruc.2015.05.032> (cit. on p. 136).
- [136] Xuan Li, Yu Fang, Minchen Li, and Chenfanfu Jiang. “BFEMP: Interpenetration-free MPM–FEM coupling with barrier contact.” In: *Computer Methods in Applied Mechanics and Engineering* 390 (2022), p. 114350. ISSN: 0045-7825. DOI: <https://doi.org/10.1016/j.cma.2021.114350> (cit. on p. 3).
- [137] Daniel S.H. Lo. *Finite element mesh generation*. Engineering and Technology. Taylor and Francis: Saxe-Coburg Publications, 2015. ISBN: 9780429176647. DOI: <https://doi.org/10.1201/b17713> (cit. on p. 2).
- [138] Hamid R. Lotfi and P. Benson Shing. “Interface Model Applied to Fracture of Masonry Structures.” In: *Journal of Structural Engineering* 120.1 (1994), pp. 63–80. DOI: [10.1061/\(ASCE\)0733-9445\(1994\)120:1\(63\)](https://doi.org/10.1061/(ASCE)0733-9445(1994)120:1(63)) (cit. on p. 57).
- [139] P.B Lourenço. “Computational strategies for masonry structures.” PhD thesis. TU Delft, Civil Engineering and Geosciences, 1996 (cit. on pp. 57, 59, 73, 99, 106, 107, 109, 110).
- [140] Paulo Lourenço, Leonardo Avila, Graça Vasconcelos, J.Pedro Alves, Nuno Mendes, and A. Costa. “Experimental investigation on the seismic performance of masonry buildings using shaking table testing.” In: *Bulletin of Earthquake Engineering* 11 (Aug. 2012). DOI: [10.1007/s10518-012-9410-7](https://doi.org/10.1007/s10518-012-9410-7) (cit. on p. 59).

- [141] Paulo B. Lourenço, René De Borst, and Jan G. Rots. “A plane stress softening plasticity model for orthotropic materials.” In: *International Journal for Numerical Methods in Engineering* 40.21 (1997), pp. 4033–4057. DOI: [https://doi.org/10.1002/\(SICI\)1097-0207\(19971115\)40:21<4033::AID-NME248>3.0.CO;2-0](https://doi.org/10.1002/(SICI)1097-0207(19971115)40:21<4033::AID-NME248>3.0.CO;2-0) (cit. on pp. 90, 91, 94, 107, 109).
- [142] Paulo B. Lourenço and Jan G. Rots. “Multisurface Interface Model for Analysis of Masonry Structures.” In: *Journal of Engineering Mechanics* 123.7 (1997), pp. 660–668. DOI: [10.1061/\(ASCE\)0733-9399\(1997\)123:7\(660\)](https://doi.org/10.1061/(ASCE)0733-9399(1997)123:7(660)) (cit. on pp. 57, 99, 107).
- [143] J. Lubliner, J. Oliver, S. Oller, and E. Oñate. “A plastic-damage model for concrete.” In: *International Journal of Solids and Structures* 25.3 (1989), pp. 299–326. ISSN: 0020-7683. DOI: [https://doi.org/10.1016/0020-7683\(89\)90050-4](https://doi.org/10.1016/0020-7683(89)90050-4) (cit. on pp. 90, 92).
- [144] Josef Maier. “Geschichte des Mauerwerks.” In: *Handbuch Historisches Mauerwerk: Untersuchungsmethoden und Instandsetzungsverfahren*. Berlin, Heidelberg: Springer Berlin Heidelberg, 2012, pp. 9–66. ISBN: 978-3-642-25468-0. DOI: [10.1007/978-3-642-25468-0\\_2](https://doi.org/10.1007/978-3-642-25468-0_2) (cit. on p. 57).
- [145] Benjamin Marussig and Thomas J. R. Hughes. “A Review of Trimming in Iso-geometric Analysis: Challenges, Data Exchange and Simulation Aspects.” In: *Archives of Computational Methods in Engineering* 30.8 (2017), p. 657. ISSN: 1134-3060. DOI: [10.1007/s11831-017-9220-9](https://doi.org/10.1007/s11831-017-9220-9) (cit. on p. 31).
- [146] Benjamin Marussig, Jürgen Zechner, Gernot Beer, and Thomas-Peter Fries. “Stable isogeometric analysis of trimmed geometries.” In: *Computer Methods in Applied Mechanics and Engineering* 316 (2017), pp. 497–521. ISSN: 00457825. DOI: [10.1016/j.cma.2016.07.040](https://doi.org/10.1016/j.cma.2016.07.040) (cit. on p. 31).
- [147] C. Melbourne, J. Wang, A. Tomor, G. Holm, M. Smithand P.E. Bengtsson, T J. Bien, Kaminski, P. Rawa, J. R. Casas, P. Roca, and C. Molins. *Masonry Arch Bridges, Background document D4.7*. 2007 (cit. on pp. 103, 129, 130, 134).
- [148] F. Messali, R. Esposito, G. J. P. Ravenshorst, and J. G. Rots. “Experimental investigation of the in-plane cyclic behaviour of calcium silicate brick masonry walls.” In: *Bulletin of Earthquake Engineering* 18.8 (2020), pp. 3963–3994. DOI: [10.1007/s10518-020-00835-x](https://doi.org/10.1007/s10518-020-00835-x) (cit. on p. 59).
- [149] Manuel Meßmer, Tobias Teschemacher, Lukas F. Leidinger, Roland Wüchner, and Kai-Uwe Bletzinger. “Efficient CAD-integrated isogeometric analysis of trimmed solids.” In: *Computer Methods in Applied Mechanics and Engineering* 400 (2022), p. 115584. ISSN: 0045-7825. DOI: <https://doi.org/10.1016/j.cma.2022.115584> (cit. on pp. 29, 31, 41, 187, 188).

- [150] Mark Michael, Frank Vogel, and Bernhard Peters. “DEM–FEM coupling simulations of the interactions between a tire tread and granular terrain.” In: *Computer Methods in Applied Mechanics and Engineering* 289 (2015), pp. 227–248. ISSN: 0045-7825. DOI: <https://doi.org/10.1016/j.cma.2015.02.014> (cit. on p. 3).
- [151] Enrico Milani, Gabriele Milani, and Antonio Tralli. “Limit analysis of masonry vaults by means of curved shell finite elements and homogenization.” In: *International Journal of Solids and Structures* 45.20 (2008), pp. 5258–5288. ISSN: 0020-7683. DOI: <https://doi.org/10.1016/j.ijsolstr.2008.05.019> (cit. on pp. 124, 127, 136, 137, 139–141).
- [152] G. Milani, M. Rossi, C. Calderini, and S. Lagomarsino. “Tilting plane tests on a small-scale masonry cross vault: Experimental results and numerical simulations through a heterogeneous approach.” In: *Engineering Structures* 123 (2016), pp. 300–312. ISSN: 0141-0296. DOI: <https://doi.org/10.1016/j.engstruct.2016.05.017> (cit. on p. 140).
- [153] Gabriele Milani, Michele Simoni, and Antonio Tralli. “Advanced numerical models for the analysis of masonry cross vaults: A case-study in Italy.” In: *Engineering Structures* 76 (2014), pp. 339–358. ISSN: 0141-0296. DOI: <https://doi.org/10.1016/j.engstruct.2014.07.018> (cit. on p. 135).
- [154] Gabriele Milani and Antonio Tralli. “A simple meso-macro model based on SQP for the non-linear analysis of masonry double curvature structures.” In: *International Journal of Solids and Structures* 49.5 (2012), pp. 808–834. ISSN: 0020-7683. DOI: <https://doi.org/10.1016/j.ijsolstr.2011.12.001> (cit. on pp. 124, 136–140).
- [155] Gihad Mohamad, Paulo B. Lourenço, and Humberto R. Roman. “Mechanics of hollow concrete block masonry prisms under compression: Review and prospects.” In: *Cement and Concrete Composites* 29.3 (2007), pp. 181–192. ISSN: 0958-9465. DOI: <https://doi.org/10.1016/j.cemconcomp.2006.11.003> (cit. on p. 74).
- [156] Climent Molins and Pere Roca. “Load capacity of multi-arch masonry bridges.” In: Dec. 2020, pp. 213–222. ISBN: 9781003078494. DOI: [10.1201/9781003078494-31](https://doi.org/10.1201/9781003078494-31) (cit. on p. 129).
- [157] *Mortex*. Accessed: 2021-02-23. URL: <https://australbricks.com.au/nsw/product/mortex/> (cit. on p. 68).
- [158] Alexander Müller and Manfred Bischoff. “A Consistent Finite Element Formulation of the Geometrically Non-linear Reissner-Mindlin Shell Model.” In: *Archives of Computational Methods in Engineering* (2022). DOI: [10.1007/s11831-021-09702-7](https://doi.org/10.1007/s11831-021-09702-7) (cit. on p. 23).

- [159] Attila P. Nagy and David J. Benson. “On the numerical integration of trimmed isogeometric elements.” In: *Computer Methods in Applied Mechanics and Engineering* 284 (2015), pp. 165–185. ISSN: 00457825. DOI: [10.1016/j.cma.2014.08.002](https://doi.org/10.1016/j.cma.2014.08.002) (cit. on p. 31).
- [160] M.A. Najafgholipour, Mahmoud R. Maheri, and P.B. Lourenço. “Capacity interaction in brick masonry under simultaneous in-plane and out-of-plane loads.” In: *Construction and Building Materials* 38 (2013). 25th Anniversary Session for ACI 228 – Building on the Past for the Future of NDT of Concrete, pp. 619–626. ISSN: 0950-0618. DOI: <https://doi.org/10.1016/j.conbuildmat.2012.08.032> (cit. on p. 73).
- [161] K.B. Nakshatrala, A. Prakash, and K.D. Hjelmstad. “On dual Schur domain decomposition method for linear first-order transient problems.” In: *Journal of Computational Physics* 228.21 (2009), pp. 7957–7985. ISSN: 0021-9991. DOI: <https://doi.org/10.1016/j.jcp.2009.07.016> (cit. on p. 56).
- [162] Julien Nembrini, Steffen Samberger, and Guillaume Labelle. “Parametric scripting for early design performance simulation.” In: *Energy and Buildings* 68 (2014), pp. 786–798. ISSN: 0378-7788. DOI: <https://doi.org/10.1016/j.enbuild.2013.09.044> (cit. on p. 178).
- [163] N. Nguyen-Thanh, J. Kiendl, H. Nguyen-Xuan, R. Wüchner, K. U. Bletzinger, Y. Bazilevs, and T. Rabczuk. “Rotation free isogeometric thin shell analysis using PHT-splines.” In: *Computer Methods in Applied Mechanics and Engineering* 200.47 (2011), pp. 3410–3424. ISSN: 0045-7825. DOI: [10.1016/j.cma.2011.08.014](https://doi.org/10.1016/j.cma.2011.08.014) (cit. on p. 22).
- [164] Simona Di Nino and Angelo Luongo. “A simple homogenized orthotropic model for in-plane analysis of regular masonry walls.” In: *International Journal of Solids and Structures* 167 (2019), pp. 156–169. ISSN: 0020-7683. DOI: <https://doi.org/10.1016/j.ijsolstr.2019.03.013> (cit. on p. 60).
- [165] Sarkar Noor-E-Khuda. “An Explicit Finite-Element Modeling Method for Masonry Walls Using Continuum Shell Element.” In: *Journal of Architectural Engineering* 27.4 (2021), p. 04021040. DOI: [10.1061/\(ASCE\)AE.1943-5568.0000518](https://doi.org/10.1061/(ASCE)AE.1943-5568.0000518) (cit. on p. 117).
- [166] Sarkar Noor-E-Khuda, Manicka Dhanasekar, and David P. Thambiratnam. “An explicit finite element modelling method for masonry walls under out-of-plane loading.” In: *Engineering Structures* 113 (2016), pp. 103–120. ISSN: 0141-0296. DOI: <https://doi.org/10.1016/j.engstruct.2016.01.026> (cit. on p. 117).
- [167] T. Oberbichler, R. Wüchner, and K. -U Bletzinger. “Efficient computation of nonlinear isogeometric elements using the adjoint method and algorithmic differentiation.” In: *Computer Methods in Applied Mechanics and Engineering* 381

- (2021), p. 113817. ISSN: 0045-7825. DOI: [10.1016/j.cma.2021.113817](https://doi.org/10.1016/j.cma.2021.113817) (cit. on p. 52).
- [168] Bastian Oesterle. “Intrinsisch lockingfreie Schalenformulierungen.” PhD thesis. Stuttgart : Institut für Baustatik und Baudynamik, Universität Stuttgart, 2018. DOI: [10.18419/opus-10046](https://doi.org/10.18419/opus-10046) (cit. on pp. 23, 24, 27).
- [169] Bastian Oesterle, Ekkehard Ramm, and Manfred Bischoff. “A shear deformable, rotation-free isogeometric shell formulation.” In: *Computer Methods in Applied Mechanics and Engineering* 307 (2016), pp. 235–255. ISSN: 00457825. DOI: [10.1016/j.cma.2016.04.015](https://doi.org/10.1016/j.cma.2016.04.015) (cit. on p. 35).
- [170] Bastian Oesterle, Renate Sachse, Ekkehard Ramm, and Manfred Bischoff. “Hierarchic isogeometric large rotation shell elements including linearized transverse shear parametrization.” In: *Computer Methods in Applied Mechanics and Engineering* 321 (2017), pp. 383–405. ISSN: 00457825. DOI: [10.1016/j.cma.2017.03.031](https://doi.org/10.1016/j.cma.2017.03.031) (cit. on p. 35).
- [171] Sergio Oller, Salvador Botello, J Miquel, and Eugenio Oñate. “An anisotropic elastoplastic model based on an isotropic formulation.” In: *Engineering Computations* (1995) (cit. on pp. 90, 94, 95).
- [172] Sergio Oller, Eduardo Car, and Jacob Lubliner. “Definition of a general implicit orthotropic yield criterion.” In: *Computer Methods in Applied Mechanics and Engineering* 192 (Feb. 2003), pp. 895–912. DOI: [10.1016/S0045-7825\(02\)00605-9](https://doi.org/10.1016/S0045-7825(02)00605-9) (cit. on pp. 90, 94–96).
- [173] Michael Ortiz, Yves Leroy, and Alan Needleman. “A finite element method for localized failure analysis.” In: *Computer Methods in Applied Mechanics and Engineering* 61.2 (1987), pp. 189–214. ISSN: 0045-7825. DOI: [10.1016/0045-7825\(87\)90004-1](https://doi.org/10.1016/0045-7825(87)90004-1) (cit. on p. 42).
- [174] Adrian Page. “The biaxial compressive strength of brick masonry.” In: *Ice Proceedings* 71 (Jan. 1981), pp. 893–906. DOI: [10.1680/iicep.1981.1825](https://doi.org/10.1680/iicep.1981.1825) (cit. on pp. 59, 90).
- [175] Alexander Paolini, Stefan Kollmannsberger, Ernst Rank, Thomas Horger, and Barbara Wohlmuth. “A mortar formulation including viscoelastic layers for vibration analysis.” In: *Computational Mechanics* 63.1 (2019), pp. 23–33. DOI: [10.1007/s00466-018-1582-9](https://doi.org/10.1007/s00466-018-1582-9) (cit. on p. 36).
- [176] Alexander Paolini, Nina Korshunova, Stefan Kollmannsberger, and Ernst Rank. “Multiscale Analysis of High Damping Composites Using the Finite Cell and the Mortar Method.” In: *International Journal of Structural Stability and Dynamics* 21.11 (2021), p. 2150149. DOI: [10.1142/S0219455421501492](https://doi.org/10.1142/S0219455421501492) (cit. on p. 49).
- [177] Jamshid Parvizian, Alexander Düster, and Ernst Rank. “Finite cell method.” In: *Computational Mechanics* 1 (2007). DOI: [10.1007/s00466-007-0173-y](https://doi.org/10.1007/s00466-007-0173-y) (cit. on p. 35).

- [178] T. Pasch, L. F. Leidinger, A. Apostolatos, R. Wüchner, K. -U Bletzinger, and F. Duddeck. “A priori penalty factor determination for (trimmed) NURBS-based shells with Dirichlet and coupling constraints in isogeometric analysis.” In: *Computer Methods in Applied Mechanics and Engineering* 377 (2021), p. 113688. ISSN: 0045-7825. DOI: [10.1016/j.cma.2021.113688](https://doi.org/10.1016/j.cma.2021.113688) (cit. on pp. 42, 51).
- [179] Luca Pelà, Miguel Cervera, and Pere Roca. “An orthotropic damage model for the analysis of masonry structures.” In: *Construction and Building Materials* 41 (2013), pp. 957–967. ISSN: 0950-0618. DOI: <https://doi.org/10.1016/j.conbuildmat.2012.07.014> (cit. on pp. 5, 58, 59, 90, 91, 95, 107, 109, 110).
- [180] Luca Pelà, Miguel Cervera, and Pere Roca. “Continuum damage model for orthotropic materials: Application to masonry.” In: *Computer Methods in Applied Mechanics and Engineering* 200.9 (2011), pp. 917–930. ISSN: 0045-7825. DOI: <https://doi.org/10.1016/j.cma.2010.11.010> (cit. on pp. 90, 95, 96).
- [181] Massimo Petracca. “Computational multiscale analysis of masonry structures.” PhD thesis. Universitat Politècnica de Catalunya. Departament d’Enginyeria Civil i Ambiental, 2016. URL: <http://hdl.handle.net/2117/96337> (cit. on pp. 5, 57, 58, 91–93).
- [182] Massimo Petracca, Luca Pelà, Riccardo Rossi, Sergio Oller, Guido Camata, and Enrico Spacone. “Multiscale computational first order homogenization of thick shells for the analysis of out-of-plane loaded masonry walls.” In: *Computer Methods in Applied Mechanics and Engineering* 315 (Nov. 2016). DOI: [10.1016/j.cma.2016.10.046](https://doi.org/10.1016/j.cma.2016.10.046) (cit. on pp. 58, 60, 91–94, 117, 123, 189, 190).
- [183] Massimo Petracca, Luca Pelà, Riccardo Rossi, Sergio Oller, Guido Camata, and Enrico Spacone. “Regularization of first order computational homogenization for multiscale analysis of masonry structures.” In: *Computational Mechanics* 57 (Feb. 2016), pp. 257–276. DOI: [10.1007/s00466-015-1230-6](https://doi.org/10.1007/s00466-015-1230-6) (cit. on pp. 91, 94, 107).
- [184] B. Philipp, M. Breitenberger, I. D’Auria, R. Wüchner, and K.-U. Bletzinger. “Integrated design and analysis of structural membranes using the Isogeometric B-Rep Analysis.” In: *Computer Methods in Applied Mechanics and Engineering* 303 (2016), pp. 312–340. ISSN: 00457825. DOI: [10.1016/j.cma.2016.02.003](https://doi.org/10.1016/j.cma.2016.02.003) (cit. on pp. 28, 41, 51).
- [185] Les Piegl and Wayne Tiller. *The NURBS Book (2Nd Ed.)* New York, NY, USA: Springer-Verlag New York, Inc., 1997. ISBN: 3-540-61545-8 (cit. on pp. 20, 21, 38).
- [186] Bora Pulatsu, Eduardo Bretas, and Paulo Lourenco. “Discrete element modeling of masonry structures: Validation and application.” In: *Earthquakes and Structures* 11 (Oct. 2016), pp. 563–582. DOI: [10.12989/eas.2016.11.4.563](https://doi.org/10.12989/eas.2016.11.4.563) (cit. on p. 99).

- [187] Bora Pulatsu, Ece Erdogmus, and Eduardo Bretas. “Parametric Study on Masonry Arches Using 2D Discrete-Element Modeling.” In: *Journal of Architectural Engineering* 24 (Mar. 2018). DOI: [10.1061/\(ASCE\)AE.1943-5568.0000305](https://doi.org/10.1061/(ASCE)AE.1943-5568.0000305) (cit. on p. 99).
- [188] S. Hashemi Rafsanjani, P.B. Lourenço, and N. Peixinho. “Dynamic interface model for masonry walls subjected to high strain rate out-of-plane loads.” In: *International Journal of Impact Engineering* 76 (2015), pp. 28–37. ISSN: 0734-743X. DOI: <https://doi.org/10.1016/j.ijimpeng.2014.09.002> (cit. on p. 57).
- [189] T. Ramos, A. Furtado, S. Eslami, S. Alves, H. Rodrigues, A. Arêde, P.J. Tavares, and P.M.G.P. Moreira. “2D and 3D Digital Image Correlation in Civil Engineering - Measurements in a Masonry Wall.” In: vol. 114. 2015, pp. 215–222. DOI: [10.1016/j.proeng.2015.08.061](https://doi.org/10.1016/j.proeng.2015.08.061) (cit. on p. 67).
- [190] E. Rank, M. Ruess, S. Kollmannsberger, D. Schillinger, and A. Düster. “Geometric modeling, isogeometric analysis and the finite cell method.” In: *Computer Methods in Applied Mechanics and Engineering* 249-252 (2012). Higher Order Finite Element and Isogeometric Methods, pp. 104–115. ISSN: 0045-7825. DOI: <https://doi.org/10.1016/j.cma.2012.05.022> (cit. on p. 35).
- [191] Emanuele Reccia, Antonio Cazzani, and Antonella Cecchi. “FEM-DEM Modeling for Out-of-plane Loaded Masonry Panels: A Limit Analysis Approach.” In: *The Open Civil Engineering Journal* Volume 6 (Nov. 2012), Pages 231–238. DOI: [10.2174/1874149501206010231](https://doi.org/10.2174/1874149501206010231) (cit. on p. 99).
- [192] Ulrich Reif and Peter Schröder. “Curvature integrability of subdivision surfaces.” In: *Advances in Computational Mathematics* 14.2 (2001), pp. 157–174. ISSN: 1572-9044. DOI: [10.1023/A:1016685104156](https://doi.org/10.1023/A:1016685104156) (cit. on p. 22).
- [193] Rhinoceros. URL: [www.rhino3d.com](http://www.rhino3d.com) (cit. on pp. 177, 178).
- [194] Felix Rickhey, Minsoo Kim, Hyungyil Lee, and Naksoo Kim. “Evaluation of combined hardening coefficients of zircaloy-4 sheets by simple shear test.” In: *Materials & Design* 65 (2015), pp. 995–1000. ISSN: 0261-3069. DOI: <https://doi.org/10.1016/j.matdes.2014.10.027> (cit. on p. 79).
- [195] *RILEM TC24-BW. General recommendations for methods of testing load-bearing walls.* 1980 (cit. on p. 64).
- [196] Trevor T. Robinson, Cecil G. Armstrong, and Hung Soon Chua. “Determining the parametric effectiveness of a CAD model.” In: *Engineering with Computers* 29.1 (2013), pp. 111–126. ISSN: 1435-5663. DOI: [10.1007/s00366-011-0248-4](https://doi.org/10.1007/s00366-011-0248-4) (cit. on p. 178).
- [197] Martin Ruess, Dominik Schillinger, Ali I. Özcan, and Ernst Rank. “Weak coupling for isogeometric analysis of non-matching and trimmed multi-patch geometries.” In: *Computer Methods in Applied Mechanics and Engineering* 269 (2014), pp. 46–71. ISSN: 00457825. DOI: [10.1016/j.cma.2013.10.009](https://doi.org/10.1016/j.cma.2013.10.009) (cit. on p. 31).

- [198] E. M. Kober S. G. Bardenhagen. “The Generalized Interpolation Material Point Method.” In: *Computer Modeling in Engineering & Sciences* 5.6 (2004), pp. 477–496. ISSN: 1526-1506. DOI: [10.3970/cmes.2004.005.477](https://doi.org/10.3970/cmes.2004.005.477) (cit. on p. 48).
- [199] A. Sadeghirad, R. M. Brannon, and J. Burghardt. “A convected particle domain interpolation technique to extend applicability of the material point method for problems involving massive deformations.” In: *International Journal for Numerical Methods in Engineering* 86.12 (2011), pp. 1435–1456. DOI: <https://doi.org/10.1002/nme.3110> (cit. on p. 48).
- [200] Amir Hosein Salmanpour and Nebojsa Mojsilovic. “Application of Digital Image Correlation for strain measurements of large masonry walls.” In: Dec. 2013 (cit. on p. 67).
- [201] Miquel Santasusana Isach, Joaquín Irazábal González, Eugenio Oñate, and Josep Carbonell. “The Double Hierarchy Method. A parallel 3D contact method for the interaction of spherical particles with rigid FE boundaries using the DEM.” In: *Computational Particle Mechanics* 3 (Apr. 2016). DOI: [10.1007/s40571-016-0109-4](https://doi.org/10.1007/s40571-016-0109-4) (cit. on p. 3).
- [202] MMM Sarcar, K Mallikarjuna Rao, and K Lalit Narayan. *Computer aided design and manufacturing*. PHI Learning Pvt. Ltd., 2008 (cit. on p. 9).
- [203] Klaus Bernd Sautter, Helene Hofmann, Corinna Wendeler, Peter Wilson, Philipp Bucher, Kai-Uwe Bletzinger, and Roland Wüchner. “Advanced Modeling and Simulation of Rockfall Attenuator Barriers Via Partitioned DEM-FEM Coupling.” In: *Frontiers in Built Environment* 7 (2021). DOI: [10.3389/fbuil.2021.659382](https://doi.org/10.3389/fbuil.2021.659382) (cit. on p. 3).
- [204] Klaus Bernd Sautter, Manuel Meßmer, Tobias Teschemacher, and Kai-Uwe Bletzinger. “Limitations of the St. Venant–Kirchhoff material model in large strain regimes.” In: *International Journal of Non-Linear Mechanics* 147 (2022), p. 104207. ISSN: 0020-7462. DOI: <https://doi.org/10.1016/j.ijnonlinmec.2022.104207> (cit. on p. 198).
- [205] Klaus Bernd Sautter, Tobias Teschemacher, Miguel Ángel Celigueta, Philipp Bucher, Kai-Uwe Bletzinger, and Roland Wüchner. “Partitioned Strong Coupling of Discrete Elements with Large Deformation Structural Finite Elements to Model Impact on Highly Flexible Tension Structures.” In: *Advances in Civil Engineering* 2020 (2020). ISSN: 1687-8086. DOI: [10.1155/2020/5135194](https://doi.org/10.1155/2020/5135194) (cit. on pp. 3, 55, 187).
- [206] Robert Schmidt, Roland Wüchner, and Kai-Uwe Bletzinger. “Isogeometric analysis of trimmed NURBS geometries.” In: *Computer Methods in Applied Mechanics and Engineering* 241-244 (2012), pp. 93–111. ISSN: 00457825. DOI: [10.1016/j.cma.2012.05.021](https://doi.org/10.1016/j.cma.2012.05.021) (cit. on p. 31).

- [207] Uwe Schramm and Walter D. Pilkey. “The coupling of geometric descriptions and finite elements using NURBs — A study in shape optimization.” In: *Finite Elements in Analysis and Design* 15.1 (1993), pp. 11–34. DOI: [10.1016/0168-874X\(93\)90067-Z](https://doi.org/10.1016/0168-874X(93)90067-Z) (cit. on p. 29).
- [208] Michael A. Scott, Michael J. Borden, Clemens V. Verhoosel, Thomas W. Sederberg, and Thomas J. R. Hughes. “Isogeometric finite element data structures based on Bèzier extraction of T-splines.” In: *International Journal for Numerical Methods in Engineering* 88.2 (2011), pp. 126–156. ISSN: 00295981. DOI: [10.1002/nme.3167](https://doi.org/10.1002/nme.3167) (cit. on p. 22).
- [209] Roberto Scotta, Renato Vitaliani, Anna Saetta, Eugenio Oñate, and Alex Hanganu. “A scalar damage model with a shear retention factor for the analysis of reinforced concrete structures: theory and validation.” In: *Computers & Structures* 79.7 (2001), pp. 737–755. ISSN: 0045-7949. DOI: [https://doi.org/10.1016/S0045-7949\(00\)00178-4](https://doi.org/10.1016/S0045-7949(00)00178-4) (cit. on p. 101).
- [210] Jean-François Sigrist. *Fluid-Structure Interaction: An Introduction to Finite Element Coupling*. Wiley, 2015. ISBN: 9781118927748 (cit. on p. 49).
- [211] Luís Silva, Paulo Lourenco, and Gabriele Milani. “Rigid block and spring homogenized model (HRBSM) for masonry subjected to impact and blast loading.” In: *International Journal of Impact Engineering* 109 (Nov. 2017), pp. 14–28. DOI: [10.1016/j.ijimpeng.2017.05.012](https://doi.org/10.1016/j.ijimpeng.2017.05.012) (cit. on p. 58).
- [212] Hrvoje Smoljanović, Nikolina Zivaljic, and Željana Nikolić. “Overview of the methods for the modelling of historical masonry structures.” In: *Gradevinar* 65 (July 2013), pp. 603–618. DOI: [10.14256/JCE.890.2013](https://doi.org/10.14256/JCE.890.2013) (cit. on p. 57).
- [213] Michael Steffen, Robert M. Kirby, and Martin Berzins. “Analysis and reduction of quadrature errors in the material point method (MPM).” In: *International Journal for Numerical Methods in Engineering* 76.6 (2008), pp. 922–948. ISSN: 1097-0207. DOI: [10.1002/nme.2360](https://doi.org/10.1002/nme.2360) (cit. on p. 48).
- [214] *Step, ISO 10303-21*. International Organization for Standardization, 2016. URL: <https://www.iso.org/standard/63141.html> (cit. on p. 13).
- [215] Bilal Succar. “Building information modelling framework: A research and delivery foundation for industry stakeholders.” In: *Automation in Construction* 18.3 (2009), pp. 357–375. ISSN: 0926-5805. DOI: <https://doi.org/10.1016/j.autcon.2008.10.003> (cit. on p. 7).
- [216] D. Sulsky, Z. Chen, and H. L. Schreyer. “A particle method for history-dependent materials.” In: *Computer Methods in Applied Mechanics and Engineering* 118.1 (1994), pp. 179–196. ISSN: 0045-7825. DOI: [10.1016/0045-7825\(94\)90112-0](https://doi.org/10.1016/0045-7825(94)90112-0) (cit. on p. 46).

- [217] Deborah Sulsky and Ming Gong. “Improving the Material-Point Method.” In: *Innovative numerical approaches for multi-field and multi-scale problems*. Ed. by Kerstin Weinberg and Anna Pandolfi. Lecture notes in applied and computational mechanics. Cham: Springer, 2016, pp. 217–240. ISBN: 978-3-319-39022-2. DOI: [10.1007/978-3-319-39022-2](https://doi.org/10.1007/978-3-319-39022-2) (cit. on p. 48).
- [218] Michael A. Sutton, Jean-Jos Orteu, and Hubert Schreier. *Image Correlation for Shape, Motion and Deformation Measurements: Basic Concepts, Theory and Applications*. 1st. Springer Publishing Company, Incorporated, 2009. ISBN: 0387787461. DOI: <https://doi.org/10.1007/978-0-387-78747-3> (cit. on p. 67).
- [219] Barna Szabó and Ivo Babuška. “Finite Element Analysis: Method, Verification and Validation.” In: (2021) (cit. on p. 28).
- [220] Barna Szabó, Alexander Düster, and Ernst Rank. “The p-Version of the Finite Element Method.” In: *Encyclopedia of Computational Mechanics*. John Wiley and Sons, Ltd, 2004. Chap. 5. ISBN: 9780470091357. DOI: <https://doi.org/10.1002/0470091355.ecm003g> (cit. on p. 28).
- [221] Alberto Taliercio. “Closed-form expressions for the macroscopic in-plane elastic and creep coefficients of brick masonry.” In: *International Journal of Solids and Structures* 51.17 (2014), pp. 2949–2963. ISSN: 0020-7683. DOI: <https://doi.org/10.1016/j.ijsolstr.2014.04.019> (cit. on p. 60).
- [222] T. Teschemacher, A. M. Bauer, T. Oberbichler, M. Breitenberger, R. Rossi, R. Wüchner, and K.-U. Bletzinger. “Realization of CAD-integrated shell simulation based on isogeometric B-Rep analysis.” In: *Advanced Modeling and Simulation in Engineering Sciences* 5.1 (2018), pp. 1–54. ISSN: 2213-7467. DOI: [10.1186/s40323-018-0109-4](https://doi.org/10.1186/s40323-018-0109-4) (cit. on pp. 6, 13, 18, 19, 29, 30, 34, 42, 160–162, 184).
- [223] Tobias Teschemacher, Anna M. Bauer, Ricky Aristio, Manuel Messmer, Roland Wüchner, and Kai-Uwe Bletzinger. “Concepts of data collection for the CAD-integrated isogeometric analysis.” In: *Engineering with Computers* (2022), pp. 1435–5663. DOI: <https://doi.org/10.1007/s00366-022-01732-4> (cit. on pp. 6, 41, 177, 187).
- [224] Tobias Teschemacher, Anna Maria Bauer, Ricky Aristio, Manuel Messmer, Roland Wüchner, and Kai-Uwe Bletzinger. <https://github.com/CocodriloCAD/Cocodrilo>. URL: [Cocodrilo](https://github.com/CocodriloCAD/Cocodrilo) (cit. on pp. 177, 188).
- [225] Tobias Teschemacher and Kai-Uwe Bletzinger. “CAD-integrated parametric modular construction design.” In: *Engineering Reports* (2023). DOI: <https://doi.org/10.1002/eng2.12632> (cit. on p. 188).
- [226] Tobias Teschemacher, Miguel Ángel Celigueta Jordana, Guillermo Casas González, R Wüchner, and K-U Bletzinger. “Particle-structure interaction using cad-based boundary descriptions and isogeometric B-REP analysis (IBRA).” In: (2019) (cit. on pp. 3, 187).

- [227] Tobias Teschemacher, Philip Kalkbrenner, Luca Pelà, Roland Wüchner, and Kai-Uwe Bletzinger. “An orthotropic damage model for masonry walls with consistent damage evolution laws.” In: *Materials & Structures* 56:151 (2023). DOI: <https://doi.org/10.1617/s11527-023-02220-x> (cit. on p. 6).
- [228] Tobias Teschemacher, Peter Wilson, Roland Wüchner, and Kai-Uwe Bletzinger. “Macroscopic characterization of modern masonry.” In: *Engineering Structures* 268 (2022), p. 114630. ISSN: 0141-0296. DOI: <https://doi.org/10.1016/j.engstruct.2022.114630> (cit. on pp. 6, 61, 68, 180).
- [229] Tobias Teschemacher, Roland Wüchner, and Kai-Uwe Bletzinger. “Parametric CAD-integrated simulation of masonry structures based on the isogeometric analysis.” In: *Computers & Structures* 289 (2023), p. 107148. ISSN: 0045-7949. DOI: <https://doi.org/10.1016/j.compstruc.2023.107148> (cit. on p. 6).
- [230] Julian Ajith Thamboo and Manicka Dhanasekar. “Correlation between the performance of solid masonry prisms and wallettes under compression.” In: *Journal of Building Engineering* 22 (2019), pp. 429–438. ISSN: 2352-7102. DOI: <https://doi.org/10.1016/j.jobe.2019.01.007> (cit. on pp. 65, 186).
- [231] D. Theodossopoulos, B. P. Sinha, and A. S. Usmani. “Case Study of the Failure of a Cross Vault: Church of Holyrood Abbey.” In: *Journal of Architectural Engineering* 9.3 (2003), pp. 109–117. DOI: [10.1061/\(ASCE\)1076-0431\(2003\)9:3\(109\)](https://doi.org/10.1061/(ASCE)1076-0431(2003)9:3(109)) (cit. on p. 136).
- [232] Roel Tielen, Elizaveta Wobbles, Matthias Möller, and Lars Beuth. “A High Order Material Point Method.” In: *Procedia Engineering* 175 (2017), pp. 265–272. ISSN: 1877-7058. DOI: [10.1016/j.proeng.2017.01.022](https://doi.org/10.1016/j.proeng.2017.01.022) (cit. on p. 48).
- [233] B. H. V. Topping. *Finite element mesh generation*. Saxe-Coburg publications on computational engineering. Stirling and Scotland: Saxe-Coburg Publications, 2004. ISBN: 1-874672-10-5 (cit. on p. 2).
- [234] Stephen W. Tsai and Edward M. Wu. “A General Theory of Strength for Anisotropic Materials.” In: *Journal of Composite Materials* 5.1 (1971), pp. 58–80. DOI: [10.1177/002199837100500106](https://doi.org/10.1177/002199837100500106) (cit. on pp. 90, 94).
- [235] Jaroslav Vaculik and Michael C. Griffith. “Out-of-plane load–displacement model for two-way spanning masonry walls.” In: *Engineering Structures* 141 (2017), pp. 328–343. ISSN: 0141-0296. DOI: <https://doi.org/10.1016/j.engstruct.2017.03.024> (cit. on pp. 85, 117).
- [236] Jaroslav Vaculik and Michael C. Griffith. “Out-of-plane shaketable testing of unreinforced masonry walls in two-way bending.” In: *Bulletin of Earthquake Engineering* 16 (2017), pp. 2839–2876. DOI: <https://doi.org/10.1007/s10518-017-0282-8> (cit. on pp. 85, 117).

- [237] John Vassberg, Mark Dehaan, Melissa Rivers, and Richard Wahls. “Development of a Common Research Model for Applied CFD Validation Studies.” In: *26th AIAA Applied Aerodynamics Conference*. DOI: [10.2514/6.2008-6919](https://doi.org/10.2514/6.2008-6919) (cit. on pp. 33–35).
- [238] Alban de Vaucorbeil, Vinh Phu Nguyen, and Christopher R. Hutchinson. “A Total-Lagrangian Material Point Method for solid mechanics problems involving large deformations.” In: *Computer Methods in Applied Mechanics and Engineering* 360 (2020), p. 112783. ISSN: 0045-7825. DOI: [10.1016/j.cma.2019.112783](https://doi.org/10.1016/j.cma.2019.112783) (cit. on p. 48).
- [239] Bundesministerium für Verkehr und digitale Infrastruktur. *Stufenplan Digitales Planen und Bauen*. URL: [www.bmvi.de](http://www.bmvi.de) (cit. on p. 7).
- [240] A. T. Vermeltoort. “Analysis and experiments of masonry arches.” In: 2001 (cit. on pp. 103, 124, 126, 127).
- [241] A.Th. Vermeltoort and T.M.J. Raijmakers. *Deformation controlled tests in masonry shear walls, Part 2*. 1993 (cit. on pp. 73, 103, 106–109, 111–115).
- [242] M.R.A. van Vliet. “Shear tests on masonry panels; Literature survey and proposal for experiments.” In: *TNO Building and Construction Research* (2004). URL: [http://www.esecmase.org/doc/deliverables\\_public/D\\_6.1\\_TNO.pdf](http://www.esecmase.org/doc/deliverables_public/D_6.1_TNO.pdf) (cit. on p. 76).
- [243] Benjamin Wassermann, Stefan Kollmannsberger, Tino Bog, and Ernst Rank. “From Geometric Design to Numerical Analysis: A direct approach using the Finite Cell Method on Constructive Solid Geometry.” In: *Comput. Math. Appl.* 74.7 (2017), pp. 1703–1726. ISSN: 0898-1221. DOI: [10.1016/j.camwa.2017.01.027](https://doi.org/10.1016/j.camwa.2017.01.027) (cit. on p. 35).
- [244] Benjamin Wassermann, Stefan Kollmannsberger, Shuohui Yin, László Kudela, and Ernst Rank. “Integrating CAD and numerical analysis: ‘Dirty geometry’ handling using the Finite Cell Method.” In: *Computer Methods in Applied Mechanics and Engineering* 351 (2019), pp. 808–835. ISSN: 0045-7825. DOI: <https://doi.org/10.1016/j.cma.2019.04.017> (cit. on p. 35).
- [245] *What Is Digital Twin Technology*. Accessed: 2021-08-24. URL: <https://www.forbes.com/sites/bernardmarr/2017/03/06/what-is-digital-twin-technology-and-why-is-it-so-important/?sh=60ac3fd12e2a> (cit. on p. 13).
- [246] Peter Wilson, Tobias Teschemacher, Philipp Bucher, and Roland Wüchner. “Non-conforming FEM-FEM coupling approaches and their application to dynamic structural analysis.” In: *Engineering Structures* 241 (2021), p. 112342. ISSN: 0141-0296. DOI: [10.1016/j.engstruct.2021.112342](https://doi.org/10.1016/j.engstruct.2021.112342) (cit. on pp. 6, 32, 55, 56, 174, 187).

- [247] Peter Wilson, Roland Wüchner, and Dilum Fernando. “Distillation of the material point method cell crossing error leading to a novel quadrature-based C0 remedy.” In: *International Journal for Numerical Methods in Engineering* 122.6 (2021), pp. 1513–1537. ISSN: 1097-0207. DOI: [10.1002/nme.6588](https://doi.org/10.1002/nme.6588) (cit. on p. 48).
- [248] Peter J. Wilson. “A computational impact analysis approach leveraging non-conforming spatial, temporal and methodological discretisations.” PhD thesis. The University of Queensland, School of Engineering, 2022 (cit. on p. 48).
- [249] Jian Ying Wu, Jie Li, and Rui Faria. “An energy release rate-based plastic-damage model for concrete.” In: *International Journal of Solids and Structures* 43.3 (2006), pp. 583–612. ISSN: 0020-7683. DOI: <https://doi.org/10.1016/j.ijsolstr.2005.05.038> (cit. on pp. 90, 91).
- [250] Roland Wüchner. “Mechanik und Numerik der Formfindung und Fluid-Struktur-Interaktion von Membrantragwerken.” Dissertation. München: Technische Universität München, 2006. URL: <http://mediatum.ub.tum.de/?id=601102> (cit. on pp. 3, 49, 55).
- [251] Walter Wunderlich and Walter D. Pilkey. *Mechanics of Structures*. 2002. ISBN: 978-0-429-11509-7. DOI: <https://doi.org/10.1201/9781420041835> (cit. on p. 15).
- [252] Yong Gan, Zheng Sun, Zhen Chen, Xiong Zhang, and Yu Liu. “Enhancement of the material point method using B-spline basis functions.” In: *International Journal for Numerical Methods in Engineering* 113.3 (2018), pp. 411–431. ISSN: 1097-0207. DOI: [10.1002/nme.5620](https://doi.org/10.1002/nme.5620) (cit. on p. 48).
- [253] Nils Zander, Tino Bog, Stefan Kollmannsberger, Dominik Schillinger, and Ernst Rank. “Multi-level hp-adaptivity: high-order mesh adaptivity without the difficulties of constraining hanging nodes.” In: *Computational Mechanics* 55.3 (2015), pp. 499–517. DOI: [10.1007/s00466-014-1118-x](https://doi.org/10.1007/s00466-014-1118-x) (cit. on pp. 22, 41).
- [254] Qiaoling Zhang, Malcolm Sabin, and Fehmi Cirak. “Subdivision surfaces with isogeometric analysis adapted refinement weights.” In: *Computer-Aided Design* 102 (2018), pp. 104–114. ISSN: 0010-4485. DOI: [10.1016/j.cad.2018.04.020](https://doi.org/10.1016/j.cad.2018.04.020) (cit. on p. 22).
- [255] Yanyang Zhang, Lorenzo Macorini, and Bassam A. Izzuddin. “Mesoscale partitioned analysis of brick-masonry arches.” In: *Engineering Structures* 124 (2016), pp. 142–166. ISSN: 0141-0296. DOI: <https://doi.org/10.1016/j.engstruct.2016.05.046> (cit. on pp. 57, 99, 130).
- [256] Xue-Feng Zhu, Zheng-Dong Ma, and Ping Hu. “Nonconforming isogeometric analysis for trimmed CAD geometries using finite-element tearing and interconnecting algorithm.” In: *Proceedings of the Institution of Mechanical Engineers, Part C: Journal of Mechanical Engineering Science* 231.8 (2017), pp. 1371–1389. ISSN: 0954-4062. DOI: [10.1177/0954406216688491](https://doi.org/10.1177/0954406216688491) (cit. on p. 31).

- [257] O. C. Zienkiewicz and R. L. Taylor. *The finite element method*. Butterworth-Heinemann, 2000. ISBN: 978-0-750-65049-6 (cit. on p. 15).
- [258] O. C. Zienkiewicz, Robert L. Taylor, and J. Z. Zhu. *The Finite Element Method, Its Basis and Fundamentals*. 6th. Oxford: Elsevier, 2005 (cit. on p. 2).
- [259] R. Zorrilla, R. Rossi, R. Wüchner, and E. Oñate. “An embedded Finite Element framework for the resolution of strongly coupled Fluid–Structure Interaction problems. Application to volumetric and membrane-like structures.” In: *Computer Methods in Applied Mechanics and Engineering* 368 (2020), p. 113179. ISSN: 0045-7825. DOI: <https://doi.org/10.1016/j.cma.2020.113179> (cit. on p. 42).
- [260] A Zucchini and P.B Lourenço. “A micro-mechanical model for the homogenisation of masonry.” In: *International Journal of Solids and Structures* 39.12 (2002), pp. 3233–3255. ISSN: 0020-7683. DOI: [https://doi.org/10.1016/S0020-7683\(02\)00230-5](https://doi.org/10.1016/S0020-7683(02)00230-5) (cit. on pp. 58, 60).
- [261] A. Zucchini and P.B. Lourenço. “A micro-mechanical homogenisation model for masonry: Application to shear walls.” In: *International Journal of Solids and Structures* 46.3 (2009), pp. 871–886. ISSN: 0020-7683. DOI: <https://doi.org/10.1016/j.ijsolstr.2008.09.034> (cit. on p. 58).



# Previous titles in the series

## Volume Title

- 1 Frank Koschnick, *Geometrische Lockingeffekte bei Finiten Elementen und ein allgemeines Konzept zu ihrer Vermeidung*, 2004.
- 2 Natalia Camprubi, *Design and Analysis in Shape Optimization of Shells*, 2004.
- 3 Bernhard Thomee, *Physikalisch nichtlineare Berechnung von Stahlfaserbetonkonstruktionen*, 2005.
- 4 Fernaß Daoud, *Formoptimierung von Freiformschalen - Mathematische Algorithmen und Filtertechniken*, 2005.
- 5 Manfred Bischoff, *Models and Finite Elements for Thin-walled Structures*, 2005.
- 6 Alexander Hörmann, *Ermittlung optimierter Stabwerkmodelle auf Basis des Kraftflusses als Anwendung plattformunabhängiger Prozesskopplung*, 2006.
- 7 Roland Wüchner, *Mechanik und Numerik der Formfindung und Fluid-Struktur-Interaktion von Membrantragwerken*, 2006.
- 8 Florian Jurecka, *Robust Design Optimization Based on Metamodeling Techniques*, 2007.
- 9 Johannes Linhard, *Numerisch-mechanische Betrachtung des Entwurfsprozesses von Membrantragwerken*, 2009.
- 10 Alexander Kupzok, *Modeling the Interaction of Wind and Membrane Structures by Numerical Simulation*, 2009.
- 11 Bin Yang, *Modified Particle Swarm Optimizers and their Application to Robust Design and Structural Optimization*, 2009.
- 12 Michael Fleischer, *Absicherung der virtuellen Prozesskette für Folgeoperationen in der Umformtechnik*, 2009.
- 13 Amphon Jrusjrunkiat, *Nonlinear Analysis of Pneumatic Membranes - From Subgrid to Interface*, 2009.
- 14 Alexander Michalski, *Simulation leichter Flächentragwerke in einer numerisch generierten atmosphärischen Grenzschicht*, 2010.
- 15 Matthias Firl, *Optimal Shape Design of Shell Structures*, 2010.
- 16 Thomas Gallinger, *Effiziente Algorithmen zur partitionierten Lösung stark gekoppelter Probleme der Fluid-Struktur-Wechselwirkung*, 2011.

- | Volume | Title  |
|--------|--|
| 17     | Josef Kiendl, <i>Isogeometric Analysis and Shape Optimal Design of Shell Structures</i> , 2011.  |
| 18     | Joseph Jordan, <i>Effiziente Simulation großer Mauerwerksstrukturen mit diskreten Rissmodellen</i> , 2011.   |
| 19     | Albrecht von Boetticher, <i>Flexible Hangmurenbarrieren: Eine numerische Modellierung des Tragwerks, der Hangmure und der Fluid-Struktur-Interaktion</i> , 2012.     |
| 20     | Robert Schmidt, <i>Trimming, Mapping, and Optimization in Isogeometric Analysis of Shell Structures</i> , 2013.  |
| 21     | Michael Fischer, <i>Finite Element Based Simulation, Design and Control of Piezoelectric and Lightweight Smart Structures</i> , 2013.                                |
| 22     | Falko Hartmut Dieringer, <i>Numerical Methods for the Design and Analysis for Tensile Structures</i> , 2014.   |
| 23     | Rupert Fisch, <i>Code Verification of Partitioned FSI Environments for Lightweight Structures</i> , 2014.  |
| 24     | Stefan Sicklinger, <i>Stabilized Co-Simulation of Coupled Problems Including Fields and Signals</i> , 2014.  |
| 25     | Madjid Hojjat, <i>Node-based parametrization for shape optimal design</i> , 2015.  |
| 26     | Ute Israel, <i>Optimierung in der Fluid-Struktur-Interaktion - Sensitivitätsanalyse für die Formoptimierung auf Grundlage des partitionierten Verfahrens</i> , 2015. |
| 27     | Electra Stavropoulou, <i>Sensitivity analysis and regularization for shape optimization of coupled problems</i> , 2015.  |
| 28     | Daniel Markus, <i>Numerical and Experimental Modeling for Shape Optimization of Offshore Structures</i> , 2015.  |
| 29     | Pablo Suárez, <i>Design Process for the Shape Optimization of Pressurized Bulkheads as Components of Aircraft Structures</i> , 2015.                                 |
| 30     | Armin Widhammer, <i>Variation of Reference Strategy - Generation of Optimized Cutting Patterns for Textile Fabrics</i> , 2015.                                       |
| 31     | Helmut Masching, <i>Parameter Free Optimization of Shape Adaptive Shell Structures</i> , 2016.   |
| 32     | Hao Zhang, <i>A General Approach for Solving Inverse Problems in Geophysical Systems by Applying Finite Element Method and Metamodel Techniques</i> , 2016.          |
| 33     | Tianyang Wang, <i>Development of Co-Simulation Environment and Mapping Algorithms</i> , 2016.  |
| 34     | Michael Breitenberger, <i>CAD-integrated Design and Analysis of Shell Structures</i> , 2016.   |
| 35     | Önay Can, <i>Functional Adaptation with Hyperkinematics using Natural Element Method: Application for Articular Cartilage</i> , 2016.                                |
| 36     | Benedikt Philipp, <i>Methodological Treatment of Non-linear Structural Behavior in the Design, Analysis and Verification of Lightweight Structures</i> , 2017.       |

- 
- | Volume | Title   |
|--------|---|
| 37     | Michael Andre, <i>Aeroelastic Modeling and Simulation for the Assessment of Wind Effects on a Parabolic Trough Solar Collector</i> , 2018.  |
| 39     | Andreas Apostolatos, <i>Isogeometric Analysis of Thin-Walled Structures on Multipatch Surfaces in Fluid-Structure Interaction</i> , 2019.   |
| 40     | Altuğ Emiroğlu, <i>Multiphysics Simulation and CAD Integrated Shape Optimization in Fluid-Structure Interaction</i> , 2019.   |
| 41     | Reza Najian Asl, <i>Shape optimization and sensitivity analysis of fluids, structures, and their interaction using Vertex Morphing parametrization</i> , 2019.  |
| 42     | Anna Maria Bauer, <i>CAD-integrated Isogeometric Analysis and Design of Lightweight Structures</i> , 2020.  |
| 43     | Ahmed Abodonya, <i>Verification Methodology for Computational Wind Engineering Prediction of Wind Loads on Structures</i> , 2020.   |
| 44     | Andreas Winterstein, <i>Modeling and Simulation of Wind-Structure Interaction of Slender Civil Engineering Structures Including Vibration Mitigation Systems</i> , 2020.                                |
| 45     | Franz-Josef Ertl, <i>Vertex Morphing for constrained shape optimization of three-dimensional solid structures</i> , 2020.   |
| 46     | Michael Andre, <i>On the grid-based shape optimization of structures with internal flow and the feedback of shape changes into a CAD model</i> , 2020.  |
| 47     | Mohamed Magdi Mohamed Mohamed Khalil, <i>Combining Physics-Based Models and Machine Learning for an Enhanced Structural Health Monitoring</i> , 2021.   |
| 48     | Long Chen, <i>Gradient Descent Akin Method</i> , 2021.  |
| 49     | Aditya Ghantasala, <i>Coupling Procedures for Fluid-Fluid and Fluid-Structure Interaction Problems Based on Domain Decomposition Methods</i> , 2021.  |
| 50     | Ann-Kathrin Goldbach, <i>The CAD-Integrated Design Cycle for Structural Membranes</i> , 2021.   |
| 51     | Iñigo Pablo López Canalejo, <i>A Finite-Element Transonic Potential Flow Solver with an Embedded Wake Approach for Aircraft Conceptual Design</i> , 2022.   |
| 52     | Mayu Sakuma, <i>An Application of Multi-Fidelity Uncertainty Quantification for Computational Wind Engineering</i> , 2022.  |
| 53     | Suneth Warnakulasuriya, <i>Development of Methods for Finite Element-Based Sensitivity Analysis and Goal-Directed Mesh Refinement Using the Adjoint Approach for Steady and Transient Flows</i> , 2022. |
| 54     | Klaus Bernd Sautter, <i>Modeling and Simulation of Flexible Protective Structures by Coupling Particle and Finite Element Methods</i> , 2022.   |
| 55     | Efthymios Papoutsis, <i>On the incorporation of industrial constraints in node-based optimization for car body design</i> , 2023.   |
| 56     | Thomas Josef Oberbichler, <i>A modular and efficient implementation of isogeometric analysis for the interactive CAD-integrated design of lightweight structures</i> , 2023.                            |